Technische Universität München
TUM School of Natural Sciences

The molecular architecture of cellular actin networks studied by cryo-electron tomography

Jonathan Schneider

Vollständiger Abdruck der von der TUM School of Natural Sciences der Technischen Universität München zur Erlangung eines Doktors der Naturwissenschaften (Dr. rer. nat.) genehmigten Dissertation.

Vorsitz: Prof. Dr. Michael Sattler

Prüfende der Dissertation:

1. TUM Junior Fellow Dr. Marion Jasnin
2. Hon.-Prof. Dr. Wolfgang Baumeister
3. Prof. Dr. Martin Zacharias

Die Dissertation wurde am 02.04.2024 bei der Technischen Universität München eingereicht und durch die TUM School of Natural Sciences am 12.07.2024 angenommen.

Abstract

The actin cytoskeleton provides the structural and mechanical foundation for an exceptionally wide range of cellular processes. Dynamic assembly and disassembly of actin filaments orchestrated by regulatory proteins is manifested in a plethora of characteristic architectures. Many of these networks exert forces in the nanonewton range, while individual actin filaments generate piconewton forces only. Distinct architectures and interconnection of filaments allow the realization of these forces. How these filament networks are assembled, allowing cells to generate such forces on the molecular level remains poorly understood. This thesis uses cryo-electron tomography in combination with subtomogram averaging to unveil the molecular sociology of actin filaments within podosomes from human macrophages and contractile sarcomeres from neonatal rat cardiomyocytes, and to provide molecular insights into their assembly and mechanisms of force generation.

Human macrophage podosomes are essential during tissue infiltration, where they exert protrusive forces at the basal membrane in the nanonewton range, permitting mechanosensing of the tissue microenvironment, and orchestrate local remodeling of the extracellular matrix. They consist of an actin-rich core surrounded by an adhesion ring, but their molecular architecture remains elusive. In this work, cryo-electron tomography allowed to retrieve a near-complete picture of filament organization, and to decipher the underlying mechanisms of assembly and force generation at the molecular level. The development of a subtomogram averaging-based workflow revealed the polarity of all actin filaments within the network, showing that most filaments have their barbed ends closer to the ventral membrane. Moreover, lateral filaments adopt highly radial conformations, predominantly having their barbed ends away from the core. These filament patterns are orchestrated by the Arp2/3 complex during podosome assembly. The dense podosome core contains upright filaments which flatten under the effect of force and adopt shallow orientations. Continuous polymerization of new filaments lifts pre-existing filaments up, concomitantly increasing the filament density in the core, and enabling the bulk of filaments to generate nanonewton forces.

Sarcomeres are the basic contractile unit of muscle cells, where they generate contractile forces through cross-bridge interactions between thin and thick filaments. Direct visualization of contraction at the molecular level has remained elusive. Using cryo-electron tomography, the molecular architecture permitting sarcomere contraction was visualized across scales. The hexagonal arrangement of thick filaments is established at the neonatal stage, but an excess of thin filaments is found outside the trigonal positions of the lattice. Subtomogram averaging resolved the thin filament polarity and visualized their relative sliding during contraction, forming overlapping arrays at the sarcomere center. The degree of overlap was directly correlated to structural differences in the thin filament attributed to distinct functional states, highlighting sarcomere contraction across scales.

Zusammenfassung

Das Aktin-Zytoskelett bildet die strukturelle und mechanische Grundlage für ein außergewöhnlich breites Spektrum an zellulären Prozessen. Der dynamische Auf- und Abbau von Aktinfilamenten, der von regulatorischen Proteinen orchestriert wird, spiegelt sich in einer Vielzahl charakteristischer Architekturen wider. Viele dieser Netzwerke üben Kräfte im Bereich von Nanonewton aus, während einzelne Aktinfilamente nur Piconewton-Kräfte erzeugen können. Die ausgeprägte Architektur und die Interaktion vieler Filamente ermöglichen die Realisierung dieser Kräfte. Wie diese Filamentnetzwerke zusammengesetzt sind, sodass Zellen solche Kräfte auf molekularer Ebene erzeugen können, ist noch nicht gut untersucht. In dieser Arbeit wird die Kryo-Elektronentomographie in Kombination mit der Mittelung von Subtomogrammen eingesetzt, um die molekulare Soziologie der Aktinfilamente in Podosomen aus menschlichen Makrophagen und in kontraktilen Sarkomeren aus neonatalen Rattenkardiomyozyten zu enthüllen und Einblicke in ihren Aufbau und die Mechanismen der Krafterzeugung auf molekularer Ebene zu geben.

Podosome aus menschlichen Makrophagen sind während der Gewebsinfiltration von entscheidender Bedeutung, da sie an der Basalmembran ausstülpende Kräfte von mehreren Nanonewton ausüben, die es ermöglichen, die Mikroumgebung des Gewebes mechanisch zu erfassen, und die lokale Umgestaltung der extrazellulären Matrix orchestrieren. Sie bestehen aus einem aktinreichen Kern, umgeben von einem Adhäsionsring, jedoch ist ihre molekulare Architektur nicht genau untersucht. Mit Hilfe der Kryo-Elektronentomographie konnte ein nahezu vollständiges Bild der Filamentorganisation gewonnen und die zugrunde liegenden Mechanismen des Zusammenbaus und der Krafterzeugung auf molekularer Ebene entschlüsselt werden. Durch die Entwicklung eines auf der Mittelung von Subtomogrammen basierenden Ansatzes konnte die Polarität der Aktinfilamente innerhalb des Netzwerks ermittelt werden, wobei sich zeigte, dass die meisten Filamente ihre Plus-Enden näher an der ventralen Membran haben. Laterale Filamente haben radiale Orientierungen an und haben ihre Plus-Enden überwiegend vom Kern entfernt. Die Orientierungen der Filamente wird dabei durch den Arp2/3-Komplex während des Podosomenaufbaus orchestriert. Der dichte Podosomenkern enthält vertikale Filamente, die unter Krafteinwirkung abflachen und flachere Orientierungen einnehmen. Durch die kontinuierliche Polymerisation werden bereits vorhandene Filamente angehoben, wodurch sich die Filamentdichte im Kern erhöht und die Masse der Filamente Kräfte im Nanonewton-Bereich erzeugen kann.

Sarkomere sind die grundlegende kontraktile Einheit von Muskelzellen, wo sie kontraktile Kräfte durch Querbrücken-Interaktionen zwischen dünnen und dicken Filamenten erzeugen. Eine direkte Visualisierung der Kontraktion auf molekularer Ebene war bisher nicht möglich. Mit Hilfe der Kryo-Elektronentomographie wurde die molekulare Architektur, die die Kontraktion der Sarkomere ermöglicht, in verschiedenen Größenordnungen sichtbar gemacht. Die hexagonale Anordnung der dicken Filamente ist im Neugeborenenstadium etabliert, aber überschüssige dünne Filamente befinden sich außerhalb der trigonalen Positionen des Gitters. Durch Mittelung von Subtomogrammen wurde die Polarität der dünnen Filamente aufgezeigt und ihre relative Verschiebung während der Kontraktion sichtbar gemacht, wobei sich überlappende Anordnungen im Zentrum des Sarkomers bildeten. Das Ausmaß der Überlappung steht in direktem Zusammenhang mit strukturellen Unterschieden in den dünnen Filamenten, die verschiedenen funktionalen Zuständen zugeordnet werden können, was die Kontraktion des Sarkomers über verschiedene Skalen hinweg verdeutlicht.

List of publications

The contributions to the following publications were performed throughout the course of my PhD:

Schneider J, Jasnin M: Molecular architecture of the actin cytoskeleton: from single cells to whole organisms using cryo-electron tomography. Curr. Opin. Cell Biol. 2024, 88:102356

Schiotz OH, Kaiser CJO, Klumpe S, Morado DR, Poege M, **Schneider J**, Beck F, Klebl DP, Thompson C, Plitzko JM: Serial Lift-Out: sampling the molecular anatomy of whole organisms. Nat Methods 2023.

Jasnin M, Hervy J, Balor S, Bouissou A, Proag A, Voituriez R, **Schneider J**, Mangeat T, Maridonneau-Parini I, Baumeister W, Dmitrieff S, Poincloux R: Elasticity of podosome actin networks produces nanonewton protrusive forces. Nat Commun 2022, 13:3842.

Schneider J, Jasnin M: Capturing actin assemblies in cells using in situ cryo-electron tomography. Eur J Cell Biol 2022, 101:151224.

The results of this first-author publication are discussed in Chapter 4:

Burbaum L*, **Schneider J***, Scholze S, Bottcher RT, Baumeister W, Schwille P, Plitzko JM, Jasnin M: Molecular-scale visualization of sarcomere contraction within native cardiomyocytes. Nat Commun 2021, 12:4086.
*Equal contribution

The following manuscript is currently under preparation, including the main results of this thesis regarding the podosome in Chapter 3:

Schneider J*, Rey-Barroso J*, Balor S, Bouissou A, Maridonneau-Parini I, Plitzko J, Baumeister W, Poincloux R, Jasnin M: Arp2/3 complex shapes both branched actin networks and the emergence of parallel lateral filaments *(working title, in preparation)*.
*Equal contribution

Table of Contents

List of figures

Chapter 1: Cryo-electron tomography

1.1 Principles of structural biology

Macromolecules such as proteins are folded in distinct ways so that their shape enables dedicated functions and interactions with their environment, permitting complex molecular machines to execute sophisticated biological processes. Accordingly, to understand the function of a protein, it is essential to study its structure. The field of structural biology is dedicated to elucidating and understanding how macromolecules are shaped and how they function. Key techniques include X-ray crystallography, nuclear magnetic resonance and (cryo-) electron microscopy, all of which have made significant contributions and have dedicated applications. Perhaps the most famous example in scientific literature is the discovery of the DNA double-helix structure by Watson, Crick and Franklin, using X-ray crystallography, which immediately suggested the mechanism of DNA replication and transcription [1,2]. From small protein crystals to large protein complexes to structures determined directly within the cell, structural biology has transformed our understanding of biology at the molecular level [3]. In recent years, (cryo-) electron microscopy has seen a significant increase in popularity due to advances in technology and image processing, and has become the method of choice for many research questions in structural biology.

1.2 Electron microscopy

1.2.1 Electron properties and principles of image formation

In quantum mechanics, electrons can be described by the wave-particle duality, exhibiting properties of particles and of waves. Both models are necessary to describe the principles of electrons interacting with a sample and subsequent image formation. Unlike photons, electrons are charged particles with mass. According to de Broglie, published exactly 100 years ago, every particle of mass m at a velocity v has a distinct wavelength λ, with h being the Planck constant [4].

$$\lambda_{DB} = \frac{h}{m_e * v}$$

Electrons interact with matter and electromagnetic fields, so they can be focused through electromagnetic lenses [5]. As such, imaging with electrons allows to retrieve both amplitude and phase information of the sample, in contrast to diffraction analysis by X-rays. The majority of electrons do not interact with the sample and are unscattered (Figure 1A) [6]. However, some electrons do interact with charged particles of the specimen, both with electrons and nuclei. Therefore, the obtained image is a direct result of the Coulomb potential of the specimen. Interaction with the charged particles in the sample trigger scattering events of the incident electrons, of which there are two major types, elastic and inelastic scattering (Figure 1A). Scattering of electrons by an atom depends on the atomic number, in particular the scattering cross-section. The scattering cross-section describes the scattering probability of an electron interacting with the atom, and increases for elements with higher atom numbers.

Elastic scattering is characterized by interaction of the incident electron with a nucleus of the specimen. Due to the mass difference of the nucleus and the electron, there is no energy loss of the electron. The nucleus Coulomb field triggers electrostatic deflection of the electron, where its energy is conserved, but the electron experiences a phase-shift [6]. As such, elastic scattering events contain information about the sample and are responsible for image formation in transmission electron microscopy (TEM). In contrast, inelastic scattering is characterized by interaction with outer shell electrons of the atoms and results in measurable energy-loss. This energy is lost to the sample, where it is responsible for the beam-induced damage and contributes to noise in the image [7].

As electrons possess wave-like properties, the image formation process in TEM is a product of constructive and destructive wave interference (Figure 1B). Destructive interference is characterized by the interaction of waves with opposing phase shifts, so that their amplitudes are canceled out. In contrast, constructive interference results from overlapping waves that are in phase, so their amplitudes are summed. According to Bragg's law, a lattice with spacing d will result in a diffraction pattern, enabled through constructive interference, if the following conditions are met [8].

$$2 * d \sin(\theta) = n \lambda$$

In this equation, λ is the wavelength and θ is the scattering angle. While this equation was initially derived for diffraction of crystals through X-rays, the concept can be also adopted to describe scattering of electrons. For elastic scattering, the electrons are considered as coherent, as there is a phase relationship between the incident wave and the scattered wave that emerges from the sample.

A sample can be described by multiple spacings d (Figure 1C) [9]. For higher resolution information, d gets smaller and the scattering angle θ increases to maintain constructive interference. Accordingly, the waves are inversely sorted by frequency ($1/d$) with the highest resolution information spread out the furthest. The scattered waves are collected by the objective lens. All parallel scattered waves meet in the back focal plane of the lens, where they will interfere [9]. Accordingly, a diffraction pattern is formed that can be understood as the Fourier transform of the image [6]. The objective aperture removes strongly scattered electrons and enables scattering contrast (see below). A new image is formed at the image plane that is then magnified by a projection lens system and ultimately recorded on a detector.

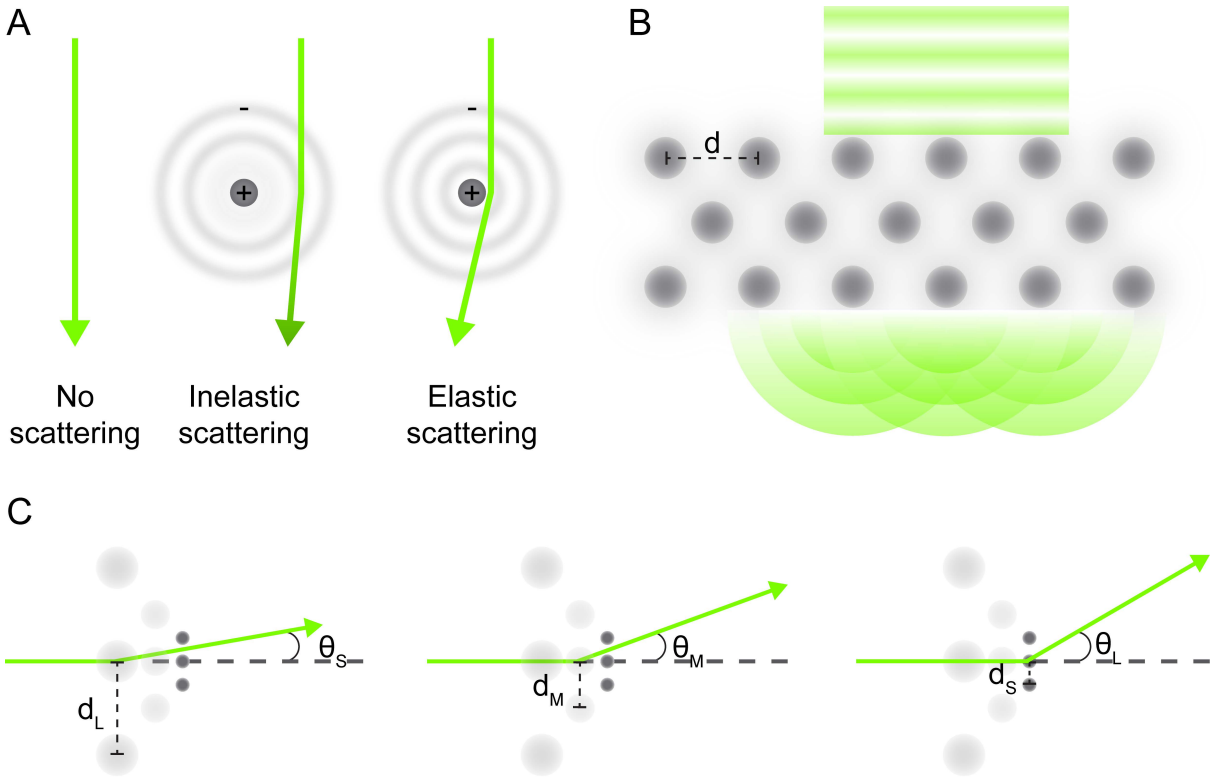

Figure 1: Physical principles of electron interactions with a sample. A: Types of scattering upon interaction with an atom (gray). Most electrons do not interact with the sample (left). Inelastic scattering occurs upon interaction with shell electrons and triggers energy-loss (dark green, middle). Elastic scattering occurs through interaction with the Coulomb field of the nucleus (right). B: Sample consisting of a lattice of atoms spaced by d. A plane-wave is elastically scattered by the sample. The resulting waves are modulated constructive and destructive interference and generate a diffraction pattern at the back-focal plane. C: Scattering angle as a function of the spacing. A sample consisting of several distances d. Left: Large distances (d_L) between scattering points result in small angular deviations (θ_S). Middle: Smaller spacings (d_M) trigger scattering events at larger angles (θ_M). Left: Smallest spacings (d_S) in the samples lead to strong scattering at high angles (θ_L). The resulting scattering pattern at the back-focal plane is inversely sorted by resolution.

Amplitude and phase contrast are the two main types of contrast in TEM, with the latter being most important for biological samples [10]. In amplitude or scattering contrast, heavy atoms lead to severe scattering of electrons at larger angles. Through the objective aperture at the back focal plane of the objective lens, severely scattered electrons are filtered out, leading to less electrons involved in the image formation and therefore darker appearance of heavy atoms. In biological TEM, samples typically consist of elements with low atom numbers that lead to very little amplitude contrast only. Therefore, phase contrast is the predominant source of contrast to visualize biological material, where atoms of biological samples behave as weak phase objects. Phase contrast is characterized by the phase differences introduced in the electron wave upon its interaction with the sample [11].

Through constructive or destructive interference, the phase shift between the elastically scattered and unscattered electron waves modulates the amplitudes of the resulting wave and therefore the contrast that is being detected. Phase contrast can be increased by acquiring an image out of focus, which is also called defocusing. By applying defocus, which is modulated by the objective lens, the imaging plane is shifted away from the sample, which alters its interaction with the electron. The phase relationship between the scattered and unscattered electrons is more pronounced at lower spatial frequencies as the defocus is increased [10]. The phase shift of the scattered electrons varies with spatial frequency, which

in turn generates a frequency-dependent interference pattern (Figure 2). The underlying contrast of a weakly scattering object can be described in Fourier space by the contrast transfer function (CTF) [12]. It is analogues to the real space equivalent point spread function (PSF) and describes the frequency-dependent phase shift of the scattered electrons.

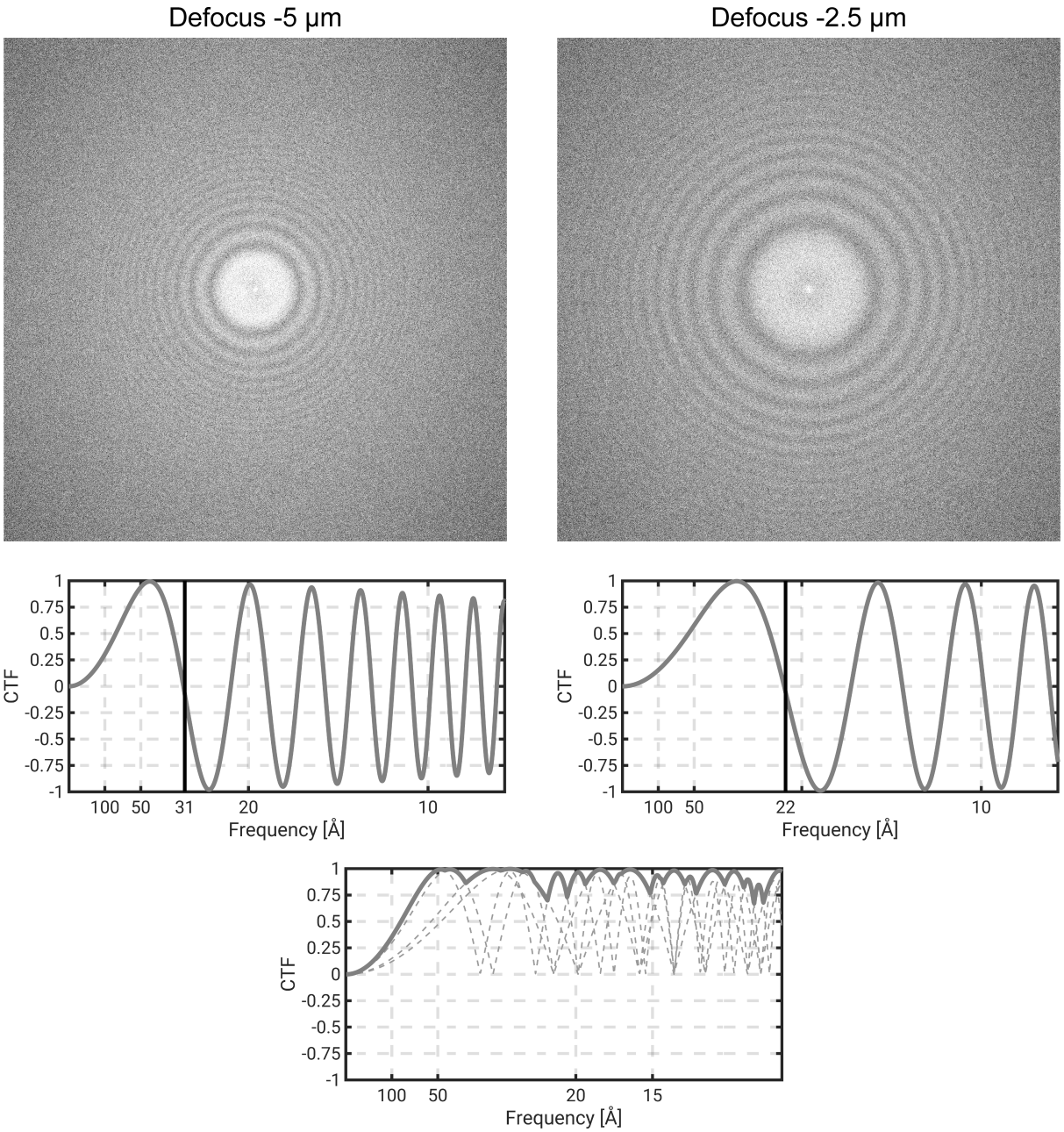

Figure 2: Contrast transfer function. Top: Power spectra of a single projection image with a pixel size of 2.06 Å at high defocus (-5 µm, left) and low defocus (-2.5 µm, right). Middle: Corresponding simulated contrast transfer functions, where the only varied parameter was the defocus. The first zero-crossing are indicated by black lines, located at 31 Å and 22 Å, respectively. Bottom: Phase-flipping and combining of multiple images with varying defocus values results a relatively flat contrast transfer across the entire frequency domain.

$$CTF(k, \Delta z) = \sin\left(\frac{\pi}{2}(C_s\lambda^3 k^4 - 2\Delta z\lambda k^2)\right)$$

The CTF describes the total phase shift as a function of the spatial frequency *k*, the applied defocus Δz, and the spherical aberration (C_s) of the system. The CTF is periodic, and it oscillates faster at higher spatial frequencies. Moreover, it is attenuated by an envelope function that further dampens the contrast transfer at higher spatial frequencies. As a result of the CTF, frequency-dependent contrast is periodically reversed and the spatial information is delocalized. Furthermore, total loss of information occurs at zero-crossings of the CTF that cannot be recovered. To recover the delocalized information, the micrograph needs to be CTF corrected during data processing. This includes estimation of the defocus value for the respective image and subsequent inversion of the phases. As the oscillation of the CTF increases at higher spatial frequencies, errors in the defocus estimation are more pronounced at higher resolution. As the CTF-corrected image still contains amplitude differences and no contrast information at zero-crossings, typically multiple images acquired at varying defocus are combined to obtain a flat transfer of information along the spatial frequency domain (Figure 2 bottom).

1.2.2 Transmission electron microscopy

Electrons have much shorter wavelengths than visible light, which allows electron microscopy (EM) to resolve features well below the diffraction limit [13]. This is ideally suited for studying biological specimen. The first electron microscopy was designed by Ernst Ruska and Max Knoll in 1931 [14]. The typical design of an electron microscope consists of several key components, which will be briefly introduced in the following.

Electron sources can be differentiated into thermionic sources, such as a tungsten wire or lanthanum hexaboride crystals, and field-emission guns (FEGs) [6]. Typically, for modern cryo-TEMs, electrons are accelerated at 200-300kV, while higher acceleration voltages are better suited for thicker samples and tomographic applications. To date, FEGs produce the most coherent electron beam, both spatially and temporally. This coherence refers to as to how close to a singular point the source can be approximated, and how constant the emanating electron wavelength is, respectively [6].

Electrons interact with magnetic fields, and can therefore be shaped by electromagnetic lenses, which are used to focus the beam and magnify the resulting image. In a typical top-down electron microscope, the beam is shaped by the condenser lens system, which consists of 2-3 condenser lenses (C1-C3). This lens system controls the spot size and beam intensity, and also ensures parallel illumination. The objective lens is a twin-lens and consists of two electromagnetic fields above and below the specimen, respectively. This lens system controls the interaction of the beam with the sample through focusing. Subsequently, the diffraction lens is followed by the projection lens system that consists of several lenses to magnify the final image [10].

There are several aberrations regarding electromagnetic lenses which need to be considered for image acquisition. Spherical aberration (C_s) describes the process in which electrons interact differently with the electromagnetic field the further it deviates from the center. This results in a focal area in the diffraction plane, rather than a single point function.

To overcome this, typical microscope settings involve very small opening angles and use coma free alignment, which is aligning the microscope parallel to the optical axis. This prevents uneven rotational contribution of the C_s of the objective lens, referred to as coma [9]. C_s correctors create a negative spherical aberration and correct the signal. Chromatic aberration (C_c) describes the process where electrons pass through the lens at various speed and therefore possess different wavelengths. Slower electrons are affected more by the electromagnetic field compared to fast electrons. C_c can be corrected for by using an energy filter or monochromators. Finally, astigmatism describes the extend of the non-uniform strength of the electromagnetic field, that leads to an oval-shaped beam in the condenser lenses, as well as focus gradients in the objective lenses [6].

Energy filters act as prisms that sort electrons according to their energy. By introducing a narrow slit into the beam, it allows to select zero-loss electrons, i.e., electrons with no energy transfer towards the sample, therefore removing inelastically scattered electrons with different wavelengths. However, it can be also used to filter electrons with specific energies, which is often used in material sciences.

In the past, electron micrographs were recorded either on film, which was very labor intensive, or on charge-coupled device (CCD) cameras. The latter system comprises an indirect detection method, as the incoming electrons are converted into photons through a scintillator layer. However, this results in multiple electron scattering events due to the scintillator thickness, and due to the emitted photons spreading to neighboring pixels. In contrast, direct electron detectors (DEDs) revolutionized the detection of macromolecules in cryo-EM applications [15]. Electrons are directly detected and charges accumulate in a semiconductor pixel that can be read out rapidly, and the detective quantum efficiency (DQE) is significantly improved compared to film or conventional CCD cameras [16]. Moreover, the back-thinned chip is considerably thinner and results in fewer multiple scattering events from back-scattering. The fast read out of DEDs allows for images to be recorded as movies, with the individual frames describing sample movement during acquisition due to beam-induced motion.

Phase plates are commonly used in EM, especially for thick or small samples, but lost their broader application in recent years. In cryo-EM, the Volta phase plate (VPP) is most common, but also laser phase plates are currently developed [17,18]. The phase object, in case of the VPP a continuous carbon film, modulates the phases of passing electrons by generating a Volta potential, and creates an additional phase shift of $\pi/2$. The additional phase shift between scattered and non-scattered electrons leads to improved contrast for lower spatial frequencies and facilitates the detection of smaller particles.

1.3 Cryo-electron microscopy

Cryo-electron microscopy (cryo-EM) is an increasingly popular method in structural biology and becomes the method of choice for studying the structure of various macromolecules [19]. Since the often-termed resolution revolution, that consisted in the development of DEDs and advanced image processing tools, the routinely achievable resolution limits dropped significantly from around 8 Å to 3 Å, permitting to resolve side chains and allow *de novo* model building. Today, resolutions close to atomic resolution are achievable and resolution is nowadays mainly limited by the sample [20,21].

As hydrated specimen such as biological material are extremely volatile to TEM imaging due to radiation damage and evaporation in the high vacuum, the sample needs to be fixed before imaging. Traditional methods include negative staining, where an electron-dense material such as uranyl acetate is used to stain the material. However, this method only allows for amplitude contrast and there is no phase contrast information retrievable. The highest preservation is obtained through cryo-fixation, where the sample is embedded in vitreous ice [22]. Here, a water-based sample, such as biological specimens, is frozen in a way that the water is trapped in a liquid-like state and the formation of ice crystals, which would damage the sample, is prevented [23]. This is either realized by plunge-freezing, where the sample is rapidly cooled using a cooling agent with high heat transfer capacity, typically liquid ethane, or by high-pressure freezing, where the temperature is decreased and the pressure simultaneously increased and the phase transition from liquid to solid is prevented. To date, vitrification is the preservation method of choice that allows a near-native preservation and minimizes the introduction of artefacts.

Cryo-EM comes in two major disciplines, single-particle analysis (SPA) and cryo-electron tomography. SPA is the most popular method and was instrumental for most high-resolution structures that were solved by cryo-EM [24]. It works on isolated and purified macromolecules, such as proteins, that are distributed randomly across the grid. Individual particles with random orientations are then iteratively aligned and subsequently averaged to generate a high-resolution structure with substantially improved signal to noise ratio.

1.4 *In situ* cryo-electron tomography

The promise of *in situ* cryo-electron tomography (cryo-ET) is to perform structural biology within the cell [25,26]. In biology, macromolecules rarely perform their tasks in isolation, but interact with a variety of other proteins and cofactors. Furthermore, many proteins are inherently flexible and only adopt functional states when bound to a dedicated ligand. Finally, the spatial organization of molecules in the cell and with respect to each other is essential for many cellular reactions to function as intended. To understand this molecular sociology, cryo-ET emerged as the method of choice.

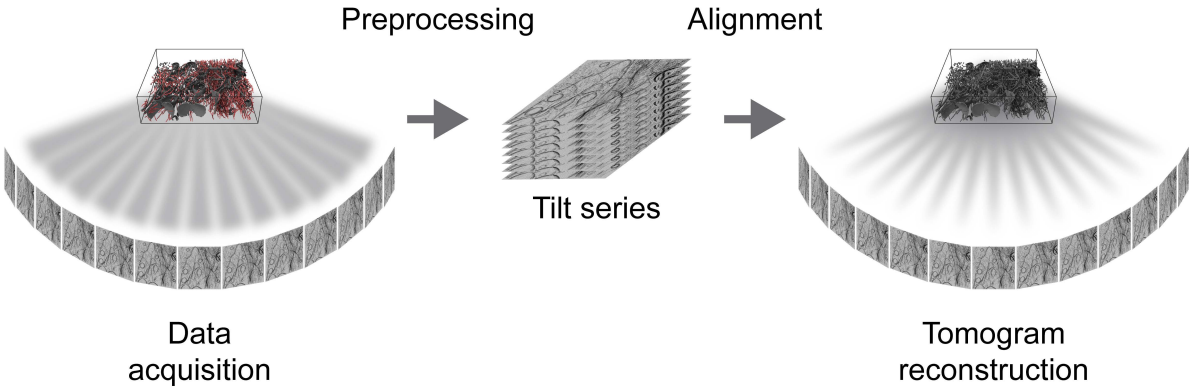

Figure 3: Principle of cryo-electron tomography. The stage containing the cellular sample is tilted to generate a set of projection images, the so-called tilt series. Alignment of the individual tilts and reconstruction of a 3D volume, the so-called tomogram, is achieved through weighted back-projection.

Instead of acquiring a single micrograph, the stage is rotated successively and a series of projection images is generated, the so-called tilt series. These images are subsequently aligned and back-projected computationally to generate a 3D volume, the tomogram. This concept has been first introduced in 1968 and was called the polytropic montage [27]. Following decades of pioneering work, the actin cytoskeleton was the first successful target for *in situ* cryo-ET, and has remained an ideal sample for studies using this method [28,29].

1.4.1 Cryo-focused ion beam milling

For cryo-ET, the sample needs to be sufficiently thin, as the mean-free path of an electron is limited and the amount of inelastic scattering increases. For electrons accelerated at a voltage of 300 kV, this mean free path is around 300 nm [30]. For biological specimen, this poses an additional challenge. Accordingly, many early tomographic studies focused on small prokaryotic cells. As most eukaryotic cells are several orders of magnitude thicker, only the cell periphery and the cell edges are directly amendable for tomographic acquisition [28].

Cryo-focused ion beam milling (cryo-FIB milling) emerged as the method of choice in terms of biological sample thinning in the past few years [31]. It was conceptualized for vitrified samples and further developed to optimize the instrument and reduce artifacts and contamination [32-34]. An ion beam of medium-heavy ions, typically gallium ions, is focused on the sample and locally ablates material. Modern instruments contain a dual FIB-SEM instrument and the SEM is used to monitor the milling process [35]. Different milling geometries are possible. Usually, material above and below the region of interest are targeted and removed, leaving a small slab-like region of the cell interior behind. This geometry is referred to as lamellae and allows access to the cellular interior. A second geometry ablates cellular material from the top only and at very shallow milling angles, thereby generating a wedge. This is used to access structures at the basal membrane of the cell. However, as there is only one milling direction, the thickness is more difficult to control than for standard lamellae. Furthermore, due to the wedge-shaped geometry, only the front edge is sufficiently thin and the remaining area becomes too thick [36]. A recent development is the use of plasma for milling, from sources such as Xenon or Oxygen [37]. This allows for faster milling rates in the future and give access to a larger variety of biological samples.

1.4.2 Cryo-correlative light and electron microscopy

Unlike ribosomes, most macromolecules or cellular processes of interest are not abundant in the typical cell. The total volume captured by a single tomogram typically corresponds to less than 0.1 % of the cellular volume. To circumvent this issue, correlative light microscopy is employed to identify a target region [38,39]. Typically, one or two proteins of interest are tagged with a fluorescent label. The frozen grid is then visualized in a cryo-fluorescence microscope and suitable cells and target areas are identified. To precisely localize a target in 3D, 3D correlation is employed [40]. Fluorescent and contrast-intensive beads are identified in both the fluorescence, and in the FIB image and the respective transformation is calculated to reveal the precise 3D coordinates of the target area [40,41].

1.5 Data acquisition

The most significant limitation for interpretability of tomographic data is the low signal-to-noise ratio, due to the low electron dose used for imaging the sample [7]. This is owed to vitrified samples being highly sensitive to radiation, which is especially problematic in the case of tomography, where the same spot within a sample is continuously imaged over the course of a tilt series acquisition. The total dose that the sample is exposed to has to be kept to a minimum, today this is typically ~100-150 $e^-/Å^2$.

Multiple strategies were invented to optimize acquisition while limiting exposure. Most importantly, in low dose-mode the beam is blanked constantly, unless an image is acquired [42]. Tracking and focusing is not performed on the area of interest, but next to it. Therefore, the entire dose that is put on the sample is used exclusively for image formation.

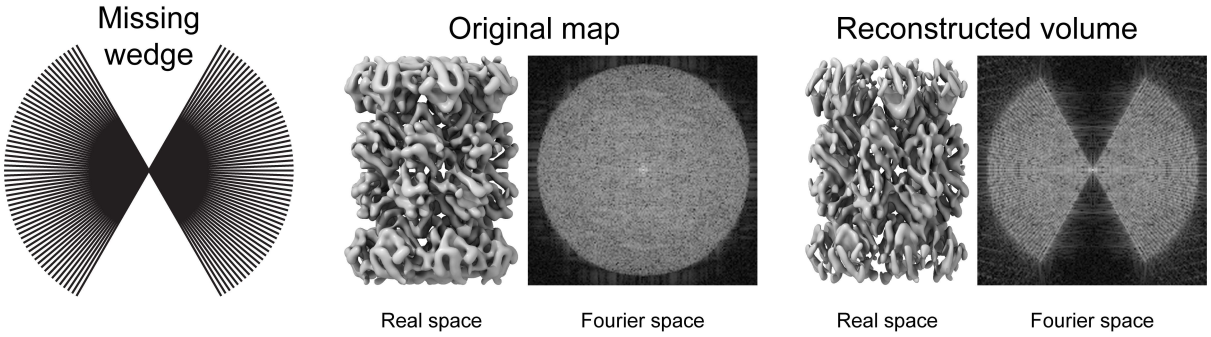

Figure 4: Effects of the missing wedge during reconstruction. Visualization of the sampled region in Fourier space, ranging from -60° to +60°. 3D volume of a 20S proteasome (emd-3455), visualized both in real space and Fourier space. The map was projected in a range from -60° to +60° in 2° steps, and the volume was reconstructed using weighted back-projection. The volume is shown in real space and Fourier space, and the sampling artifacts due to the missing wedge are visible.

Unlike rod-like samples, slap-like samples, which comprise virtually all current applications in cryo-EM, present a major challenge for imaging. As the stage is tilted, the sample increases significantly in thickness and the amount of multiple scattering events is increased. Next to adjacent grid bars that will eventually block the beam at high tilt angles, the mechanical properties of the stage set additional boundaries for the tilt range that can be realized. For these reasons, the tilt range is typically from -60° to +60° with either 2° or 3° increments.

This incomplete sampling leads to artifacts in the reconstructed volume, specifically reduces the resolution in the z dimension and limits reconstructability in the xy plane and along the x axis, given that the tilt axis is aligned with the y axis [43]. This is referred to as the missing wedge problem, termed after the wedge shaped absence of information in Fourier space [44]. It influences the direct interpretability of tomographic data. The real space effect is a deformation along the z dimension. As a consequence, the top of membranes or vesicles is not resolved and other structures usually appear elongated along z. Additional measures are required to retrieve the complete 3D information. In the case of macromolecules, by computationally averaging several copies with different orientations, the full 3D information is recovered in the reconstructed volume. This process is called subtomogram averaging [45-47] (see below). Additionally, new methods based on neural networks aim to estimate the information in the missing wedge by comparing different parts within a tomogram that ideally contain the same macromolecule in various orientations and thereby restoring the information in the entire tomogram [48].

Another limitation of the direct interpretability results from the discontinuous sampling. Tilts are recorded typically every 2 or 3 degrees which leads to additional regions in Fourier space with missing information. This effect comes into play at larger Fourier shells and increasing resolution. Akin to restoring the missing wedge information, by averaging over multiple copies of the same molecule, the Fourier space can be filled completely and the full sampling information can be restored. The maximum obtainable artefact-free resolution is determined by the Crowther criterion, defining the number of projections N that are needed to obtain resolution d of a particle with diameter D [49].

$$N = \frac{\pi D}{d}$$

Traditionally, tilt series were acquired from -60° to +60° (unidirectional, Figure 5, middle). However, the highest tilt angles have the largest sample thickness which in turn limits the maximum obtainable resolution. On the other hand, the first tilt images have the least electron exposure and high-resolution information has not been compromised by radiation damage. To optimize data acquisition for maintaining high-resolution information, the first tilt image to be acquired should be the 0° tilt image (Figure 5, left and right). To do so, a dose-symmetric tilt scheme was devised (Figure 5, left) [50]. Here, data acquisition begins at 0°, followed by tilting the stage to +2° and then -2°. This way, the total dose is evenly distributed between the positive and negative tilt range, while simultaneously preserving the highest resolution information in the first tilt images [51].

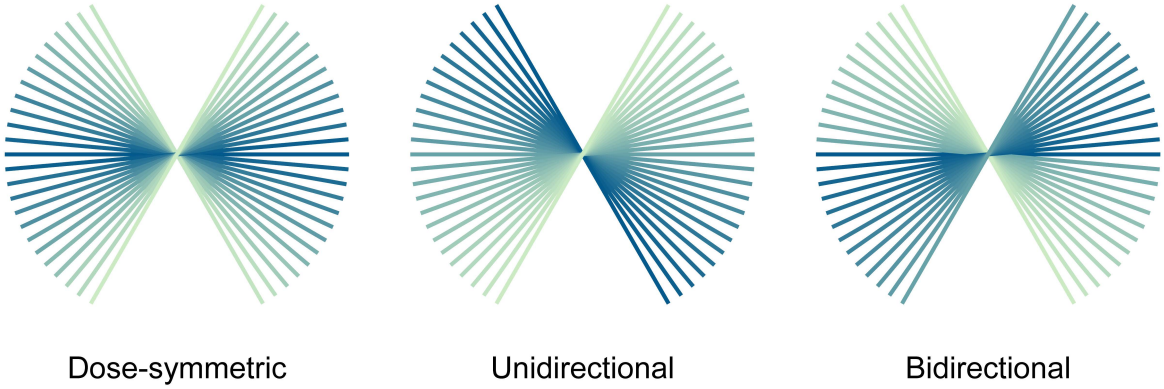

Figure 5: Tilt schemes for tomographic data acquisition. The first acquired tilt is depicted in dark blue, the last tilt is shown in light green.

1.6 Tomogram reconstruction

1.6.1 Motion correction

An immediate consequence of imaging with an electron beam is beam-induced movement of the specimen [52]. Therefore, when a projection image is acquired over a few seconds, significant sample movement occurs and the image becomes blurry. This effect is more severe at higher spatial frequencies, thereby limiting the maximum achievable resolution. The introduction of DEDs allowed to circumvent this problem. As their readout speed is fast, a movie consisting of several frames can be recorded instead of a single image. This increases the temporal resolution and allows to account for the sample movement by subsequently aligning the frames to return a single image [53]. However, while the signal in a projection image is low, it is even lower in an individual frame. Therefore, algorithms employ a rolling window approach and track the motion over several frames. This ensures also a smooth trajectory, as rapid directional changes of movement are unlikely. The most significant movement occurs within the first few frames and is smooth over all subsequent frames. Moreover, the specimen movement is not isotropic. To account for this, following a global motion correction, local patch-based tracking of the image resolves spatial variations in the movement pattern [54].

The newest generation of DEDs allows for an even faster read-out of up to 300 s^{-1}. A new data format termed electron event representation (EER) enables a memory-efficient storage of these images, as only the coordinates of an electron captured by the detector are stored [55]. Since the read-out is so fast, this allows for individual electrons to be detected. Several frames can be summed to generate a fraction that will be corrected for beam-induced motion as outlined above. A major advantage, although mostly useful for high-resolution SPA [20], is the flexible frame time.

1.6.2 Dose-filtering

In cryo-EM, the sample suffers from radiation damage as soon as it interacts with an electron. Radiation damage is first manifested as a high frequency component, such as the disruption of the atomic bonds in carboxyl groups, and is later extended to lower resolutions as more and more radicals are created that in turn disrupt the atomic structure [7]. Severe radiation damage may even be directly visible as large fractions of the specimen start to show bubble formation. However, even low levels of radiation damage, if untreated, impede the final reconstruction, specifically through the re-amplification of noise. Therefore, the acquired images need to be dose-filtered to down-tune the radiation damage-induced noise. Essentially, the projection image is lowpass filtered, and the resolution cut-off is increased as a function of the accumulating electron dose. As a consequence, in cryo-ET, the highest resolution information is preserved in the first 1-3 tilt images only and later tilt images only contribute low resolution information to the reconstruction process. The exact shape and parameters for the lowpass filter have been determined empirically for SPA data and were subsequently adapted for cryo-ET [56-58].

1.6.3 CTF estimation and correction

In cryo-EM, data acquisition is performed out of focus, and as a consequence, the signal is delocalized by the contrast transfer function [12,59]. If unaccounted for, this limits data interpretability to a resolution of 2-3 nm for typical acquisition settings. At this resolution, the contrast transfer function reaches a zero-crossing and the contrast is inverted (see Figure 2). As discussed above, the defocus at which the image was acquired influences the CTF significantly. Due to imperfections in the data acquisition and offsets in the correct z height of the sample, the target defocus may not match the actual defocus at which the image was recorded. To estimate the defocus of an image, first the power spectrum is calculated. The FT of the image is calculated and the amplitudes are squared, resulting in the so-called power spectrum. This results in the emergence of so-called Thon rings. A set of theoretical CTF curves with varying defocus values are fitted to the power spectrum [60,61]. Upon determining the precise defocus of the image, the phases can either be multiplied or flipped. Thereby, the correct contrast transfer is ensured and the data becomes interpretable at higher resolution. However, there are still resolution ranges where there is little to no spatial information transferred that cannot be recovered. This is compensated for by acquiring imaging at different defocii and subsequent averaging of the particles. This ensures complete coverage of the spatial frequencies in the resulting structure (see Figure 2).

For cryo-ET, there are two further consequences that need to be considered as compared to SPA. SPA samples are rather thin, usually below 100 nm, therefore the thickness of the sample can be neglected at first, and later compensated for by CTF refinement during data processing [62]. For thicker samples, as it is usually the case for tomography, the sample thickness needs to be considered, as this is reflected in a defocus gradient and macromolecules at the top of the tomogram have a different defocus value than macromolecules at the bottom. Likewise, they have been modulated differently by the CTF, and global CTF reconstruction will therefore be a compromise and limit the obtainable resolution. A global CTF estimation corresponds to the center of mass of a tomogram, as this contributes to the signal most. 3D CTF correction has been devised to account for this [63].

Another consideration for tomographic data that limits CTF correction, is the defocus estimation itself. Importantly, errors in determining the defocus will lead to phase shifts of the CTF and false CTF correction. It is neglectable at lower resolution but becomes more severe as the CTF oscillates more rapidly at higher resolution ranges [47]. Recording tilted samples presents a significant z shift that is eminent in a defocus gradient perpendicular to the tilt axis, typically along the x axis [61]. While the thicker sample reduces the image quality, the defocus gradient leads to destructive interference and prevents precise defocus estimation. Several software solutions were presented to circumvent this limitation [60,64-67].

1.6.4 Tilt series alignment

Upon pre-processing the tilt series, the individual tilt images need to be aligned before reconstructing the tomogram [68]. This includes refining translations between successive tilt images, as well as refining individual tilt angles and the tilt axis. Images are first coarsely aligned by cross-correlation to determine shifts between tilts. For sufficiently stable microscopes and well-behaved samples, this is often sufficient to retrieve a usable reconstruction. However, for cellular samples, this alignment is usually not sufficient. Traditionally, small gold beads, so-called fiducials, were added to the sample before freezing.

The beads are electron dense and are therefore easy to track throughout the tilt series. Based on this movement pattern of several fiducials, the motion of the entire tilt series can be modelled and this improves alignment significantly. However, as for most cellular samples that were generated using cryo-FIB milling, introducing beads to the sample is not feasible as they would be milled away. A different approach consists in correlating patches within the image, so-called patch tracking, or identifying landmarks with strong gray value variations, and following these patches throughout the tilt series by means of cross-correlation [69,70]. Various parameters are fitted to the resulting model to best estimate the transformation required for subsequent reconstruction.

There are several algorithms for reconstructing an aligned tilt series. The Fourier transform of each projection image corresponds to a slice through the Fourier space of the reconstructed volume, which is also referred to as Fourier slice theorem [71]. By placing the Fourier images for each tilt into a 3D volume according to their tilt and then taking the inverse transform, the 3D volume can be calculated [49,72]. Back-projection, most popular weighted back-projection (WBP), describes the real-space equivalent [73]. Weighting is necessary to counteract the domination of low-resolution information from the high-angle tilt images.

1.6.5 Denoising

Several denoising methods can be applied to improve contrast and suppress noise. Image-based methods, such as Non-local means or Frangi filtering, can be employed [74,75]. Recently, AI-based methods are becoming popular. The AI-based denoising method cryoCARE, adapted from CARE (Content Aware Image Restoration), is based on the noise2noise algorithm [76-78]. The individual frames from the tilt series are split in odd and even half sets, each of which is used to reconstruct another tomogram. This ensure the same underlying signal in both half sets, but different noise levels that can subsequently be estimated by the network.

Real space distortions of the tomogram due to incomplete sampling in Fourier space can be partially accounted for using AI-based methods, such as IsoNET [48]. By extracting random sub volumes throughout the tomogram, that each contain particles with different orientation, the network tries to learn how the entire tomogram is affected by the missing wedge. This information can help to restore some information in the xy plane of the tomogram.

1.7 Subtomogram averaging

Tomograms inherently suffer from low signal to noise ratios that impede direct extraction of high-resolution features from individual molecules. A common technique to increase the signal to noise ratio *in silico*, is to identify multiple copies of the same molecule within the tomographic volume, extract a small box from the tomographic volume, determine their poses, i.e., the exact orientation and translation, and average them together [46,47,79]. This method is called subtomogram averaging and it can substantially improve the obtainable resolution from tomographic data [80]. The process is akin to SPA with an additional dimension that requires a third translational component to be considered. However, 3D rotations are computationally more expensive than 2D rotations, hence exhaustive global searches are not favorable. Usually, prior knowledge on sample geometry is exploited to facilitate initial alignment and permit local searches [47]. A particle pose is defined by 6 variables, three translational variables describing xyz shifts, as well as 3 rotational parameters, most commonly described by Euler angles [81-83]. All parameters are determined relative to a common frame of reference. There are several conventions for defining Euler angles, most commonly used are zxz- and zyz-convention [46,84]. These are defined as consecutive rotations around the z axis, then the new x or y axis, respectively, and a final rotation around the new z axis. Moreover, rotations can be decoupled in cone angles, or out-of-plane angles, and in-plane rotations.

1.7.1 Particle localization

In SPA the molecule of interest is typically purified biochemically and the dataset is compositional homogeneous. Heterogeneity exists primarily in the form of flexible subdomains or incomplete interactions in case of multimeric complexes. In tomography, however, cellular samples typically display an enormous compositional heterogeneity, as countless macromolecules are located in crowded environments. The major challenge consists in localizing relevant copies of the molecule of interest, while keeping the number of false positives as low as possible. This is still a relevant challenge in cryo-ET and active research is performed to design new algorithms to deal with this problem.

Traditional methods to localize macromolecules in tomographic data consist in manual picking, template matching, membrane segmentation or filament tracing [85-87]. Template matching requires a reference structure which is rotated according to a predefined set of orientations to generate a template library. This library is then used to search the full tomographic volume by means of cross-correlation or other scoring function, and the scores as well as the best fitting orientation for each position are stored. The highest correlation peaks correspond to the most probable particle positions [46,85]. This step poses the challenge of introducing template bias, as shown in the famous Einstein from noise experiment [88]. High-resolution information that is present in the template may be retrieved from noise and therefore introduce artificial density in the resulting structure. Therefore, it is necessary to ensure the reliability of the structural features. Common approaches to reduce the influence of template bias consist in lowpass filtering the template structure, which avoids introducing high-resolution components. Another approach modifies the template structure to some extent, usually by removing a part of the structure. If this missing density is restored in the final structure, it also indicates that the picks were reliable.

A priori knowledge of the structure of interest is beneficial. In case of membrane-associated proteins, prior segmentation of the membrane can be used to mask the region around the membrane and speed up template searches [79]. For instance, pyseg employs algorithms based on spatially embedded graphs to accurately detect membrane-bound proteins [89].

Filamentous structures, such as the cytoskeleton or some neurodegenerative aggregates, have dedicated algorithms for segmentation [90,91]. Typically, filament segmentation relies on a modified version of template matching with a cylindrical template structure that matches the dimensions of the filament. Based on the resulting correlation and orientation maps, a filament tracing algorithm is employed subsequently [91]. Determined by a given threshold, seeds with high correlation values are identified that serve as starting points for filament elongation. Based on the correlation score and the respective orientation, that penalizes strong deviations from the filament tangent, the filament is elongated in both directions until a second threshold is reached, marking the end of the filament. As correlation scores are significantly lower at filament ends, this value might need several adjustments. Similarly, the correlation scores are also negatively influenced by cross sections and overlapping filaments, which poses severe challenges for dense networks, moreover, since crosslinkers and branching points are key elements of filament networks.

Moreover, AI-based approaches are becoming increasingly popular and new algorithms are developed recently. For particle picking, various AI-based software solutions for detecting one or several target structures in a crowded and heterogeneous environment were developed [92-94]. Finally, automated membrane segmentation allows for fast and accurate segmentation of vesicles and membranes, replacing labor-intensive manual segmentation [95].

1.7.2 Subtomogram alignment

Subtomogram averaging is a method to significantly enhance the signal to noise ratio *in silico* of the target structure to resolutions that are an order of magnitude higher than what is directly extractable from a tomogram. Typically, due to all the reconstruction artifacts discussed above, resolution in a tomogram is around 3 nm. In contrast, subtomogram averaging nowadays routinely achieves sub-nanometer resolution, and for ideal samples can go as low as 3 Å, slowly approaching other high-resolution methods, but permitting to retain contextual information [96].

Upon target identification, small boxes around the target structure are extracted, the so-called subtomogram. The subtomograms are typically accompanied by a set of Euler angles, which describe the pose of the particle. These can be used to generate a structure by applying the respective rotations to the volume and then summing all particles together (Figure 6). All particles are aligned iteratively to the target structure to optimize each individual pose [47]. The reference structure is rotated by a set of predefined orientations that depend on the current resolution, particle and box size, and correlated against the respective particles. Each round of alignment is followed by averaging the particles with their new poses. Ideally, this leads to an improved reference structure with higher resolution. These higher resolution details allow for a more precise alignment of the particles in the subsequent iteration, which in turn results in an improved resolution. This process is iterated until alignment converges and no improvement in resolution is obtained (Figure 6).

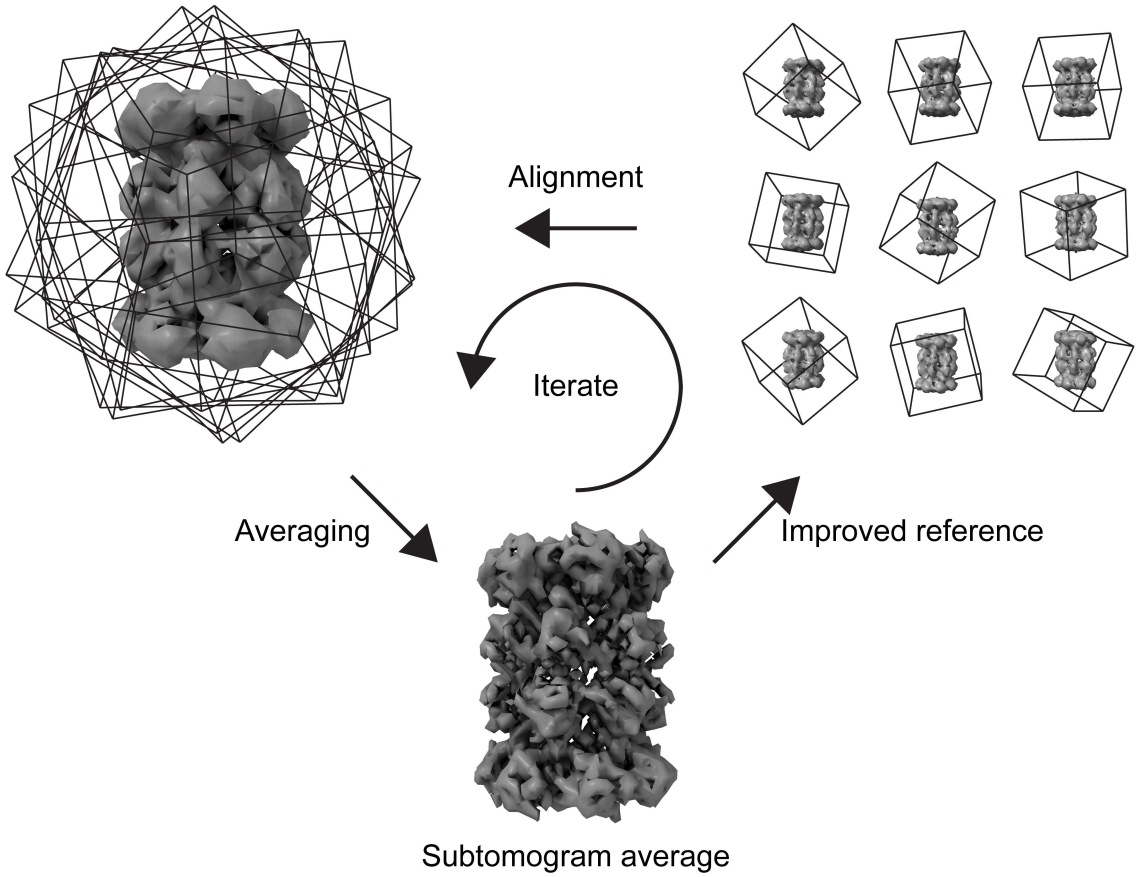

Figure 6: Basic principle of subtomogram averaging. Extracted particles are aligned to a common reference. The aligned particles are summed to obtain an average. This structure serves as improved reference to re-align the particles at higher accuracy. This process is iterated until the alignment converges.

To prevent falling in local minima during the alignment process and sub-optimal poses, the template structure is lowpass filtered. Accordingly, only low and medium-resolution features are used for alignment and correlation initially, which limits the alignment to reliable resolution ranges and prevent high-resolution noise from driving the alignment. While only low spatial frequencies are used to correlate, high-resolution features beyond the lowpass filter are recovered, depending on the quality of the alignment. The lowpass filter is progressively optimized and higher resolution features are introduced as a consequence, that further improve the alignment while simultaneously preventing noise from diverging the correct alignment.

Aside from increasing the SNR in the averaged structure, subtomogram averaging is also used to remove structural artefacts that are introduced during data acquisition. As discussed above, tomograms suffer from incomplete sampling due to the limited tilt range. This is eminent in Fourier space as the missing wedge. Multiple particles throughout the tomogram are ideally oriented in different orientations with respect to the tilt axis and are therefore affected differently by the missing wedge. By averaging over the different copies, the information is distributed and the sampling is completed [79]. Similarly, incomplete sampling over all spatial frequencies due to CTF modulation leads to an incomplete description of the target structure. Despite CTF correction, amplitude fluctuations persist, and, at zero crossings, there is no information transfer for this spatial frequency at all. By

combining tomographic data with different defocus values, these amplitude fluctuations are shifted and averaged out.

Several scoring functions exist that need to be optimized to achieve the best-possible alignment. A popular method for subtomogram averaging is maximizing constrained cross-correlation (CCC) [46,79]. It aims to achieve higher correlation scores with each iteration, thereby returning a structure that maximizes in similarity to the dataset. Importantly, only overlapping sampling regions in FT space are considered for the calculation of the correlation to account for difference caused by the missing wedge.

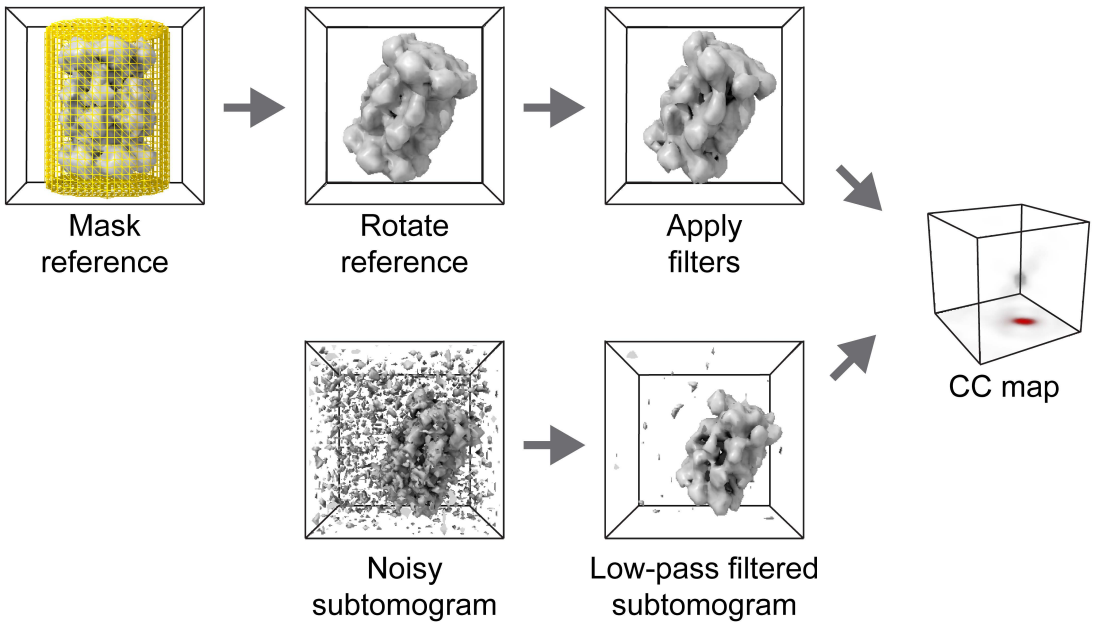

Figure 7: Principles of subtomogram alignment. The current reference structure is masked to reduce the effects of noise. It is then rotated according to a set of predefined orientations that are based on the size and current resolution of the structure, and appropriate filters are applied, such as CTF- or exposure weighting. As such, the reference is comparable to the subtomogram. The subtomogram is lowpass filtered, to prevent the alignment from being driven by noise-features. The filtered reference and the subtomogram are then correlated using different possible scoring functions, and the resulting cross-correlation map (CC-map) can be evaluated to determine the optimal position and orientation of the subtomogram. The structures describe the 20S proteasome (emd-3455), and manipulations were generated using MATLAB. The figure was inspired from [47].

A direct consequence of an artifact-free reference is that it loses similarity to the target structure. To improve correlation accuracy, the reference is modulated by filters to reintroduce these alterations and mimic the target as closely as possible (Figure 7) [97]. These filters are introduced by removing appropriate regions in Fourier space that are not sampled in the target structure, and are also updated iteratively. This ensures the highest possible similarity of the reference with the target structure at that given point. Likewise, masking the target region prevents excess noise or neighboring particles from contributing to the correlation, further improving the correlation (Figure 7).

1.7.3 Resolution estimation

Resolution estimation in cryo-EM is less intuitive than for other methods. In cryo-EM, the dataset is split in two half sets, that are refined independently while using the same alignment parameters. This is often referred to as gold standard refinement [98]. The two resulting maps are then compared by Fourier Shell Correlation (FSC) to assess the resolution [99]. The FSC is based on the Fourier Ring Correlation that is the equivalent for 2D images [100]. The Fourier transform of each volume is calculated and for each resolution range, i.e., shell, the correlation value is calculated. This is iterated for the next resolution range, until the Nyquist limit is reached. The retrieved correlation scores are plotted against the spatial frequency. For low-resolution information, the similarity between both half sets is high and therefore the correlation score will be close to 1. With increasing resolution, the influence of noise becomes more severe, and small difference in the alignment of structure are considered. Both factors decrease the similarity of the two half sets and therefore reduce the correlation score. Eventually, the effect of noise becomes the primary factor and the correlation scores fluctuate around 0. The threshold, which serves as resolution cutoff, was heavily debated in the field. With the introduction of gold-standard refinement, new calculations suggested a threshold of 0.143 as resolution cutoff, based on a SNR of 0.5 in each half set [101]. Masking the half sets improves the correlation, and hence the resolution, further by reducing the noise component in the average.

The two half sets are combined and the volume is filtered to the determined resolution. Furthermore, as a consequence of the back-projection, low-resolution features dominate the reconstruction. B-factor sharpening restores high-resolution details by amplifying high-resolution frequencies [101]. In cryo-ET, the final structure can be exploited to improve the initial tilt series alignment by serving as fiducial markers. As there is sufficient high-resolution information available, this can be used to model geometrical parameters of the consensus volume and improve the overall alignment. This is referred to as multi-particle refinement [96,102,103]. It showed that the predominant factor that limits resolution in cryo-ET is the imprecise initial alignment of the tilt series [96].

Chapter 2: Force-generating cellular actin networks

2.1 Actin structure and function

The actin cytoskeleton contributes to a variety of essential cellular processes, including cell motility, morphology, phagocytosis, and endocytosis [104,105]. This is realized through constant assembly and disassembly of monomeric actin (G-actin) into polar filaments (F-actin) that form complex and highly dynamic filament networks [106]. Critical to these processes is the generation or transmission of force. The variety of networks is realized by a set of actin-binding proteins (ABPs) that tightly regulate and tune the actin cytoskeleton to fulfill its various purposes [107].

2.1.1 Globular actin

Actin is a small, 42 kDa sized protein that is termed globular actin (G-actin) in its monomeric form [108]. It adopts a flat shape with dimensions of 55 x 55 x 35 Å and consists of four subdomains (SD 1-4), two of which form a larger domain each (Figure 8A). Those are referred to as α/β domains, or large and small domains, respectively [106]. There are two clefts in between the domains. The nucleotide-binding cleft binds adenosine triphosphate (ATP) and a divalent cation, preferably Mg^{2+}, and is important for stability and regulation of turnover [109]. Several ABPs have overlapping target regions, and some preferentially bind in a hydrophobic cleft between subdomains 1 and 3, which is also termed target-binding cleft. Subdomains 1 and 3 are structurally very similar, while subdomains 2 and 4 are considered to be insertions into subdomains 1 and 3, respectively [106]. The sequence of actin is highly conserved among eukaryotic species, highlighting its importance in a plethora of cellular processes [110]. Vertebrates express three different isoforms, with α-actin as the predominant form in skeletal, cardiac and smooth muscles, and β- and γ-isoforms in non-muscle cells.

G-actin encompasses slow ATP hydrolysis rates with no significant ATPase activity. In contrast, upon filament polymerization, subdomains 1 and 2 are rotated by ~20° relative to subdomains 3 and 4 (Figure 8B) [111]. The ATPase activity is 42,000 fold enhanced, and ATP hydrolysis and subsequent phosphate release are key markers for filament aging and consequently for regulating actin turnover (Figure 8D) [112]. H161 was identified to act as catalytic base triggering the nucleophilic attack of a water for the hydrolysis. Key structural differences between different nucleotide states are observed in the D-loop region within SD 2, a flexible linker that interacts with the C- terminal tail of the adjacent subunit [113].

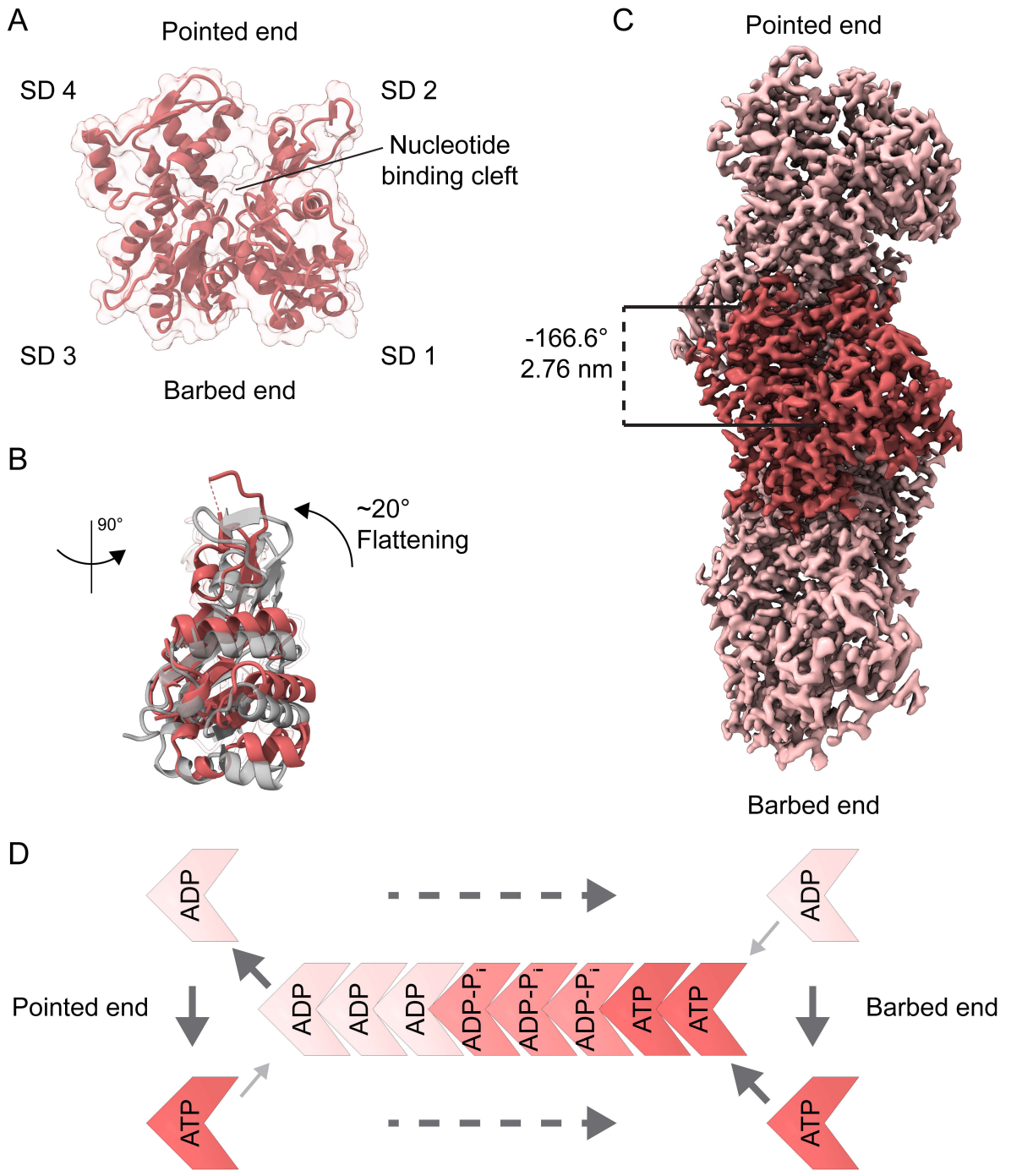

Figure 8: Actin structure and dynamics. A: Structure of monomeric actin (G-actin). The four subdomains 1-4 are indicated (SD 1-4), as well as the nucleotide binding cleft, and the barbed and pointed end. B: Comparison of the monomeric G-actin (gray) and filamentous F-actin structure (red) superimposed on each other. Upon polymerization, the actin monomer flattens by ~20°. C: High-resolution structure of the actin filament (emd-15104). Barbed and point end are indicated, and the helical parameters rise and twist are noted. The central subunit is highlighted. D: Dynamics of actin polymerization. The barbed end is considered as the fast-growing end, where ATP-bound actin monomers are incorporated rapidly. During filament aging, ATP is first hydrolyzed (ADP- P_i) and the phosphate is then released (ADP). At the pointed end, actin monomers (typically ADP-bound) dissociated much faster. ADP-bound actin monomers subsequently exchange their nucleotide for ATP, before being re-incorporated at the barbed end. Of note, dissociation can also happen at the barbed end, as well as elongation at the pointed end. In general, these reactions are considered only to a minor extend.

2.1.2 Filamentous actin

G-actin can polymerize spontaneously under physiological salt concentrations into a polar filament with distinct kinetics; the fast growing plus end, or barbed end, as well as the slow growing minus end, or pointed end (Figure 8D). The polarity of the filament was identified through EM of negatively stained actin filaments that were decorated with myosin heads, which adopt an arrowhead shape [114]. The helical symmetry describes the rise between two adjacent monomers along, as well as their relative rotation around the pseudo-symmetry axis. For actin filaments, the twist is typically -166.6°, while the rise is 2.76 nm (Figure 8C) [106]. Since the twist is close to 180°, the filament can either be described as a right-handed (clockwise), double-stranded, also termed long pitched, filament, or as a left-handed (counter-clockwise) single-stranded, also termed short pitched, filament. The long pitch repeat is close to 36 nm and contains ~13 subunits. The two filament ends exhibit drastically different polymerization kinetics. The fast-growing barbed end polymerizes ten times more rapidly than the pointed end, with association rate constants of ~10 $\mu M\ s^{-1}$ [107]. It is rich in ATP or ADP+P_i, while the pointed end predominantly contains ADP (Figure 8D) [115]. ATP hydrolysis occurs rapidly, while phosphate release is substantially slower, which is important to enable subsequent depolymerization [116-118]. Released actin monomers undergo a nucleotide exchange reaction and are regenerated with ATP, which in turn can be incorporated again at the barbed end (Figure 8D). Adding ATP-bound actin to the barbed end, while simultaneously removing ADP-bound actin from the pointed end at the same rate leads to so-called treadmilling and results in constant filament length [107].

2.1.3 Actin nucleation

Spontaneous actin nucleation is a kinetically unfavorable step. Specifically, a tetrameric nucleus is required for subsequent elongation, but kinetically unfavorable below a critical concentration [119,120]. To overcome this issue, ABPs are employed to overcome this rate-limiting step. There are several nucleators that lead to distinct filament networks.

The Arp2/3 complex is a heptameric, 224 kDa complex and consists of the two name-giving actin-related proteins (Arp) 2 and 3, as well as five additional subunits ArpC1-5 [121,122]. Together with a pre-existing, so-called mother filament, it forms Arp2/3 complex-mediated branch junctions that serve as basis for a new so-called daughter filament to branch of the mother filament (Figure 9A) [123]. The branch junction is characterized by an angle of 70° [124]. Multiple branching events lead to highly entangled, so-called dendritic networks, and a prominent network of this type is the lamellipodium, the leading edge of cells undergoing mesenchymal migration [125,126]. Activation of the Arp2/3 complex is regulated on several levels, and it requires nuclear promoting factors (NPFs), such as members of the Wiskott-Aldrich syndrome protein (WASP) or Scar/WAVE families [127]. In the lamellipodium, the main NPF is the WAVE regulatory complex (WRC) [128]. Activation of the Arp2/3 complex occurs at the membrane and full activation of the complex is achieved once the mother filament is bound. Upon activation, the complex undergoes significant structural rearrangement. Specifically, two subcomplexes (consisting of Arp2, ArpC1, ArpC4 and ArpC5, and Arp3, ArpC2 and ArpC3, respectively) rotate relative to each other, thereby positioning the Arp2 and Arp3 subunits toward the direction of the new filament [124]. In the active conformation, five of the subunits are in contact with the mother filament, while the two Arp2 and Arp3 subunits mimic a free barbed end that is then elongated by new actin

monomers. Further regulation is realized by incorporating different subunit isoforms. ArpC5 and ArpC5L isoforms lead to distinct morphologies at the leading edge, with the former being attributed to higher cell motility [129]. This is facilitated by further interactions of the complex with elongation proteins from the Ena/VASP family. Activation of the Arp2/3 complex can be inhibited by the small molecule CK666 [130]. It stabilizes the inactive form of the complex, and inhibits movement of Arp2 and Arp3 to the activated confirmation.

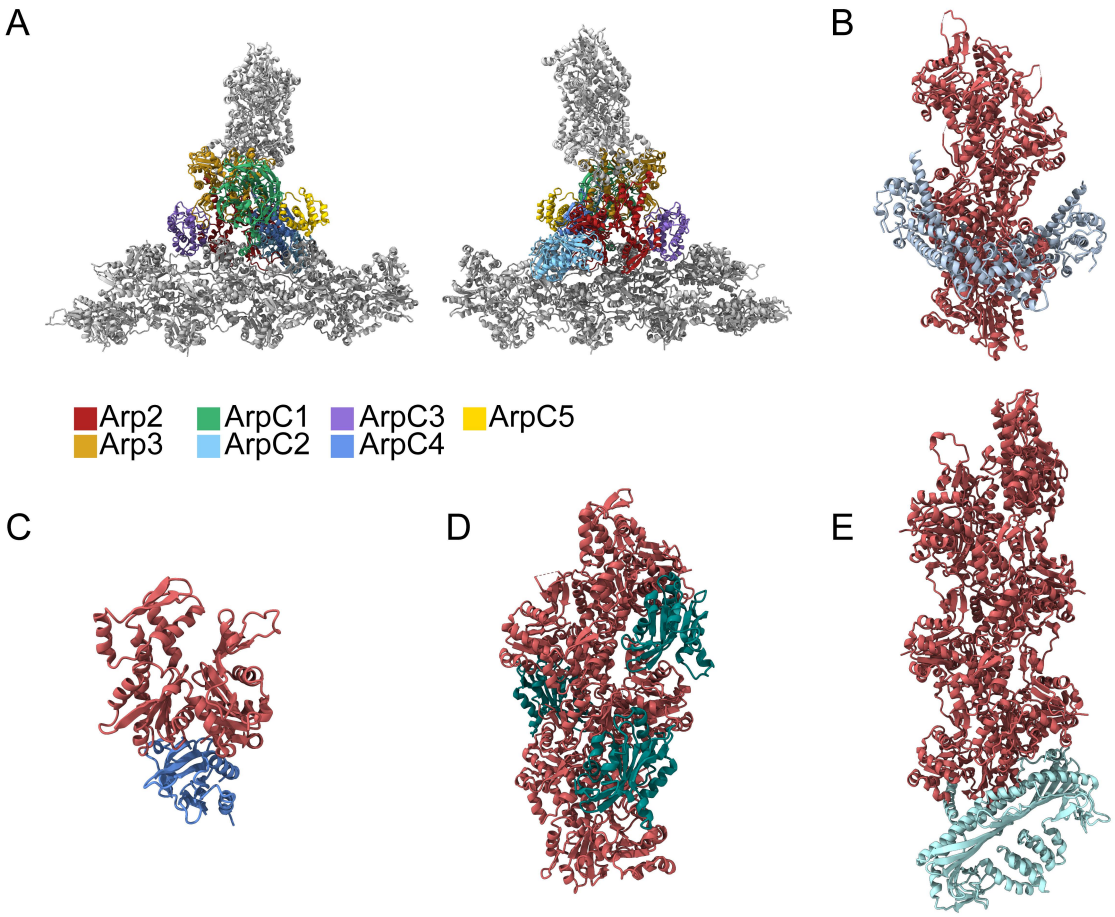

Figure 9: Gallery of actin binding proteins. A: The Arp2/3 complex (pdb 7aqk) binds to a pre-existing filament, so-called mother filament. The Arp2 and Arp3 subunits mimic actin monomers of a newly generated filament (so-called daughter filament), from which new monomers can elongate. B: Model of formin superimposed to the actin structure (pdbs 4eah, 8a2r). C: G-actin in complex with profilin (pdb 2btf). D: F-actin in complex with cofilin (cofilactin, pdb 5yub). E: F-actin in complex with capping protein (pdb 5adx). Color code B-E: actin is shown in red, ABPs are colored in blue/green.

In contrast to branched, Arp2/3-mediated networks, formins nucleate and polymerize linear filaments which are often bundled (Figure 9B) [127]. The formin family consists of homodimeric proteins, that each contain a canonical formin homology domain 1 and 2 (FH1 and FH2) [131]. FH2 tightly dimerizes in a head-to-tail manner, surrounding the barbed end [132,133]. It remains processively attached to the growing end while it incorporates new actin monomers, which are in turn recruited by the FH1 domain. The FH1 domain contains a polyproline repeat that attracts actin monomers, usually complexed with profilin [133]. However, the exact role of formins in *de novo* nucleation of new filaments is not completely understood. It is suggested, that their main contribution to actin dynamics within cells could solely be the processive elongation of barbed ends [120].

2.1.4 Actin-binding proteins

As shown above for actin polymerization, actin-binding proteins regulate virtually all aspects of actin assembly and turnover, highlighting the importance of considering ABPs in amplifying the dynamics of actin filaments [104]. This allows turnover of entire networks in short time spans as observed *in vivo*, rather than the more static behaviors found *in vitro*. Furthermore, through utilizing ABPs, the cells can create a substantial number of complex networks dedicated to various different functions, based on the same building blocks of actin filaments. To prevent spontaneous polymerization, G-actin is usually bound to profilin [134] (Figure 9C). Profilin is a small protein and it sterically inhibits nucleation. Its binding affinity to ATP-bound actin is higher than for ADP-bound actin, so it promotes nucleotide exchange [135]. Its affinity for actin drops significantly upon filament binding, and it dissociates rapidly after binding to a filament, permitting subsequent polymerization.

F-actin can be severed by the protein actin depolymerizing factor (ADF)/cofilin which can cooperatively bind to ADP-bound stretches of F-actin (Figure 9D) [136]. Binding triggers a subtle change of the filament twist from -166° to -162°, thereby reducing the long-pitch repeat from 36 to 27 nm [136]. This alters the physical properties of F-actin and increases its flexibility [137]. Moreover, sites of abrupt change of these helical parameters are prone for severing. Cofilin is also able to dissociate Arp2/3 mediated branches [138].

Capping protein tightly binds to barbed ends of filamentous actin (Figure 9D) [139,140]. Together with profilin, capping protein orchestrates the available concentration of monomeric G-actin in the cell [107]. In contrast, tropomodulin binds to pointed ends [141].

Complex actin architectures are shaped by strategically located, physical interactions in form of crosslinker proteins. Many of these proteins contain a similar actin-binding domain (ABD), originally identified in α-actinin, with their linkers stretching a wide range of distances and possible crosslinking configurations [142]. These proteins either contain two such domains or are able to dimerize, to enable crosslinking of two neighboring filaments. L-plastin is found in leukocytes such as neutrophils, monocytes and macrophages, where it promotes tight crosslinking of actin filaments into parallel bundles [143]. As homolog to fimbrin, it corresponds to the smallest and simplest actin crosslinking structure, consisting of a tandem ABD within the same polypeptide chain [144]. Fascin is another crosslinker that permits formation of actin bundles, as found in various protrusions, and it is a major crosslinker in filopodia [145]. Here, actin tightly organizes in bundles which are characterized by reduced movement and increased stiffness. Fascin consists of four β-trefoil domains and two ABDs in domains 1 and 3. They are 5 nm apart, resulting in a tight bundling of actin filaments spaced by 8 nm. Parallel filaments can be further crosslinked by α-actinin, a member of the spectrin superfamily [146]. At its N-terminus, α-actinin contains an ABD, followed by a central domain of four spectrin-like repeats and a C-terminal calmodulin-like domain [147]. Through antiparallel dimerization of the spectrin-like repeats, α-actinin exposes its ABPs toward F-actin. Its crosslinking properties was first identified in the Z-disk within sarcomeres, but other isoforms are involved in various other actin networks.

In contrast to tight bundlers, filamin displays widely separated actin-binding domains, crosslinking less dense structures, typically found in dendritic networks [148]. It consists of a single ABD and flexible linker region that is also used for dimerization. Due to its longer flexible linker, filamin is capable to bind F-actin in a larger angular range and distance. Furthermore, it can also directly link filaments to the extracellular matrix [149].

2.1.5 Force generation

Actin polymerization can generate forces [150,151]. The polymerization force (f) is defined as the maximum force of an antagonist load that the filament can polymerize against. Theoretical calculations, as outlined below, estimate the polymerization force at around 9 pN [152,153], while experiments designed to directly measure the polymerization force of an isolated filament estimated it around 1 pN [154]. In a biological context, the polymerization force is considered as a type of "Brownian ratchet" [120,150]. Based on rapid thermal fluctuations of both the filament end and the membrane, appropriate gaps are created that permit the addition of an additional monomer that in turn causes a displacement of the membrane [155].

The following theoretical considerations of actin polymerization follow those described by Dmitrieff and Nedelec [153]. Binding of a new actin monomer to the barbed end of a filament causes a change of free energy ΔG, and if ΔG<0, the filament will polymerize spontaneously. Polymerization depends on the concentration of available actin monomers (c) and will only occur above the critical concentration (c*) of ~0.14 μM in solution [115].

$$\Delta G = -k_B T \ln\left(\frac{c}{c^*}\right) < 0$$

The Boltzmann constant is denoted by k_b and T as the absolute temperature. If polymerization occurs against a load, such as the plasma membrane, it conducts work (W). For polymerization to occur spontaneously, the work needs to be considered:

$$\Delta G + W < 0$$

The addition of a single actin monomer causes a displacement equivalent to the size of actin (∂ = 2.76 nm). Therefore, the mechanical work is defined as:

$$W = f \times \delta$$

Considering a physiological concentration of actin of 40 μM [156], the upper thermodynamic limit for the polymerization force is therefore:

$$f = \frac{-k_B T \ln\left(\frac{c}{c^*}\right)}{\delta} \approx 9\ pN$$

The theoretical calculations above consider the filament growth to be perpendicular to an antagonistic load. Realistically, filaments approach the plasma membrane with an angle (α). Thus, the total displacement per added monomer decreases and concomitantly, the polymerization force increases.

$$\delta_\alpha = \delta \times \sin(\alpha)$$

$$f_\alpha = \frac{f}{\sin(\alpha)}\ with\ 0 \leq \alpha \leq \pi$$

The polymerization force for inclined filaments is higher than for straight filaments and it increases, the flatter the filament approaches the membrane [153]. However, this comes

with the tradeoff of smaller local displacement. This balance allows for significant force amplification, which is typically seen in complex filament networks [157,158]. This indicates that straight bundled networks, such as filopodia, represent a less efficient architecture in terms of force generation, as compared to branched networks, such as the lamellipodium. In practice, both types of networks can exert forces higher than the theoretical limit. This is realized through crosslinking, bundling and branching of filaments, which provide additional anchor points and therefore increase their stability [153]. Accordingly, to fully understand a force-generating filament network, the entire system needs to be considered, rather than individual filament at the tips of the network [159].

A second role of the actin cytoskeleton exists in providing a scaffold for the ATPase motor protein myosin that binds to actin filaments and can move along by using energy from ATP hydrolysis [160]. Most prominently, this interaction exists in muscle cells in the sarcomere (see below), but there are various types of non-muscle myosin [161]. Those force-generating connections are involved in various key cellular processes and are thought to act similarly to actomyosin interactions within the sarcomere. However, detailed structural information on non-muscle myosin is missing so far. Myosin consists of a light and a heavy chain which contains a long tail that is used for dimerization [162]. The heavy chain also contains the motor domain which binds to the actin filament. Within this motor domain, the upper and lower domain are separated by a cleft and are followed by the lever arm. Nucleotide hydrolysis only leads to small structural changes in the active site, which are then amplified throughout the protein, resulting in large structural rearrangements, enabling the myosin head to move along the actin filament [133].

2.2 Human macrophage podosomes

2.2.1 Human macrophages and cell migration

Macrophages are myeloid immune cells that are found in all types of tissue across the human body, where they ingest and digest dead cells, debris, and pathogens [163]. As professional phagocytes, they are key players in innate immunity, by further presenting antigens to lymphocytes and triggering additional immune response [164]. Moreover, they are essential in tissue homeostasis and organ development during embryogenesis [165]. Macrophages within tissues are very heterogeneous, indicating the diverse plasticity of this cell type, allowing them to rapidly adapt to constantly changing environmental signals.

Upon infection, monocytes migrate from the blood stream through tissue to the site of entry and differentiate into pro-inflammatory macrophages, called M1 type (Figure 10) [166]. A second type of macrophages, called M2 phenotype, are subsequently found to facilitate wound healing, immunosuppression and termination of inflammation [167]. Failure to differentiate into M2 type may lead to autoimmune diseases and chronic inflammation, and also favors some forms of cancer [164]. In some cancers, macrophages infiltrate the tumor and can account for up to 1/3 of the entire cell mass, thereby promoting tumor growth and metastasis [168]. Accordingly, limiting macrophage tissue infiltration is an attractive therapeutic strategy [164].

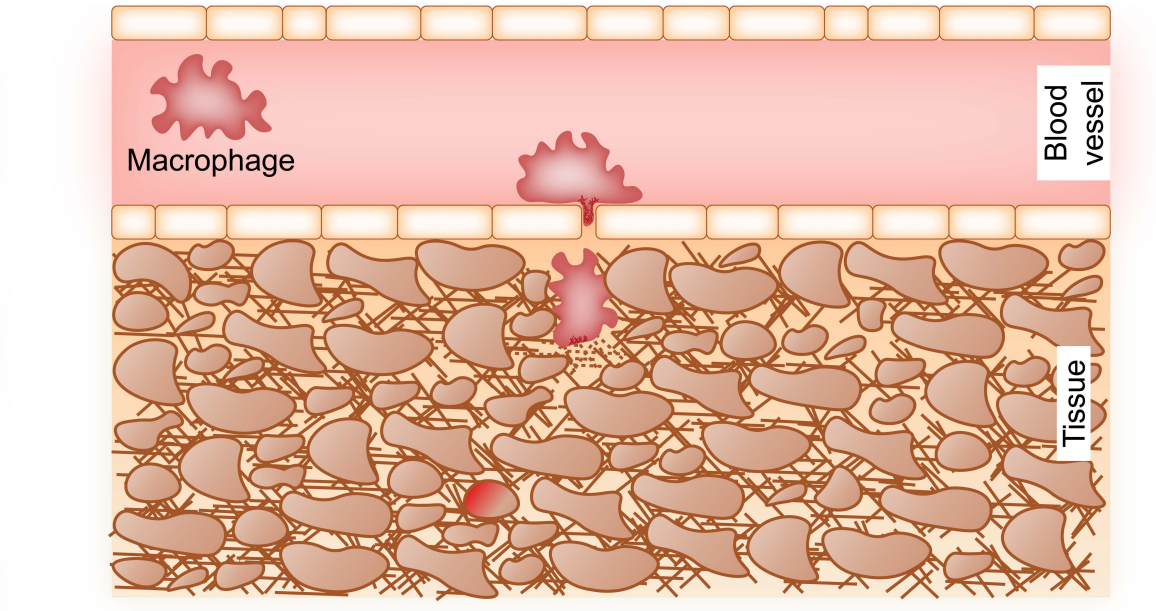

Figure 10: Schematic visualization of tissue infiltration by macrophages. Macrophages circulate through the blood stream and need to enter the surrounding tissue at appropriate location to reach an infected or damaged cell. They have to pass through a thick layer of cells, as well as dense extracellular matrix. Macrophages express highly specialized cytoskeletal networks, called podosomes or invadosomes, to enable this process.

In order to successfully migrate to the site of infection, macrophages need to infiltrate tissue with various biophysical properties, alternating between 2D, such as the blood stream, and 3D environments, as it is found within the tissue. Besides specialized cells, tissues are largely composed of the extracellular matrix (ECM) [169]. The ECM is compositionally heterogeneous with various biophysical properties depending on the tissue type. It contains several molecules and filaments, such as collagen which is the most abundant ECM protein. Further components include elastin, microfibrillar proteins, and other proteoglycans [170].

Another key remodeling factor is tumor tissue, which is often characterized by stiffer and denser ECM [171]. All the factors mentioned above provide a significant challenge for macrophages to successfully migrate through the various tissues.

Macrophages have two modes of migration. Amoeboid movement is characterized by a rounded cell shape with transient bleb formation, rapid and non-directional movement, and it is independent of proteases [164,172]. This migration pattern is observed for various cell types, including monocytes and lymphocytes. In contrast, the mesenchymal mode of migration is described by an elongated cell shape, directional and slow migration, and it is protease-dependent [172]. Macrophages can switch their mode of migration depending on the surrounding environment. In a matrix with large pores, macrophages can use amoeboid migration to navigate through the ECM, whereas in dense matrices with small pores they rely on mesenchymal migration [172]. In mesenchymal migration, macrophages are able to degrade and compact the ECM to form tunnels and clear paths to facilitate tissue migration [173]. It is suggested that this also depends on the size of the cell nucleus, as this is the largest organelle that needs to be squeezed [174]. During migration, the cell can release proteases, such as matrix metalloprotease (e.g., MT1-MMP), to locally degrade and remodel the matrix [175].

The above-mentioned considerations and obstacles highlight the importance for the migrating cell to sense its environment end elucidate the biophysical properties of its surrounding. This happens through a process called mechanosensing [176,177]. Here, adhesive structures exert mechanical force on the extracellular environment, and the resulting information triggers a biochemical response in the cell.

2.2.2 Podosomes and their role in mechanosensing

Podosomes are cell-matrix adhesion structures that are found in various migrating cells [178]. They are expressed constitutively in monocytes [179], macrophages [180], immature dendritic cells [181] and osteoclasts [182]. Transiently, they are also found in other cell types, such as endothelial cells upon growth factor stimulation [183], or neural crest cells during embryo development [184]. In cancer cells, such as breast cancer, related protrusive structures are found, which are called invadopodia [185]. As they share similar properties, both types of structures are commonly referred to as invadosomes.

These structures were first described in chicken embryo fibroblasts transfected with Rous sarcoma virus containing the v-src oncogene, which led to the reorganization of cytoskeletal proteins to form circular clusters [186]. It was later shown that these clusters coincide with protrusions of the ventral membrane [187]. As such, these structures were considered as cellular feet and termed podosomes.

Throughout the various cell types, podosomes accomplish several functions, including mechanosensing, adhesion, and matrix degradation (Figure 11) [178]. In addition, they are highly dynamic structures [188]. Therefore, they are key hubs for cells to sense and interact with their environment. Accordingly, their functions need to be highly regulated, even more so, to shift between opposing functions such as adhesion and degradation [189]. To do so, podosomes are equipped with a growing number of currently over 300 identified components that are involved in establishment, regulation, turnover, force production and signal transduction [190]. This large set of molecules is not consistently found in all types, but

depends on cell type, organism, and migratory state of the cell. However, there is a set of key modules that are essential for podosomes.

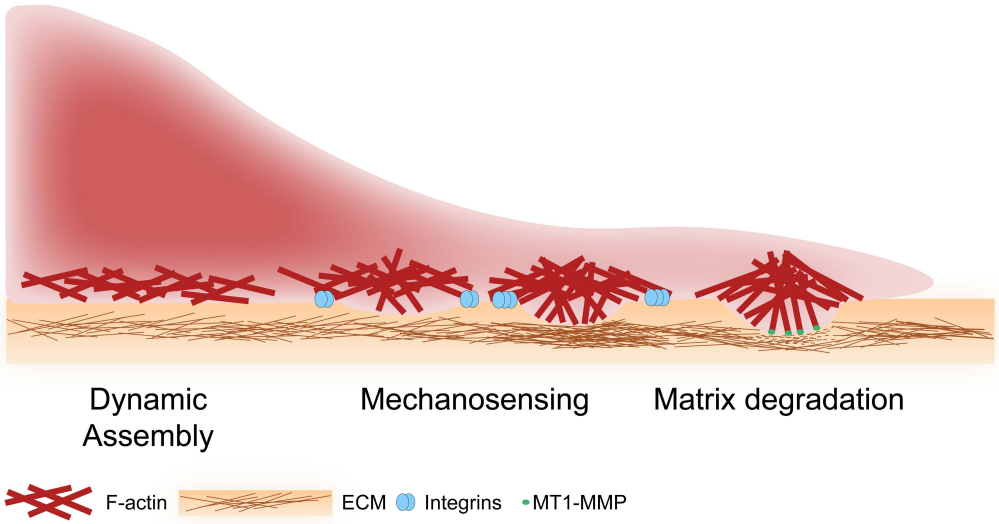

Figure 11: Hallmarks and key characteristics of human macrophage podosomes. Dynamic assembly and disassembly with fast turnover of the actin network. Mechanosensing the local environment and determining the stiffness of the local environment is reflected by the architecture and size of the podosome. Degradation of the extracellular matrix through release of metalloproteases such as MT1-MMP.

Podosomes are predominantly composed of actin filaments and display a modular architecture (Figure 12, top) [177,178]. The dense and highly crosslinked actin filament-rich core is around 500-1000 nm in diameter and up to 800 nm in height, with the Arp2/3 complex being the predominant nucleator [179]. The core is surrounded by an adhesion ring, characterized by talin and vinculin, which in turn bind to integrins that mediate cell-matrix adhesion [191]. Both the ring and the core are connected through lateral actin filaments that are thought to be unbranched. A third module exists in the podosome cap that sits on top of the core and mediates proteolytic and regulatory activity, and maintains connection between core and cap filaments. Within the cap, many regulatory proteins are found, such as formin INF2, or crosslinkers such as α-actinin [192,193]. Thus, the cap is considered as the regulatory hub for the podosome [189].

Podosomes can dynamically push against the plasma membrane and invade the ECM, where they can display proteolytic activity through the release of proteases, and locally degrade the ECM. This enables the clearance of paths and tunnels for the cell to subsequently migrate through the tissue [194]. In a 2D environment, podosomes can form larger super-structures that consist of several podosomes interconnected by actin filaments and myosin II, as their force generation and turnover are highly concerted [195,196]. Such super-structures depend on the cell type. In macrophages, podosomes are found throughout the ventral adhesion site or, during migration, they cluster at the leading edge [180]. In contrast, other cell types can form rosettes of podosomes, while osteoclast podosomes form belt-like super-structures, or exhibit ring formation, for instance, sealing zones [197-200].

Podosomes are very dynamic, with a turnover of 2-20 min [182]. The high turnover rate of podosomes and the larger numbers of podosomes per cell suggests the ECM degradation is likely to be shallow and widespread [178]. Podosomes exert perpendicular force toward the substrate (Figure 12, bottom) [188,201]. The force can extend up to tens of

nanonewtons, depending on the substrate stiffness, and is reflected in larger podosome architectures. This provides the basis for mechanosensing. Relevant physical parameters include rigidity, density and crosslinking, as well as general topography of the substrate. Substrate discontinuities, such as holes, can be detected this way. The mechanical parameters are then converted to biochemical signals which in turn trigger appropriate cell response [176]. Likely via interaction with microtubules, specific proteases, such as matrix metalloproteases MT1-MMP, or cathepsins, are recruited to the podosome, which in turn orchestrate ECM degradation [202].

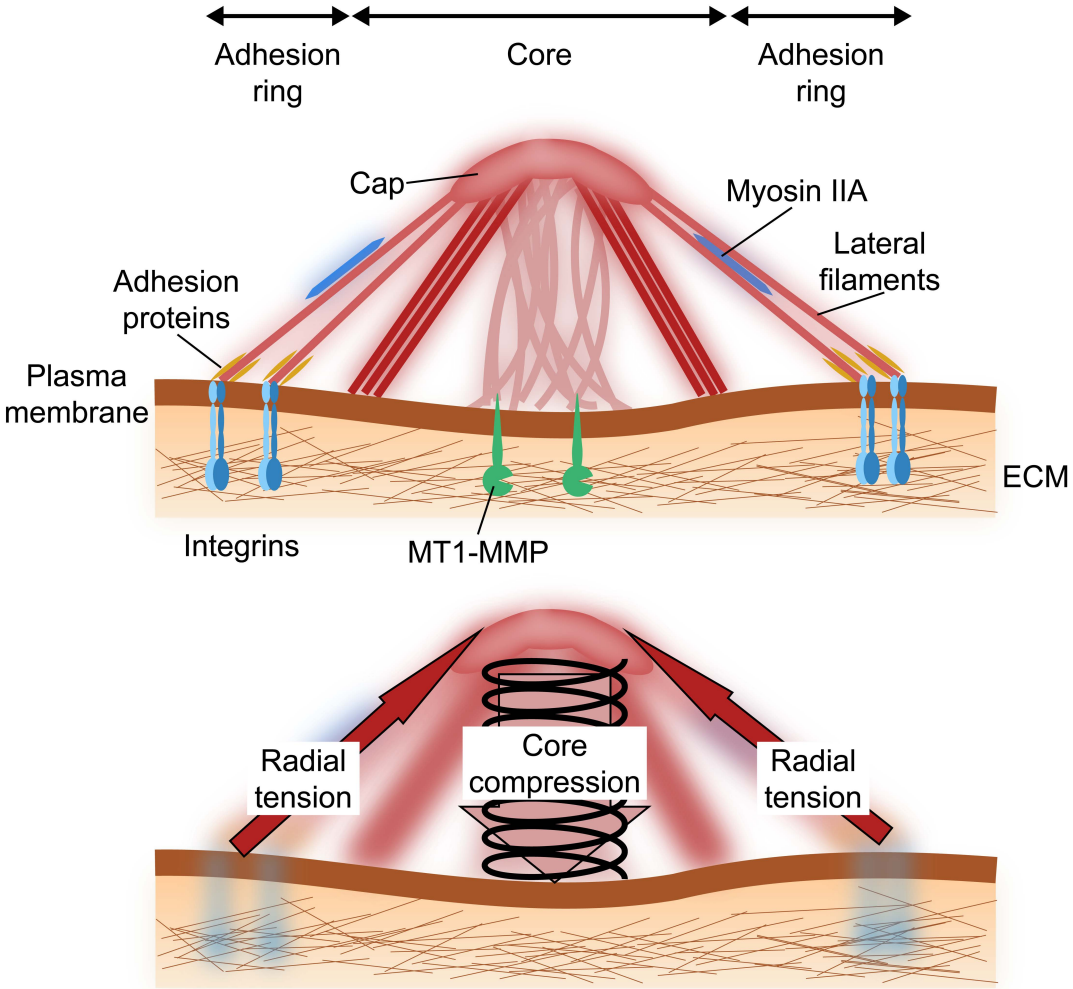

Figure 12: Overview of podosome architecture. Top: The main components of the podosome are the podosome core, the adhesion ring which is connected to the core through lateral filaments, and the podosome cap. The core consists of very dense and highly-crosslinked filaments, which are also curved. The protrusive force of the podosome is exerted at the core. The outside of the core is characterized through crosslinked actin filaments that are less branched. The adhesion ring connects the actin cytoskeleton via integrins to the ECM, which is established via the adhesion proteins talin, vinculin and paxilin. Lateral filaments connect the adhesion ring to the podosome core and likely contain non-muscle myosin IIA filaments. Lateral filaments intersect with the core at the cap structure which sits on top of the core. It consists of highly crosslinked actin filaments as well as many regulatory proteins. Matrix-metalloproteases such as MT1-MMP are located below the core and can locally degrade the ECM. Bottom: Model of protrusive force generation during mechanosensing and invasion. Bent and compressed core filaments store elastic energy and therefore act as an elastic spring, allowing the podosome to exert forces of up to 10 nN [159]. The elastic force is counterbalanced by radial tension at the lateral filaments.

Podosome formation is heavily dependent on the topological features of the cellular surroundings and the type of ECM, as outlined above, and initiation occurs at ventral regions of low contractility [203]. In general, phosphatidylinositolphosphate lipids (PIPs) are important factors during remodeling of the actin cytoskeleton [204]. Phosphorylated $PI(4,5)P_2$ and $PI(3,4,5)P_3$ accumulate toward the leading edge of the cell, where both lipids recruit Tks5 and N-WASP [205,206]. N-WASP is a key activator for the Arp2/3 complex that drives branched actin nucleation. Upon initial establishment of the network, further amplification of filament growth consists in locally inactivating RhoGTPases, such as Rho, Rac and CDC42, which leads to zones of decreased contractility, facilitating further polymerization [203,207]. CDC42 contributes to further actin polymerization through the recruitment of N-WASP and subsequent Arp2/3 activation, and activation of INF2 [192,208]. Further regulators of this process include the Src kinases Src and Hck, both of which are essential for podosome formation [209,210]. The maturation and growth of the network is further regulated and limited by various cap proteins, such as caldesmon, fascin and IFN2 [192,211,212].

Podosomes can exert forces in the range of 10-100 nN, depending on the substrate stiffness [201,213]. Coordinated actin polymerization in the core and concomitant bending of filaments, effectively storing elastic energy, leads to an amplified force that presses against the substrate. Concomitantly, a traction force is realized by lateral filaments connecting the core to the adhesion ring to counterbalance the protrusive force [214]. Mechanosensitive proteins like talin within the adhesion ring are stretched, promoting interaction with vinculin and further activating downstream signaling cascades [215,216]. However, the polymerization force applied by core filaments pushing against the membrane is not sufficient to explain the large forces exerted by the podosome. Instead, core filaments are compressed and therefore bent, which allows them to store elastic energy [159]. The whole network is therefore described as a loaded spring, whose force is counterbalanced by the lateral filaments anchored to the adhesion ring.

2.3 Sarcomere organization in striated muscles

The basic contractile unit of striated muscle cells is called sarcomere and is composed by two sets of filaments [217]. The polar thin filament consists of actin, tropomyosin (Tpm) and troponin (Tpn), and is interconnected with the myosin-based, bipolar thick filament. Their relative organization within the sarcomere is well studied and is commonly divided axially in different zones (Figure 13) [218]. Thick filaments are crosslinked at the M-line that is void of thin filaments in the relaxed state. The region spanned by thick filaments is called A (anisotropic) -band. On both sides of the M-line, thin and thick filaments interdigitate and form hexagonal arrays, depending on the muscle type and organism [219]. The region exclusively occupied by thin filaments is termed I (isotropic)-band [219]. At each sarcomere end, in the so-called Z-disc, thin filaments of adjacent sarcomeres are anchored and crosslinked with their barbed ends in an antiparallel fashion through α-actinin [220]. Additional interactions are realized to other sarcomere proteins such as nebulin and titin [221].

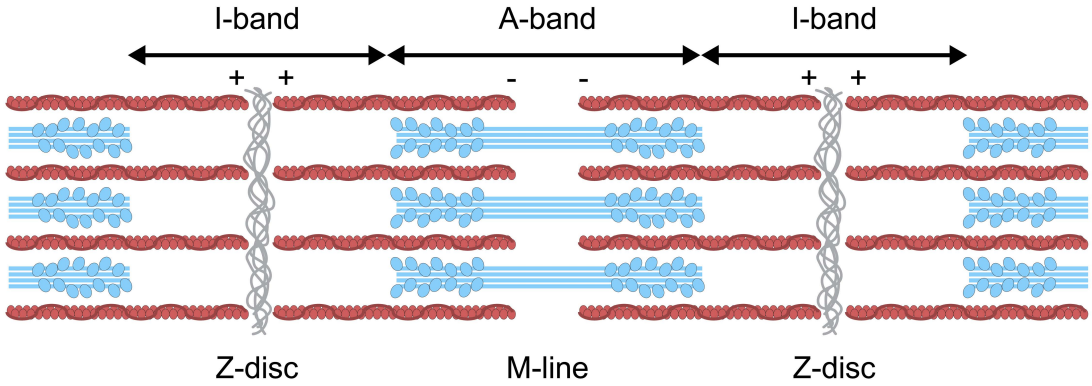

Figure 13: Schematic visualization of the sarcomere organization. The interconnection of thin filaments (red) and thick filaments (blue) at the Z-discs (gray) and at the M-line (center) are indicated. The polarity of the thin filaments is noted as + (barbed) and – (pointed) ends.

The sliding filament theory describes muscle contraction on a molecular level [218,222,223]. Thin and thick filaments slide past each other during contraction and each sarcomere is pulled together, enabled through the cyclic binding of myosin heads to the thin filament. This binding mechanism is called the power stroke cycle and consists of several states [224-226].

The rigor state is defined as the absence of a nucleotide in the motor domain. In this state, the myosin head is tightly bound to the actin filament. Upon ATP binding, myosin detaches from F-actin. In the following recovery stroke, the myosin head moves into the pre-power stroke position, enabled by rearrangements of the lever arm. Subsequent ATP hydrolysis enables reattachment to the actin filament. This reattachment results in further conformational changes in the motor domain that promote phosphate release. Upon phosphate release, the lever arm snaps back into its original position in the so-called power stroke, causing a relative displacement of myosin and actin. ADP-bound myosin then binds strongly to the actin filament, before the nucleotide detaches and the cycle repeats.

Further regulation of this key process consists in the accessibility of the myosin binding site on the thin filament. Tropomyosin (Tpm) is a large ABP, consisting of two long helices, that roughly follow the helical twist of the actin filament as two sets of cables twisting around the filament [227]. Their relative azimuthal position is regulated by the third

component of the thin filament, troponin, as a function of the Ca^{2+} concentration [228]. In the absence of Ca^{2+}, Tpm occupies the same binding site on the actin filament where myosin heads would bind, thereby blocking their interaction. Binding of Ca^{2+} to troponin causes troponin to act upon Tpm, triggering an azimuthal shift in a clock-wise orientation, partially opening the myosin binding site [227]. In this Ca^{2+}-state, binding of myosin to the filament is enabled but with lower affinity [228]. The head binding then causes a further displacement of Tpm leading to full activation in the so-called myosin state [162].

Aim of this work

Force-generating cellular actin networks provide the foundation for various essential cellular processes. Various structural techniques have made it possible to explain many phenomena on either microscopic or macroscopic scale. However, an integrated view on these cellular networks is missing. This thesis discusses how cryo-electron tomography accompanied with subtomogram averaging, as well as quantitative analysis of filament parameters, can provide an integrated picture of the architecture of force-generating cellular actin networks across scales.

The development of a workflow based on subtomogram averaging to determine the polarity of actin filaments in a 3D context will be presented. Concomitantly, the workflow enables to reveal the molecular sociology of actin machineries, and to understand the structural principles governing actin assemblies *in situ*. In particular, two force-generating actin assemblies will be investigated in this work, human macrophage podosomes and cardiac sarcomeres from neonatal rat cardiomyocytes.

Chapter 3: The molecular architecture of human macrophage podosomes

This work was realized in collaboration with the laboratory of Dr. Renaud Poincloux at the Institute of Pharmacology and Structural Biology (IPBS), Toulouse. All cell preparation steps, including plunge freezing, were performed by Stéphanie Balor at the Center for Integrative Biology (CBI), Toulouse. Cells were prepared by Stéphanie Balor and Javier Ray-Barroso at IPBS who also contributed significantly to the cell biological work, which is not included in this thesis. All discussed data, including cryo-FIB milling of *in situ* macrophages, data acquisition, tomogram reconstruction, and all analysis steps including subtomogram averaging were performed by myself.

3.1 *In situ* cryo-electron tomography of human macrophage podosomes

In this study, human macrophages were exploited to study podosome architecture at the molecular level. Macrophages are one of the main cell lineages expressing podosomes and have been used as primary model system in the field to study podosome behavior and biophysical properties. There are several possible sources to retrieve macrophages. In this study, primary macrophages were employed. While other stable cell lines, for example derived from mouse macrophages, allow for stable knock-outs of distinct proteins, primary cells are most relevant in a clinical context. Furthermore, this cell type has been used extensively in previous studies which allows for a direct comparison with the data presented in the thesis.

Monocytes were extracted from human blood and subsequently differentiated into macrophages by incubating them with Macrophage Colony-Stimulating Factor (M-CSF). The cells were then seeded on EM grids followed by plunge freezing (Figure 14A). Podosomes are found at the ventral membrane of migrating cells. Accordingly, cells had to be prepared using cryo-FIB milling to allow access to the basal membrane, located just above the grid surface. Instead of regular lamellae milling, a wedge geometry was employed. Here, milling is performed exclusively from the top with very shallow angles, typically less than 8° effective milling angle. This results in a wedge that uncovers part of the cellular interior, in particular the cytoplasm in proximity to the ventral membrane (Figure 14B-C).

In general, wedges can be larger compared to lamellae due to increased stability and more of the basal cell wall can be covered, reaching 40-50 μm in width (Figure 14C). However, thickness is harder to control than for standard lamellae, as there is no milling from below the area of interest. If there is a significant ice layer below the grid, this cannot be accounted for and will add up to the final specimen thickness, rendering the wedge often unusable. Furthermore, as a consequence of the wedge geometry, only the front part of the wedge is sufficiently thin and accessible in the TEM (Figure 14D-E). The overall thickness will increase rapidly, depending on the effective milling angle, as can be seen from the wedge overviews (Figure 14E-G). Therefore, even a few degrees can have a drastic effect on the accessible area. An effective milling angle of 4° allows for a length of ~3.5 μm before the wedge thickness surpasses 250 nm, while a milling angle of 8° reaches this thickness already at a length of ~1.8 μm, effectively halving the accessible acquisition area.

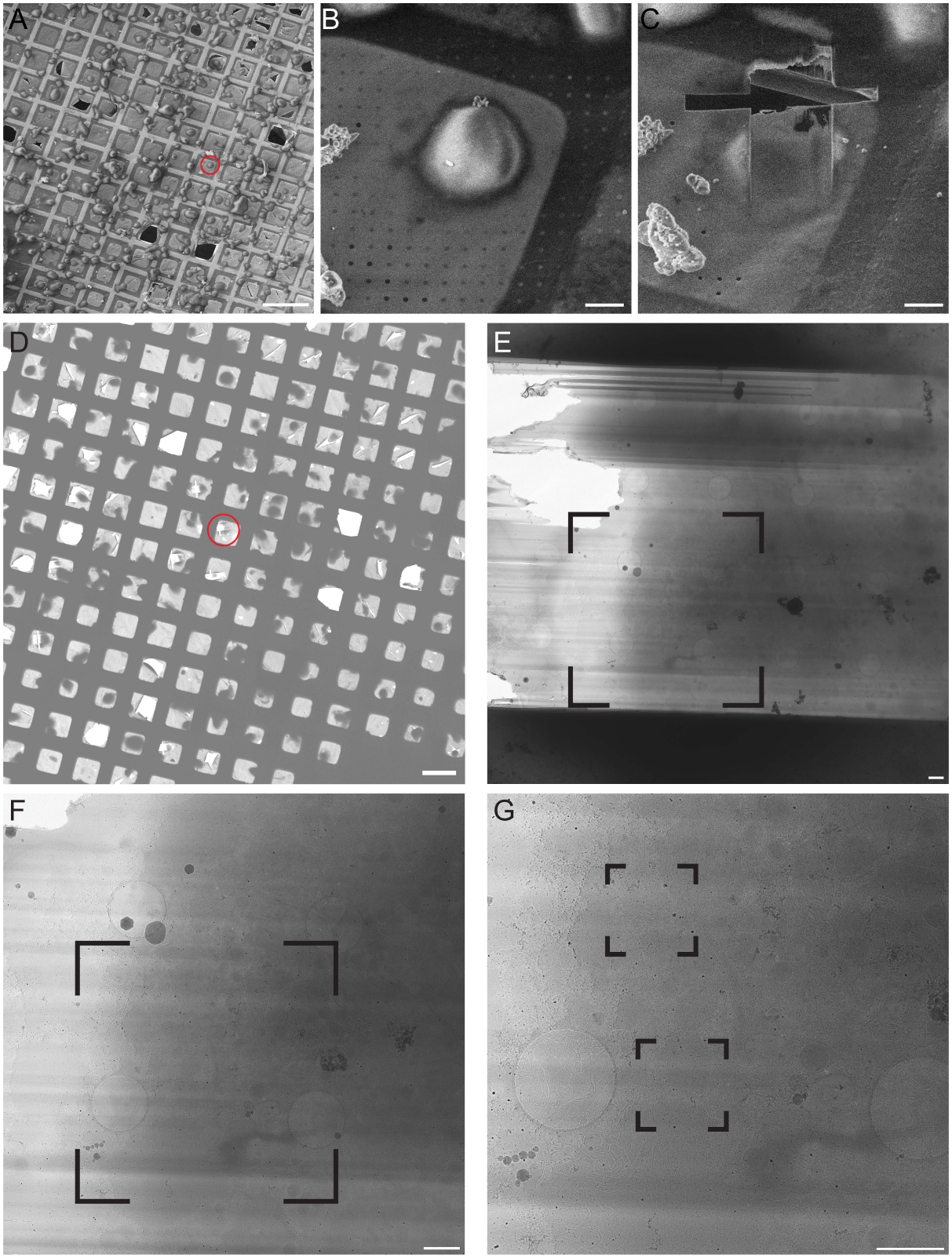

Figure 14: Sample preparation of human macrophages. A: SEM overview image of an EM grid containing plunge-frozen human macrophages. The encircled cell was targeted for milling. Scale bar 200 µm. B: Close-up SEM image of the same cell before milling. Scale bar 10 µm. C: Close-up of the same cell after milling a wedge geometry. Scale bar 10 µm. D: TEM overview of the same grid. The same cell is highlighted in red. Scale bar 100 µm. E-G: Close-up TEM image of the same wedge prior to data acquisition. Scale bars 1 µm. The rectangular areas indicate the next highest magnification. The two rectangles in G are the positions of the tomograms displayed in Figure 15 A and B, respectively.

From the same cell highlighted in Figure 14, three podosomes were located in close vicinity to each other, highlighting the formation of super-clusters. These podosomes are displayed in Figure 15. Two of these examples (Figure 15A and B) were located in direct proximity (Figure 14G). Both examples are found in contact with the same bundled arrangement of filaments. Segmentation of the filaments, highlighting those belonging to the podosome, reveals their close interaction with the bundle (Figure 15D and E). This suggests the connection of podosomes as anchor points with the actin bundle running transversally across the cellular front. Each example contains a single microtubule, two of which are running directly toward the podosome core (Figure 15D and F). Microtubules are thought to interact with podosomes and deliver important cargo for their functional and regulatory basis, such as matrix-lytic enzymes [202]. The direct localization of microtubules and their radial orientation with respect to the core supports this notion. Interestingly, ribosomes were found in close proximity to the podosome core in all examples (Figure 15D-F). However, none were found within the dense network of actin filaments of the podosome, or within the actin bundle.

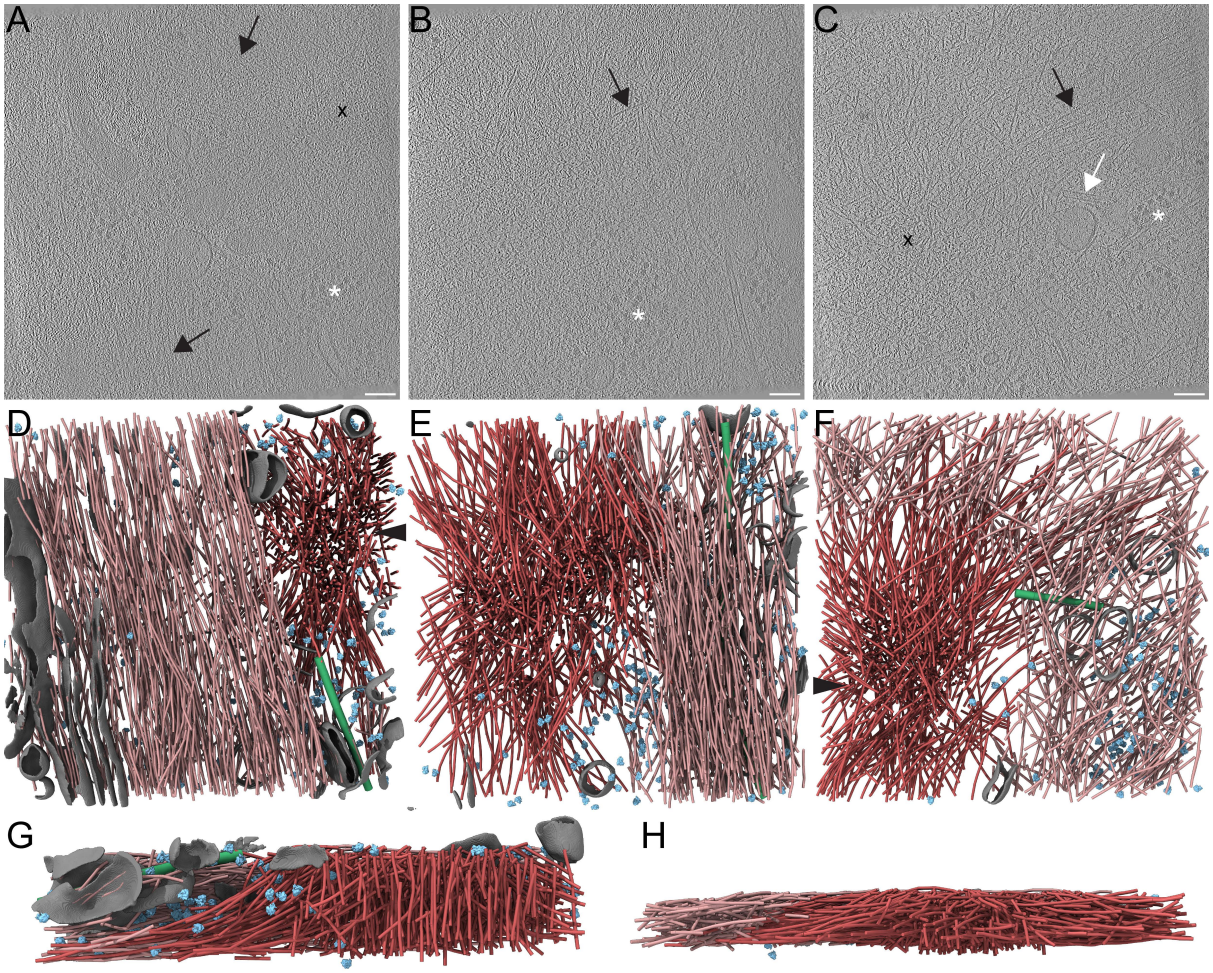

Figure 15: *In situ* tomograms of podosomes from human macrophages. A-C: Tomographic slices showing human macrophage podosomes in their native context. The black crosses indicate the dense core region, asterisks indicate ribosomes. Black arrows highlight individual actin filaments, white arrows point at microtubules. Scale bars 100 nm. D-F: Corresponding segmentations to A-C. Filaments associated to the podosome are indicated in dark red, other filaments are shown in light red. Microtubules are depicted in green, ribosomes in blue. Membranes are shown in gray. G-H: Side views of the segmentations in D and F, respectively. Points of view are indicated by black arrowheads, with the plasma membrane located at the bottom of the image.

The overall architecture of the podosome-associated filaments is highly similar to those described in a previous study, forming the basis of this work [159]. The core is characterized by upright filaments that extend beyond the layer of cortex filaments into the plasma membrane (Figure 15G). They are surrounded by a set of lateral filaments that flatten as they approach the plasma membrane, connecting the core to the cortex layer and the extracellular matrix. This set of radial filaments is interrupted at the barrier between the podosome and the bundle, suggesting that this bundle emerged prior to the establishment of the podosome. Interestingly, the arrangement of radial filaments is also perturbed at a region where many ribosomes were found (Figure 15E). The reason for this is not obvious, but there could be other proteins expressed locally in this area, as suggested by the large number of ribosomes, that prevent the incorporation of actin filaments.

The examples in Figure 15D and E do not contain filaments at the top of the core, where the podosome cap is located, as the top was removed during cryo-FIB milling. However, the podosome shown in Figure 15F is substantially smaller and its top was preserved (Figure 15H). It shows several radial filaments running across the core, where they intersect with other lateral filaments.

The tomograms displayed here are typical of those that were observed during this study. The contrast is suboptimal, as the tomograms are quite thick. While the cellular part is not primarily contributing to this thickness, the wedge geometry during cryo-FIB milling prevents the removal of material below the cell. This includes the carbon layer and any residual ice that is found below the grid. These factors contribute to the additional thickness to the tomogram and limit the contrast and obtainable resolution of the data. As such, this did not allow any high-resolution structure to be retrieved for the actin filaments.

Furthermore, the success rate in capturing podosomes *in situ* was very low and only a few examples were captured. Podosomes are transient structures that adapt rapidly to the cellular environment. The time delay between removing the grids from their medium and plunge freezing might be sufficient for podosomes to disassemble. Furthermore, primary cells are less viable than stable cell lines and cells disintegrate more quickly. This is enhanced by the non-typical growth environment of a metal grid. Morphological changes might not immediately be visible before plunge-freezing. In particular, this was reflected in the large number of apoptotic cells, rounded mitochondria without cristae, and cytoplasm containing predominantly vesicles while other cellular features were absent. For these reasons, the investigation of *in situ* tomograms was limited to descriptive analysis of the filament architecture.

3.2 Unroofed human macrophage podosomes

Another specimen preparation method is unroofing [229,230]. Unroofing is a widely explored technique in the podosome field, where it is used in traditional light microscopy and super-resolution microscopy studies of migrating and motile cells. The bulk of the cell, including the cytoplasm, is washed off by a shear-flow, removing most of the cytoplasm, and leaving only the ventral cell membrane and its periphery. To stabilize the filaments, the unroofing mix contains phalloidin, a toxin-derived small molecule, that bind in the nucleotide-binding cleft and enhance intra-strand interactions, without altering the actin ultrastructure. It was shown for podosomes, that the overall architecture remains highly similar between unroofed and cryo-FIB prepared networks [159]. Despite this, unroofing is not an artefact-free method. The comparison revealed that unroofed filaments are less curved, presumably due to the loss of the cytoplasm and the accompanied release of strain on the network. Moreover, some connections between actin filaments and the plasma membrane may have been dissolved. PFA can be added as additional support, as it crosslinks the filaments and preserves the architecture. It comes at the expense of disrupting the plasma membrane, causing further alterations. Unroofing is a cruder method as compared to traditional cryo-FIB milling and violates the term *in situ* in a stricter sense. Nevertheless, for studying the ventral membrane periphery, and the actin cytoskeleton in particular, it proved to be a versatile tool as it preserves the cytoskeletal architecture and is a higher throughput method than cryo-FIB milling. Moreover, the entire cell surface is accessible for cryo-ET and cells can quickly be evaluated for podosome expression.

Unroofed podosomes can readily be identified in the overview images, where they manifest as dark spots (Figure 16). The overview images also reveal podosome super-structures as commonly observed in light microscopy studies. The example shown in Figure 16A contains a cell that expressed many podosomes at once, presumably at its leading edge. In contrast, the majority of cells evaluated from the overview images did not contain any podosomes at all. This supports the low success rate of targeting podosomes *in situ*.

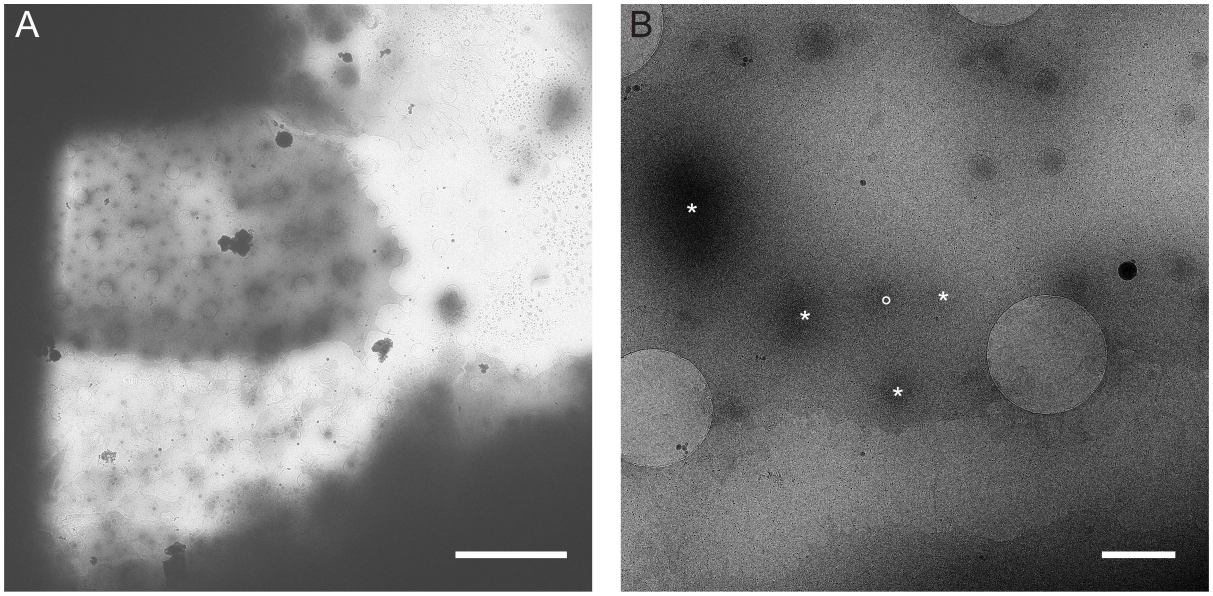

Figure 16: Unroofed macrophage podosomes. A: TEM overview image of an unroofed macrophage, dark spots are podosomes. Scale bar 10 μm. B: Close-up TEM image of an unroofed macrophage. The central podosome is marked in a circle, neighboring podosomes are marked with asterisks. Scale bar 1 μm.

The data quality and contrast of the resulting tomograms were substantially improved compared to the *in situ* data, in particular due to the absence of any cytoplasm (Figure 17A and Figure 18A). Post-processing the tomograms via denoising and missing wedge-correction significantly boosted the contrast (Figure 17B-C). In particular, missing wedge-correction improved the interpretability in xz direction and allows to identify filaments perpendicular to the field of view, especially those in the core (Figure 17C). The xz slice also shows the plasma membrane, the supporting carbon layer as well as an additional layer of ice underneath the grid.

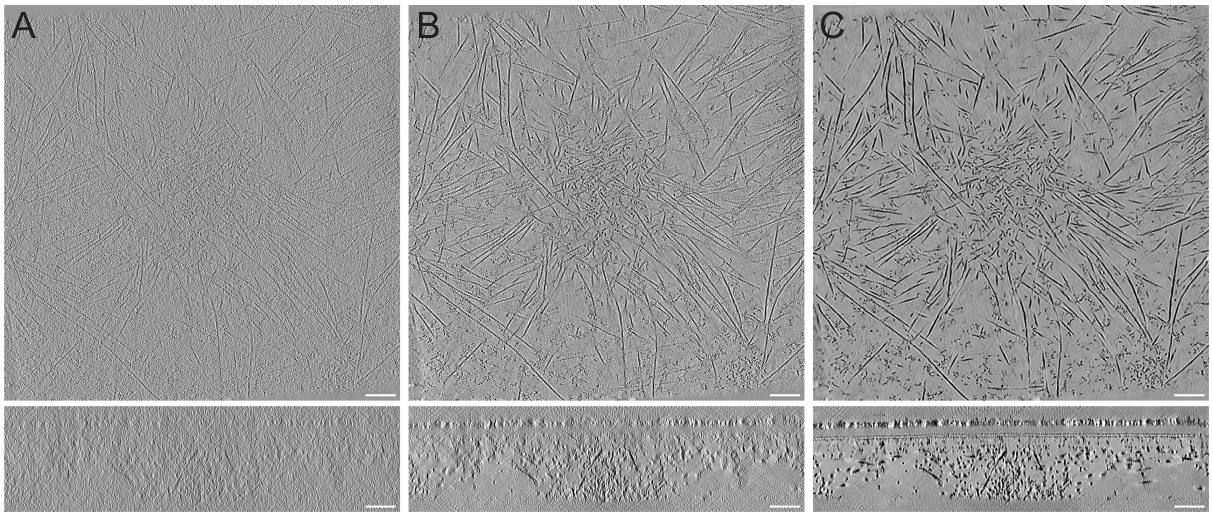

Figure 17: Post-processing of an unroofed podosome tomogram. Central tomographic slices are shown for the original tomogram after weighted back projection (A), after denoising with cryoCARE (B), and after denoising and missing wedge-correction using IsoNET (C), respectively. Upper row: xy slices. Bottom row: xz slices. Scale bars 100 nm.

The contrast of post-processed tomograms of unroofed podosomes allows to resolve the twist of the actin filaments as well as allows to identify individual actin monomers (Figure 18A). Additionally, it improves interpretability of the dense core region, although not all the small connections can be resolved. This is also reflected in the improved filament segmentation (Figure 18B). The podosome core can be clearly recognized in the center of the tomogram. Both the density and amount of actin filaments within the core is striking. As shown in a previous cryo-ET study of podosomes, core filaments are mostly upright and rather short [159]. The core is enclosed by a set of lateral filaments, radiating evenly from the core. As such, the architecture is reminiscent of the *in situ* architecture shown above. This confirms that unroofing did not substantially influence the architecture. Moreover, two additional cores from neighboring podosomes can be detected in the tomogram (asterisks in Figure 18B). This example corresponds to the overview image shown in Figure 16B, where those neighboring podosomes are visible as well. A third neighbor is presumably just outside the field of view.

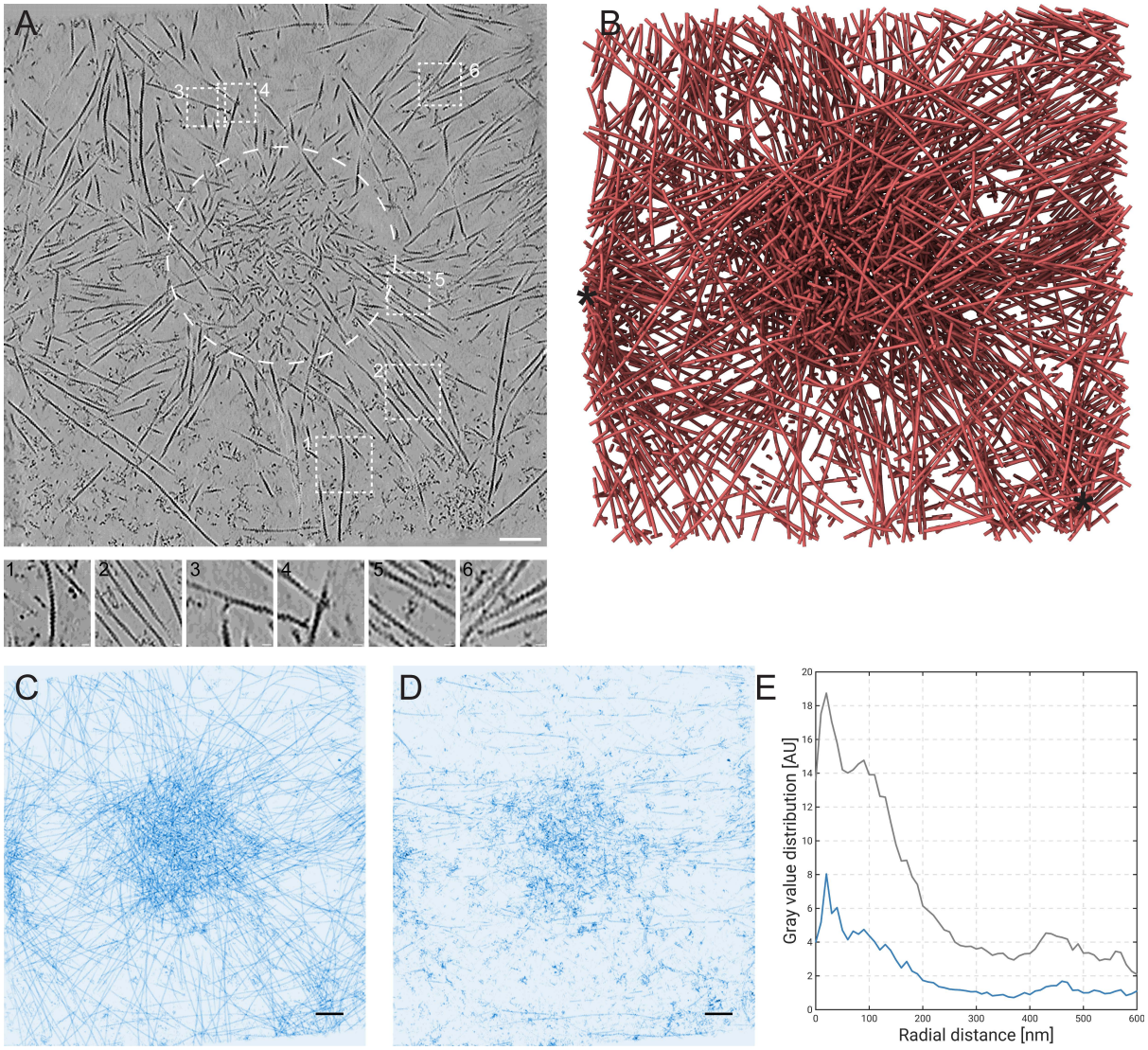

Figure 18: Segmentation of unroofed podosomes. A: Annotated tomographic slice (1.4 nm thickness) from the same tomogram shown in Figure 17. The dense podosome core is encircled. Boxed close-up images are shown as a gallery below. Scale bar 100 nm and 10 nm for the close-ups. B: Filament segmentation of the tomogram in A. Asterisks indicated cores of adjacent podosomes. C: Maximum intensity projection of a central slab of the tomographic volume after Frangi-filtering and binarization. Scale bar 100 nm. D: Maximum intensity projection after subtracting segmented density from the Frangi-filtered volume, highlighting densities that are not included in the segmentation shown in B. Scale bar 100 nm. E: Radially averaged intensity profile of the images shown in C (gray) and D (blue).

The segmentation presented in Figure 18B is incomplete. The podosome is a highly complex cytoskeletal network and consists of many overlapping filaments. Importantly, the density of filaments in the core poses a significant challenge for the tracing. Moreover, the crosslinker and overlap of filaments contributes to this challenge. While the improved contrast facilitates filament segmentation, the high resolution of the individual filaments deteriorates standard segmentation approaches. Traditional filament segmentation occurs in a two-step process. First, a cylindrical template with the appropriate dimensions is generated, and is then correlated against the entire tomographic volume. This approach was conceptualized when data quality was still poorer and tomograms were acquired at lower magnifications. As such, filaments could easily be approximated as a cylinder. For new data, this is not the case anymore. Due to this discrepancy the correlation is deteriorated, decreasing the correlation

score of true positive hits, reducing the sharpness of the peaks. It also leads to false positive hits, as a featureless cylindrical structure is more similar to membranes than a filament would be. More importantly, the correlation score is heavily affected by filament density and especially at crossovers of filaments. Here, the tomographic data strongly deviates from an ideal cylinder which decreases the correlation score in these areas. Consequently, the subsequent tracing is affected and incomplete at such positions. The resulting filaments are shorter or are interrupted and subsequently treated as separate filaments altogether. In the worst case, the filament is then too short to be considered at all, increasing the number of false-negatives.

As mentioned above, for the podosome, this poses a significant limitation. The core is composed of a highly dense and strongly crosslinked filament network. Despite best efforts in carefully choosing segmentation parameters and manual curation, the traced network remains incomplete, in particular in the core. The lower correlation values within the dense core require to lower the overall detection threshold. This comes at the expense of picking up more false-positive filaments across the podosome, which need to be removed subsequently. To get an estimate on the overall completeness of the segmentation, a central slab of 78 pixels along z was additionally filtered slice by slice by a 2D Frangi-filter and then binarized (Figure 18C). Frangi-filtering is used to emphasize elongated features while removing salt and pepper-style noise features [74]. The filament segmentation was used to generate a binary mask which was then used to subtract the traced density from the Frangi-filtered slab. The resulting volume contains only density that was not accounted for by the filament segmentation (Figure 18D).

As expected, most of the unaccounted density can be found in the core region, while the lateral filaments are traced close to completion. In the periphery only filaments that are orthogonal to the tilt axis (y axis) were missed (Figure 18D). Filaments in this orientation are more affected by the missing wedge which could explain why they were not picked up during tracing. In contrast, unaccounted density in the core does not primarily represent filamentous density. Instead, most density appears globular and highly connected, suggesting this density corresponds to crosslinkers and other actin-associated proteins. Evaluating the distribution of this unaccounted density as a function of the radial distance from the center shows the same distribution as the original density (Figure 18E blue and gray curves, respectively). It confirms that indeed most of the remaining density is found in the center. However, it also shows that the majority of filaments were successfully identified in the core and the unaccounted density is likely derived from short and highly crosslinked or bundled filaments. This serves as the basis for meaningful subsequent structural and quantitative analysis of the podosome architecture by subtomogram averaging.

3.3 Subtomogram averaging of actin filaments

3.3.1 Filament resampling

The actin cytoskeleton is ideally suited for structural investigations by means of subtomogram averaging. In podosomes, actin filaments are highly abundant, the helical symmetry ensures a complete angular sampling, and filaments comprise a defined geometric shape that allows to restrict the search space. Furthermore, the data quality of unroofed tomograms is sufficient to enable higher obtainable resolutions. For these reasons, subtomogram averaging was employed to study the molecular architecture of the podosome at the molecular level. To do so, a defined workflow needed to be established to obtain a refined filament structure. Subtomogram averaging requires filaments to be precedingly identified by segmentation. The primary output of the tracing algorithm is a set of 3D coordinates that correspond to the filament position. It also comes with a basic angular orientation of the respective segment. However, both types of information are insufficient for averaging.

The point coordinates are not equidistantly spaced and the angular information does not correspond to commonly used Euler conventions. Furthermore, additional information required for subsequent averaging is missing. For these reasons, the output coordinates need to be resampled and formatted into an appropriate particle list (Figure 19). This algorithm is based on previous work where the equidistant sampling was introduced [231]. An additional feature derived from this work is the principal component analysis of the coordinates to define the main orientational component of the filament. This ensures that the sampling of bundled filaments is in unison and prevents diverging orientations within a single filament. For podosomes, this was usually the principal component corresponding to the z dimension, i.e., the filament height.

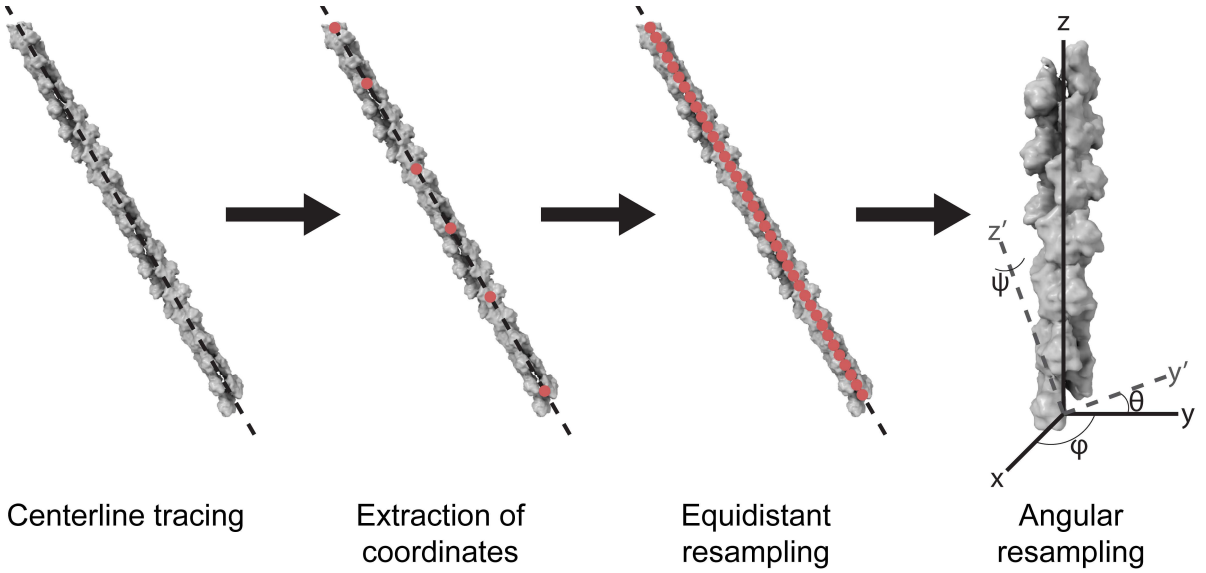

Figure 19: Filament resampling workflow. Filament centerlines are traced and initial coordinates per filament are derived. These coordinates are then resampled equidistantly with a spacing of 1.38 nm. Initial Euler angles are calculated from the cartesian positions using the zxz-convention. The angles are calculated in a way that the filament centerline corresponds to the Z-axis and the helical twist is described by the in-plane angle ϕ.

For actin filaments, the sampling was chosen as half the helical rise of 2.76 nm, where a sampling distance of 1.38 nm corresponds to 2x oversampling. This is important to precisely locate the individual subunits during the averaging procedure, as their exact location cannot be directly retrieved from the segmentation. This form of oversampling ensures that, at most, the sampling point is 1.38 nm away from its true position and can converge appropriately during refinement. Particle shifts are restricted to the same distance during alignment, preventing individual positions to shift further than the adjacent subunit and therefore avoid missing any subunits during alignment. Finally, distance cleaning is performed to remove duplicate hits, resulting in one position centered on each monomer.

Initial Euler angles are calculated as spherical coordinates Azimuth and Elevation from the Cartesian coordinates of two adjacent sampling points and converted to Euler angles, following the zxz-convention, that is commonly used by various STA software. As the in-plane angle ϕ cannot directly be derived from two coordinates, it is initially randomized. The sampling ensures that the z-axis corresponds to the helical axis of the filament and the in-plane angle describes the helical twist (Figure 19).

This substantially reduces search space during alignment, as the general orientation of the filament is already approximately known from filament tracing. Accordingly, costly full cone search, can be avoided and the angular search split into in-plane and out-of-plane searches. Initial in-plane search is conducted as global search before local refinement can be performed. This ensures that for each filament, apart from its correct position, also the correct orientation can be found. This alignment procedure allows to precisely identify the helical parameters for each subunit, as the twist can be calculated between the Euler angles of two neighboring positions and the rise can be derived from the vector between both adjacent sampling points.

3.3.2 Polarity determination of actin filaments

As actin is a polar filament, averaging filaments in random orientations will result in an average with mixed polarity. This will limit the resolution to approximately 25-30 Å and will render the structural information meaningless. When averaging a straight bundle, such as those found in filopodia, the polarity may be neglected, as most filaments will be of uniform polarity. However, in case of the podosome, where the filament orientation is not known, this will lead to an average that cannot be interpreted. In addition, knowing the exact position and orientation for all of the filaments is critical to understanding the network architecture. Therefore, reductionist approaches, where only parts of the network are considered for averaging and high-resolution structure generation, are not suited for this work.

Accordingly, a workflow was developed within the scope of this work, to precisely determine the polarity of actin filaments across a variety of orientations and determine the refined positions of all filaments (Figure 20). Previous polarity determination workflows were developed for filaments in flat orientations and are based on projecting filaments in 2D [232]. This is problematic for a few reasons, in particular artifacts introduced by the missing wedge, as outlined in the Discussion section, but those effects are less severe for flatly oriented filaments. For 3D filaments, especially filaments close to an upright position, a 2D approach is insufficient.

The here presented workflow was developed to address these issues (Figure 20). It is based on supervised multi-reference alignment, comparing cross-correlation (CC) values between the subtomogram and two reference structures with opposite polarities. As the polarity of an actin filament can only be confidently determined at a resolution of less than 25 Å, the CC scores for both orientations will be very similar. For these reasons, CC scores are compared on the filament level, exploiting the prior that a filament can only have a single orientation. The respective CC scores are grouped and statistically evaluated. Importantly, each filament is evaluated independently. As the observations are paired (each subtomogram is compared to both references) and the scores approximate a normal distribution, a Student's t-test was chosen to assess the statistical significance of the average scores per orientation. If the difference between both populations is significant ($p < 0.05$), the respective polarity is assigned to the filament. Otherwise, the filament is excluded from further averaging. Of note, other statistical tests that compare median values or do not assume normal distribution, led to similar results.

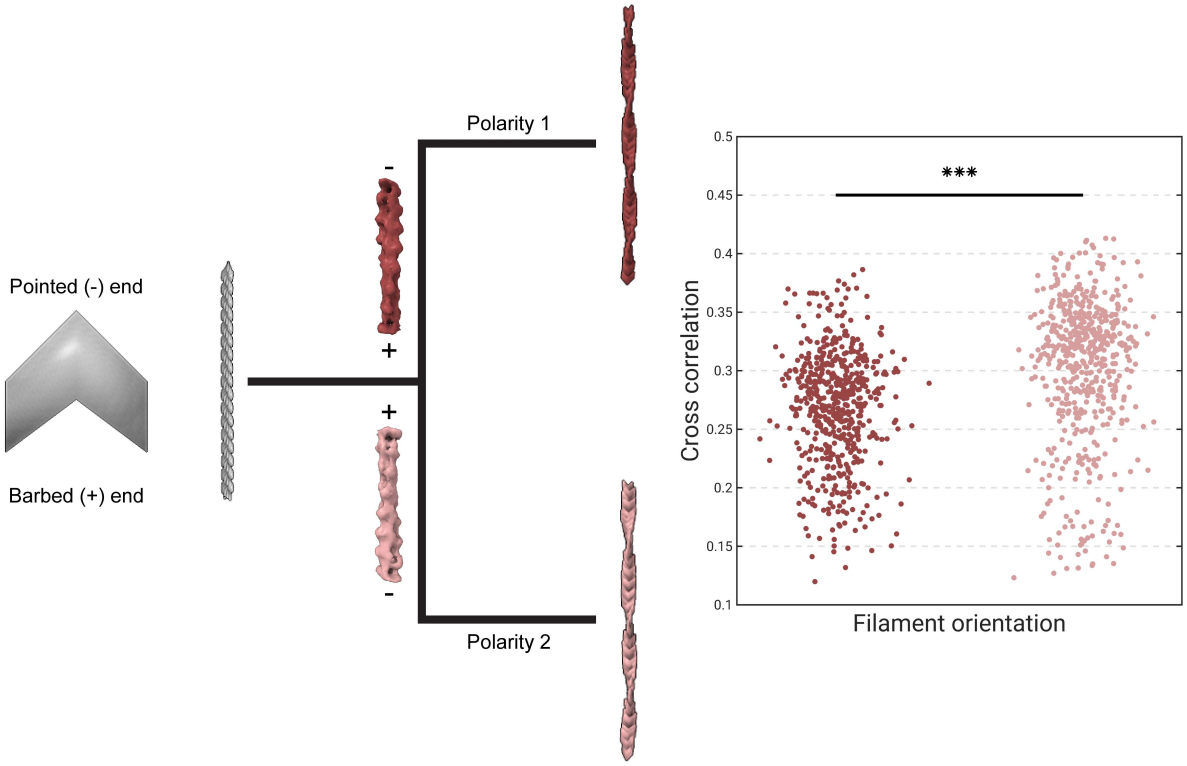

Figure 20: Polarity determination workflow. Each sampling position is represented by an arrowhead, barbed and pointed ends are indicated, respectively. The initial oversampling is shown in gray. Each position is aligned against two references of opposite polarity (polarity 1 and 2, dark and light red, respectively). The resulting cross correlation scores of all sampling points are statistically evaluated and the respective polarity is assigned if the difference is significant. ***: $p < 0.001$

3.3.3 Generating a *de novo* actin filament structure of uniform polarity

The main caveat of this method is the generation of two reference structures with opposite polarity. While external structures, i.e., derived from the EMDB or PDB databases, can be used, it is best to work with structures derived from the same data. This ensures the correct gray value distribution matching the target data. More importantly, generating a *de novo* structure also avoids the introduction of template bias, and strengthens the reliability of the output structure.

In case of the podosome, this was addressed in several steps as follows (Figure 21). First, 57 of the longest filaments from a single tomogram were selected, and subtomograms for each filament were aligned individually using a multi-class alignment approach. Accordingly, each average contained only one orientation. During the initial iterative alignment using binned data, 16 filaments emerged that displayed a helical pattern. Yet, the signal was not sufficiently high for each filament, as not all filaments displayed this pattern. As the alignment begins with a global search, it is likely that it may get trapped in a local minimum. Furthermore, some filament classes may have contained too few particles in the first place to achieve sufficient signal. For these reasons, only filaments with a helical pattern visible were selected and processed further. Upon refinement using unbinned data (bin1), the helical pattern strongly improved for most classes. The best resolved class was then used as reference for a supervised classification with two classes. A second class was generated by rotating the first by 180°. The classification led to two classes with filaments of opposite polarity and the resolution improved concomitantly. It was measured at around 25 Å which was sufficient to differentiate their polarity. Thus, these structures were employed for a first round of polarity assignment of a subset of filaments, as outlined in the previous chapter.

The assignment was not complete, as many filaments were still ambiguous. To improve the structure, the assigned filaments were combined and an improved single structure with uniform polarity was obtained. The cycle was then repeated and subsequently, all 16 filaments were attributed their respective polarity with confidence. A second refinement run led to a better resolved structure and resolution around 20 Å. This *de novo* structure, and a rotated version, was then used to determine the polarity of all filaments across 5 podosomes.

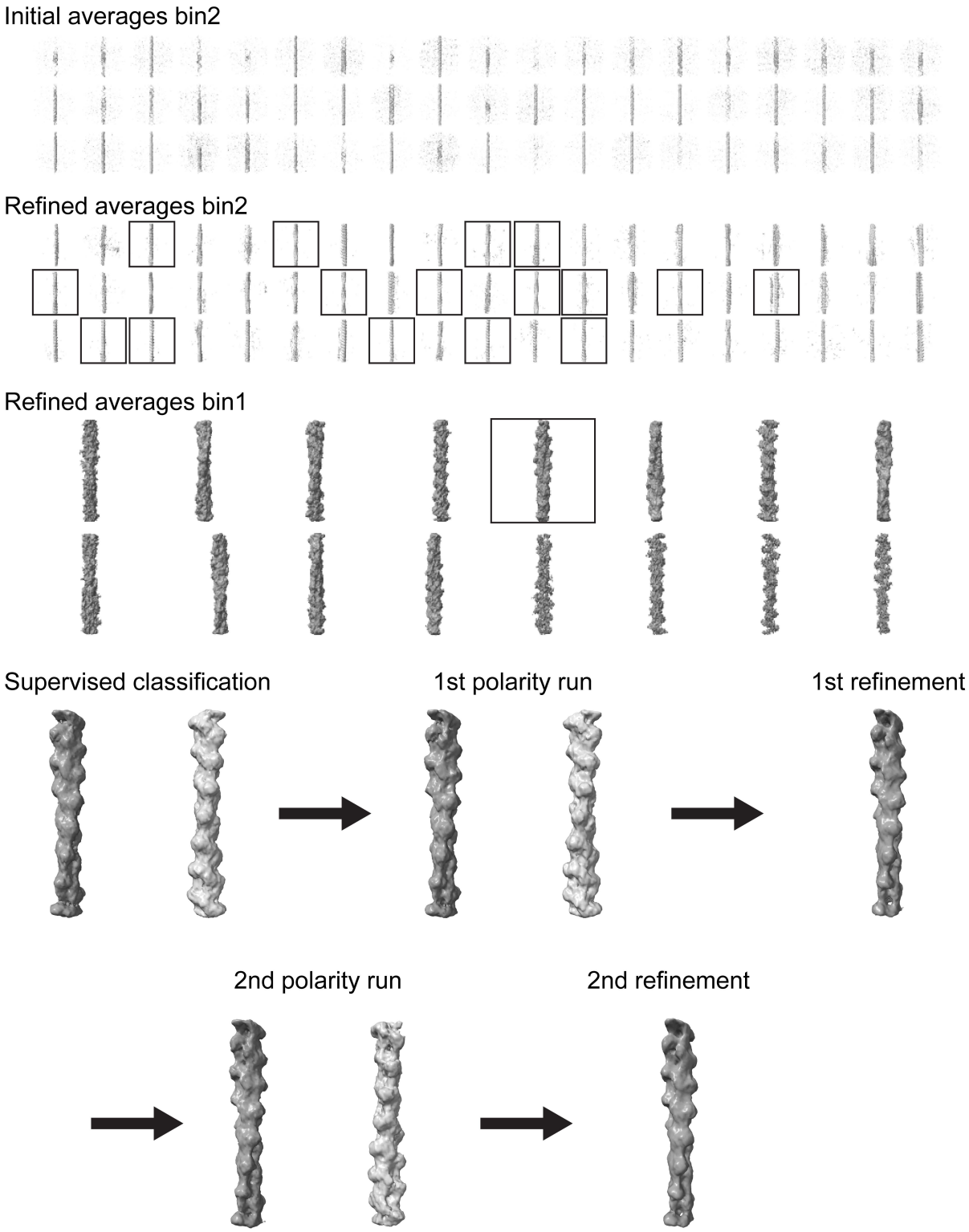

Figure 21: Generating a *de novo* reference structure. Top row: initial averages at bin2 (pixel size 7.04 Å) without alignment of subtomograms belonging to each filament class, respectively. Second row: The same averages upon global alignment. Boxed filaments indicate emergence of a helical twist. These were selected for further processing. Third row: Refined structures of unbinned volumes (bin1). A single class was chosen for subsequent supervised classification with two classes. Forth row left: Final classes of the supervised classification. Fourth row middle: Final averages after initial polarity assignment using the classes from the supervised classification. Fourth row right: Refined average after combining the polarities of assigned filaments. Bottom row left: Result of the second polarity run using the previously refined structure as reference. Bottom row right: Refined average after combining the polarities of assigned filaments of the 2nd polarity run.

3.3.4 Polarity assignment of actin filaments

By employing the above-mentioned algorithm, filaments for all podosomes were evaluated and their respective polarity was assigned. Across all investigated podosomes, 79 ± 15 % of filaments were confidently assigned their respective orientation (Figure 22A). The main limitations that prevented a confident classification were the overall reconstruction quality of the tomogram (Figure 22B and B'). This was pronounced within the core, where the alignment often appeared worse than in the periphery, owed to the increased thickness and crowdedness of filaments, that negatively affect the alignment. Additional parameters were filament length, as short filaments had less sampling points for evaluation, as well as filament density and crossover percentage, as these factors negatively influence cross correlation scores and therefore alter the comparison. Again, both factors are more pronounced in the core.

For tomograms with high reconstruction quality, and podosomes which did not exhibit a high core density, the polarity assignment was close to complete, with up to 94% of all filaments being assigned (Figure 22A). As can be seen in the examples of Figure 22C-D and C'-D', only those filaments marked in purple were unassigned, corresponding to mostly very short filaments and potential false-positive picks. For instance, filaments found at the corners of the tomogram do not represent any actual density but harbor artifacts from the reconstruction. Consequently, these filaments are false-positives and were discarded by the polarity assignment algorithm accordingly.

Importantly, the success rate was lower for the initial 5 tomograms. The remaining tomograms were analyzed using a high-resolution subtomogram average that was obtained from the first subset and with improved alignment parameters. Most of these tomograms then scored well above 80 %, corroborating the reliability of this approach but underlining the importance of a reference that fits the data best.

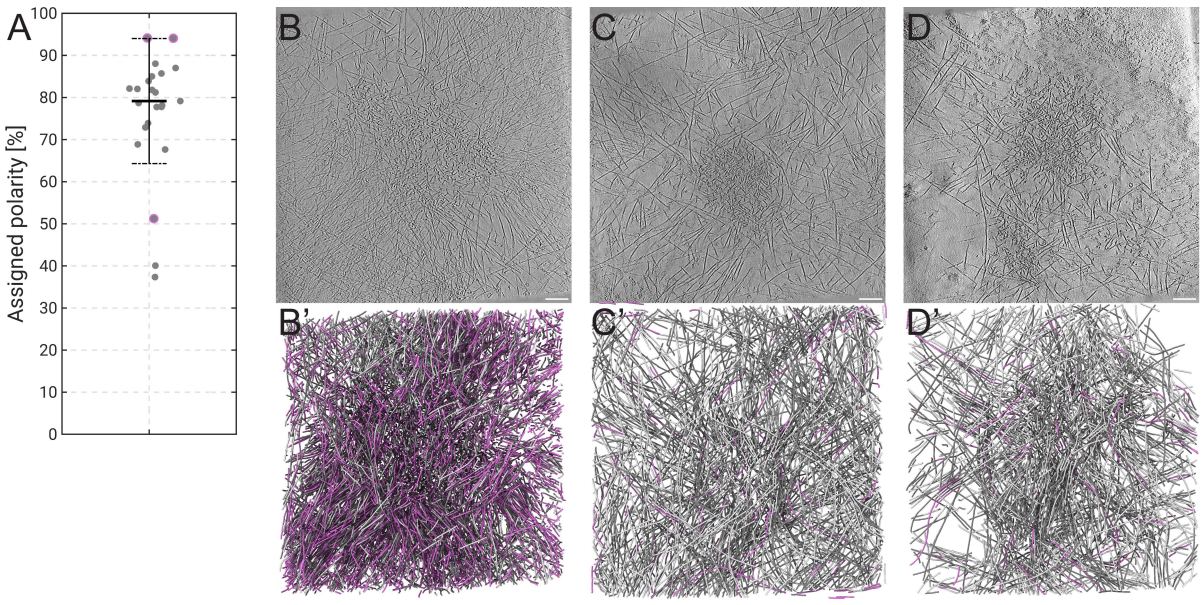

Figure 22: Success rate of polarity identification. A: Scatter plot of all investigated podosomes showing the success rate in confidently assigned polarities of all filaments within a tomogram. The examples presented in B-D are highlighted in purple. Bars show median value and standard deviation, respectively. B-D: Tomographic slice of an unroofed podosome. Scale bars 100 nm. B'-D': Outcome of the polarity assignment of the respective tomogram. Gray filaments were confidently assigned, purple filaments were discarded.

There are several possibilities to confirm the result of the polarity detection workflow. Those are conformity with existing knowledge of the polarity derived from other methods, emergence of patterns with uniform orientation, i.e., bundles with the same polarity, and significant improvement of the resolution of the resulting average. All three criteria were used to evaluate and to confirm the polarity results for the podosome. The workflow was initially applied on thin filament data derived from neonatal rat cardiomyocytes. In the sarcomere, the polarity of the thin filament has been extensively studied in the past decades. Accordingly, this provided an ideal test case to cross check the polarity determination results. Satisfyingly, the determined polarities were in accordance with previous knowledge, corroborating the general polarity determination workflow. The outcome and biological implications of this study are extensively discussed in a following chapter.

However, the sarcomere is an ideal case with parallel filaments that each share the same repeating polarity pattern. In contrast, the podosome is a complex 3D meshwork of filaments and there is no confident knowledge of the filament orientation. In a previous work, the filament polarity in actin networks from osteoclasts, including podosomes, was studied using rotary shadowing electron microscopy, but the results were not uniform [233]. Therefore, there is no confident prior knowledge that the outcome of the polarity analysis can be compared to. Instead, to confirm the results of the polarity determination in the podosome, both the emergence of repeating patterns with uniform polarity were tested, as well as improvement of the actin filament structure. Across all evaluated podosomes, the same filament pattern emerged, indicating that the result is reproducible, and affirming the robustness of the polarity analysis workflow (see also Figure 31). However, in theory, these patterns could also be derived from an unknown bias introduced during the sampling. Therefore, an additional significant improvement of the resolution has to be detected to corroborate the correctness of the identified orientations. In particular, the resolution of the actin filament has to substantially exceed 20 Å and exhibit structural features such as individual subunits or even their subdomains.

3.3.5 Structure of the actin filament at 8.8 Å resolution

For a subset of 5 tomograms, filaments with confidently identified polarity were aligned and averaged by subtomogram averaging. The obtained subtomogram average structure was refined to 8.8 Å resolution (Figure 23). The map significantly exceeds the resolution threshold of 25 Å and, given a pixel size of 3.42 Å, approaches the theoretical Nyquist limit of the data (Figure 23F). The helical twist and rise, as calculated from the refined positions and orientations, is 2.765 nm and -167.9°, which is in accordance with the literature [106]. The refined average contains 15 subunits which are clearly separated from each other, including a full 13 subunit repeat spanning a total distance of 35.9 nm (Figure 23A). Moreover, each subunit also displays secondary structure elements of its four subdomains in form of α-helices, in particular subdomains 1 and 4 (Figure 23B-C). The map agrees with pre-existing atomic models of an actin filament composed of five actin subunits docked into the central region of the average using rigid body fitting (Figure 23B). There is no strong density for the D-loop region, underlining the flexibility of this region which is also present across the different filaments within the podosome (Figure 23C).

Of note, the secondary structural densities are also directly visible in the xz slice of the structure with no apparent noise features, eliminating the possibility of introducing bias towards artifacts from over-sharpening the structure (Figure 23D). Furthermore, the radially averaged power spectrum did not show any signs of over-sharpening either (Figure 23E). The FSC drops below 0 and continues to oscillate randomly, indicating no duplicate particles (Figure 23F). However, in the second to last Fourier shell, there is a sharp spike at 0.5 before returning back to 0, which is likely a reconstruction artifact. It could result from the continuous filament touching the box edge, introducing a sharp feature. However, as this is only visible at a resolution below the FSC cutoff, it does not influence the interpretability of the map.

Importantly, there was no classification or curation step involved, and all filaments were considered until the final averaging step. As filaments were sampled from a wide range of origins, i.e., ranging from the dense core to peripheral filaments, it is most likely that these filaments display a large degree of structural variability. This potentially limits the obtainable resolution but underlines the applicability of the approach to assess the orientation of all filaments. Of note, the resolution might have been improved further by employing classification and multi-particle refinement, but was not conducted as the resolution was already sufficient to confirm the polarity results. The final average significantly went below a resolution of 20 Å, corroborating the correctness and the reliability of the described polarity determination approach. This serves as basis for subsequent quantitative analysis of the resulting filament patterns.

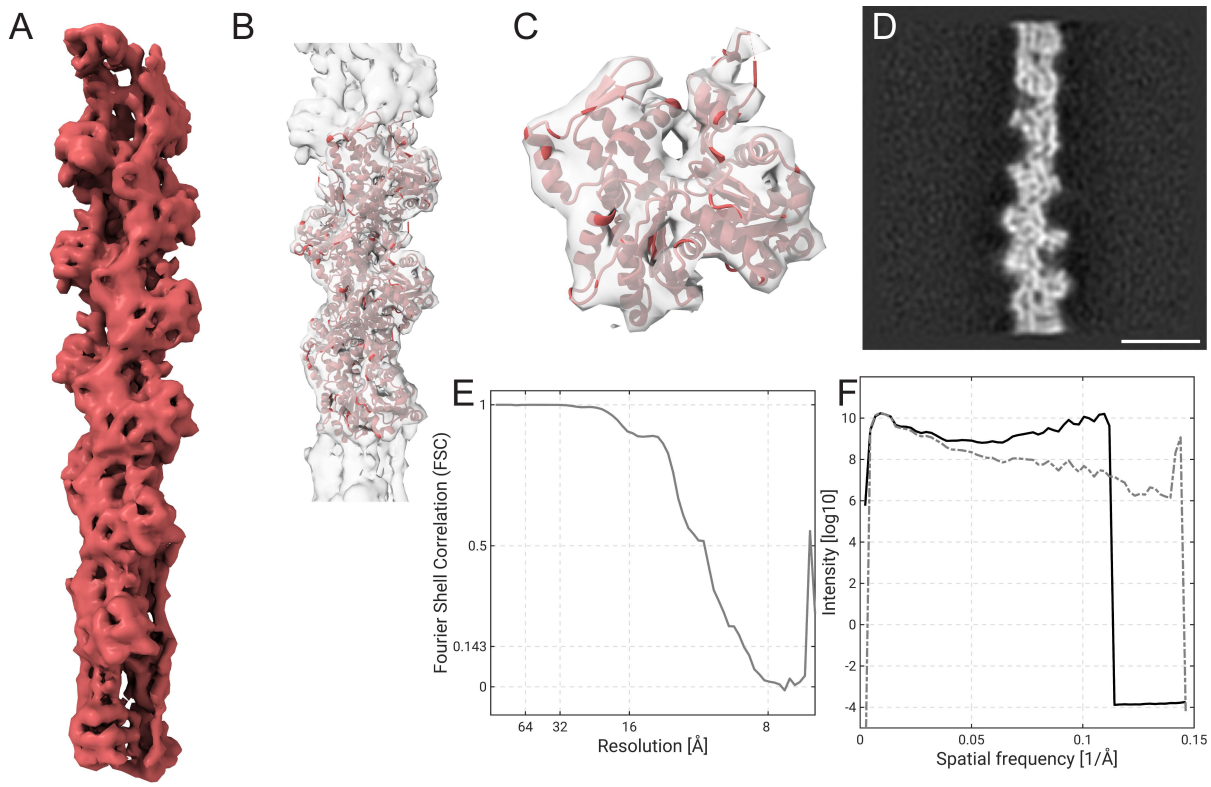

Figure 23: Subtomogram average of the actin filament at 8.8 Å resolution. A: Coulomb potential map of the refined average. The final map was figure-of-merit-weighted and sharpened with a B-factor of -1000 Å^2. B-C: Atomic model (pdb: 8a2t) docked into the central region of the average using rigid body fitting. D: Central xz slice through the map. Scale bar 10 nm. E: Fourier Shell Correlation of the average indicating a resolution of 8.8 Å at the FSC=0.143 resolution cutoff. F: Radially averaged power spectrum of the unfiltered map (gray) and post-processed and sharpened map (black).

3.4 Analysis of core filaments

3.4.1 Definition of core filaments and membrane orientation

The podosome is a complex meshwork of actin filaments. It consists of several sets of filaments, also referred to as modules, that each comprise distinct characteristics and functions [176,177]. Those include core filaments, cap filaments and lateral filaments. To understand the biophysical properties and elucidate their respective context, each module was first analyzed separately and their filament patterns were quantified. The podosome core is the primary module. It is the location where protrusive force is generated and applied to the ventral membrane. In addition, it is the densest region of the podosome, containing most filaments and expressing high interconnectivity. Moreover, it was shown that core filaments are predominantly positioned in an upright orientation [159].

A major difficulty is to introduce an exact definition of which filaments are considered core filaments, as there is no clear boundary and the transitions are seamless. For this work, core filaments were assigned based on proximity to the podosome center. The area enclosing the core was estimated from central tomogram slices, forming a polygon (Figure 24A-C). Properties that were considered were filament density and presence of upright filaments. The latter serves as good parameter, as upright filaments can be detected within all xy slices and form a visible boundary that was used to guide the polygon definition. A few examples are visualized in Figure 24A-C. Filaments whose arithmetic mean fell within the boundaries enclosed by the polygon were considered as core filaments. The respective filaments are highlighted in red below (Figure 24A'-C').

As can be seen from these examples, there are some limitations to this simplified approach. The assignment imposes a clear boundary between core and surrounding lateral filaments. In reality, this transition is smooth and there is no clear boundary between the different podosome modules. It may not be clear for some filaments whether they should be considered core or lateral filaments as, in fact, they could be labeled as both. The proposed classification of core filaments is a simplification that allows for quantification of the filament patterns.

Another parameter that needs to be defined is the position and orientation of the ventral plasma membrane underneath the podosome. This is necessary for a precise quantification of the filament orientation with respect to the ventral membrane. As the membrane lays relatively flat within the xy plane, it is partially obscured by the missing wedge. In addition, the PFA treatment of the cells prior to plunge freezing partially impaired membrane integrity. Thus, the definition of the membrane location was incomplete. Accordingly, the ventral membrane was approximated by fitting splines to regions where the membrane was intact and interpolating between these lines to generate a continuous and smooth surface. This preserved the minor undulations of the membrane on the otherwise flat carbon grid surface and serves as approximation of the cell membrane (Figure 24D). The points defining the core polygon were placed on this surface and a flat plane was fitted (Figure 24D-E). The corresponding normal vector was calculated and served as the average orientation of the membrane underneath the core (Figure 24E). These parameters are sufficient to perform quantitative analysis of filament patterns in the podosome core.

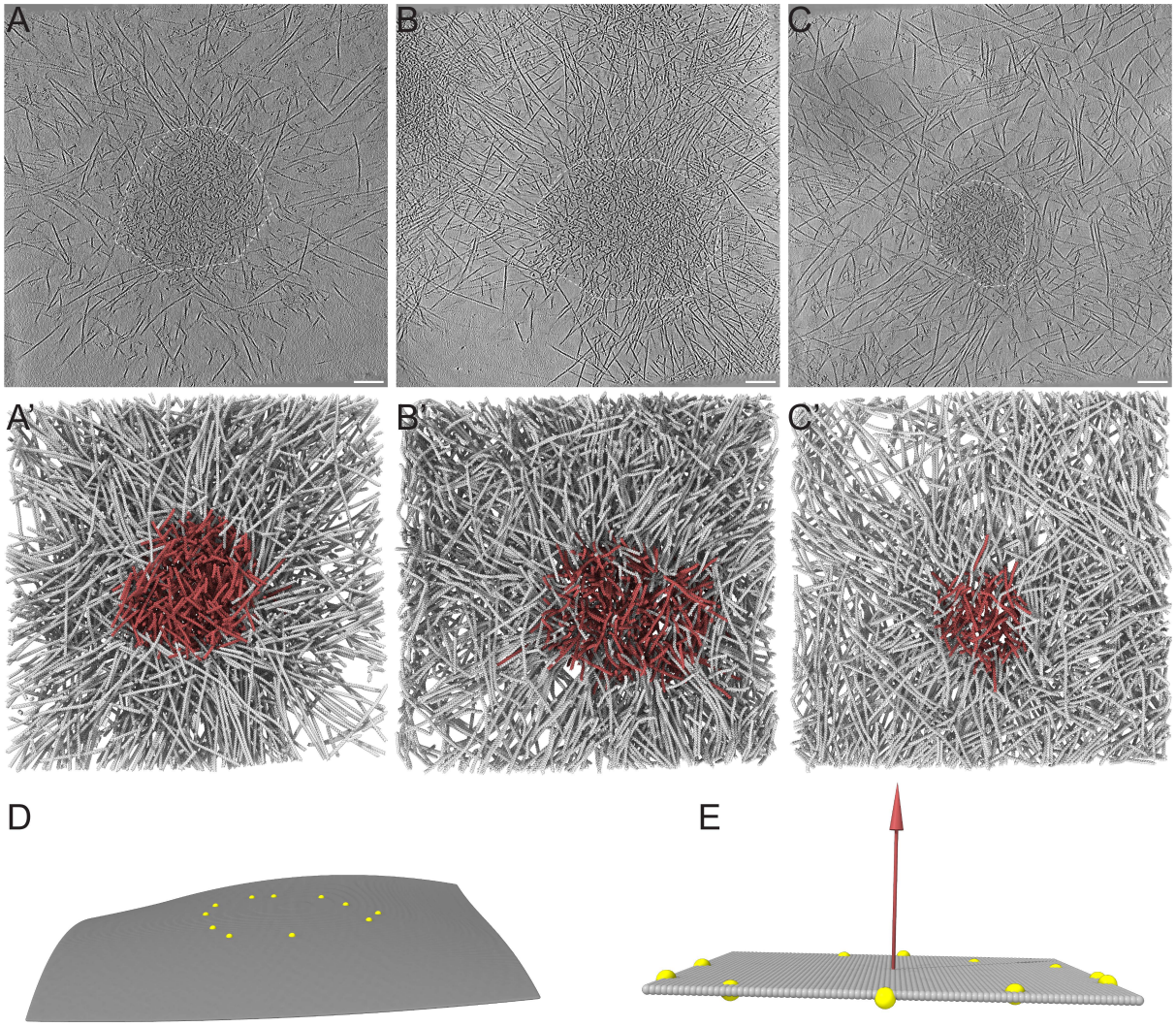

Figure 24: Assignment of core filaments. A-C: Central tomographic slices of different podosomes. The polygons used to determine core filaments are indicated. Scale bars 100 nm. A'-C': Corresponding segmentation of actin filaments with assigned core filaments highlighted in red. D: Example of a ventral membrane surface fit below a podosome including some undulations. The core is marked by yellow spheres sitting on top of the membrane fit. E: Fitting of a flat plane (gray) through the spheres marking the core (yellow) and corresponding normal vector (red) describing the average orientation of the ventral membrane underneath the core.

3.4.2 Quantitative analysis of core filaments

The mean core diameter was 366 ± 58 nm, calculated from fitting an ellipse to the polygon defining the core boundary (see also Figure 37). This is in line with published cryo-ET characterizations of *in situ* podosomes, where the core diameter was estimated around 400 nm [159]. The cores were very round, with a sphericity value of 0.81, calculated as the ratio of the short and long axes of the ellipse, respectively. The median number of core filaments was 369 but varied substantially between examples, ranging from 80 to 983 core filaments. This indicates a variety of podosome sizes in the data and necessitates a subsequent comparison that considers the podosome size. In addition, these differences could have also been enhanced in part by the tracing and polarity identification success rates within the core, as only those filaments are considered for averaging.

Core filaments presumably do not share all the same properties, as they vary in length, orientation, and height. Therefore, a differentiated analysis is necessary to dissect their properties. In a first step, for each core filament, its proximity to the membrane and its relative orientation to the normal vector of the ventral membrane, defined by a flat plane fitted underneath the core, was calculated (Figure 24E and Figure 25A). Plotting filament orientation with respect to the membrane normal vector against its closest proximity against the membrane plane revealed an interesting pattern (Figure 25A). Filaments whose closest distance toward the membrane is less than 60 nm are oriented in a wide range of angles with respect to the normal vector, with clusters at orientations below 30° and above 60°. Until this distance, filaments can be considered to still have interactions with the membrane, either through direct contact or through tethering with actin-related proteins. Moreover, owed to the inherent difficulty of the filament tracing algorithm to properly trace filament ends, some filaments may be terminated too early. By employing a larger distance threshold of 60 nm, those filaments are still considered to contribute to membrane interaction.

Angles of less than 30° to the normal plane are considered as upright filaments, approaching the membrane with steep orientation, while filaments with orientations upward of 60° are considered shallow filaments. Importantly, steep filaments are only found at distances of less than 60 nm and are completely absent in filaments further away from the membrane. This suggests that these upright filaments are indeed true core filaments (Figure 25A). These filaments could correspond to nascent core filaments that have not yet been remodeled through force generation, while the shallow core filaments might have been flattened as a result of the applied force.

The analysis suggests a third set of core filaments which is characterized by an increasing distance from the ventral membrane. Contrary to the other core filaments, this set of filaments barely contains any upright filaments. Instead, most filaments are flat with respect to the membrane and angles above 60°. This class is suggested to contain aged core filaments, which are related to the shallow core filaments, as their angular characteristics are highly similar. As more filaments are continuously generated and elongated at the membrane, pre-existing filaments could be lifted up and incorporated into the bulk of the core. Therefore, filaments within the bulk are considered older than those found directly at the membrane.

Of note, the podosome cap is located on top of the core where it connects core filaments with lateral filaments and has various important regulatory roles. As such, these filaments are included in the set of aged core filaments. However, as the main characteristics of the cap are defined by actin-associated proteins and regulatory molecules, their contribution was not further investigated.

Upright core filaments are the smallest set of core filaments and contain around 23% of all core filaments (Figure 25B). Interestingly, their contribution to the overall distribution of filaments remains relatively constant, with a standard deviation of 8.5%. This suggests a defined number of nucleation events trigger the formation of new upright filaments, that is dependent on the overall podosome dimensions. The population of shallow core filaments is larger and its size is close to that of the aged core filaments (median values of 34% and 36%). However, both exhibit larger standard variations of 19% and 16%, suggesting that filaments are transferred within both sets as the podosome changes in size (Figure 25B). As the aging of core filaments is transient, the fixed threshold that was employed to define aged core filaments may only serve as an approximation. The continuous transition of shallow core to aged filaments supports that aged core filaments directly emerged from preceding core filaments.

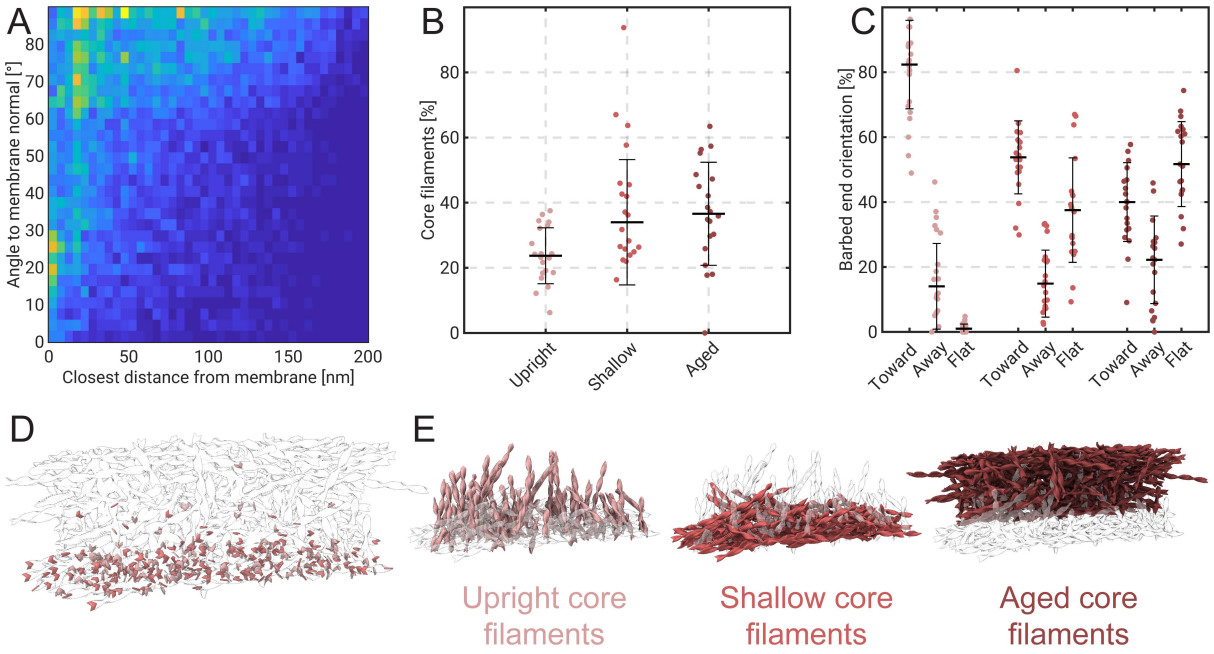

Figure 25: Quantitative analysis of core filaments. A: Heat map of all core filament angular orientation with respect to the normal vector of the membrane plane and distance from the membrane. Orange and yellow colors indicate higher abundance, green and blue colors correspond to low abundance. B: Percentage of upright core, shallow core and aged core filament numbers, respectively. C: Percentage of barbed end orientation for upright core (left), shallow core (middle) and aged core filaments (right) with respect to the membrane. Barbed end orientation was estimated for each filament individually. Filaments with non-conclusive orientations were considered flat. B-C: Bars indicate median values and standard deviations, respectively. D-E: Example of the 3D visualization of filament module distribution within a podosome core. D: Barbed ends of upright and shallow core filaments are indicated by an arrowhead; all other monomers are transparent. E: Each monomer is represented by an arrowhead. B-E: Color code: upright core filaments: light red, shallow core filaments: medium red, aged core filaments; dark red.

The polarity analysis allows for a finer dissection of the filament orientation across the different sets of core filaments (Figure 25C-D). As expected, the vast majority of upright core filaments approaches the core with their barbed ends and grows toward the membrane (Figure 25C "toward" and D). The positioning of the barbed end toward the membrane is consistent with Arp2/3-mediated nucleation which is activated at the membrane, and suggests elongation by membrane-bound elongation factors.

Upright core filaments are oblique to the membrane. Interestingly, these filaments extend beyond the layer comprising shallow core filaments (Figure 25E). In fact, almost all of these filaments extend far into the bulk of aged core filaments which is placed on top. This extension throughout the full height of the podosome core suggests that upright core filaments may provide a physical linker, that stabilizes the core. Their orientation further indicates that these filaments could emerge from branches derived from aged core filaments. In addition, this extension could also serve as sensor transmitting the current force from the membrane to the cap, where various regulatory proteins are located which in turn trigger respective signaling pathways, and regulate additional filament growth.

A similar distribution of filament orientation can be seen for shallow core filaments (Figure 25C-D), where the majority of filaments have their barbed ends closest to the membrane (Figure 25D). However, approximately half of the shallow core filaments are oriented almost parallel with respect to the membrane and can be considered as flat, as their barbed and pointed ends are too similar in terms of their distance from the membrane to

confidently draw a conclusion (Figure 25C "flat"). Nevertheless, the distribution of barbed ends for shallow and upright core filaments shows a strong enrichment in close vicinity to the plasma membrane (Figure 25D).

In contrast, aged core filaments were distributed more randomly and most filaments were considered flat (Figure 25C). Nevertheless, there are still more aged core filaments that have their barbed ends oriented toward the membrane, displaying the same pattern as in the shallow core filaments. This further suggests that these classes of filaments are correlated. Aged core filaments have been subjected to more force and thus more extensive remodeling, so they adopt a flatter distribution, concomitantly increasing the filament density in the bulk of the core.

3.5 Analysis of lateral filaments

3.5.1 Quantitative analysis of lateral filaments

Lateral filaments comprise another essential module of podosome architecture. They connect the podosome core to the surrounding adhesion ring and counterbalance the protrusive forces applied by the core. In addition, they connect neighboring podosomes and enable concerted generation of protrusive forces. However, the appearance of lateral filaments is, at first glance, as convoluted as for core filaments. Therefore, these filaments needed to be classified further in order to enable their quantitative analysis.

Lateral filaments were defined as such if one filament end was located within 1.25x the core radius. This ensures a direct interaction with the core and excludes filaments passing through. Based on this initial pre-classification, filament polarity was evaluated. Filaments that had their barbed ends away from the core (Figure 26A,F,H, blue filaments) were differentiated from filaments with their barbed ends toward the core (Figure 26A,G,I, green filaments). Side views of the respective filament sets reveal that filaments growing away from the core contribute significantly to the typical dome shape of the podosome (Figure 26F and H), where filaments close to the core are found across various Z-heights in correspondence with the core filaments, and filaments emerging further from the core move closer to the membrane. In contrast, this pattern was absent from filaments with opposite polarity which had a more random distribution across the z dimension (Figure 26G and I).

To compare the orientations of both polarities, a radial vector from the podosome center to the arithmetic mean of the respective filament was calculated and the difference to the actual orientation of the filament was determined (Figure 26A). A smaller deviation indicates a radial orientation, while a deviation of up to 90° indicates tangentiality where the filament neither emerges from nor elongates toward the core. Strikingly, these radial deviation patterns of both polarities reveal a significant difference (Figure 26B). For filaments with their barbed ends away from the core, the probability of a radial orientation with deviations of less than 20° is significantly increased (Figure 26B). Accordingly, this set of filaments is defined as radial filaments. The radial deviation for filaments with opposite polarity shows a flat distribution with tangentiality almost as likely as radiality. This indicates a certain degree of randomness for these filaments, and suggests they may be derived from remains of preceding cortex filaments, but they could also originate from neighboring podosomes and therefore contribute to the concerted interaction between podosomes. These filaments were classified as non-radial.

Probability analysis of barbed and pointed end distances with respect to the podosome center reveals a similar pattern for both radial and non-radial filaments (Figure 26C). As expected, the barbed ends of radial filaments are found to extend further than their non-radial counterparts, as the additional peak at around 600 nm suggests. Surprisingly, both sets contain many short filaments where both barbed and pointed ends are close to the center, i.e., less than 400 nm. These filaments are in direct contact with the core and might be functionally distinct from the longer filaments extending into the periphery. Alternatively, they could correspond to freshly nucleated filaments that have not yet been elongated towards the periphery. Filaments whose barbed and pointed ends were found within two times the core radius were considered as short, core-associated lateral filaments. These filaments form the outer rim of the podosome core and may stabilize the inner core or provide a boundary to confine the protrusive forces. While these filaments may be also considered as core filaments,

they are defined as a separate set of transient filaments, as they are not directly associated to upright filaments found in the core.

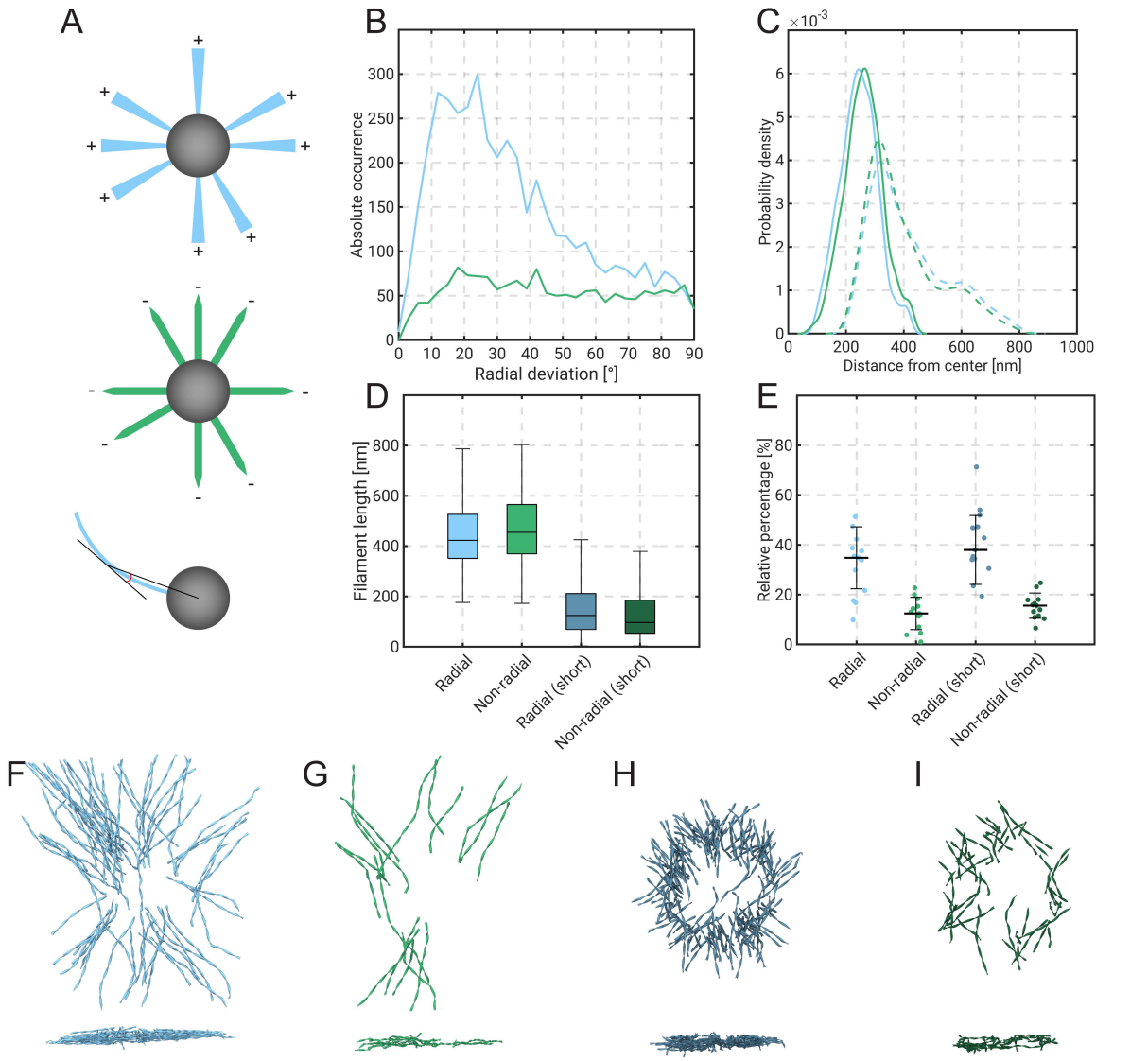

Figure 26: Quantitative analysis of lateral filaments. A: Filaments are classified based on their orientation with respect to the core (gray): filaments with their barbed ends away from the core ("+", blue, top), and filaments with their pointed ends away from the core ("-", green, middle). Bottom: The radial deviation is calculated as the angle between the vector from the core center and the arithmetic mean of the filament, and the average filament orientation. B: Distribution plot showing the radial deviation for filaments with their barbed ends away from the core (blue), and toward the core (green). Smaller angles indicate radial orientation. C: Probability distribution plot using a kernel smoothing function showing the location of barbed and pointed ends for both radial and non-radial filaments as function of the distance from the center. Closest filament ends (pointed: blue and barbed: green) are indicated as continuous lines, distal filament ends (barbed: blue and pointed: green) are shown as discontinuous lines. D: Box chart showing the relative contribution of long, radial filaments (light blue), long, non-radial filaments (light green), short, core-associated radial filaments (dark blue), and short, core-associated non-radial filaments (dark green). E: Box chart showing the length distribution of radial filaments (light blue), non-radial filaments (light green), short core-associated radial filaments (dark blue) and short core-associated non-radial filaments (dark green). F-I: 3D visualization of filament distribution across different sets. Top: top view, bottom: side view. Color code is the same as in D-E.

Lateral filaments extend further into the periphery and in consequence are significantly longer than the short lateral filaments in vicinity to the core (Figure 26D). This highlights these as true lateral filaments connecting the core components with the adhesion machinery and provide counterbalance to the protrusive force in the core. However, the short filaments in vicinity of the core could develop into true lateral filaments as they continue elongating with concomitant growth of the podosome core. Interestingly, the median length of both radial and non-radial filaments is comparable with approximately 400 nm. This is in the same range as the core diameter, suggesting a functional relationship between the length of lateral filaments acting as stabilizers, and the size of the core, akin to tree height versus root depth.

Notably, radial filaments make up the majority of lateral filaments, both for those extending from the core, as well as those in close vicinity (Figure 26E). The filament orientation is reminiscent to those observed in the podosome core, suggesting a common source in their assembly. Radial filaments might have been polymerized together with core filaments, and subsequently extended into the core periphery where they are eventually anchored to the ventral membrane.

The 3D visualization of these sets of filaments corroborates the analysis (Figure 26F-I). Specifically, both sets of filaments comprise long filaments that extend well into the periphery, with filaments growing away from the core (light blue filaments) dominating (Figure 26F-G). In addition, both sets harbor an additional set of short filaments in close vicinity to the podosome core (Figure 26H-I). Importantly, the shorter filaments are highly radial as well, as observed for those extending into the periphery (Figure 26H). In contrast, short non-radial filaments do not exhibit a clear orientational preference and adopt a more random distribution (Figure 26I).

3.5.2 Quantitative analysis of parallel filament sections

The direct identification of actin crosslinkers and bundlers proved to be highly challenging and might not be feasible for the data analyzed within this work. Despite significant efforts, no confident structural assignment was achieved. Instead, an indirect approach emanating from actin filaments appears more feasible. Specifically, parallel filaments indicate some form of crosslinking and/or bundling. A deviation of 10° or less between adjacent filaments was considered as parallel. Moreover, for core filaments a maximum distance of 15 nm was chosen, while for lateral filaments this distance was increased to 20 nm, to accommodate slightly larger distances.

Accordingly, parallel filament sections were identified and quantitatively analyzed across the different podosome modules (Figure 27). The relative amount was calculated by comparing the length of parallel sections to the total length within a given module. Surprisingly, only a small fraction of core filaments contained parallel sections (Figure 27A). The median value was below 5%, with upright core filaments being the lowest. The largest relative amount of parallel sections were found among radial filaments with a median value of around 20%. On the other hand, non-radial filaments contain parallel sections to a level comparable to other podosome modules. For all core filaments combined, the amount of parallel sections across different modules was insignificant and therefore excluded from the analysis. In contrast, parallel sections between radial and non-radial sections were found with a fraction of around 7%

Comparing the lengths of these parallel sections across the different modules shows a similar pattern (Figure 27B). Core filaments, as well as most non-radial filaments, have shorter parallel sections of less than 50 nm. In contrast, parallel sections in radial filaments and in radial/non-radial populations tend to be longer, extending up to more than 100 nm.

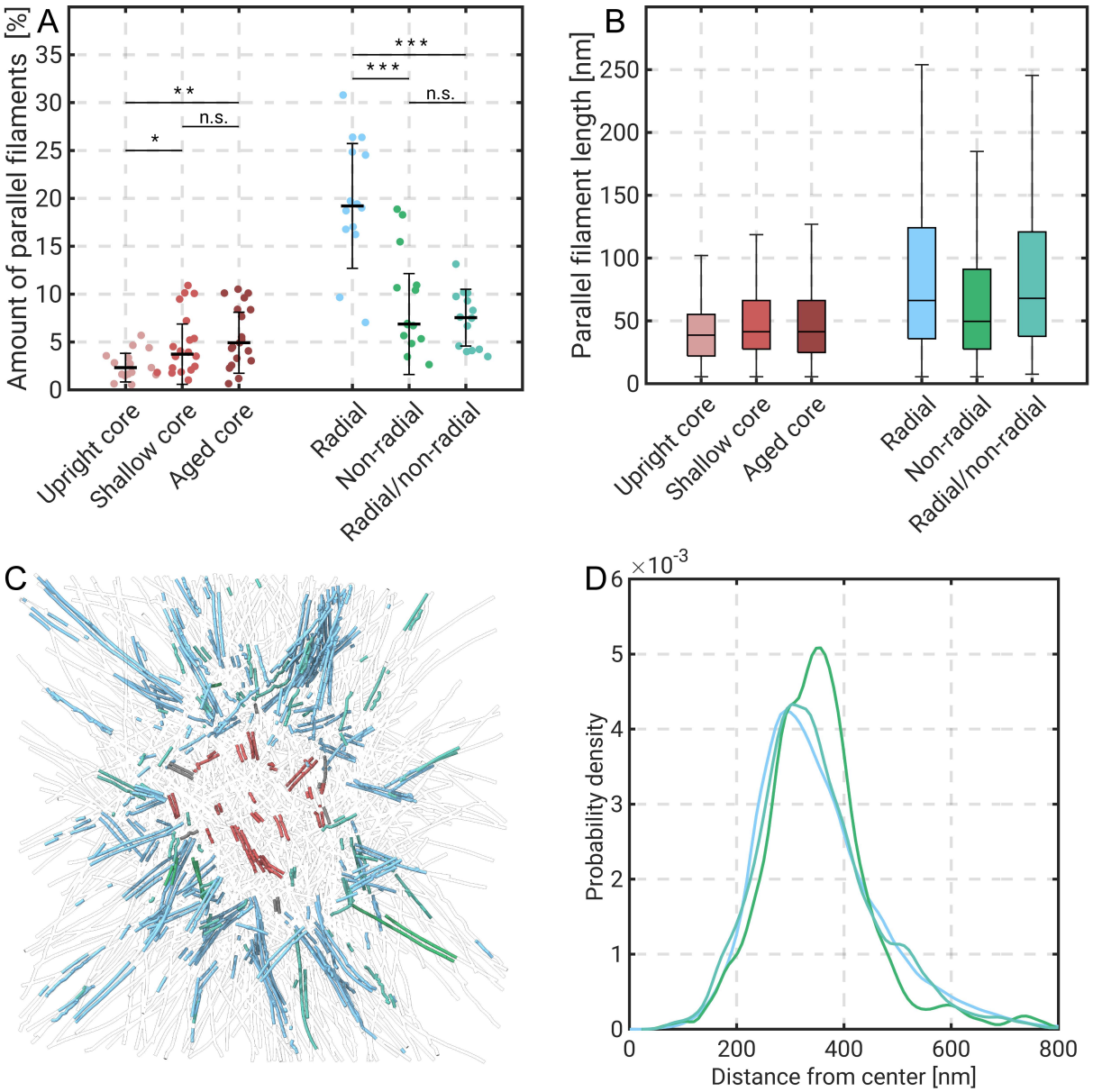

Figure 27: Quantification of parallel filament sections. A: Relative amount of parallel sections within the respective podosome modules. Angular deviation of <= 10° is considered parallel, for core filaments a parallel filament distance of <15 nm and for lateral filaments <20 nm was included. Bars indicate median and standard deviation, respectively. Significance was tested using two-sided Wilcoxon rank sum test. *: p<0.05, **: p<0.01, ***: p<0.001, n.s.: not significant. B: Box plot visualizing the length of parallel sections across the respective podosome modules. C: Example of the 3D distribution of parallel sections within a podosome. D: Probability distribution plot using a kernel smoothing function showing the distance of parallel and antiparallel section from the podosome center. Color code for the entire figure: light red: upright core filaments, medium red: shallow core filaments, dark red: aged core filaments, blue: lateral filaments, green: non-radial filaments, cyan: radial/non-radial filaments, gray: parallel sections between other filament modules.

An interesting pattern emerges when these parallel sections are placed into the tomographic volume (Figure 27C). While the parallel sections within the core are sparsely located, most of the lateral parallel sections, as well as antiparallel sections, cluster in direct periphery to the core. This is confirmed by calculating their distance from the podosome center (Figure 27D). The average distance clusters around 350 nm from the core, both for radial parallel sections and interactions between radial and non-radial filaments, while non-radial parallel sections appear to extend slightly further from the core. This distribution pattern is reminiscent to that described in Figure 26, revealing the short, core-associated radial filaments to be substantially parallel. The clustering of parallel sections of these radial filaments in close vicinity to the core suggest high crosslinking in this area, which in turn could be necessary to provide a stable confinement for the core filaments, locally restricting their growth and preventing them from diluting into the periphery. On the other hand, crosslinking of parallel sections in the core seems to be less critical, confirming the importance of branching in the core for both filament nucleation and crosslinking.

Of note, some parallel sections might have been missed due to the incomplete tracing within the core. Nevertheless, crosslinking within the core likely contains non-parallel and mixed orientations of filaments that accommodate different orientations.

3.6 The molecular sociology of actin filaments in macrophage podosomes

Combining the structural and quantitative data across all podosome modules enables to draw a complete picture of the modular architecture of actin filaments in the podosome at the molecular level. The advantage of the subtomogram averaging approach employed in this work is its capability to retrieve the position and orientation of all actin monomers within the network. These poses can be used to place the respective actin structure into the volume and generate a complete representation of the network, spanning the scale from sub-nanometer resolution of the actin filament structure to the micrometer sized architecture of the podosome (Figure 28). The individual monomers are placed in the volume based on their respective pose and filaments are colored based on their respective module, as analyzed in the previous chapters. Various close ups highlight the relative positions of monomers in different parts of the podosome network that exhibit the typical helical twist of the filament, underlining the successful averaging workflow (Figure 28, bottom).

Of note, the volume representation in Figure 28 is incomplete, as it is based on the filament tracing and subsequent polarity determination. Therefore, only filaments that were identified properly and whose polarity could be determined, are considered and displayed below. Furthermore, the volume does not include any crosslinkers which significantly contribute to the podosome architecture. Nevertheless, the image below contains a near-complete visual representation of the podosome architecture and the molecular sociology of actin filaments.

Upright core filaments are under severe tension in the podosome, causing them to bend. Likewise, radial filaments might be pulled which likely also causes some structural rearrangement. This presumably reflects in structural changes of the filament and within the monomers. Despite significant effort invested in this direction, classification and advanced image analysis of the actin filament revealed no obvious structural differences between the different modules. Likewise, calculating the helical parameters from the refined poses per podosome module did not reveal significant differences. This could arise due to a few reasons. First, the nominal magnification of 42,000x represents a compromise between high-resolution imaging and retaining an entire podosome in the field of view which corresponds to 1.3x1.3 µm. This magnification could have been too low to accurately resolve the small structural variations. Second, the obtained subtomogram average of the actin filament is a mixture in which the flexibility of the filament is, as the name implies, averaged out. Therefore, also the refined poses obtained from subtomogram averaging might not accurately enough reflect the true pose of the monomer and tiny fluctuations of the structure might be unnoticed. Third, structural deviations could be limited locally and might be too small to be detected on a modular basis. Finally, the analyzed podosomes are unroofed which were shown to contain filaments in the podosome core that are less compressed, presumably due to the loss of connections between lateral filaments and the plasma membrane. This reduces the opposing traction forces and consequently the protrusive force in the core. As such, it is likely this also affects the structure of the filaments and cancels any force-induced structural changes. For these reasons, the investigations of structural flexibility across actin filaments *in situ* will be the focus of a future project.

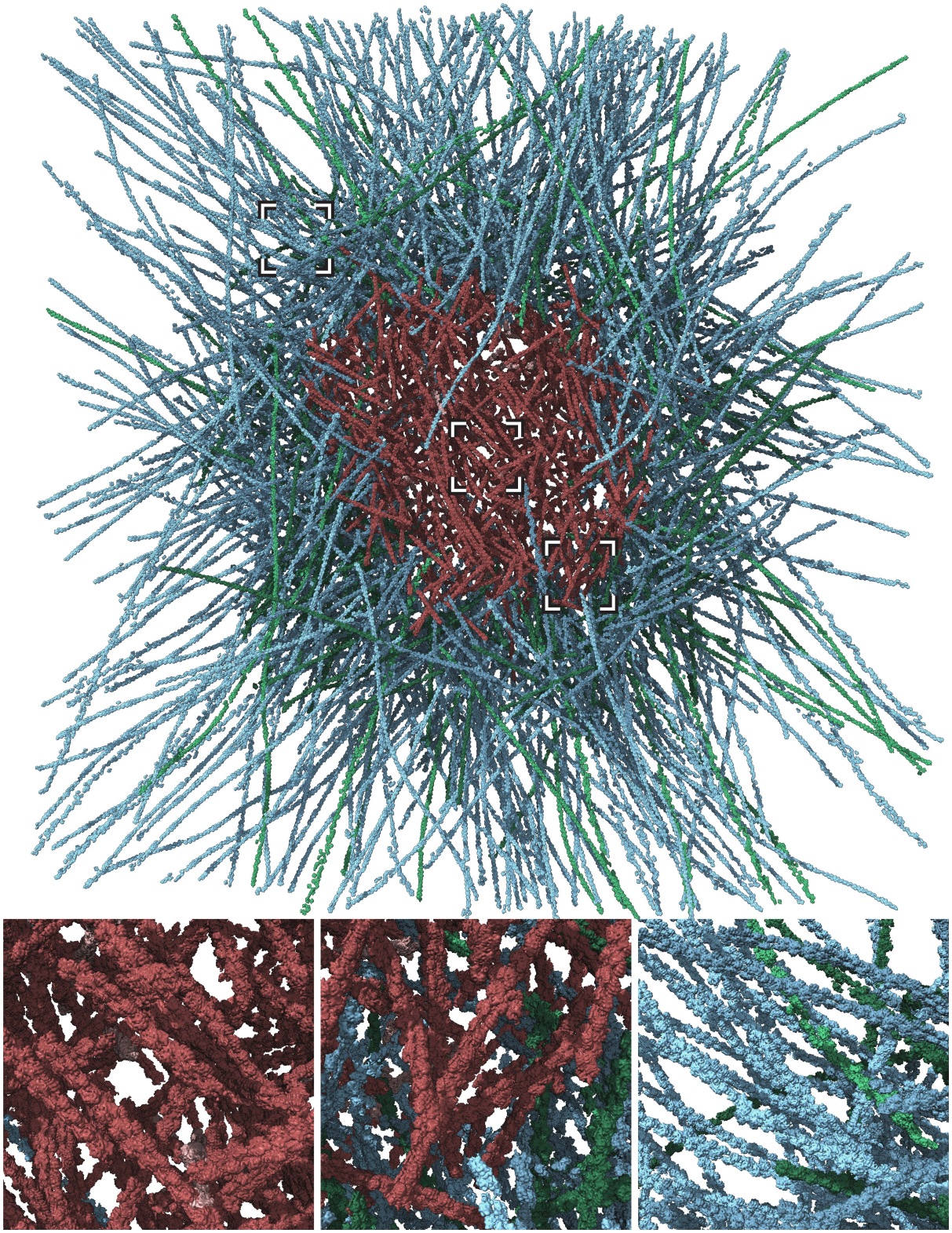

Figure 28: Molecular architecture of human macrophage podosomes. Top: Complete visualization of actin filaments in the podosome derived from refined poses after subtomogram averaging for each actin monomer that is pasted into the volume. Bottom: Close-up of different regions indicated above by squares, highlighting core and lateral filaments, respectively. Color code: light red: upright core filaments, medium red: shallow core filaments, dark red: aged core filaments, light blue: radial filaments, light green: non-radial filaments, dark blue: short, core-associated radial filaments, dark green: short, core-associated non-radial filaments,

3.6.1 Visualization of podosome super-structures

Podosomes can cluster and form super-structures, depending on the cell type and substrate. Moreover, podosomes from these super-structures can oscillate in concert, indicating their spatial connectivity and suggesting regulated interaction between neighboring podosomes. Some of the podosomes analyzed within this work originate from such super-structures. An example is given in Figure 16, showing multiple podosomes in the overview image. As mentioned above, the podosome shown in Figure 17 and Figure 18 was acquired in this area and contains a neighboring podosome in the field of view. While the core is cut off from the tomogram, the lateral filaments are retained. This enables a closer look at the overlap of filaments originating from both cores (Figure 29).

Analyzing the lateral filament distribution with respect to the second core (projected to be outside the volume), reveals the same pattern that was quantitatively discussed above (Figure 26A and Figure 29A). The majority of these filaments qualify as radial filaments, emerging radially from the core with their barbed ends facing away. In addition, filaments from the central podosome are displayed as transparent, highlighting a region in between both cores where many filaments overlap and where filaments are likely to interact with both cores. While radial filaments were shown to deviate from the central core in a very radial fashion, non-radial filaments did not follow this pattern and appear more randomly distributed. The comparison in Figure 29 B and C shows lateral filaments assigned with respect to each core, respectively. As highlighted for a few examples indicated by arrows, depending on the core they are attributed to, the orientation is flipped. For some of these examples, filaments which were not assigned as radial filaments of the first core are classified as radial filaments for the second core and vice versa. This provides an explanation for the origin of non-radial filaments and suggests that non-radial filaments likely originate from neighboring podosomes. Moreover, their interaction with radial filaments might be important to coordinate and stabilize podosome super structures.

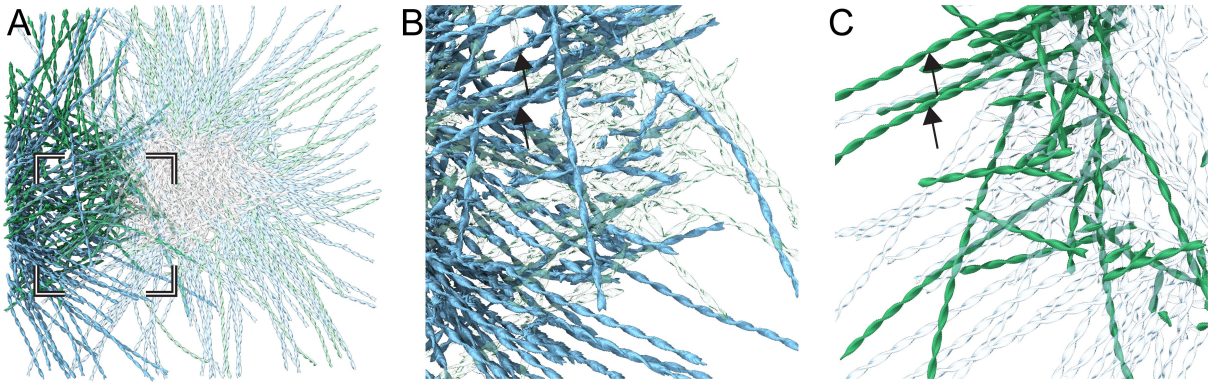

Figure 29: Visualization of podosome super-structures. A: The lateral filament pattern is shown for a neighboring podosome, whose core is placed just outside of the field of view. The color code follows Figure 26 for radial and non-radial filaments. The original assignment of lateral filaments in the central podosome is shown in transparent colors. B and C: Lateral filaments in between the two neighboring cores, classified with respect to the 2nd podosome core (B) and the central primary podosome (C). Examples of filaments which are classified as non-radial in one assignment and classified as radial in the other, or vice versa, are highlighted by arrows. The area highlighted in B-C corresponds to the indicated area in A.

3.7 Evolution of podosome architecture

The evolution of podosome architecture is of particular interest due to their dynamic assembly and disassembly. In addition, the previous analyses showed a size-dependent plasticity of the filament parameters. However, in cryo-ET it is not yet possible to directly assess the precise dynamic state of a given podosome, as they are momentary captures. Therefore, the exact state of the podosomes analyzed within this work is unknown. Instead, podosome height and cumulative filament length can serve as parameters to estimate the podosome state.

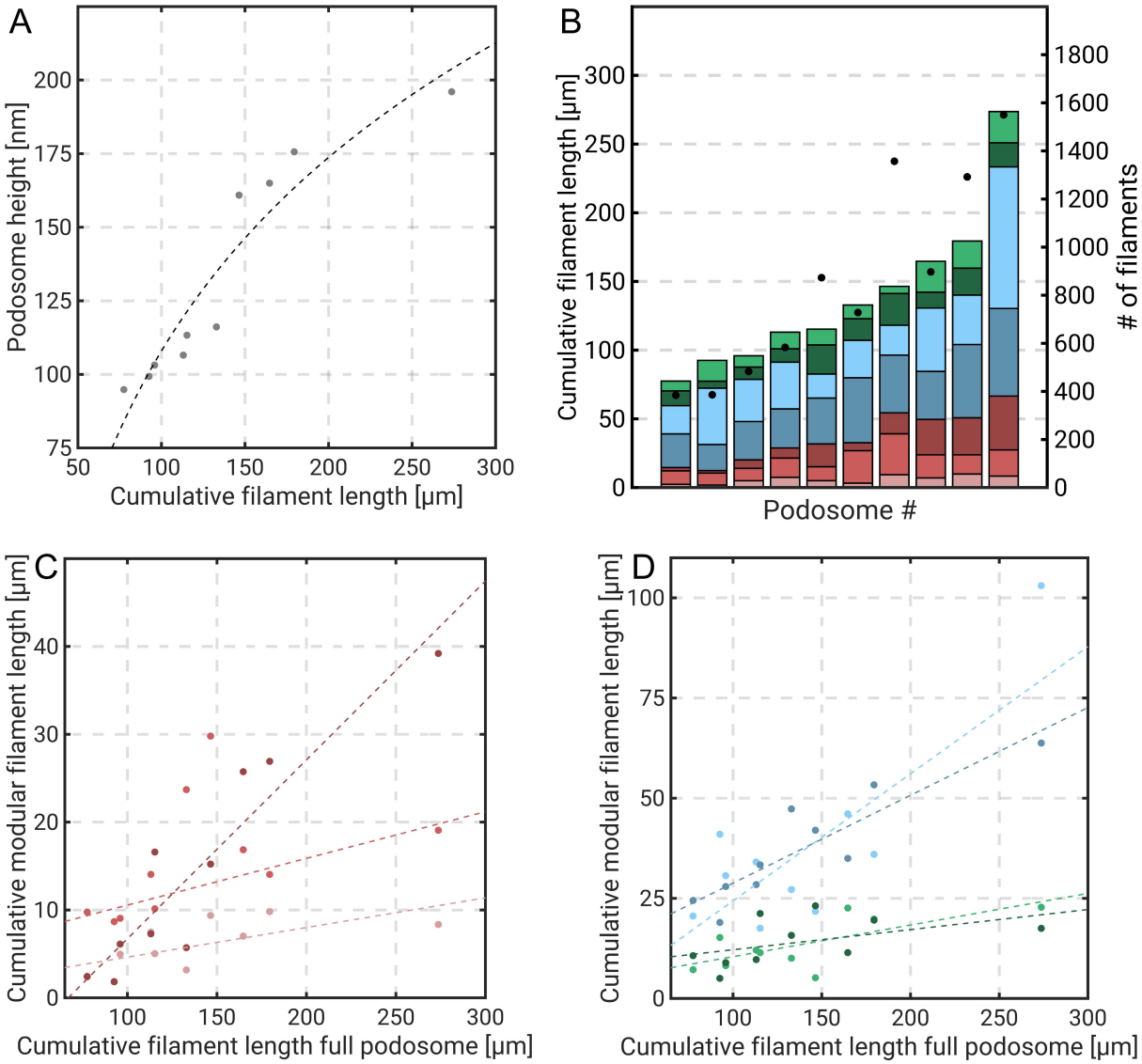

Figure 30: Evolution of podosome architecture. A: Scatter plot of podosome height plotted against cumulative filament length. Dashed line corresponds to a 2nd order polynomial fit with bisquare robust fitting. B: Bar chart showing the contribution of each filament module to the total cumulative filament length (left y-axis), sorted in ascending order (see Figure 31). In addition, the total number of filaments is shown as scatter plot (right y-axis). C-D: Cumulative filament length per podosome module plotted against the cumulative filament length of the entire podosome, separated by core filaments (C) and lateral filaments (D). Dashed lines correspond to linear fits for each module, respectively. Color code: light red: shallow core filaments, medium red: upright core filaments, dark red: aged core filaments, light blue: radial filaments, green: non-radial filaments, dark blue: short radial filaments, dark green: short non-radial filaments.

Both parameters correlate linearly with each other initially, where longer total filament length is reflected by a higher core (Figure 30A). Upon reaching a height of approximately 170 nm, this linearity is flattening, upon which additional podosome growth is directed horizontally rather than vertically. The polynomial fit reaches a height of 300 nm for podosomes twice as large as those analyzed in this work, which is smaller than what is reported in literature, where the maximum podosome height is above 600 nm [179]. This discrepancy is likely caused by differences in substrate stiffness. Carbon grids, on which the podosomes on display were acquired on, are less stiff than glass surfaces. This could explain the reduced overall height of the investigated podosomes. To provide a better visual understanding of the podosome architecture and its development during podosome growth, the respective podosomes are displayed below (Figure 31). The podosomes are sorted based on total cumulative filament length. Figure 30B shows the contribution of each filament module to the total filament length of the podosome, sorted in ascending order (same order as in Figure 31). As the podosome increases in size, each set of filaments contributes to this growth, with the exception of non-radial filaments whose contribution seems to stagnate. Concomitantly, the increase in filament length is accompanied by an increase in total filament numbers (Figure 30B, black dots and right y-axis).

The two parameters appear to follow a linear correlation, indicating that both new filaments are nucleated as well as existing filaments are elongated. To further dissect the role of each podosome module to the total filament length during podosome growth, their individual contribution in terms of cumulative filament length was plotted against the total filament length of the entire podosome, sorted again in ascending order (Figure 30C-D). The accompanied fits reveal the relative increase for each module.

Upright and shallow core filaments increase in size, more specifically length, at the same rate, as their linear fits have similar slopes (Figure 30C). Moreover, aged core filaments outgrow both modules, approximately at the same rate as both modules combined. This synchronized growth corroborates their close interconnection. Of note, the numbers for upright core filaments are highly susceptible to errors in filament tracing, as there are the fewest filaments of all modules. As such, false-negative filaments manifest in a distorted length contribution more significantly. Nevertheless, the growth rates of all modules are in accordance with each other, suggesting there is no substantial bias against tracing upright filaments.

The growth speed of radial filaments outpaces that of core filaments (Figure 30D). This shows that lateral filaments, in particular radial filaments, need to keep extending to counterbalance the forces generated by a growing core and the need for these filaments to be elongated primarily. Interestingly, both short and long radial filaments increase at comparable rates, indicating their interconnected relationship. In contrast, both short and long non-radial filaments increase slowly, as their slopes are close to 0. This suggests that these filaments are less critical for the podosome architecture and might be derived from pre-existing cortex filaments and their elongation is disfavored. As such, the orientation of lateral filaments is progressively optimized in favor of radial filaments.

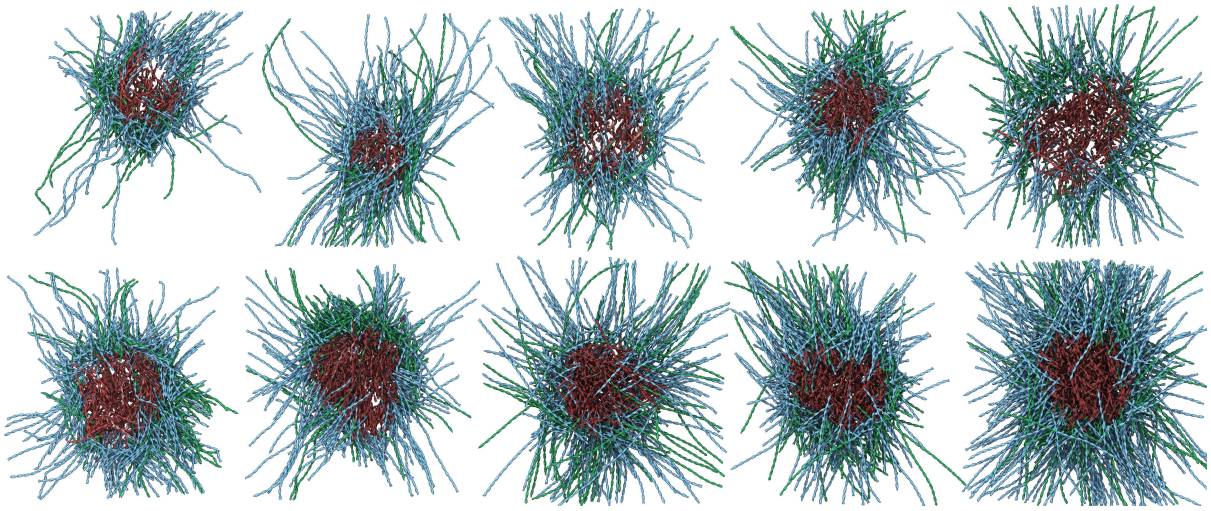

Figure 31: 3D visualization of podosome architecture evolution. Podosomes are sorted according to cumulative filament length, with the same order as in Figure 30. Filaments are colored according to their modular affiliation, light red: upright core filaments, medium red: shallow core filaments, dark red: aged core filaments, blue: radial filaments, green: non-radial filaments.

3.7.1 Modular architecture of an emerging podosome

Among the captured podosomes was one particularly interesting example. The tomogram contains a very flat cortex in which a very small podosome is centrally located (Figure 32). The podosome is composed of a few filaments only but the tomogram shows some membrane displacement (Figure 32A, z=106), indicative of protrusive force applied by the network. This membrane displacement was used to draw a polygon in order to define core filaments, as there were no upright filaments present. The assignment of core filaments revealed them as shallow core filaments only (Figure 32B). Even so, the number of shallow filaments is small, but is sufficient to trigger a membrane displacement. It is also possible that some upright filaments have accommodated this shallow orientation upon force application.

Strikingly, the polarity pattern that was identified above is also present in this example. The majority of filaments is considered radial, accompanied by a close-to-complete radial angular distribution (Figure 32B-C). Only a minority of filaments is classified as non-radial. Moreover, the lateral filaments can mostly be classified as short and core-associated filaments (Figure 32D), using the same criterion of two times the core radius as boundary. Interestingly, the short filaments are exclusively found in the center in vicinity to the core and also exhibit a strong radial pattern.

This example further demonstrates the importance of the lateral filament pattern, which radiates from a singular point in the center of the podosome. This pattern appears to be critical for force generation, as the network is already capable of pushing against the membrane. This suggests that these filaments were nucleated together with core filaments. As their outward directed growth is not limited, they can be elongated more easily. In contrast, filaments located at the center of this filament pattern are spatially confined and therefore might slowly accommodate a more upright orientation, eventually transforming into the distribution of core filament orientation found in mature podosomes. Alternatively, these filaments may have emerged as short upright filaments which subsequently adopted a shallow orientation upon force generation.

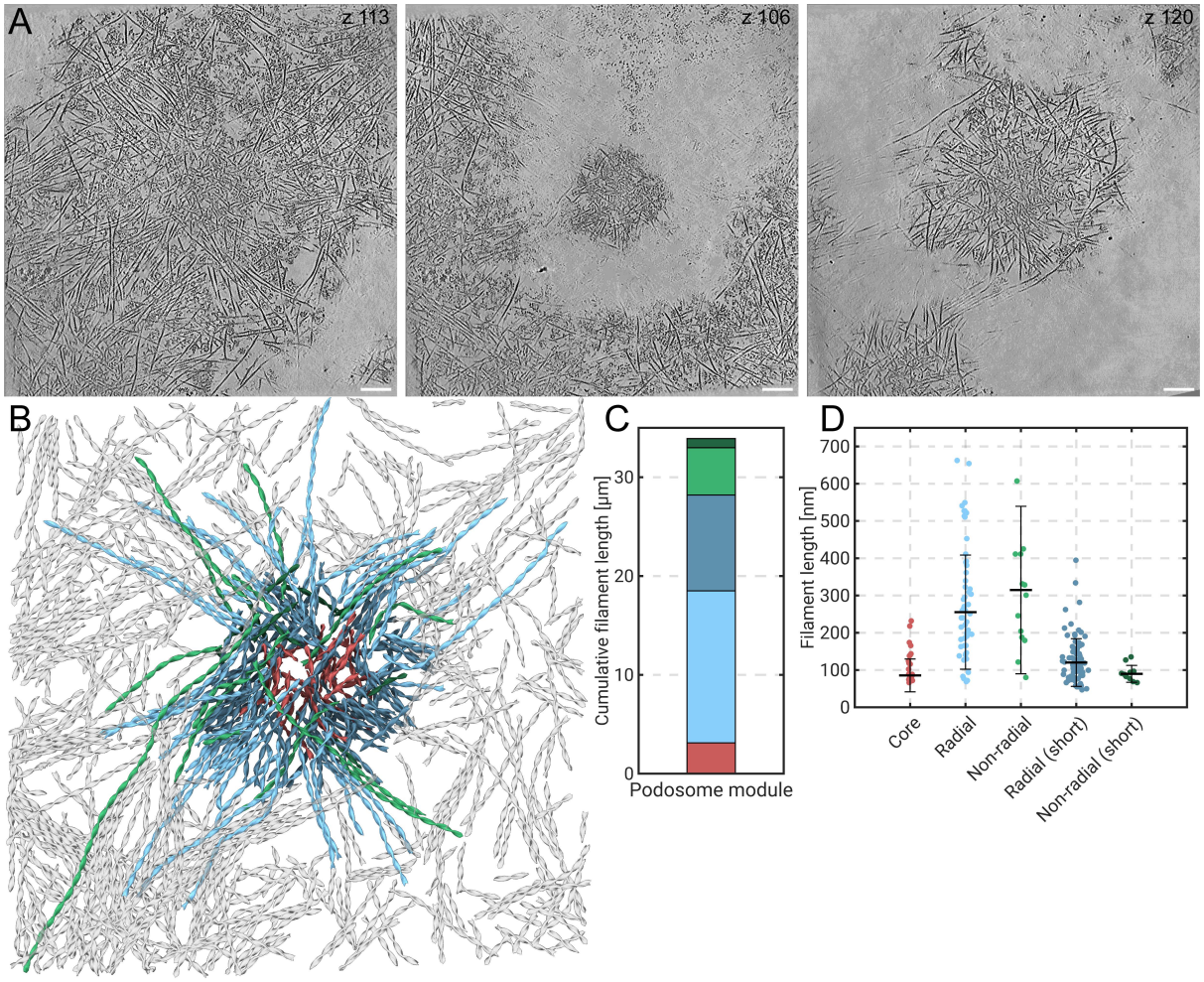

Figure 32: Modular architecture of an emerging podosome. A: Tomographic slices at different z heights of the same tomogram. Left: central slice (z=113), middle: bottom slice (z=106), right: top slice (z=120). Scale bars 100 nm. B: 3D visualization of filament module distribution within the podosome. Each monomer is represented by an arrowhead. Color code: shallow core filaments: medium red, radial filaments: light blue, non-radial filaments; light green, short radial filaments: dark blue, short non-radial filaments: dark green, filaments not associated with the core: dark gray. C: Cumulative filament length per podosome module. D: Scatter plot showing the distribution of filament length across different podosome modules. The median and standard deviations are indicated as bars.

3.8 The role of the Arp2/3 complex in podosome formation

3.8.1 Localization of Arp2/3 complex-mediated branches

The Arp2/3 complex is an essential component of podosomes [180]. It nucleates new filaments by branching off pre-existing filaments, resulting in a branch structure. Surprisingly, the mature podosomes that were characterized in the previous chapters did not contain any branches. Despite numerous efforts to identify and localize Arp2/3 complex-mediated branches, none were identified. However, Arp2/3 is required for podosome formation. This obvious contradiction could arise due to several reasons. The PFA treatment and unroofing prior to plunge-freezing could have destroyed some branches. Second, the tomogram quality might not have been sufficient. As mentioned earlier, the chosen magnification of 42,000x is a compromise between obtaining high-resolution information and retaining a complete podosome in the field of view. However, tomograms might be too thick to successfully detect branches, especially within the dense region of the core where branches could be buried within the bulk of the core. In fact, due to the many crosslinkers and overlapping filaments, many candidate points exist that, at first, appear to be Arp2/3 complex-mediated branches. However, a closer inspection identifies them as false-positives. Finally, debranching can occur, as upon successful nucleation and elongation of the new filament, the branch is processed and eventually dismantled. Another possibility could be that nucleation through Arp2/3 predominantly occurs during initial establishment of the podosome, and other nucleators, such as formins, dominate in mature networks, as was shown for invadopodia [234].

To address this potential mismatch, a new dataset was acquired at higher magnification using the latest generation of cryo-TEM microscope with improved electron source and improved detector (Methods). Specifically, a magnification of 64,000x with a pixel size of 2.06 Å was chosen, resulting in a field of view of 844x844 nm, given the slightly larger detector. In addition, fixation with PFA was avoided to retain membrane integrity. Finally, the carbon support of the grid was coated with the pro-inflammatory molecule fibrinogen to enhance podosome formation.

Upon reconstruction and subsequent denoising, the difference between datasets was remarkable. The higher magnification permitted an even higher resolution of the actin filament structure within a single tomographic slice (Figure 33). The density within the core is still significant, but it is not as crowded as for the lower magnification, allowing to identify many potential crosslinkers and additional densities. In contrast, the complete podosome does not fit within the field of view of a single tomogram anymore. Therefore, the full architecture cannot be analyzed properly, as it was conducted above. Instead, this dataset serves as basis to study actin-related proteins such as the Arp2/3 complex.

While Arp2/3-mediated branches were not found in all tomograms, the dataset contains many tomograms where Arp2/3 complex-mediated branches are readily visible by eye. The example shown in Figure 33A displays multiple branches within a single slice, and many more throughout the tomographic volume. A gallery of Arp2/3 complexes is shown below (Figure 33A, insets).

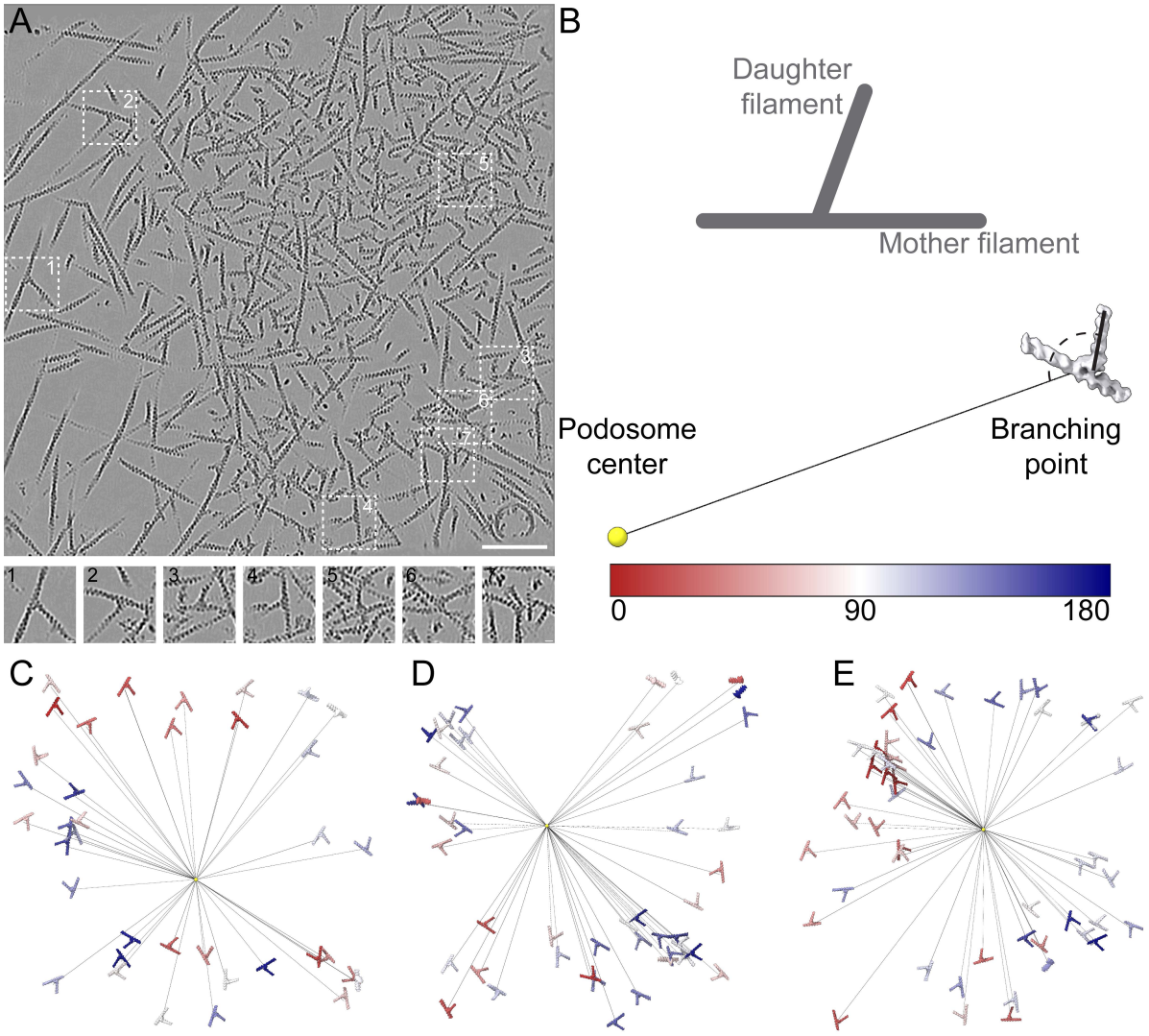

Figure 33: Localization of Arp2/3-mediated branches in podosomes. A: Tomographic slice of a denoised and missing wedge-corrected tomogram. Insets 1-7 show close ups of individual branches. B: Top: Schematic illustration of the definition of daughter filament angle to describe the geometry and orientation of the branch. Bottom: Example of the calculation of branch orientation. The angle between the vector from podosome center to branching point (black line) and daughter filament angle of the branch (black line) is calculated. The color code used for C-E ranges from 0° (red) to 180° (blue). C-E: Examples of identified branches pasted back into the tomogram. The branch structure was obtained through subtomogram averaging (Figure 35). The podosome centers are indicated by a yellow sphere, black lines describe the vectors to the respective branching points. The visualization in E corresponds to the tomogram in A.

To investigate the role of Arp2/3 within these networks, their spatial context was studied. Specifically, the orientation of the daughter filament was used to assess the branch geometry (Figure 33B). This parameter describes the branch orientation with a single value and emphasizes the orientation of newly polymerized filaments, as the origin of the pre-existing mother filament cannot be known. To study the orientation with respect to the podosome core, the arithmetic mean of the core, as defined by a polygon similar to the previous core analysis, was defined as podosome center. The vector from the center to the branching point of the respective Arp2/3 complex and the associated daughter filament angle of the branch form an angle, which was used to describe the orientation of the branch with respect to the core (Figure 33B). This angle ranges from 0°, where the daughter filament directly points toward the core, to 180°, where the filament points away. A color code from

red to blue was chosen to visualize the results. Branches were identified using template matching using a previously published cryo-ET structure of the Arp2/3 complex, followed by several rounds of classification to remove false-positives. To ensure only true-positive particles were retained, the exposed density corresponding to the ArpC1 domain was removed from the template. Accordingly, only particles where this density re-emerged were kept for further processing.

Upon classification, it became obvious that the vast majority of branches were identified outside of the core and only sporadically localized within the core. This could be caused by the still considerable filament density within the core that impairs proper localization due to the higher risk of selecting false-positives. Indeed, there were a few false-negative examples found in the core upon manual inspection. Since the number of particles within the cores is very low, quantitative analysis of their spatial context is difficult and may be non-conclusive. For these reasons, core particles were omitted from further analysis and only peripheral branches were considered for subsequent quantifications.

This can be seen in some examples presented in Figure 33C-E, where Arp2/3 complex-mediated branches cluster around the periphery. The central yellow spheres indicate the podosome centers and the black lines describe the vectors to the respective branching points. These examples show an approximately evenly distributed arrangement of Arp2/3-mediated branches, spread throughout the periphery of the core. Individual branches are colored based on their orientation with respect to the core as described in Figure 33B.

3.8.2 Quantitative analysis of Arp2/3-mediated branches

The correctly identified Arp2/3 complexes in the periphery of the podosome core and their respective branch orientation, as defined in Figure 33, are quantitatively analyzed to dissect the role of the complex in the formation and maintenance of the network.

Focusing on individual podosomes, it appears that their height and the number of identified branches are correlated (Figure 34A). The analyzed podosomes that contained branches were less than 150 nm in height. This suggests they might still be emerging podosomes. The number of branches is largest in the small examples, exceeding 80 particles for a single tomogram. As the podosome increases in height, the number of branches drops in an almost linear fashion. This suggests that Arp2/3-mediated branching and generation of new filaments predominantly occurs in smaller podosomes where a substantial number of filaments need to be nucleated, while in mature podosomes filaments are predominantly elongated. Another potential explanation for this trend is due to the increased thickness of larger podosomes, the tomogram quality is reduced while the filament density is increased simultaneously, aggravating the identification of branches. Due to these observations, the analysis was limited to lateral filaments, where the filament density is not as critical as in the core.

However, these podosomes are only partially smaller than the examples from the previous dataset, where no branches were found. As such, the larger size and increased filament density only partially explains the absence of any branches in the initial examples. The reduced magnification as well as artifacts of the PFA treatment and unroofing are likely to contribute to their absence additionally.

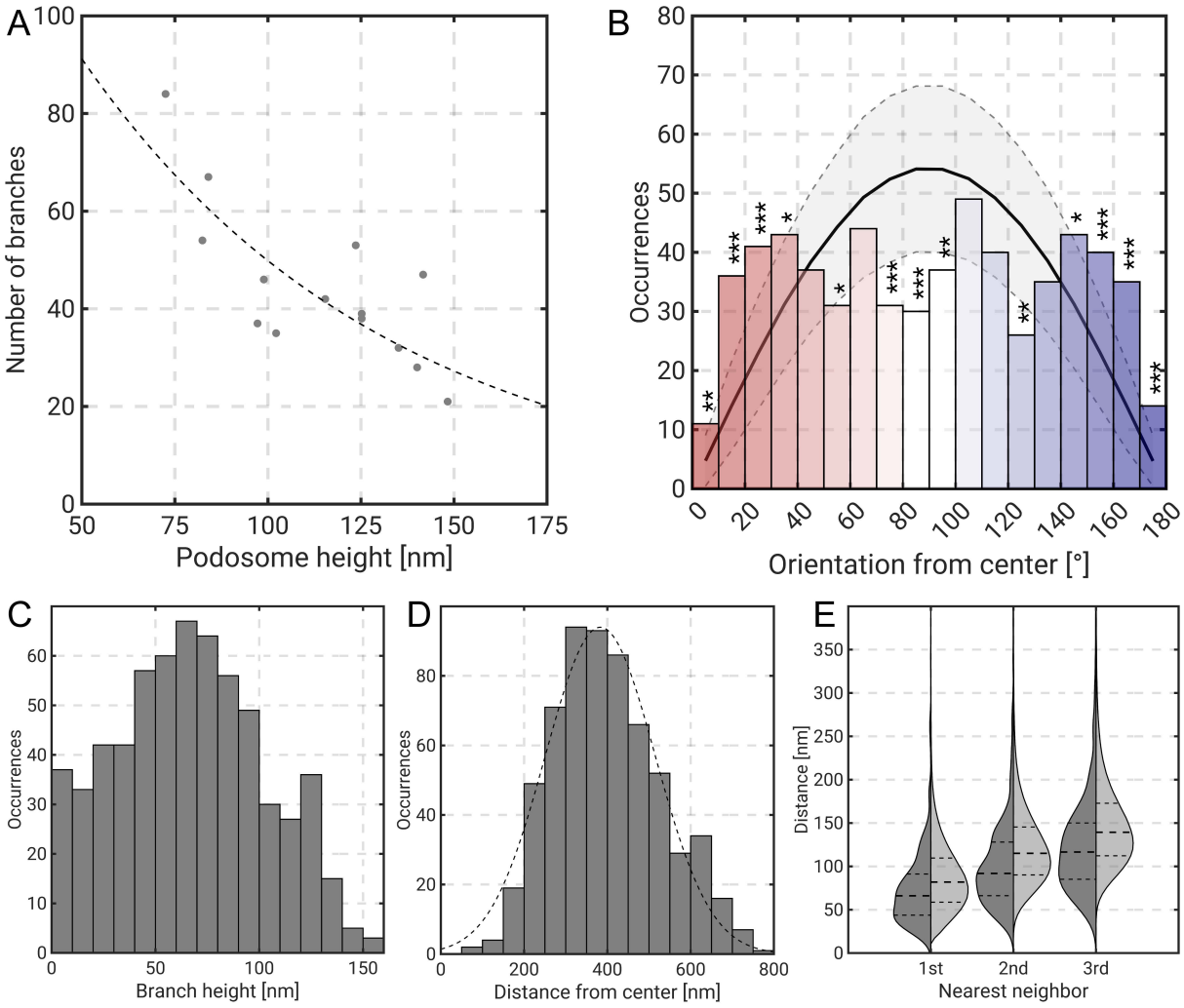

Figure 34: Quantitative analysis of Arp2/3-mediated branches. A: Scatter plot of podosome height and number of identified Arp2/3 complexes. The dashed line corresponds to a negative exponential fit. B: Comparison of branch orientation against a simulation where the orientation was randomized. Bars and gray dots indicate the number of branches within the respective bin. The black curve describes the average of 5000 random simulations, dashed curves and gray areas correspond to 2σ. Each bin was statistically evaluated by determining the number of cases in the random simulation where the obtained value was equal or higher than the observed distribution for bins exceeding the average simulation, or vice versa for bins undercutting the average simulation. This number was converted into p-values. *: $p<0.05$, **: $p<0.01$, ***: $p<0.001$. C: Branch distance from membrane, calculated by fitting a plane to the membrane. D: Branch distance from the podosome center (bars and gray dots). The dashed curve describes the average distribution of 5000 random cases, where the branches were distributed randomly. E: Violin plot describing the nearest neighbor analysis for the first three neighbors. The observed distribution is depicted on the left side of the violin plot and the random distribution is shown on the right side, respectively. Median values are indicated by horizontal dashed line, and 25th and 75th percentiles are given by thinner dashed lines, respectively.

The daughter filament angle describes the orientation of the newly polymerized daughter filaments and was quantified to understand their spatial context within the podosomes (Figure 34B, bars). The observed distribution was compared to a simulated distribution of randomly oriented branches at the same location (Figure 34B, black curve). When comparing two vectors in R^3, a random distribution approximates a cosine function, which is in agreement with the observed distribution. In addition, a confidence interval of 2σ from this random distribution is added (Figure 34B, gray area). A random distribution expects most particles to be oriented orthogonal to the center with vector approaching 90° and very little events at the extremes. In stark contrast, the observed distribution of branch orientation

deviates from the random case. Branches are substantially enriched toward both extreme points, approaching 0° and 180°, respectively, at the cost of fewer branches oriented orthogonally (Figure 34B, bars). Comparing each bin with the random distribution identifies this deviation to be statistically significant. The branch orientation toward the extremes consequently implies nucleation of radially oriented filaments, conforming with the pattern of radial filaments identified in the polarity analysis. This result strongly suggests that lateral filaments are generated through Arp2/3-mediated branching and subsequent elongation.

Importantly, neither extreme orientation is dominating and branches are equally likely to point straight at the core than away from it. While those daughter filaments oriented outbound give rise to radial filaments, branches with daughter filaments oriented toward the core could provide the source of new core filaments. This hypothesis is further supported by their close proximity to the core, and this would also partially explain the low number of branches identified within the core.

The majority of branches are found within 120 nm of the plasma membrane which is in accordance with Arp2/3 activation at the membrane (Figure 34C). This also correlates with the number of branches found per podosome with respect to the podosome height (Figure 34A). Subsequent growth of the network could trigger debranching, providing another potential possibility why the initial template matching experiments in the mature podosomes was not successful.

The average branching distance from the podosome center was found to be 380 nm (Figure 34D, bars). This does not substantially differ from a random simulation, where branches were distributed randomly within the periphery, but outside of the core (Figure 34D, dashed line). The random distribution displays a peak at around 400 nm, which is likely a result of the limited search space of the tomogram. Therefore, it remains unclear whether this distance has biological significance or if branches localize randomly around the core periphery.

However, branches form clusters (Figure 34E). The nearest neighbor distances for the closest three neighbors are significantly shorter (left side of the violin plots, respectively) than for randomly placed branches (right side of the violin plots, respectively). As such, the median distance for the nearest neighbor was 66 nm, while in the random case this distance was 82 nm. Clustering of Arp2/3 complex-mediated branches could enable synchronized bursts of branching and facilitate subsequent polymerization of new filaments. These localized clusters of Arp2/3 are potentially triggered by locally activated Arp2/3 activators such as WASP.

In summary, the identification of Arp2/3 complex-mediated branches in the core periphery suggests their involvement in the establishment of the polarity pattern of radial and non-radial lateral filaments, as well as of the core filaments, likely regulated by localized activation of Arp2/3, enabling cluster formation. Daughter filaments are preferentially oriented in a radial fashion, where the filaments growing away from the core are established as radial filaments, and daughter filaments with opposite orientation could be incorporated into the core.

3.8.3 Subtomogram average of the Arp2/3 complex

Besides revealing the spatial context of the identified branches, subtomogram averaging also revealed the structure of the Arp2/3 complex-mediated branch in podosomes (Figure 35A-B). The average displays a branching angle of around 70°, and conforms well with a published pseudo-atomic model containing the branch complex as well as actin subunits of the mother and daughter filaments (Figure 35C). The average shows differences in the mother filament before and after the branching point. Specifically, the structure prior to it (toward the pointed end) is clearly defined and individual subunits can be identified. Meanwhile, the structure toward the barbed end is less resolved and bulkier. Whether this is a result of increased compression of the filament due to the strains that act on the complex or if it is a sign of flexibility in terms of branching angle is difficult to answer, because the resolution is measured at 25.1 Å (FSC=0.143), which is quite low (Figure 35D). This is partially owed to the small number of particles, where only 700 particles were used for the final average. Furthermore, the particles display a substantial orientation bias toward top views with almost no side orientations (Figure 35E-F). In part, this could be a detection problem, where upright oriented branches are more difficult to identify correctly or might have been misclassified. In addition, these upright orientations might exist within the core where many upright filaments are located, but which were not considered during averaging due to the low detection.

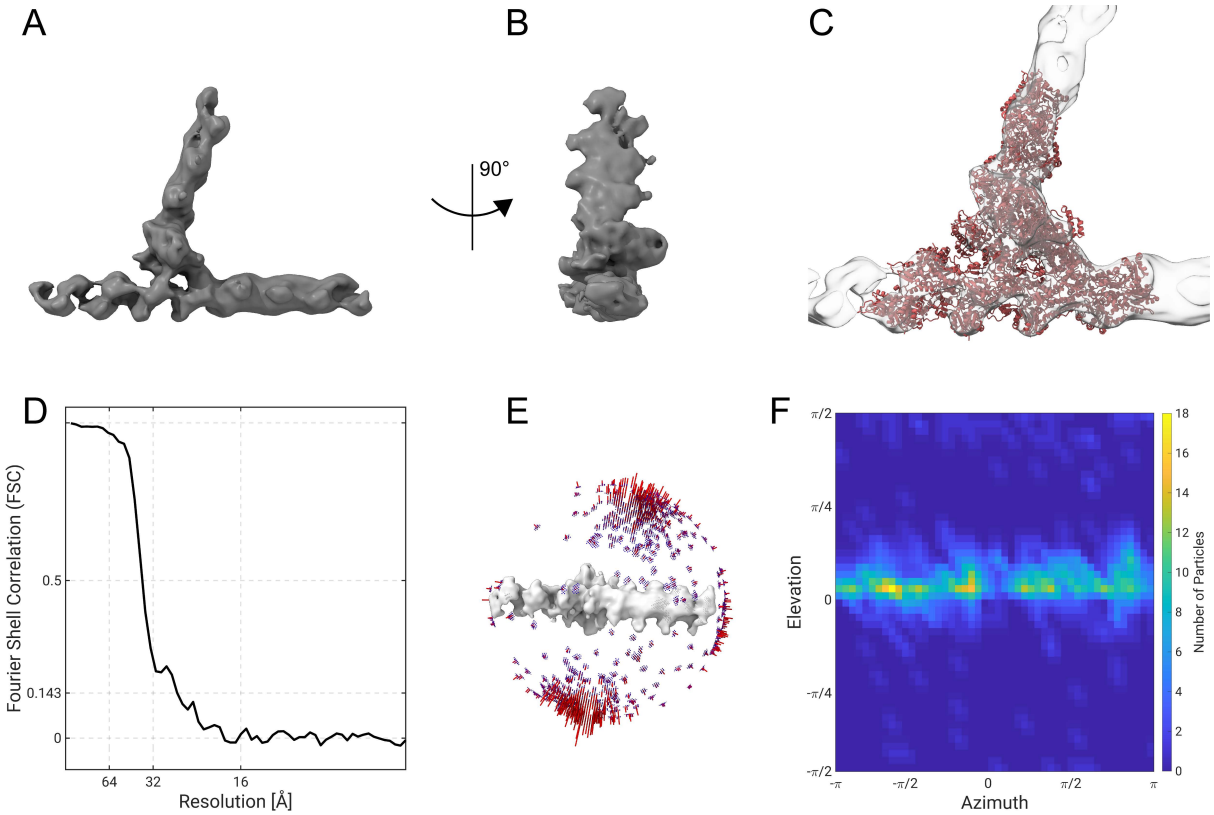

Figure 35: Subtomogram average of the Arp2/3 complex. A, B: Subtomogram average of the Arp2/3 complex-mediated branch structure. C: Docking of a pseudoatomic model (pdb: 7aqk) into the density. D: Corresponding Fourier Shell Correlation of the Arp2/3 complex average. The resolution is estimated at 25.1 Å. E: Angular distribution highlighting prevalent orientations of the final reconstruction. Red bars indicate high prevalence, indicating the structure is composed of mostly top views. F: Angular distribution plot, showing azimuth and elevation angles of the refined particles. The particles accumulate around an elevation angle of 0°, confirming the strong orientation bias.

3.8.4 Disruption of Arp2/3 impairs podosome architecture

To investigate the effect of a macromolecule of interest, a typical approach is to generate a knockout where the molecule is absent, and characterize the potential phenotype. This study is conducted on primary human macrophages. As such, these are not stable cell lines and appropriate knock-outs cannot be generated. Instead, siRNAs and drugs are employed to target specific proteins of the actin cytoskeleton. Treatment with the Arp2/3 inhibitor CK666 fully abolishes any podosome formation within macrophages at concentrations above 50 μM. This emphasizes the importance of Arp2/3 for the assembly of podosome networks and identifies it as an essential component. However, a complete knockout of Arp2/3 and concomitant disruption of the podosome architecture prevents any meaningful conclusions. Accordingly, to further dissect the role of Arp2/3 for podosome formation, cells were treated with a reduced dose of CK666 to allow for partial disruption of the network. In particular, cells were incubated with 25 μM CK666 for 30 min and were subsequently unroofed to achieve comparable data quality as for the wild type. Likewise, tomograms were acquired under similar conditions and were then processed in a similar manner, filaments were traced and their polarities were analyzed.

Notably, podosomes and the core in particular are much smaller and less dense, as compared to the wild type (Figure 36A-B and Figure 37A). Within the core, upright filaments appear more isolated from adjacent filaments. Moreover, podosomes were found to be substantially closer to each other, allowing to capture multiple instances into a tomogram with the same field of view. Figure 36A shows an example with 5 individual and separated cores. To understand the main components of the altered architecture, their polarity patterns were elucidated akin to the wild type. Due to their reduced filament density, filament polarity was assigned close to completion. The overall patterns were in agreement with those described for the wild type (Figure 36C-E). Core filaments predominantly have their barbed ends at the membrane, while lateral filaments were separated into the larger group of radial filaments, having their barbed ends away from the core, and the smaller fraction of non-radial filaments, having their barbed ends at the core. The polarity analysis also highlights the separation of the cores and shows how upright core filaments extend toward the substrate (Figure 36D-E). Due to their small size, the separation of core filaments into smaller subcategories was skipped for this analysis.

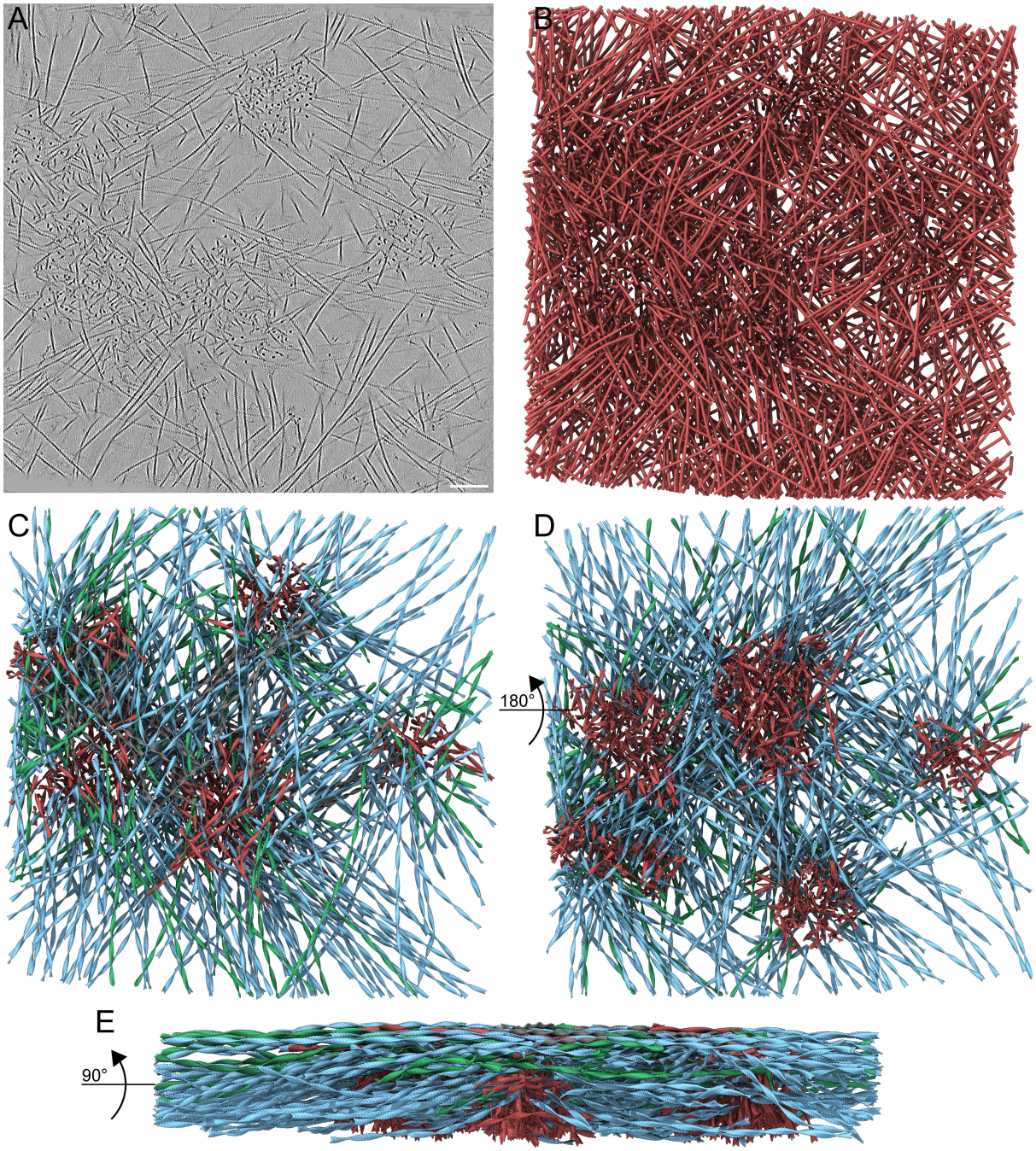

Figure 36: Podosome architecture upon treatment with CK666. Macrophages were treated with 25 µM CK666 for 30 min. A: Tomographic slice of a denoised tomogram showing multiple podosomes. Scale bar 100 nm. B: Segmentation of the tomogram shown in A. C-E: Polarity analysis of the podosomes shown in A-B in different angles, C: top view, D: bottom view, E: side view. The color code for the polarity analysis is maintained from Figure 28. Red: core filaments, blue: radial filaments, green: non-radial filaments, gray: undecided due to appearance in more than one podosome.

To obtain a better understanding of the architectural differences that drive the altered podosome architecture, the overall number of filaments were inspected, as the Arp2/3 complex is involved in nucleating filaments. Comparing absolute filament numbers for each module and assessing their relative contribution to the entire network reveals a striking difference between wild type and CK666 treatment (Figure 37B-C, respectively). For CK666 treated podosomes, the relative number of core filaments was larger than for wild type podosomes (Figure 37D). Consequently, the relative contribution of lateral filament numbers

was reduced, both for filaments classified as radial and non-radial. In contrast, the relative contribution to overall filament length was not affected (Figure 37E). As such, the altered podosome architecture is realized through fewer lateral filaments being nucleated. In addition, this may also imply why podosomes can emerge closer together, as the lateral filaments are less abundant. Accordingly, reduced lateral filament quantities can counteract less force generated by the core. As the knock-down of Arp2/3 predominantly manifests in a reduced amount of lateral filament numbers, these results support the hypothesis that lateral filaments are nucleated by Arp2/3, as suggested in the previous chapter.

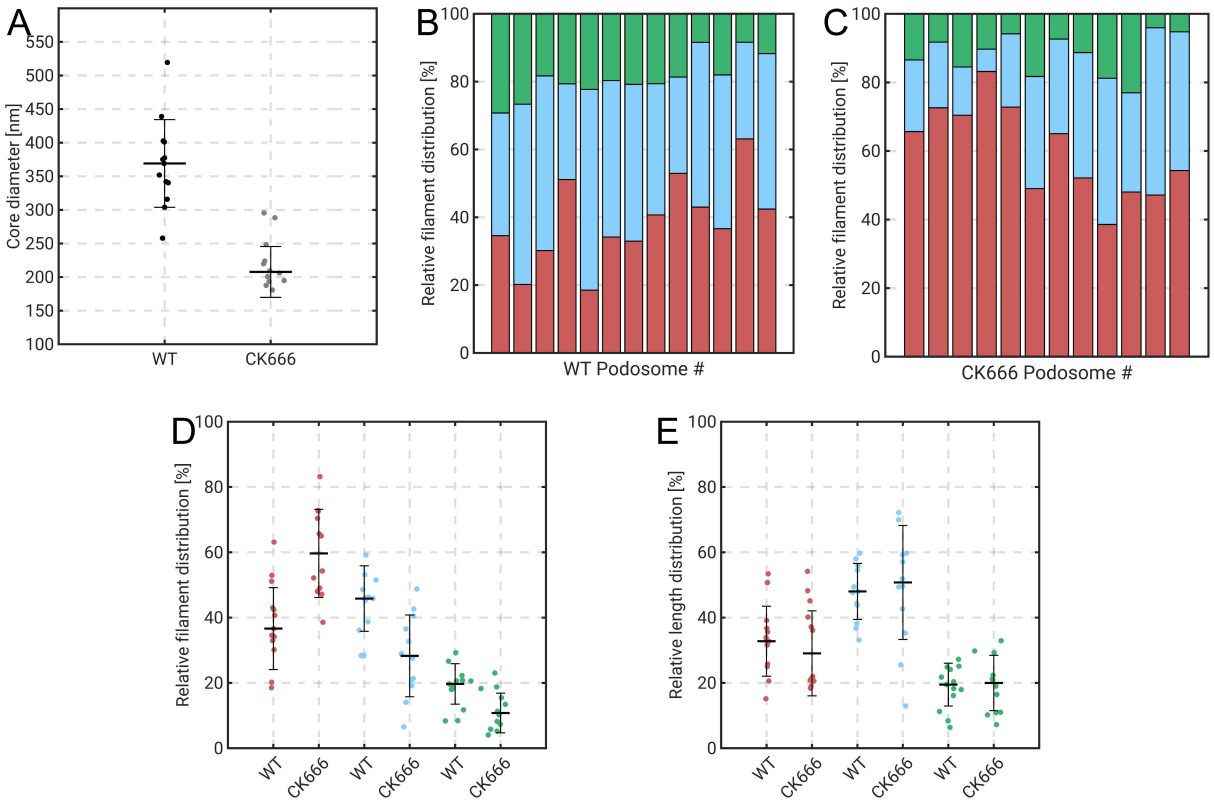

Figure 37: Quantitative analysis of CK666-treated podosome composition. A: Comparison of core diameters. Core diameters were calculated by fitting an ellipse to the polygon enclosing the core. B-C: Relative contribution of filament numbers for each module to the entire podosome, for wild type (B) and CK666-treated podosomes (C), respectively. D: Comparison of the relative filament number contributions of each module to the total number of filaments. Bars indicate median values and standard deviation, respectively. E: Comparison of relative filament length contributions of each module to the cumulative filament length of the entire podosome. Bars indicate median values and standard deviation, respectively. Color code for all images: red: core filaments, blue: radial filaments, green: non-radial filaments.

3.9 Actin-associated proteins in podosomes

3.9.1 Spatial distribution of actin-binding proteins and crosslinkers

The Arp2/3 complex is not the only actin-binding protein (ABP) involved in assembling and maintaining the podosome network. In fact, there are countless proteins described, ranging from nucleators such as formins, crosslinkers such as filamin A and α-actinin, and numerous regulatory proteins within the podosome cap. Within the scope of this work, substantial effort was put into identifying and localizing some of these important molecules and analyze their functional roles akin to the Arp2/3 complex. Unfortunately, ABPs are more difficult to detect than Arp2/3. They are thought to localize mainly within the core, where the density is high and filaments are crowded, rendering the sole detection of filaments challenging (see Figure 22). As such, many crosslinkers remain undetected. ABPs along lateral filaments, where the filament density is lower, are more sparsely located. In addition, the PFA treatment and unroofing might have negatively affected some of these connections leading to their disruption. Finally, the structural plasticity of these crosslinkers, allowing them to accommodate a variety of filament geometries, is another substantial impediment for template matching and subtomogram averaging. Moreover, not all relevant complexes were solved by other methods such as SPA, leading to a lack of template structures.

For these reasons, it was not possible to obtain meaningful averages of these molecules and provide quantitative analyses. Instead, a more descriptive approach was chosen. Figure 38 contains a gallery of various types of actin-binding proteins found across various podosomes from the dataset acquired to capture Arp2/3 complex-mediated branches. Accordingly, the presence of these different types of molecules within the podosome network is confirmed. In addition, each molecule is depicted using an isosurface derived from a denoised and missing-wedge corrected tomogram to give a glimpse of the 3D structure of the respective molecule (Figure 38, bottom row).

Filament elongation is depicted in Figure 38A, where the Arp2/3 complex nucleates a new filament. A prominent density is found 76 nm away, at the barbed end of the daughter filament. Presumably this is the actin elongator Ena/VASP, which is known to work in concert with the Arp2/3 complex [129,235]. It may drive subsequent elongation of the actin filament. Figure 38B contains a decorated filament end that could be attributed to formin, driving filament nucleation, or capping protein, suspending filament nucleation. In addition, Figure 38C displays a large, bimodal crosslinker between two parallel filaments. This density could be attributed to filamin A, which is thought to comprise a similar bimodal structure. Alternatively, it could correspond to α-actinin. The final example in Figure 38D contains a unimodal crosslinker orthogonal to the field of view. Its structure is easier to comprehend from the 3D side view, revealing its interaction with two filaments at different z heights. This crosslinker appears to have a simpler geometry, as it is found in fascin. It could also be attributed to α-actinin that usually forms a dimer, but this is not entirely clear from the volume.

Nevertheless, the allocation of various ABPs to the presented densities is highly speculative. While it is known that the presented proteins are found within the podosome, higher resolution structures are required to confidently identify them.

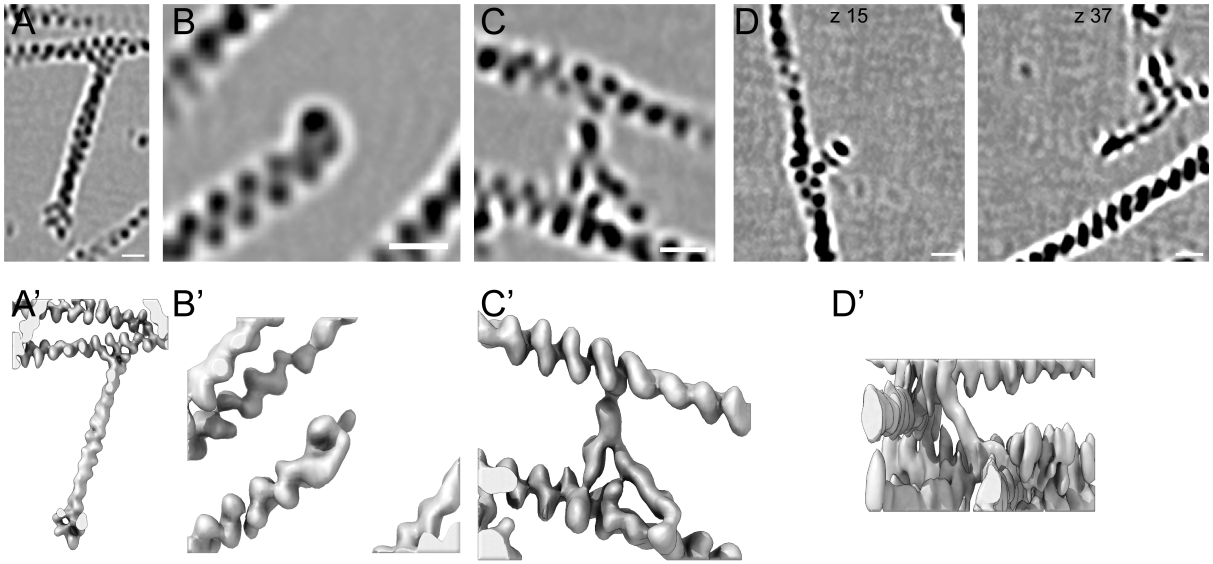

Figure 38: Gallery of actin-binding proteins. Top row: Tomographic slices of various actin-associated proteins. Scale bars 10 nm. Bottom row: Corresponding isosurface extracted from a missing wedge-corrected volume. A: Arp2/3 complex and elongator, potentially Ena. B: Free filament end, potentially decorated with formin or capping protein. C: Bimodal crosslinker, potentially filamin A. D: Unimodal crosslinker, potentially fascin. As the crosslinking is across the z dimension, two slices at different z height are shown. The 3D representation is rotated by 90° to highlight the crosslink (D').

3.9.2 Subtomogram average of an hexameric adhesion complex

A hexameric complex structure in the periphery of the podosome was observed in multiple instances. Its identity is unclear but the complex might be involved in adhesion. The complex is found in the periphery of the podosome core, interspersed between actin filaments (Figure 39A). A closer look at some examples reveals the direct interaction of the complex with actin filaments, where the filament runs across on top of the complex (Figure 39B). Moreover, extracting the corresponding density from the tomogram and segmenting the complex and actin filament provide a better 3D understanding of the arrangement (Figure 39C). Surprisingly, some unattributed density is found within the complex that appears to connect both the actin filament and the complex (Figure 39C, dark red). Moreover, as shown in xy and xz slices, the complex directly interacts with the plasma membrane (Figure 39D). The putative linker region might therefore connect the actin filament to the plasma membrane and the hexameric complex might be involved in enabling this interaction. However, this might not be the sole purpose of this structure, as there are many examples where no interaction with an actin filament can be observed. Alternatively, this interaction could be part of a dynamic process, where the complex only interacts with actin filaments in a certain assembly or disassembly state of the podosome.

Unfortunately, additional structural information remains sparse. Subtomogram averaging did not provide extensive structural details, owed to the low resolution and severe orientation bias (Figure 39E-F). Despite its C6 symmetry, only top views were detected, owed to its unique interaction with the plasma membrane. As such, the resulting subtomogram average is well resolved in a top view, but the side view exposes severely elongated structural features, preventing the extraction of meaningful structural information (Figure 39G and H, respectively). Nevertheless, this complex poses an attractive target for further studies through subtomogram averaging and perhaps lift-out to obtain other orientations of the structure.

Retrieving a higher resolution structure will allow to reveal its identity and elucidate its role in the connection of the actin cytoskeleton to the adhesion machinery.

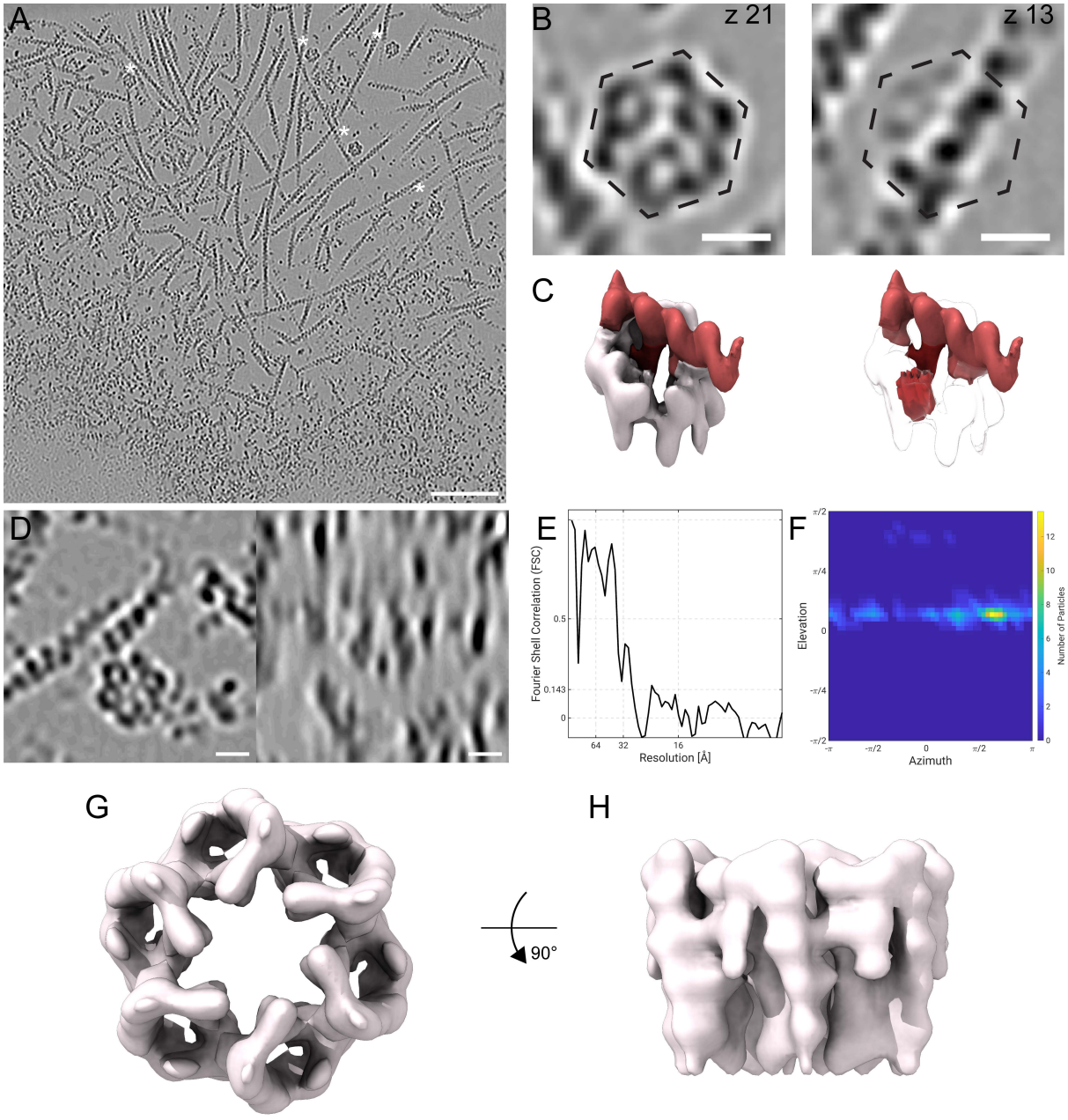

Figure 39: Structure and localization of a putative hexameric adhesion complex. A: Tomographic slice of a podosome with hexameric complexes distributed around the periphery. Complexes visible in this slice are highlighted with an asterisk. Scale bar 100 nm. B: Close-up of a single hexameric complex at different z heights, showing its interaction with an actin filament. The hexagon is drawn to show the location of the complex in the right-side image. Scale bars 10 nm. C: Isosurface rendering of the complex shown in B. The complex is colored in gray (left) or transparent (right), the associated actin filament in orange red and the remaining linker density is shown in dark red. D: Tomographic xy (left) and xz (right) slices of the hexameric complex, showing its interaction with an actin filament (left) and its direct connection to the plasma membrane (right). Scale bars 10 nm. E: Corresponding Fourier Shell Correlation of the subtomogram average. The resolution is estimated at 27.8 Å. F: Angular distribution plot, showing azimuth and elevation angles of the obtained particles. G-H: Subtomogram average of the hexameric complex, displayed as top view (G) and side view (H).

Chapter 4: Molecular-scale visualization of sarcomere contraction

This work was realized in joint collaboration with Laura Burbaum from the laboratory of Professor Petra Schwille in the Department of Cellular and Molecular Biophysics at the Max Planck Institute of Biochemistry, Martinsried. Cells were extracted by Sarah Scholze and Ralph Böttcher in the Department of Molecular Medicine at the Max Planck Institute of Biochemistry, Martinsried. Cell vitrification, cryo-FIB milling, data acquisition, tomogram reconstruction and segmentation were conducted by Laura Burbaum. Analysis of filament packing was conducted by Laura Burbaum, Marion Jasnin, and myself. Subtomogram averaging, including *de novo* structure generation, polarity determination, quantitative analysis of M-line signature, and structural analysis of the thin filament structure were performed by myself. The results of this study were published in the journal Nature Communications on the 2nd of July, 2021 [86].

4.1 The *in situ* architecture of the myofibrillar interior

Neonatal cardiomyocytes are ideally suited for investigation by cryo-ET, as they are sufficiently thin and as such easy to vitrify by plunge-freezing. Accordingly, thin lamellae were generated using cryo-FIB. Overview TEM images revealed cellular sections containing long myofibrils, various organelles, sarcoplasmic reticulum, plenty of mitochondria, as well as cytoplasmic regions filled with ribosomes (Figure 40A). The average diameter was measured at 470 ± 60 nm. Interestingly, some examples of branching were also captured, and myofibrils contained periodically aligned darker densities along their principal axis, even upon branching. These electron-dense regions are likely to be Z-discs.

Accordingly, tomograms were acquired at such positions, containing predominantly a myofibril and putative Z-discs (Figure 40A). The tomogram indicated in the lamellae overview contains two types of filaments composing the myofibril, corresponding to thick filaments (blue arrows) and thin filaments (red arrows), respectively (Figure 40B). Thick filaments were on average 17.4 ± 3.0 nm and thin filaments 8.4 ± 0.9 nm in diameter. Moreover, mitochondria and sarcoplasmic reticulum surround the myofibril, as well as ribosomes (white arrows) and glycogen granules (black arrows).

Segmentation of thin and thick filaments gave rise to their architecture and revealed regions devoid of thick filaments around the electron-dense band (Figure 40C, red and blue filaments, respectively). The region is defined as I-band and this arrangement confirms the electron-dense structure as Z-disc. The gap of this organization is emphasized when thin and thick filaments are displayed individually (Figure 40D-E). The I-bands span a distance of 240-300 nm, corresponding to 12-19% of the sarcomere length which is within range of mature myofibrils. Of note, the gap of thin filaments at the Z-disc is likely a result of the difficulty in tracing until the filament end due to the high density instead of a real feature, as thin filaments are crosslinked by α-actinin at the Z-disc. However, this facilitates measuring Z-disk diameters which are found to be between 100-140 nm. They are composed of individual sections, typically two, that form a zigzag arrangement. This suggests that that these sections are derived from separate smaller myofibrils that laterally fused. This lateral fusion during further development could result in the larger diameters of mature myofibrils.

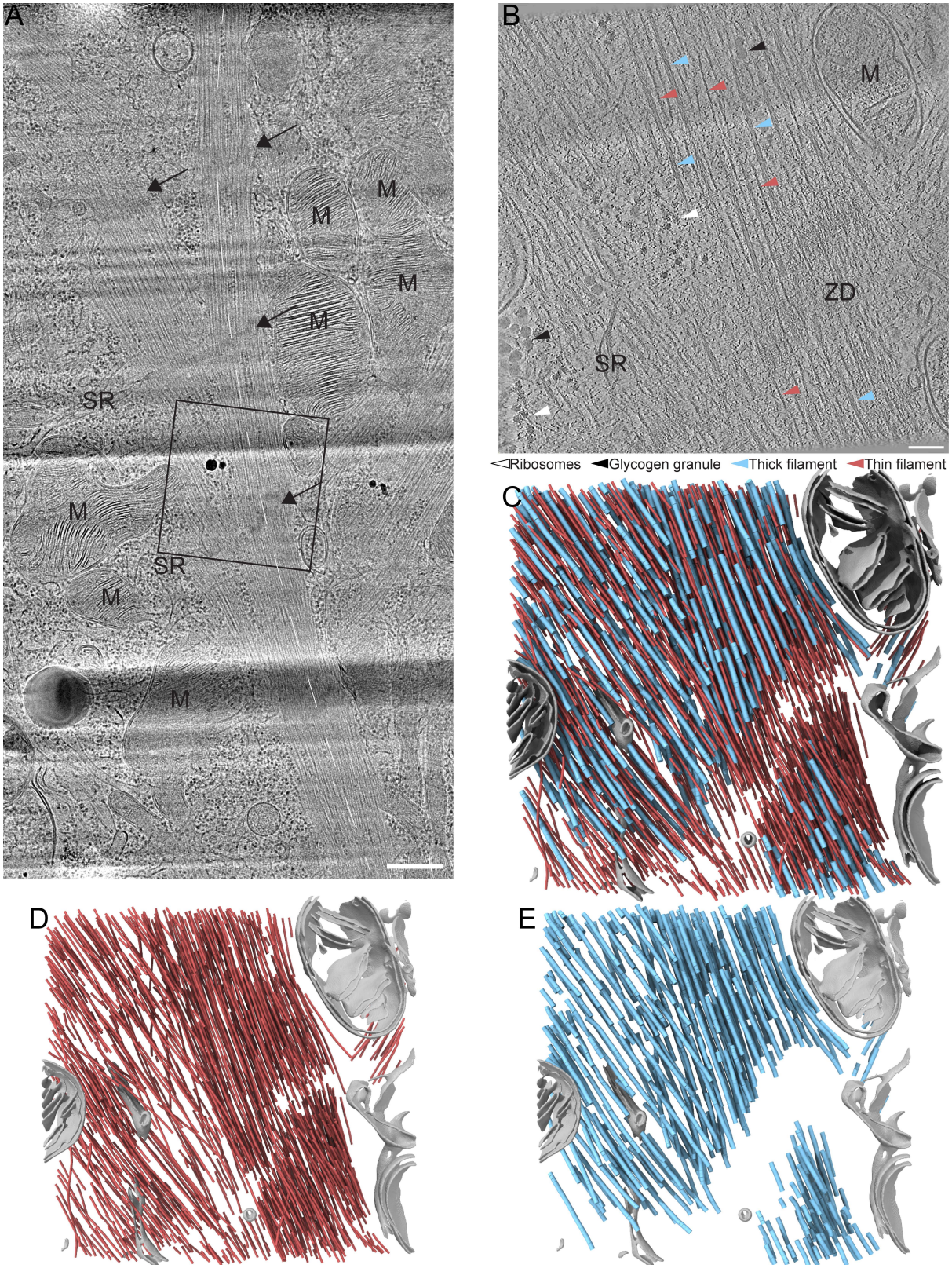

Figure 40: *In situ* architecture of the myofibrillar interior of neonatal rat cardiomyocytes. A: Overview TEM image of a neonatal rat cardiomyocyte lamella containing a central myofibril, highlighted by a dashed line. The arrows point at putative Z-discs, characterized by darker and fussy density. The square indicates the region where the tomogram in B was acquired. B: Tomographic slice of a denoised tomogram containing a myofibril, organelles and ribosomes. Thin and thick filaments, glycogen granules and ribosomes are annotated with arrows, respectively. C: Corresponding segmentation of thin (red) and thick filaments (blue), and membranes (gray). D-E: Highlighting segmentation of thin (D) and thick filaments (E). ZD: Z-disc, M: mitochondrion, SR: sarcoplasmic reticulum.

4.2 Packing analysis of thin and thick filaments

To quantify filament organization and understand potential particularities of sarcomere organization characteristic for neonatal cardiomyocytes, the 3D filament packing of parallel thin and thick filaments within the A-band were analyzed (Figure 41). Thick filaments were found to organize in a hexagonal arrangement, with an interfilament distance of 45.1 ± 3.8 nm (Figure 41A,D). The strong peaks at the hexagonal positions indicate that the lattice is sufficiently stable and intact at the neonatal stage. Thin filaments are found at the trigonal positions interspersed by thick filaments, as can be seen from the threefold symmetry in Figure 41B. The interfilament distance of thin and thick filaments is 26.0 ± 2.4 nm, which precisely corresponds to a double-hexagonal pattern with thin filaments found at the trigonal positions of the thick filament hexagonal lattice (Figure 41E). In contrast, the interfilament distance of thin filaments alone is shorter than expected with 15.5 ± 1.4 nm. Moreover, the packing of thin filaments around thick filaments is less ordered, as shown by the disrupted symmetry in Figure 41C. This suggests that thin filaments are additionally found outside the trigonal positions of the double hexagonal lattice (Figure 41F). To corroborate this finding, the ratio of thin to thick filaments in these sarcomeres was calculated to be 3:1, whereas in adult cardiomyocytes this ratio is at 2:1. This indicates that an initial excess of thin filaments over thick filaments exists and that the packing is progressively optimized and thin filaments are subsequently accommodated into the double hexagonal lattice.

Given that these sarcomeres are functional, as visualized by the contraction of these cardiomyocytes through live cell imaging, the establishment of an ordered hexagonal array of thick filaments appears to be required to allow contraction. The less-ordered arrangement of thin filaments may lead to less efficient contraction, as myosin heads are less flexible in binding the surrounding thin filaments.

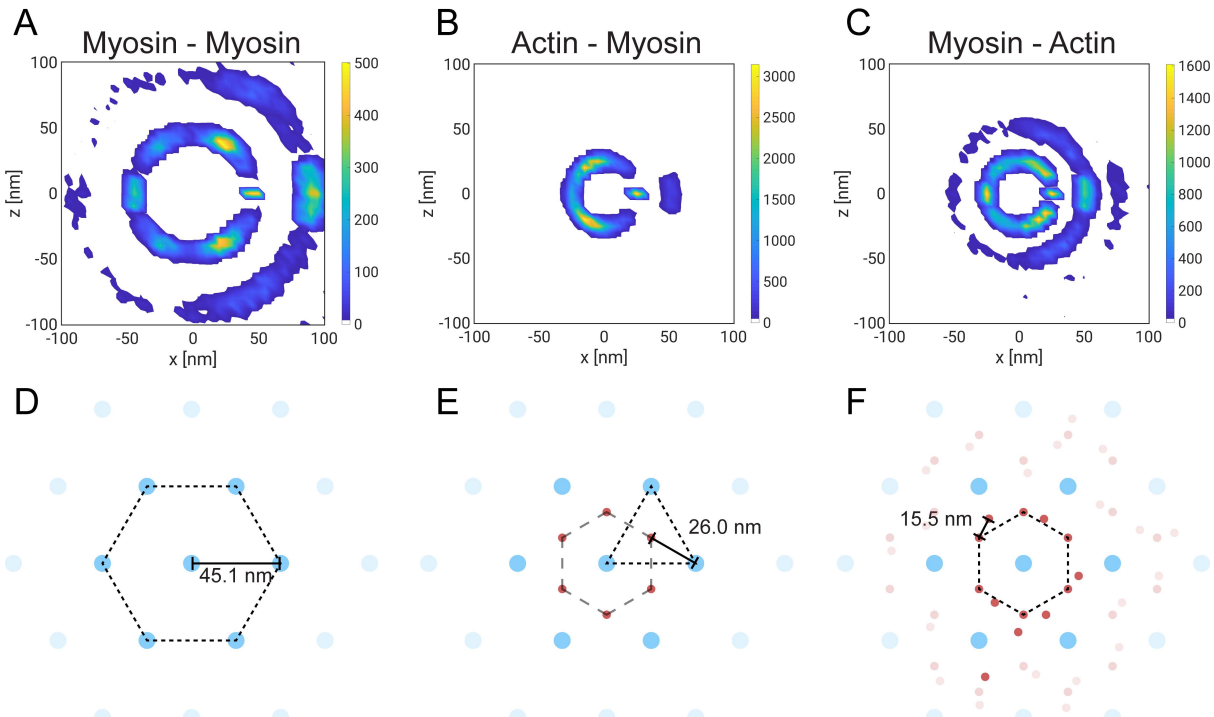

Figure 41: Hexagonal and trigonal packing analysis of thin and thick filaments. A-C: heat maps of neighbor positions around thick filaments (A,C) and thin filaments (B) perpendicular to the filament cross-sections. D-F: Schematic representation of the packing corresponding to the plots. Dashed polygons highlight the respective packing. Myosin-myosin distance: 45.1 nm, Actin-myosin distance: 26.0 nm, Actin-actin distance: 15.5 nm.

4.3 *De novo* structure generation of the thin filament

Subtomogram averaging was employed to further understand the organization of thin filaments at the molecular level. As such, the workflow to obtain the polarity of actin filaments applied in the previous chapter on podosomes, was initially tested on this data. The thin filament polarity in sarcomeres was the subject of many previous studies, confirming a distinct polarity pattern. Therefore, this data provided an ideal test case for the reliability of the workflow. As mentioned above, an initial starting reference for the polarity analysis is ideally generated *de novo* from its own data (Figure 42). As bundled filaments in the sarcomere on either side of the Z-disc share the same orientation, these filaments can be averaged together.

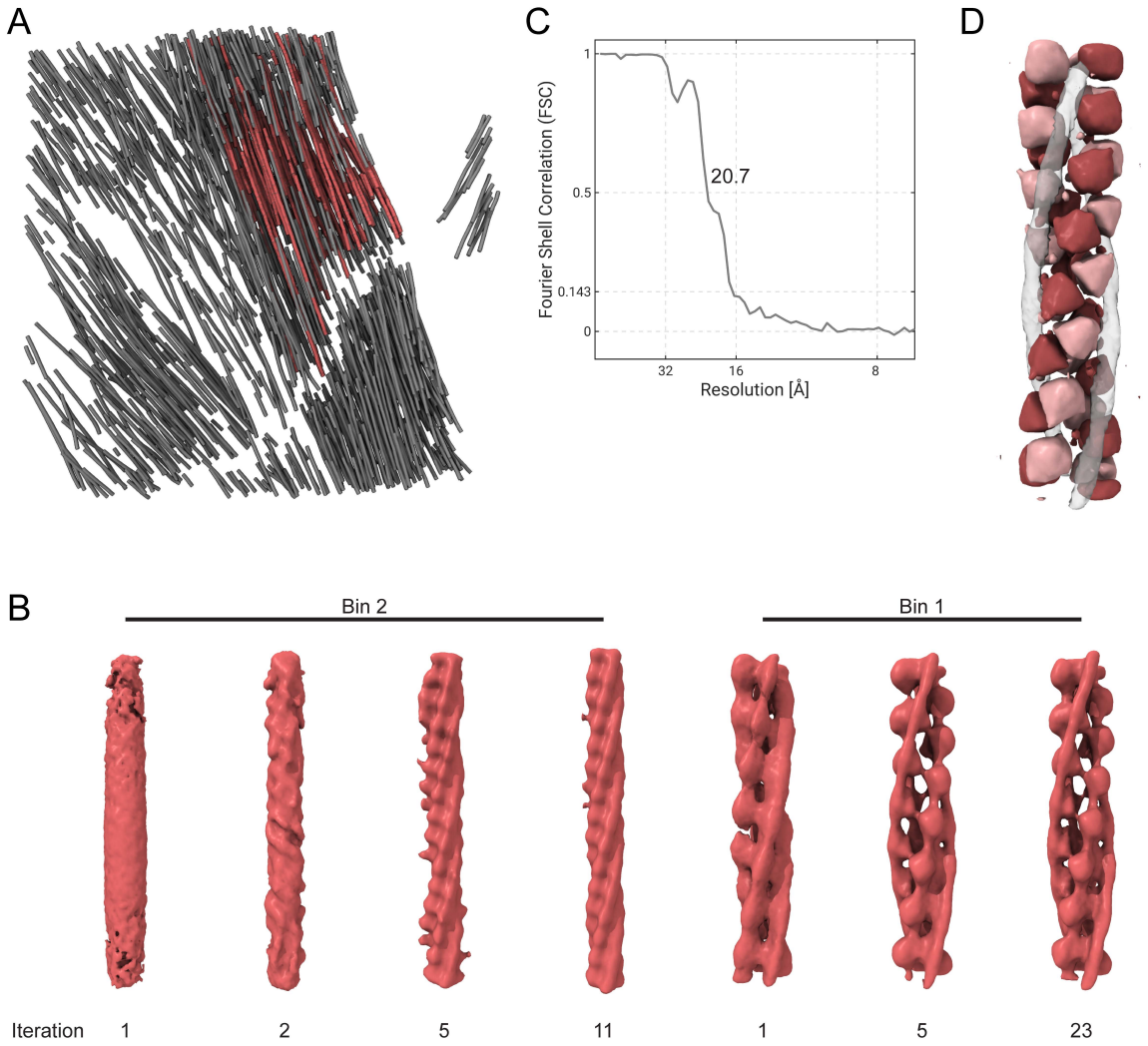

Figure 42: *De novo* structure generation of the thin filament. A: Thin filament segmentation corresponding to Figure 40. Red filaments were used for the generation of the *de novo* reference. B: Iterative alignment at bin2 (pixel size 6.84 Å) and bin1 (pixel size 3.42 Å), starting from global alignment to local alignment to resolve the helical pattern of the thin filament. C: FSC plot of iteration 23 at bin1 determining the resolution at 20.7 Å (FSC=0.5, as no gold-standard processing was performed). D: Difference map of the refined structure in opposite orientations (light and dark red, respectively) when aligned to the Tpm density (gray), revealing the positions of actin monomers of both orientations with respect to Tpm.

The filaments indicated in red in Figure 42A were used to generate a starting reference. As the in-plane angle, i.e., helical twist, is not known and therefore randomized, initial averaging was conducted using a global search, followed by local refinement of all Euler angles in subsequent iterations. This led to the emergence of a helical pattern (Figure 42B) and the final structure was resolved at 20.7 Å (Figure 42C). This is sufficient to determine the polarity of the structure. The thin filament contains actin in complex with Tpm, this facilitates polarity determination, as the actin monomer positions in relation to the two Tpm strands diverge in the difference map (Figure 42D). Consequently, this *de novo* structure is applicable as reference for polarity determination by subtomogram averaging and multireference alignment.

4.4 Thin filament polarity within the sarcomere

Using a multireference approach as described for the podosome analysis, the filament polarity of all filaments was evaluated, while treating each filament individually. For this dataset, 69% of the data was statistically significant and the filaments were assigned their respective polarity (Figure 43). Concomitantly, the averaging approach resolves the refined position and orientation for each actin monomer across the sarcomere, and thereby provides molecular details of filament organization.

For visualization, the refined positions are represented by an arrowhead with barbed and pointed end in the respective color of the polarity (Figure 43B). The refined positions aligned well to the underlying helical twist of the thin filament, indicating the success of the averaging approach to obtain the actual position of each actin monomer. As the sarcomere thin filament polarity is well understood and serves as ground truth, the obtained orientations from the polarity assignment can be compared accordingly.

Figure 43A visualizes the outcome of the assignment. Filaments of the same bundle on either side of the Z-disc share the same polarity. Both bundles face the Z-disc with their barbed ends (Figure 43C, black arrows), which is in accordance with the literature. This confirms the reliability of the polarity assignment result.

Surprisingly, the analysis revealed another change of polarity, where opposite bundles face each other with their pointed ends (Figure 43D). This signature is characteristic of the M-line, whose location was henceforth revealed. This change of polarity cannot be concluded from the segmentation alone (Figure 40), emphasizing the significance of understanding the filament orientation. There was no preference for a given polarity during the assessment, as for both orientations missed filaments were distributed evenly (Figure 43E). The majority of missed filaments were short, therefore containing too few sampling points, or found at the edges of the tomogram, where the alignment is typically worse.

Interestingly, a bundle of tightly bound filaments at the edge of the sarcomere was not assigned (Figure 43E, asterisk). The packing of these filaments appears substantially tighter than for the main body of the sarcomere, and it is also not interspersed with thick filaments. The alignment of this region is not inferior than the rest of the tomogram, suggesting that the structure of the filaments might be different than the rest of the sarcomere. Such a discrepancy with the template structure would result in lower correlation scores and therefore impair the polarity assignment. It is possible that these filaments may not yet be interacting with tropomyosin.

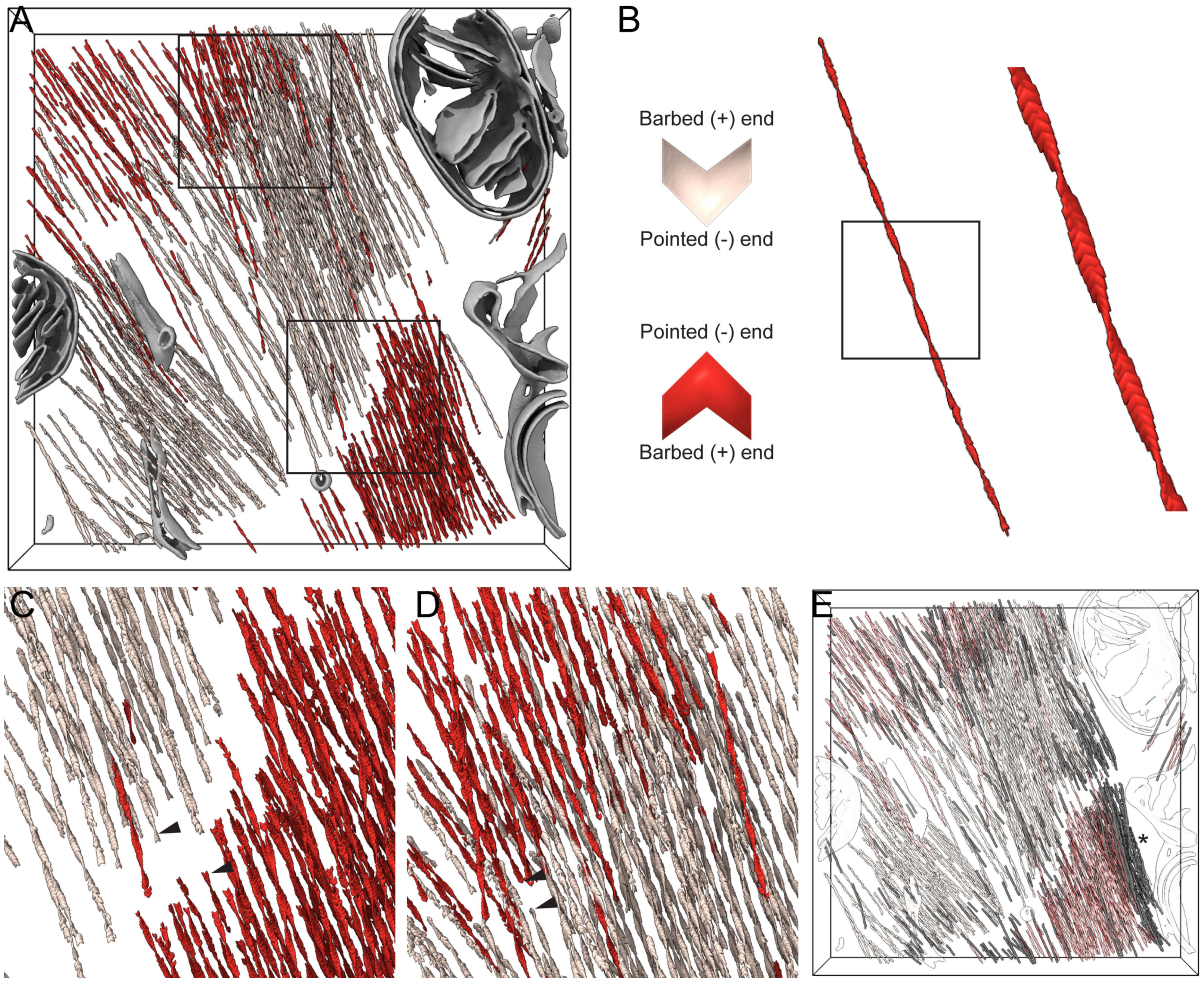

Figure 43: Thin filament polarity within the sarcomere. A: Thin filament polarity upon filament assignment. Opposite polarities are visualized in light and dark red. Zoomed regions for C and D are indicated. B: Arrowhead representation used to visualize the refined actin monomers orientation used in A-E. The individual positions follow the helical twist of the filament (right side). C: Close-up of the filament polarity at the Z-disc. Filaments face each other with their barbed ends. For each orientation, an example is highlighted with black arrows. D: Close-up of the filament polarity at the M-line where filaments face each other with their pointed ends. For each orientation, an example is highlighted with black arrows. E: Filaments whose polarity was not assigned are emphasized in gray. Individual monomers are visualized as spheres, as their orientation was not resolved. A tightly packed bundle of unassigned filaments at the edge of the sarcomere is indicated by an asterisk.

4.5 Sarcomere contraction visualized across scales

The M-line is the center of the sarcomere and thin filaments are pulled toward each other during contraction. Surprisingly, the arrangement of thin filaments at the M-line reveals the overlap of filaments of opposite polarity. This overlap indicates that filaments slid past each other during contraction, which was inferred for sarcomere lengths of less than 2 µm for frog muscles [236].

Interestingly, the overlap varied between tomograms, suggesting different degrees of sarcomere contraction (Figure 44). The example shown in Figure 44A-B exhibits a strong overlap over 281 nm which corresponds to 17% of the entire sarcomere length. As such, this is twice the length of 140 nm reported for the M-region and suggests that the thin filaments on both sides slid past the M-region. The sarcomere length is around 1.65 µm which is smaller than the average sarcomere length measured for these neonatal cardiomyocytes of 1.8 ± 0.2

µm [86]. This is in line with the observed contraction of this example and the inevitable sarcomere shortening. In contrast, the sarcomere shown in Figure 44D-E contains filaments that barely overlap at the M-line. The overlap length is 60 nm, while the total sarcomere length is 1.96 µm. The overlap at the M-line is therefore only 3% which is insignificant. Moreover, the sarcomere length is 300 µm longer than the sarcomere in Figure 44A-B, suggesting that the sarcomere is in a different contraction state and could approach a relaxed state.

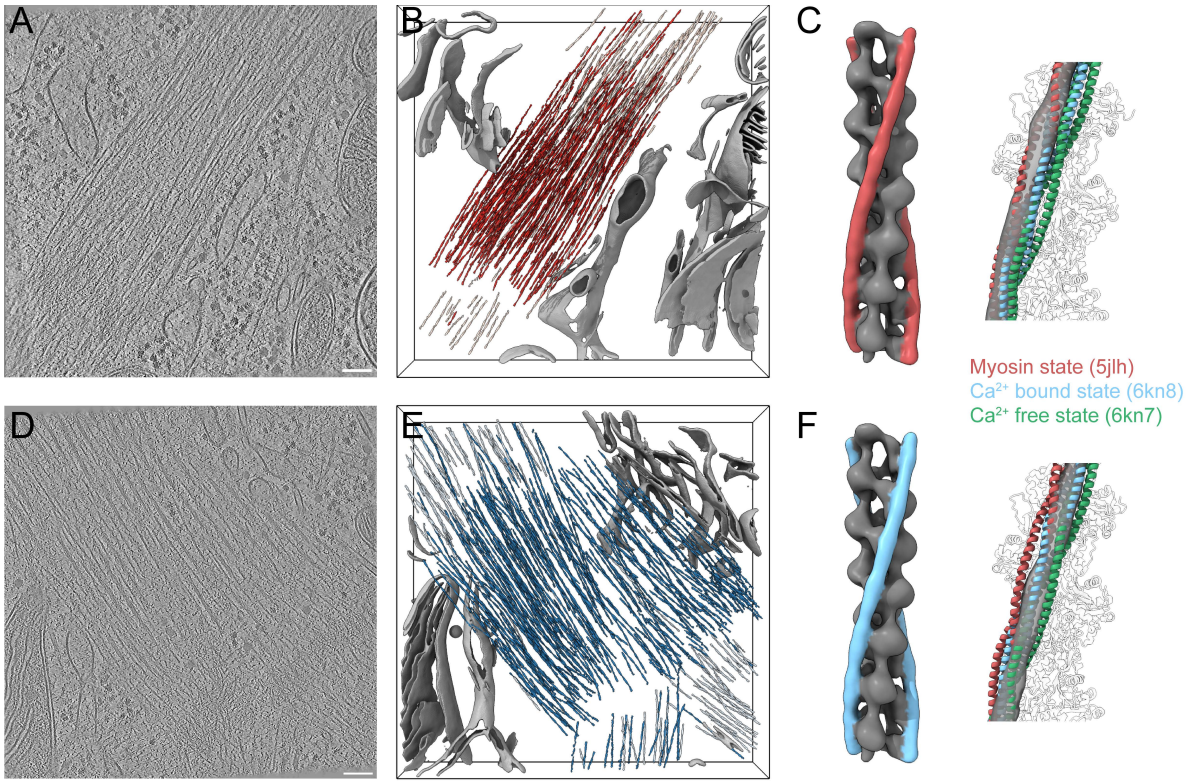

Figure 44: Polarity assignment revealing sarcomere contraction across scales. A-C: Contracted sarcomere, Tpm color coded in red. D-F: Relaxed sarcomere, Tpm color coded in blue. A,D: Tomographic slice of a sarcomere. B,E: Corresponding polarity assignment to A and D, respectively. Filaments are represented by arrowheads and in two colors each, corresponding to opposite orientations. C,F: Subtomogram averages obtained from the filaments in B and E, revealing two functional states related to the contraction state. C: Subtomogram average in the myosin state. F: Subtomogram average in an intermediate state between Ca2+ bound and Ca^{2+} free state.

A direct result of the polarity identification through subtomogram averaging was the retrieval of structural information of the thin filament associated to the different M-line organizations. Thin filaments were averaged separately for each tomogram. Notably, the obtained averages from the two extreme examples resulted in different structures that are associated to different contraction states (Figure 44C,F). Specifically, the strongly overlapping sarcomere returns a thin filament structure where the Tpm density was strongly shifted azimuthally and corresponds to the so-called Myosin or M-state (Figure 44C). This state is associated with strong binding of myosin heads and concomitantly strong sarcomere contraction, as Tpm is shifted the furthest from the myosin-binding site.

In contrast, the thin filament structure obtained from the barely overlapping sarcomere had Tpm in a different position (Figure 44F). Through comparison with pseudo-atomic models of different thin filaments states, the Tpm density was found to be between the Ca^{2+}-bound and Ca^{2+}-free state, therefore accommodating an intermediate contraction state. In the Ca^{2+}-bound state, myosin heads can bind to the myosin-binding site of the thin filament, but

the binding is less strong than for the M-state. As a result, the sarcomere contraction is less strong which is in line with the observed insignificant overlap of thin filaments. Taken together, these results combine evidence from the architectural level of filament organization to the molecular and structural level to visualize sarcomere contraction across scales.

Cross-sections through the M-line for both examples permit further understanding of the organization in 3D upon filament sliding, and how overlapping filaments are accommodated around the thick filaments (Figure 45). These cross-sections indicate that thin filaments of both polarities can contribute to the packing around the same thick filament. However, as these filaments have the wrong orientation, they will likely not enable binding of myosin heads. In addition, there is no clustering of filaments of either polarity and the reshuffling around the thick filaments appears random. Surprisingly, there was no significant increase of filaments in the overlapping region. Deviations of thin filament length throughout the sarcomere could lead to unoccupied regions in the shell around the thick filament which could then be occupied by an overlapping filament of opposite polarity.

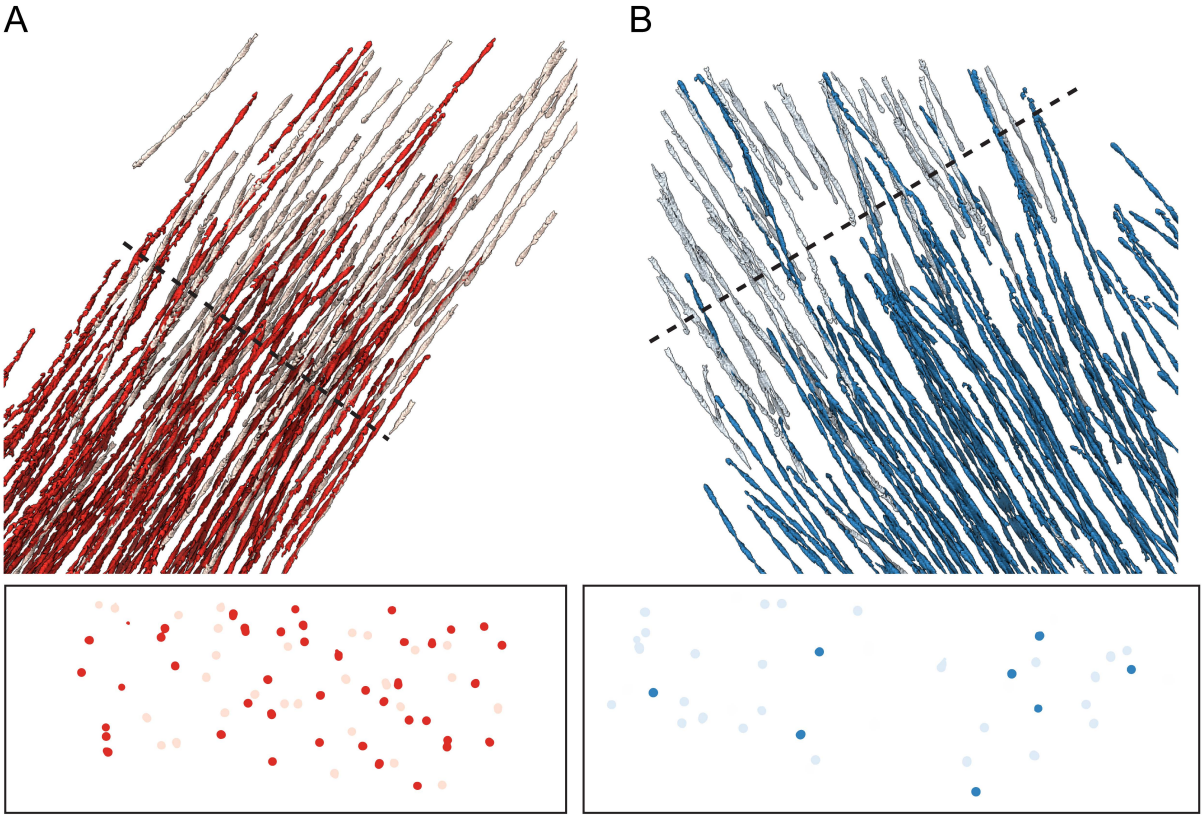

Figure 45: Sarcomere contraction at the M-line. A: Contracted sarcomere B: Relaxed sarcomere. Top rows: Focus on M-line area, highlighting strongly overlapping filaments (A, contracted), and barely overlapping filaments (B, not contracted). Bottom rows: Cross-sections indicated by the dashed line above, highlighting the interconnected packing of filaments of opposite orientation (light and dark colors).

4.6 *In situ* subtomogram average of the thin filament

The majority of sarcomeres were found to be in the contracted state. The respective filaments were combined and averaged together, to obtain a refined subtomogram average of the thin filament (Figure 46). The resolution was estimated at 15.7 Å (Figure 46D). The average contains 13 fully resolved actin monomers and features two strands of Tpm twisting around the structure, approximately following the same helical twist (Figure 46A). The helical parameters of the refined average can be calculated from the refined positions of the monomers. The full repeat distance was 35.9 nm with a helical rise of 27.6 Å, and a helical twist of -167°.

Moreover, the structure permitted docking a pseudo-atomic model of the thin filament in the M-state into the density using rigid-body fitting (Figure 46B). This confirms that a majority of thin filaments across the included sarcomeres were indeed found in the M-state. Nevertheless, the Tpm density is slightly worse resolved than the F-actin core. This could indicate that some filaments were in a different contraction state, but it could also result from the slight variations of helical parameters between F-actin and the Tpm strands. Nevertheless, the actin monomers are well resolved and allow a discrimination of the actin subdomains SD1-4 (Figure 46C), further confirming the filament polarity on the monomer level.

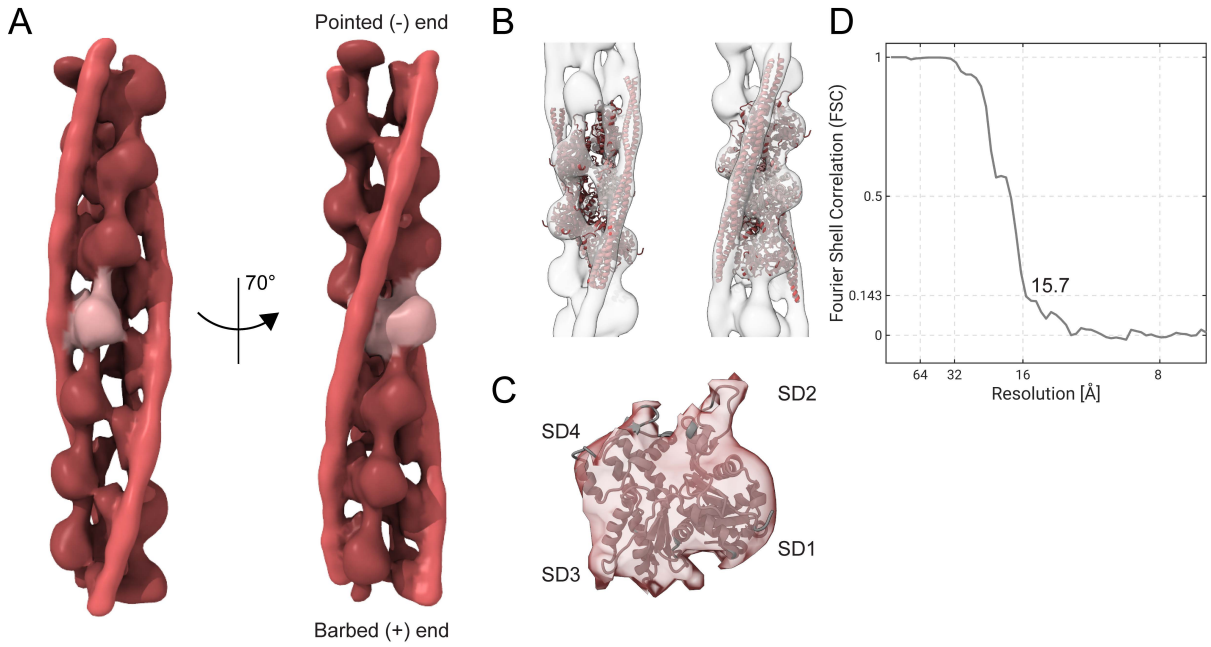

Figure 46: *In situ* subtomogram average of the thin filament. A: Subtomogram average containing 13 actin subunits (dark and light red, respectively), in complex with Tpm (orange red) in the myosin state. B: Docking of a pseudo-atomic thin filament structure in the myosin state (pdb: 5jlh). C: Associated fit of the pseudo-atomic model in the central actin monomer (highlighted in light red in A), revealing distinct densities corresponding to subdomains 1-4. D: FSC plot of the subtomogram average resolved at 15.7 Å (FSC=0.143).

Chapter 5: Discussion

5.1 The molecular architecture of human macrophage podosomes

The podosome is a complex structure, consisting of an intricate network of actin filaments and actin-associated proteins such as crosslinkers. Previous work identified three main modules, the actin-rich core which is generating the protrusive force, a surrounding adhesion ring and a cap module, located on top of the core [177,178]. Cryo-ET was employed to visualize the podosome in 3D and estimate its biophysical properties from segmenting its actin filaments [159]. It revealed that actin filaments in the core are bent and store elastic energy. The entire system acts as a spring-loaded elastic material where the elastic energy is released through applying protrusive forces against the membrane. This force is counterbalanced by lateral filaments which are anchored at the adhesion ring. Still, many questions could not be addressed at the time. Most importantly, the resolution of the tomographic data did not permit retrieval of high-resolution structural information necessary to understand force generation on a molecular level.

The present work aimed at obtaining high-resolution structural information of the podosome architecture. Moreover, it aimed to dissect the interconnectivity of highly intertwined actin filaments comprising this network and identify key biophysical parameters enabling the podosome to generate forces. Through obtaining high-resolution structural information by subtomogram averaging, the polarity of individual actin filaments was elucidated, an important parameter to understand filament behavior and growth. Concomitantly, the refined positions of virtually all actin monomers comprising the podosome network were retrieved, describing the molecular sociology of actin filaments within the podosome (Figure 47). The basic modular architecture was expanded to include further subclasses among the modules, which helped to better understand their functional role in the architecture.

The core module was subdivided into upright core filaments, comprising filaments that are oriented obliquely with respect to the ventral membrane, and shallow core filaments, which approach the ventral membrane at shallow angles, comprising the majority of core filaments. The polarity analysis revealed most core filaments have their barbed end oriented toward the membrane which is consistent with Arp2/3-driven polymerization. A third class of core filaments, i.e., aged core filaments, were located on top of the other core filaments and characterized by predominantly flat filaments. Upright core filaments extend from the membrane into the bulk of aged core filaments. This geometrical relationship indicates that upright filaments may be branched off of aged core filaments and correspond to nascent filaments that have not yet been subjected to any force. This is supported by the absence of upright filaments in the example of an emerging podosome. Moreover, this extension throughout the bulk of the core suggests that they could act as mechanical and functional linkers within the core and therefore contribute to regulating the nucleation of additional filaments.

Next, the polarity analysis identified different sets of lateral filaments; those with their barbed ends facing away from the core and growing outbound, and those with the opposite orientation, growing inward. Filaments growing outbound were the majority of filaments. Most notably, those filaments were exposed as highly radial, emerging from the core. Thus, they were defined as radial filaments, while filaments with opposite orientation did not show

a radial pattern and are thus considered as non-radial filaments. In addition, lateral filaments in close vicinity to the core were found to be shorter and highly parallel. In this set, radial filaments were the dominant class of filaments as well, reminiscent of long lateral filaments. As most lateral filaments are radial and their elongation is directed away from the core, their close functional relationship can be suggested. It is possible they share the same source of polymerization, as their polarity patterns coincide. As such, it can be concluded that short radial filaments may transform into long lateral filaments as they are continuously elongated during podosome growth and therefore constitute young lateral filaments. Finally, non-radial filaments are suggested to be nucleated by Arp2/3 only to a minor extend, and predominantly derived from neighboring podosomes or remnants of the cortex.

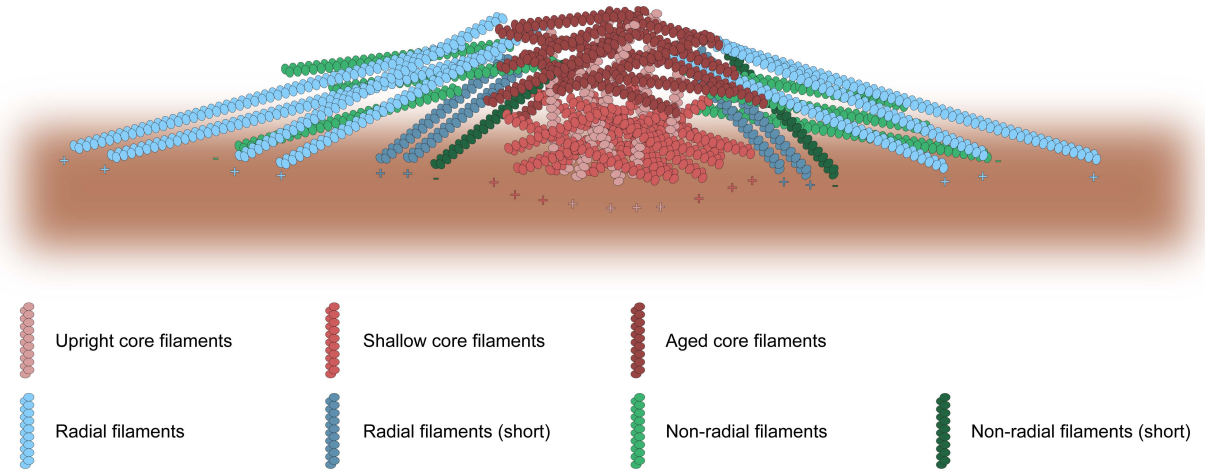

Figure 47: The molecular architecture of human macrophage podosomes. Summary of all identified and analyzed filament modules, contributing to the overall filament network, which enables force generation several orders of magnetite larger than for an individual actin filament.

5.1.1 Suggested mechanism of podosome assembly and force generation

Direct estimation of the dynamic state of the podosome is not possible, as the cells cannot be synchronized prior to plunge-freezing. Therefore, the size and height of the podosome served as parameters to estimate the state of the respective structure (Figure 48).

During podosome maturation, upright and shallow core filaments grow at comparable rates. Combined, their relative increase is similar to that of aged core filaments, confirming their relationship. Lateral filaments outpace this growth and constitute a larger fraction in bigger podosomes. Potentially, this ratio change is required to counterbalance the forces generated in the growing core. The elongation rates of short and long radial filaments are comparable, further indicating their mutual relationship. Short radial filaments elongate during podosome maturation and transform long lateral filaments. The extension of long radial filaments into the periphery is comparable to the podosome core size, suggesting a mechanistic relationship. In contrast, non-radial filaments stagnate and are not elongated. It appears that these filaments are relicts from preceding cortex filaments or mis-placed filaments, which are progressively sorted out during podosome growth.

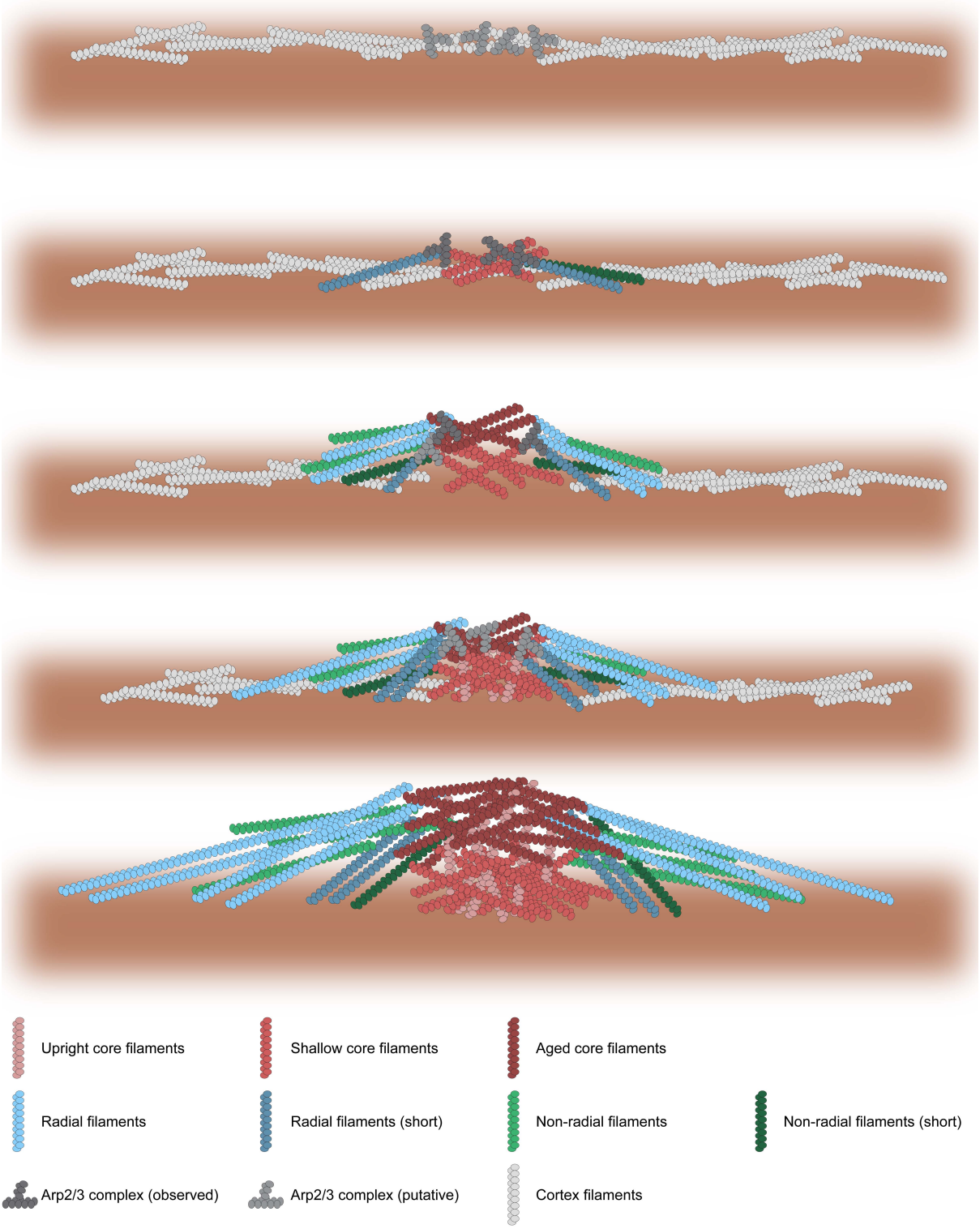

Figure 48: Podosome assembly and maturation. Top to bottom: Burst of Arp2/3 complex-mediated nucleation of filaments within the cortex layer may lead to the emergence of radially arranged filaments. Core filaments are nucleated centrally. As they are confined by outward-facing, short radial filaments, they begin to grow toward the membrane. As a result of the mechanical barrier of the plasma membrane, filaments flatten and become curved. New shallow core filaments lift older core filaments up. New core filaments are presumably nucleated by Arp2/3 and approach the membrane at upright angles, where they will eventually flatten and bend as well. The density of core filaments is continuously increased. The space for core filament growth is confined by aged core filaments on top and by crosslinked, short parallel lateral filaments at the sides. Lateral filaments counterbalance this force through anchoring at the plasma membrane through integrins.

Importantly, this polarity pattern was already found in an example of an emerging podosome. Here, radial filaments were dominating over non-radial filaments. Moreover, the network was still very shallow with filaments adopting mostly flat orientations, including core filaments which were present only to a minor extend. This orientation is reminiscent to those found for Arp2/3-mediated branches. This work identified the Arp2/3 complex as the major nucleator of lateral, in particular radial, filaments. The orientation of identified branches with respect to the podosome core indicate a significant enrichment of radially oriented daughter filaments. In addition, Arp2/3 appears to form clusters, driving local polymerization. This is likely a direct result of local activation of Arp2/3 at the plasma membrane through N-WASP.

To further investigate the role of Arp2/3, the podosome architecture upon treatment with the Arp2/3 inhibitor CK666 was compared to the wild type architecture. It revealed smaller cores, indicating the involvement of Arp2/3 in establishing the core, but which was not subject of the analysis. It also shows, that the number of lateral filaments is significantly reduced compared to the wild type. Both the reduced core size, as well as the reduced counterbalancing capabilities of fewer radial filaments result in reduced protrusive force exerted by these networks.

Local activation of Arp2/3 results in a burst of branches that generate a cluster of filaments over the cortex layer (Figure 48). This work showed that this pattern is highly radial. How this radial orientation of Arp2/3 is realized in the first place was not addressed. It is possible that a concentrated burst of nucleation leads to sterical hindrance that favors filaments elongating in a radial fashion. Moreover, additional factors such as Ena/VASP may be recruited to specifically elongate filaments with radial characteristics. Filaments which are nucleated as part of this burst but are located at the center might favor elongation that is directed more toward the ventral membrane. As such, they might form the basis of core filaments. In particular, they are reminiscent of shallow core filaments.

As the space is filling with filaments, Arp2/3 is pushed further outward, where nucleation continues and is manifested predominantly in lateral filaments (Figure 48). This is supported by reduced quantities of lateral filaments in podosomes with a partial Arp2/3 knock-down. The orientation of branches is very flat with respect to the ventral membrane and daughter filaments strongly favor radial positions. It is possible that daughter filaments which are directed at the core may be incorporated as new core filaments. However, as there were not too many branches identified within the core, the exact source of new upright core filaments could not be addressed. It is therefore assumed, that Arp2/3 is responsible for their generation as well, where branches might be found within the bulk of the core using aged core filaments as mother filaments, and daughter filaments will eventually be incorporated into the core. Upon force generation, filaments bend and start to flatten. Continuous polymerization of core filaments will trigger pre-existing core filaments to be lifted up and subsequently incorporated into the bulk of aged core filaments. As such, the core filament density is continuously increased, which leads to a build-up of elastic energy realized through increased filament bending. New monomers might be fed through and regulated by the podosome cap.

Concomitantly, the space for polymerization is enclosed by a ring of short and highly parallel radial filaments. The parallelism indicates significant crosslinking between these filaments, providing a mechanical barrier and confinement for further core filament polymerization. Taken together, these results might give a glimpse of the steps involved in assembling the complex network of podosomes, to exert forces in the nanonewton range. Importantly, as the core grows, the number of radial filaments in close vicinity to the core

increases (Figure 48). These filaments are parallel and presumably highly crosslinked. As such, they form the barrier to contain core filaments. Some of these short radial filaments continue to elongate outbound and eventually transform into long radial filaments. This suggests filament length as an indicator of age for lateral filaments.

Finally, the core grows initially horizontally and eventually also vertically. Concomitantly, radial filaments comprise larger number of filaments in bigger podosomes to counterbalance the increasing forces generated by the core, resulting in the mature architecture as analyzed in this work.

5.1.2 Comparison with existing literature

A previous study reported on the polarity of actin filaments of podosomes on apatite-grown osteoclasts [233]. The authors used rotary shadowing electron microscopy on freeze-dried samples and analyzed their polarity using Myosin S1 decoration. The architectural description of podosomes is highly similar to the examples presented within this work, with a densely packed F-actin core, surrounded by lateral filaments. The study draws similar conclusions on the polarity of lateral filaments and cap filaments, where lateral filaments mostly have their barbed end away from the membrane, and the cap contain more of a mixture of filament orientation. Surprisingly, the authors claim the opposite polarity for core filaments, where the barbed end is directed toward the core interior, rather than the membrane.

Other cytoskeletal assemblies can produce nanonewton forces, such as the lamellipodium, where force is necessary to push against the cell membrane at the leading edge [157,158]. Within these networks, a high polarization of actin filaments can be observed, where the vast majority has their barbed ends toward the membrane. This is a prerequisite for polymerization forces to act upon the membrane. Importantly, in case of the podosome, polymerization alone is not sufficient, as core filaments were found to be bent to store elastic energy that is released as protrusive force [159]. The actin filament polarity patterns presented here are in agreement with Arp2/3 complex-mediated nucleation directed toward the plasma membrane. The transition into diverse networks with distinct architectures further demonstrates the importance of confined nucleation and fine-tuning via actin-related proteins.

5.1.3 Limitations of the work and future perspectives

The filament architecture of the podosome was described in great detail, through utilizing structural information of the filament. The roles of the various filament modules were quantitively analyzed and their development during podosome maturation was studied. Furthermore, the role of Arp2/3 for network generation was dissected. This work highlighted important architectural properties that enable the generation of protrusive forces. This will help to further understand cell invasion and tissue infiltration, an important attribute of macrophages as part of the innate immune system. Importantly, it may help to find attractive targets to control the invasiveness within tumors, where macrophages may account for a larger fraction of the tumor tissue [168]. In addition, the closely related invadopodia are thought to be derivatives of podosomes in cancer cells, where the close regulation of filament assembly and disassembly is distorted [185]. Accordingly, the invasiveness of certain tumor cells can be associated with the amount of invadopodia formed within these cells. However,

the filament architecture of these structures is not known. It will be interesting to study these networks in the future and compare them to the podosome architecture. The identification of key architectural differences in its composition and regulation might ultimately lead to attractive targets to contain the invasiveness of these cells [164].

The podosome architecture is not entirely understood. Many questions are still open and new questions arose. The role of actomyosin contractility, another important concept for force generation, was not addressed in this work. Non-muscle myosin II is thought to localize outside of the podosome core, and are therefore likely interacting with lateral filaments [178]. However, its structure is currently not known, rendering its identification through cryo-ET more difficult. How this interconnection contributes to podosome force generation by providing additional layers to fine-tune the amount of force, will be the subject of future studies. Likewise, precise quantifications of actin-binding proteins and proteins at the interface of the adhesion machinery, such as talin or integrins, are needed to obtain a complete understanding of the podosome architecture.

A hexameric complex was identified in the periphery of the podosome core. It was shown to interact with both actin filaments and the ventral plasma membrane, where it may be involved in linking the cytoskeleton to the adhesion machinery. However, further studies are necessary to reveal the composition of the complex and its functional role in adhesion.

The role of Arp2/3 as nucleator for lateral filaments was investigated, but its role in establishing the podosome core was not specifically addressed. The high density within the core provides a major impediment in its analysis, rendering detection of small filaments, crosslinkers and other actin-associated proteins highly sophisticated. To circumvent this, even higher magnification tomograms need to be acquired, focusing on the core in particular. However, a prerequisite for high quality tomographic data is thin samples, ideally below 150 nm. In contrast, podosome cores on EM grids were found on average twice as high, posing a significant increase in thickness if the entire core needs to be captured. Cryo-FIB milling may circumvent this problem but in case of wedge-milling will lose the top and in particular the cap structure, or will be difficult to target if low-angle lamellae are preferred. The identified Arp2/3 complex-mediated branches within the periphery of the podosome core were significantly oriented toward the radial extremes, creating a connection to the radiality of lateral filaments. However, how these branches are oriented accordingly in the first place, remains unclear. While the Arp2/3 complex might generate branches from pre-existing radial filaments, with specific orientations allowing the creation of new filaments with radial tendencies, it poses a classical “chicken vs egg” problem. To fully understand the initial steps of podosome formation, examples need to be captured at the earliest stage possible. However, these examples might be difficult to identify as podosomes and might require additional confirmation through the use of fluorescent tags, requiring a different cell system.

Podosomes are highly dynamic structures. This implies they also disassemble rapidly. One possibility is that increasing forces eventually lead to disruption of the lateral filaments, which can no longer counterbalance the core. As such, the anchoring function is lost and the protrusion force disappears. Disassembling podosomes could be therefore characterized by a lack of lateral filaments or highly disordered radial filaments, which would not be as radial anymore. However, this remains purely speculative, as the possibility of disassembly was not considered for the networks analyzed in this work, as it is even more difficult to assess the disassembly state of a podosome. As such, this will remain the subject of a future project.

Primary human macrophages are the most widely used system in the field to study podosomes. The factors involved in the network are well studied, and they are the most

relevant cell system to study human innate immunity. For cryo-ET, the cells are suboptimal. Genetically modifying them is not possible, preventing the usage of fluorescent labels to target the podosome in specific states or to identify the hexameric complex of unknown composition. As primary cells, they are difficult to handle and their viability is lower compared to stable cell lines, especially in non-natural conditions as on an EM grid. This was reflected in the low success rate in identifying podosomes in the *in situ* data, where the majority of cells were non-viable and undergoing apoptosis. In addition, the examples which were captured could not reproduce the same quality which was obtained at lower magnification and using the VPP [159]. However, employing the VPP provides additional challenges for subsequent subtomogram averaging, in particular for CTF correction, which was the reason not to use the VPP.

Instead, cells were prepared using unroofing, where the dorsal membrane, including the cytosol is mechanically removed through shear flow of a pipette, and only the ventral periphery is retained, including the cytoskeleton. This method describes a cruder preparation method and therefore brings additional limitation, but leads to improved contrast and data quality. However, the term *in situ* in a stricter sense is violated. Nevertheless, parameters such as filament composition and orientation remain unperturbed, and also the structural integrity of the actin filament is retained, as can be seen from the sub-nanometer structure of the actin filament. However, it cannot be excluded that less stable interactions, such as the Arp2/3 complex or crosslinker were not affected by this procedure. As such, *in situ* podosomes are to be favored for future studies, since they also provide additional cellular context, apart from the actin cytoskeleton. However, to achieve higher throughput, a different cell system might need to be adopted, such as stable cell lines of mouse macrophages. On top, this would allow to introduce knock-outs and other labels to be introduced, which will facilitate the elucidation of additional parameters.

Finally, the podosomes investigated in this work, and in most studies in the field, are 2D podosomes, as they are placed on a flat surface. The relevant scenario within the human body, where the cell might encounter a 2D surface, is in the blood stream before the macrophage infiltrates the tissue. However, within the experimental setup, the podosome is not able to penetrate through an EM grid. This may lead to continuously increasing podosome sizes that may not accurately reflect the *in vivo* architectural properties. As such, those might be considered as “frustrated podosomes”, akin to “frustrated phagocytosis”. Tissue is a complex 3D environment that exhibits different environmental parameters for the protrusion. In fact, these parameters might change rapidly on a local scale, where the abundance of ECM components such as collagen influence the rigidity of the surrounding. Studying podosome-like structures in a 3D environment will be an exciting step into understanding their behavior within the human body.

However, 3D systems are very challenging, both in sample preparation and generation of appropriate lamellae for subsequent imaging. High-pressure freezing instead of plunge-freezing is necessary and cryo-lift out has to be employed to extract suitable biological material for subsequent thinning with an ion beam. Recently, an improved serialized cryo-lift out method was presented which increases throughput of lamella generation from lift-out samples [237]. This might render the study of podosomes in a 3D environment feasible in the future, posing an exciting endeavor in understanding cellular invasion and force generation in a 3D context.

5.2 Molecular-scale visualization of sarcomere contraction

Using neonatal rat cardiomyocytes, the sarcomere architecture during contraction was visualized across scales. The myofibrillar organization within these sarcomeres resembled those of adult cells, but individual fibers were less ordered. This was reflected in the actomyosin arrangement, where an excess of thin filaments was found outside the trigonal positions between the double-hexagonal lattice of thin and thick filaments. Despite this, the hexagonal packing of thick filaments was sufficiently established, suggesting the thick filament arrangement to be the predominant prerequisite enabling functional sarcomere contraction.

Subtomogram averaging was employed to unveil the polarity of thin filaments and confirmed that the correct orientation was already established at the neonatal stage, resembling those of the adult sarcomere. Moreover, the polarity analysis revealed the location of the M-lines, representing the center of the sarcomere. At these locations, filaments of opposing polarity were overlapping to varying extent, suggesting their relative sliding. The amount of overlap was directly correlated to the functional state of the thin filament structure, where a strong overlap of filaments was accompanied by a thin filament structure in the M-state, enabling the strongest actomyosin interaction (Figure 49, top). Concomitantly, the sarcomere length was reduced. In contrast, barely overlapping thin filaments were attributed to a thin filament structure in an intermediate state, where the Tpm was shifted azimuthally, permitting weaker actomyosin interaction (Figure 49, bottom) and therefore less sarcomere contraction. This work provided a direct link between architectural characteristics of sarcomere contraction and functional states on the molecular level at the neonatal stage.

Neonatal rat cardiomyocytes provide an ideal cellular system for studying the organization and development of sarcomere architecture. The cells adapt well to culture conditions and exhibit rhythmic contractions, resembling those of adult cardiomyocytes. In contrast, adult rat cardiomyocytes degenerate and subsequently regenerate their myofibrillar arrangement upon attempts to culture them. Furthermore, neonatal cardiomyocytes are thin and are ideally suited for vitrification by plunge-freezing. Adult cardiomyocytes adopt a more rectangular shape and comprise thicknesses of over 10 μm which renders complete vitrification very challenging. As such, these cells will need to be vitrified by high-pressure freezing.

Since the conclusion of this work, several studies focusing on the sarcomere architecture using cryo-ET were published [238-241]. In particular, isolated mature mouse psoas myofibrils were vitrified in the rigor state, before suitable lamellae were generated by traditional cryo-FIB milling. While this cell system is in strict terms not *in situ*, as during the purification some loss of lateral stability deriving from neighboring myofibrils is observed and the sarcomere is trapped in a specific contraction state, the system nevertheless provides an ideal case for obtaining high-resolution information on the actomyosin arrangement. A first study provided a molecular map of actomyosin cross-bridges and characterized the interactions across the sarcomere, while also obtaining a thin filament structure in complex with myosin heads [240]. It further showed the crosslinking of adjacent sarcomeres through α-actinin at the Z-disc. The study also presents a low-resolution structure of troponin, an essential component of the thin filament required for regulating the Tpm position along the thin filament. In a follow-up study, this structure was refined [239]. Moreover, the authors identified and solved the structure of the protein nebulin. Nebulin is an essential protein in skeletal muscle to regulate sarcomere length and is required for proper sarcomere contraction.

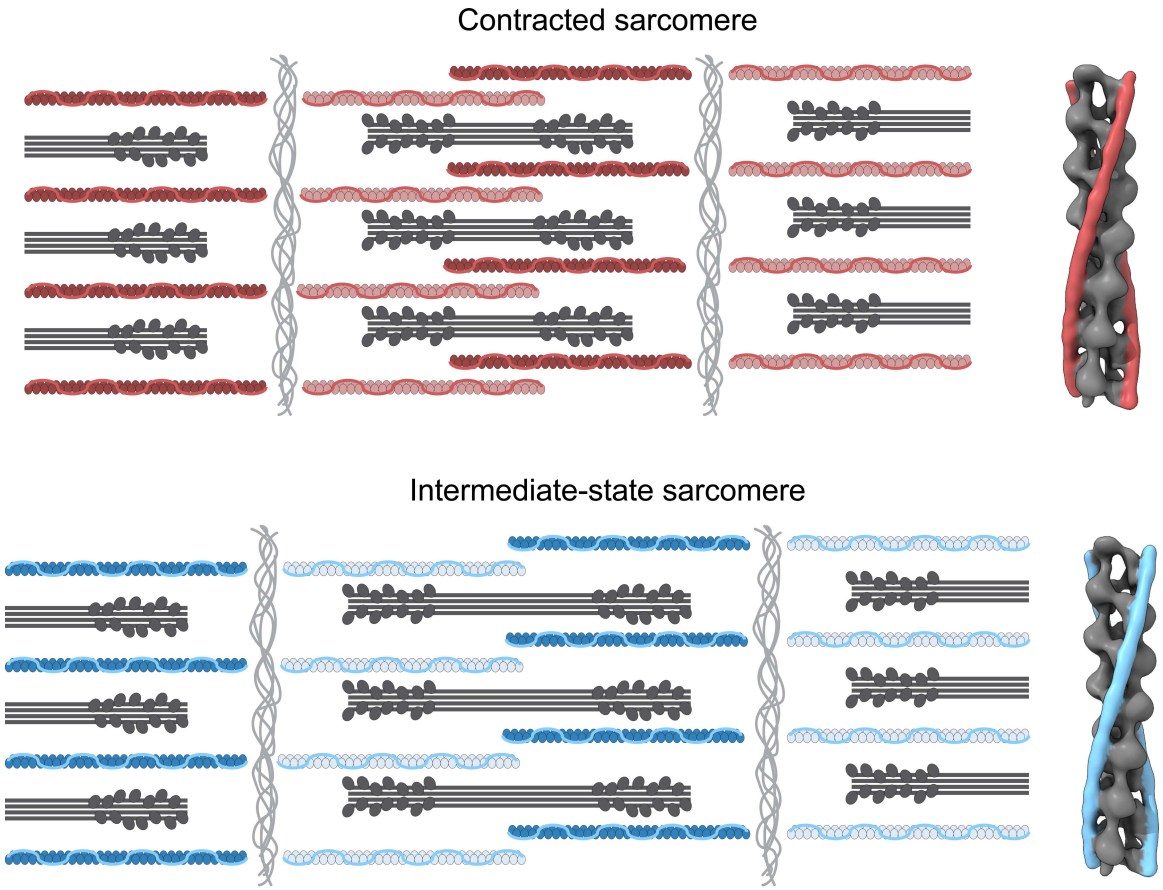

Figure 49: Sarcomere organization during sarcomere contraction. Top: In a contracted sarcomere, thin filaments overlap strongly at the M-line, and are found in the Myosin state, allowing strong actomyosin interaction. Bottom: In a less contracted sarcomere, thin filaments barely overlap at the M-line, and the corresponding thin filament structure is in an intermediate state, permitting weaker actomyosin interaction.

While these studies focused primarily on the thin filament structure, a recent study from the same laboratory resolved the molecular architecture of thick filaments within cardiomyocytes and provided structural details on the arrangement of thick filaments, including myosin heads, MyBP-C and titin [238]. This is particularly interesting, as previous efforts to obtain a structure of the thick filament using subtomogram averaging resulted in low-resolution and badly resolved structures due to the flexibility of the myosin tails.

Finally, a first description of the human cardiac sarcomere architecture using cryo-ET was published, where the authors developed a platform based on human induced pluripotent stem cell-derived cardiomyocytes [241].

Combining all cryo-ET studies on the sarcomere, the molecular sociology of the major sarcomere proteins is close to complete and an integrated functional understanding of sarcomere contraction is soon to be obtained. Future experiments will likely focus on complex samples, such as tissues and study sarcomere architecture across multiple cells [237].

5.3 Subtomogram averaging and polarity determination of filaments

A major contribution of this work is the presentation of a workflow to confidently determine the polarity of actin filaments in a complex 3D network. The workflow is based on subtomogram averaging which actin networks are ideally suited for [29]. They are present in multiple copies and various orientations throughout the search volume. At the beginning of the work, there was no literature on the determination of actin polarity in cells. For microtubules, filament polarity can be determined from the protofilament orientation in cross-sections, as the filaments are sufficiently large [242]. Actin filaments are much smaller and consequently, the twist cannot be confidently estimated from a single slice.

In SPA, actin polarity is dissected by employing a bimodal search algorithm, which searches locally around a given orientation but simultaneously performs the same search with opposite orientation to find the correct alignment parameters [243]. However, this requires high resolution information, posing a limitation for its applicability in tomograms. In addition, template matching methods are possible, including 2D template matching [244], where a high-resolution template is employed that allows to discriminate the polarity, and the highest scoring peaks are extracted, as those are most likely to conform with the correct orientation.

While these approaches might be ideally suited to obtain high-resolution information, they primarily retrieve structural information of a subset of all filaments. In this work, the goal was to generate a complete structural picture of all the filaments involved in the network, a concept often referred to as "molecular sociology". By employing the 3D information per filament, the polarity of filaments in all orientations could be retrieved, including the upright ones in the podosome core.

Another approach has emerged in the past years to dissect actin filament polarity, based on projecting filaments in 2D and treating them as single-particle data [232]. While this approach is not problematic as 2D classification to remove junk particles and returning to the corresponding 3D volumes for subsequent averaging, it creates issues when projecting the particles back in 3D. An important distinction is whether the particles are pre-rotated before projection or whether the original orientation is maintained. The latter is plausible, as all projections align with the missing wedge, and the process is a simple re-projection of the back-projected tilt series. Nevertheless, this version is limited by filament orientation, as upright filaments appear significantly different when projected compared to a flat filament. Therefore, this approach is suited for networks with flat geometries, such as the sarcomere.

In contrast, when the particles are pre-rotated prior to projecting them, this alters their orientation to the missing wedge. In fact, particles within a tomogram are not uniformly sampled and thus do not conform to a true representation of the original particle. As before, when rotating an upright filament to match the orientation of a flat filament, both particles will strongly differ from each other, despite being the exact same molecule. Again, this effect might be less significant if most filaments are in similar orientations, such as the sarcomere. Nevertheless, a 3D approach is to be favored as it avoids the possibility of introducing additional artifacts.

Chapter 6: Methods

6.1 Cell culture and vitrification

Isolation, differentiation, cultivation, and vitrification of human macrophages were performed by Stéphanie Balor at the Center for Integrative Biology (CBI), Toulouse and Javier Ray-Barroso at the Institute of Pharmacology and Structural Biology (IPBS), Toulouse.

Isolation and cultivation of neonatal rat cardiomyocytes were performed by Sarah Scholze and Ralph Böttcher in the Department of Molecular Medicine at the Max Planck Institute of Biochemistry, Martinsried. Vitrification was performed by Laura Burbaum from the Department of Cellular and Molecular Biophysics at the Max Planck Institute of Biochemistry, Martinsried.

6.1.1 Differentiation and culture of primary human monocyte-derived macrophages

Human peripheral blood mononuclear cells were retrieved from the blood of healthy donors. Isolation of monocytes was achieved by centrifugation through Ficoll-Paque Plus (Dutscher), followed by resuspension in cold phosphate buffered saline (PBS) supplemented with 2 mM EDTA and 0.5% heat-inactivated Fetal Calf Serum (FCS) at pH 7.4. Monocytes were magnetically sorted with magnetic microbeads coupled to antibodies directed against CD14 (Miltenyi Biotec #130-050-201), before seeding in six-well plates in RPMI 1640 (Invitrogen) without FCS at 1.5 x 10^6 cells per well. Upon incubation at 37° C in a humidified atmosphere with 5% CO_2 for 2h, the medium was replaced by RPMI supplemented with 10% FSC and 20 ng/mL of Macrophage-Colony Stimulating Factor (M-CSF, Peprotech). Cells were harvested at day 7 using trypsin-EDTA (Fisher Scientific), followed by centrifugation at 320xg for 10 min.

Gold EM grids with Quantifoil R1/4 holey carbon film (Quantifoil MicroTools GmbH) were glow-discharged in an EasiGlow (Pelco) glow discharcing system, followed by grid sterilization under UV light. Cells were seeded onto the grids, followed by incubation for 2 h at 37° C to allow them to adhere to the grids. Grids were then subjected to vitrification.

6.1.2 Cell unroofing

For the two major datasets, macrophages plated on grids were mechanically unroofed prior to vitrification. Cells were unroofed at 37° C using distilled water containing cOmplete protease inhibitor (Roche), 10 µg/mL phalloidin (Sigma-Aldrich P2141). Cells were maintained in this solution for 30s, followed by multiple rounds of flushing and applying a mechanical force to remove the dorsal membrane. Cells were then fixed for 10 min in a 3.7% (weight/volume) solution of paraformaldehyde (PFA, Sigma Aldrich 158127) in PBS and subsequently subjected to plunge-freezing.

A second dataset was acquired on unroofed macrophages. Here, the unroofing mix did not contain PFA. In addition, the grids were functionalized with fibrinogen. Fibrinogen was added at 100 mg/mL in PBS and grids were incubated overnight at 4° C. The solution was removed and replaced by PBS and washed twice to remove and excess fibrinogen. PBS was replaced by the medium including the cells as outlined above.

6.1.3 CK666 treatment prior to unroofing

For the dataset investigating Arp2/3 inhibition, cells were treated with 25 μM CK666 (Abcam ab141231) for 30 min prior to unroofing.

6.1.4 Vitrification of human macrophages

Grids were plunge-frozen using a Leica EM-GP automatic plunge freezer, set at 20° C and 95% humidity. Excess solution was blotted away for 10-14s using Whatman filter paper no. 1, and grids were immediately flash frozen in liquid ethane cooled at -185° C.

6.1.5 Isolation of ventricular cardiomyocytes from neonatal rats

The housing and use of laboratory animals at the Max Planck Institute of Biochemistry are fully compliant with all applicable German and EU laws and regulations regarding the care and use of laboratory animals (e.g., German Animal Welfare Act, or Annex III of Directive 2010/63/EU on the protection of animals used for scientific purposes). All animals were handled in accordance with the approved license (No.5.1-568 – rural districts office).

The rats were housed under pathogen-free conditions at RT and 45-65% humidity. They were exposed to 12 h of daylight, and had continuous access to drinking water and standard rodent food. Neonatal rat ventricular cardiomyocytes were isolated from 3-day old (P3) WT Wistar rats of both sexes. In brief, rats were killed by decapitation, followed by removal of the heart and subsequent transfer to PBS. The ventricles were chopped and digested with Neonatal Heart Dissociation kit (Miltenyi Biotec). Upon enzymatic digestion, followed by sieving using a 70 μm cell strainer and centrifugation at 300g for 15 min, the cell pellet was resuspended in cardiomyocyte medium, consisting of a 1:1 mixture of Dulbecco's modified Eagle medium and Ham's F12 medium (Life technologies, #31330-038) containing 5% horse serum, 5% fetal calf serum, 20 μM Cytarabine (Ara-C, Sigma Aldrich #C1768), 3 mM sodium pyruvate (Sigma #S8636), 2 mM L-glutamine (Thermo Fisher Scientific, #25030-081), 0.1 mM ascorbic acid (Sigma #A4034), 1:200 insulin-transferrin-selenium-sodium pyruvate (Invitrogen #51300044), 0.2% bovine serum albumin (BSA, Sigma Aldrich #A7409) and 100 U/mL penicillin-streptomycin (Thermo Fisher Scientific, #15140122). To reduce the number of fibroblasts, the resuspension was incubated on a non-coated cell culture dish for 90 min, and the supernatant was centrifuged at 300g for 15 min again. Cells were then resuspended in cardiomyocyte medium.

Gold EM grids with Quantifoil R2/1 holey carbon film (Quantifoil Micro Tools GmbH) were glow-discharged, sterilized by UV irradiation for 30 min, and coated with 10 μg/mL fibronectin (Merk #341631). Grids were placed in 35 mm Petri dishes containing 1.5 mL of cardiomyocyte medium and 300 μL of cell suspension, followed by incubation at 37° C in 5% CO_2 for 48 h.

Plunge-freezing was conducted using a Vitrobot Mark IV (Thermo Fisher Scientific) with 80% humidity and 10s blotting from the back side to remove excess liquid, followed by immediate freezing in a 2:1 ethane/propane mixture at -185° C.

6.2 Cryo-FIB milling

6.2.1 Cryo-FIB milling of human macrophages

Plunge-frozen grids were clipped into Autogrids with regular cutout for subsequent cryo-FIB milling, or into Autogrids with extra-wide cutout, to accommodate shallower milling angles. Lamella preparation was conducted by cryo-FIB milling in an Aquilos 2 dual-beam FIB/SEM system operated at liquid nitrogen temperatures. Grids were sputter-coated using 30 mA for 30 s at 10 Pa. Suitable cells for wedge-milling were selected and a rectangular void was milled through the carbon support behind the rear of the cell by positioning the grid orthogonal to the ion beam. Wedge-milling was conducted at shallow angles of 9-12°, corresponding to effective milling angles of 2-5°. Rough milling was conducted using beam currents of 300 pA to remove material from the top. Successively the current was reduced while the milling progressed and the final polishing step was carried out at 30-50 pA. Wedge thickness was estimated from SEM images taken at 5 kV.

6.2.2 Cryo-FIB milling of neonatal rat cardiomyocytes

Cryo-FIB milling of neonatal rat cardiomyocytes was performed by Laura Burbaum.

Plunge-frozen grids were clipped into Autogrids with cut-out for subsequent cryo-FIB milling, before mounting them into a custom-built FIB shuttle cooled by liquid nitrogen, which was transferred using a cryo-transfer system (PP3000T Quorum Technologies). The grids were sputter-coated with platinum in the prep-chamber at 30 mA for 30 s using inorganic platinum. The grids were then loaded onto the cryo-stage of a dual-beam Quanta 3D FIB/SEM (Thermo Fisher Scientific) system operated at liquid nitrogen temperatures. To reduce curtaining artifacts, grids were also sputter-coated with organometallic platinum using a gas injection system operated at 26° C for 8 s. Lamellae were prepared at stage tilts of 18-20°, corresponding to 11-13° effective milling angles. Milling was conducted using a gallium beam at 30 kV and 8-12 µm wide lamellae were generated in a step-wise fashion, starting from high currents of 0.5 nA for rough milling and reduced iteratively to 30 pA for fine milling and polishing until a final thickness of <200 nm. Concomitantly, the milling process was monitored through the SEM beam at 5 kV and 11.8 pA. For Volta Phase Plate (VPP) imaging, the thin lamellae were sputter-coated again with a platinum layer in the Quorum prep-chamber at 10 mA for 3 s [17]. A total of eight lamellae from randomly selected cells were included in the dataset that was analyzed for this study.

6.3 Tilt series acquisition

The *in situ* data, the first unroofed macrophages dataset, and the CK666-treated unroofed dataset, were acquired on system 1, consisting of a Titan Krios G2 transmission electron microscope (Thermo Fisher Scientific) equipped with a 300 kV field-emission gun, VPP, post-column energy filter (Gatan), and a 4k K2 Summit direct electron detector (Gatan). Data was acquired using SerialEM [245]. Low-magnification images were acquired at a nominal magnification of 6,500x to select suitable areas for acquisition, and high-magnification tilt series were acquired at a nominal magnification of 42,000x, corresponding to a pixel size of 3.42 Å. Tilt series were acquired from -60° to +60°, at 2° increments and a dose-symmetric tilt

scheme. The total dose was between 150-200 $e^-/Å^2$, and the target defocus was varied between -3 μm to -5 μm.

The second dataset of unroofed podosomes was acquired on system 2, composed of a Titan Krios G4 transmission electron microscope (Thermo Fisher Scientific) equipped with a cold-FEG operated at 300 kV, Selectris X energy filter (Thermo Fisher Scientific), and a Falcon 4i direct electron detector (Thermo Fisher Scientific). Data collection was carried out in EER format using Tomo5 software (Thermo Fisher Scientific) [55]. Overview montages were acquired at a nominal magnification of 11,500x, and tilt series were acquired at a nominal magnification of 64,000x, corresponding to a pixel size of 2.06 Å. Acquisition was conducted from -54° to +54° and 2° increments, using a dose-symmetric tilt scheme, and the total dose was 190-200 $e^-/Å^2$. The target defocus was varied between -2.5 μm and -4.5 μm.

The sarcomere dataset was acquired on system 1. Data acquisition was carried out from -50° to +70° in 2° increments, using a 10° pre-tilt to account for the lamella geometry. The total dose was kept between 100-120 e^-/A^2 and the target defocus was set between -3.25μm to -5 μm. Three tilt series used for the packing analysis were acquired unidirectional, and using the VPP and a target defocus of -0.5 μm. Data acquisition for the sarcomere project was performed by Laura Burbaum.

6.4 Tomogram reconstruction

Reconstruction of tomograms for the sarcomere dataset was conducted by Laura Burbaum.

The *in situ* dataset, the first dataset of unroofed podosomes and sarcomere dataset were reconstructed using the TOMOMAN package as follows [65]. Frames were aligned using MOTIONCOR2 [54], while stacks with odd and even frames were generated separately for subsequent denoising. Aligned tilt series were then manually inspected and bad tilts were removed. Subsequently, tilt series were dose-weighted, based on a cumulative dose dependent attenuation filter described previously, using critical exposure constants determined for single-particle cryo-EM [56-58]. Tilt series were binned 4x and aligned in IMOD using 10nm gold beads as fiducials for the unroofed dataset, and using patch-tracking for the sarcomere dataset [68,69]. Based on the aligned tilt series, defocus estimation for tilted images of the podosome dataset was carried out using tiltctf as part of the TOMOMAN package [65]. Defocus estimation of the sarcomere dataset was carried out using gctf, while excluding the VPP tilt series [246]. For subtomogram averaging, tomograms were 3D CTF corrected using novactf using phase-flip correction and 15 nm step size [64].

The second dataset of unroofed podosomes was reconstructed using the TOMOMAN package as follows[65]. Individual EER fractions were summed to frames, so that each frame contained approximately 0.1 $e^-/Å^2$. Frames were aligned using relion v4.0 and its implementation of MOTIONCOR2, generating stacks with odd and even frames as well [54,103]. Manual inspection to remove bad tilts was followed by exposure-filtering as described in the paragraph above. Tilt series were aligned using ARETOMO using cubical reconstruction initially to determine tomogram thickness, followed by reconstruction into final thickness[247]. Defocus parameters for each tilt image were estimated using tiltctf as part of the TOMOMAN package, based on the alignment parameters from ARETOMO [65]. For subtomogram averaging, tomograms were 3D CTF corrected using novactf, as described above [43].

6.4.1 Denoising

Motion-corrected stacks were split into odd and even frame stacks, either using custom MATLAB (The MathWorks) scripts, or by employing the functionalities in MOTIONCOR2 and relion-4.0 [54,103]. This way, for both odd and even tilt series, all tilt angles are preserved, rather than the typical approach of splitting the dataset in odd and even tilt images. Tilt series were aligned using the same alignment file from the full tilt series alignment and dose-weighted as described above. Odd and even tomograms were reconstructed at bin4 without CTF correction. The two tomograms were used as input for training using cryoCARE, where each tomogram was trained and denoised independently, using the following parameters [76]. The box size for training was set to 72, depth 3, train steps per epoch 75, batch size 16 and 1200 training volumes.

For visualization of the sarcomere tomograms in the original publication, contrast enhancement was conducted by applying a deconvolution filter [248]. The tomograms displayed in this thesis were denoised using cryoCARE, as described above.

6.4.2 Missing wedge reconstruction

To account for artifacts in the reconstruction introduced by the missing wedge, typically manifested in an elongation along the Z-axis, tomograms were missing wedge-corrected using IsoNET v0.1 [48]. Denoised tomograms were deconvolved with a Signal-to-Noise ratio falloff of 0.7 and deconvolution strength of 1. Deconvolved tomograms were masked with a mask density percentage of 50 and a mask standard percentage of 50. For each tomogram, between 100-300 subtomograms were extracted using a box size of 64. Training was conducted for 30 iterations, with additional noise modeling starting at iteration 10 at 0.05, and increasing to 0.2 at iteration 25.

6.5 Tomogram segmentation

6.5.1 Membrane segmentation

Segmentation of membranes was conducted as follows. For the original publication of the sarcomere, membranes were generated using TomosegmemTV using 4x binned data [249]. The initial segmentation was manually curated in Amira [250]. This segmentation was performed by Laura Burbaum.

For the purpose of displaying in this thesis, all membranes (including the sarcomere tomograms) were traced using the deep learning-based software Membrain v2 and the general model (v10) [95]. Clean-up of the segmentations was conducted in USCF Chimera and MATLAB 2022a (The MathWorks) [251].

6.5.2 Filament segmentation

Segmentation of thin and thick filaments for the sarcomere project was conducted by Laura Burbaum.

Filament centerlines were traced semi-automatically in Amira [91]. Denoised and 4x binned tomograms were filtered again using a non-local means filter in GPU standard mode on xy planes, with a search window of 21 pixels, local neighborhood of 3 pixels and a similarity value of 0.8, or with a search window of 10 pixels, local neighborhood of 3 pixels and similarity value of 0.6. Cylinder correlation was conducted by generating a featureless cylinder with the appropriate dimensions to perform subsequent correlation on the search volume. The following parameters were chosen for actin: cylinder length 420 Å or 360 Å, angular sampling 5 degrees, mask radius 80 Å, outer cylinder radius 40 Å, and using missing wedge correction. For thick filaments, the mask radius was set to 180 Å and a cylinder radius of 90 Å was used. The minimum seed correlation and minimum continuation quality values of the trace correlation lines module were estimated from orthoslices of the resulting correlation volume, defining start and end parameters for the tracing, respectively. The direction coefficient was set to 0.3, minimum distance was set to the cylinder diameter and minimum length was kept at 420 Å or 720 Å. The search cone parameters were kept at default values. Obvious false-positive hits, such as membranes, and upright filaments outside the core were removed within Amira. The centerline coordinates were exported as xml file for subsequent processing in MATLAB (The MathWorks).

6.5.3 Frangi filtering

To obtain a close-to noise-free version of the tomogram, containing only actin filament, Frangi filtering was employed, using a previously described MATLAB (The MathWorks) implementation [74,252]. The missing wedge-corrected tomogram served as basis, and the tomogram was filtered in 2D using xy slices. The scale range was set to [0 1], the scale ratio to 0.1, the factors $\beta 1$ and $\beta 2$ were set to 0.5 and 15, respectively. Each slice was subsequently stacked together to obtain a complete 3D volume which was binarized.

6.5.4 Estimation of missed filaments

The segmented and resampled filament coordinates were employed to generate a binary filament mask. Accordingly, for every sampling point a sphere with a radius of 5 pixels, corresponding to approximately 7 nm, was placed into an empty volume. The volume was binarized. The Frangi-filtered volume and the filament mask were multiplied, and the resulting volume was subtracted from the Frangi-filtered volume to retain those filaments which were not accounted for in the filament segmentation.

6.6 Subtomogram averaging of filaments

6.6.1 Filament resampling

Centerline coordinates obtained from Amira were resampled using custom MATLAB (The MathWorks) scripts as follows [86,91]. Xml files were parsed into csv table format, containing filament ID, point coordinates and point ID within the respective filament. The initial resampling is based on the equidistant resampling approach described previously [231], and was modified as described in the publication on the sarcomere [86]. The equidistant resampling was conducted at a spacing of 13.8 Å which corresponds to half the distance of an actin monomer, effectively leading to 2x oversampling. This is required for the subsequent subtomogram averaging approach to obtain the refined positions of all actin monomers. To ensure filaments point toward the same direction, principal component analysis was conducted. For the podosome, the 3rd principal component was used to align the filaments, as it usually corresponds with the z axis. Cartesian coordinates (x, y, z) were obtained for each point by calculating the vector between adjacent sampling points. (x, y, z) were then transformed to spherical coordinates azimuth and elevation, using the four quadrant arctangent of (y,x) and (z, $\sqrt{(x^2+y^2)}$), respectively. Azimuth corresponds to the counter-clockwise angle in the xy plane, and elevation angle refers to the elevation from the xy plane. Both angles were then converted to Euler angles Ψ,Θ following the zxz-convention. The first Euler angle Φ was randomized every 30°, as it cannot be calculated directly from spherical coordinates. This resampling approach results in the Z-axis being aligned with the principal filament centerline, and the in-plane angle Φ describing the helical twist of the filament. Finally, each sampling point from a respective filament was attributed a unique filament identifier. The resampled parameters were combined into a STOPGAP readable star file, and used for subsequent subtomogram averaging and quantitative analysis [97].

6.6.2 *De novo* reference generation - Podosome

Since the filament polarity is not confidently known and there is no clear pattern of uniform orientation, each filament had to be averaged independently. The workflow is also outlined in Figure 21. 57 filaments from a single tomogram which each contained more than 400 sampling points were selected for *de novo* reference generation. This corresponds to a cutoff of 550 nm in length. 27550 subtomograms were extracted at 2x binning (pixel size 6.84 Å) and a box size of 128 pixels, accommodating sufficient actin subunits for the alignment. Particles for each filament were aligned and averaged independently in STOPGAP using multi-class alignment [97]. The starting references were obtained by averaging all particles together. Due to the in-plane randomization of Φ, the references resembled cylinders. As particle numbers were low for each class, the starting averages were smoothed with additional C6 symmetry applied. A featureless cylinder was used as alignment mask. Initial alignment was conducted using global alignment of in-plane angle at 10° increments and the lowpass filter was set to 40 Å. For global alignment, hill climbing was chosen rather than stochastic hill climbing in order to find the highest-scoring orientation in each iteration. Full cone search was conducted subsequently, restricted to a local search space of ±16°. From these 57 averages, 16 showed the emergence of a helical pattern. Accordingly, these filaments were selected for further processing. 8193 subtomograms were extracted using unbinned data and a box size of 128 pixels. Particles from each filament were further refined separately. Global search of the in-plane angle Φ was conducted for 4 iterations at 4° increments, followed by 4 iterations at 2° increments, and local cone search of all Euler angles was conducted within a range of ±8°. The

best resolved filament structure was determined and used as input for supervised classification. A second reference of opposite polarity was generated by rotation the filament structure by 180°. Supervised classification was conducted using multi-reference alignment with local in-plane refinement and a final round of cone search of all Euler angles. The lowpass filter for classification was set to 30 Å. The two averages obtained after classification were used as input for a first round of polarity assessment as outlined below. Around 50% of the particles were confidently assigned. The particles of opposite polarity were rotated by 180° and aligning them to the other polarity, followed by averaging them together using local alignment to obtain a single reference. This improved reference was then used as input for another round of polarity assignment, including those that were previously not assigned. The improved reference allowed for all 16 filaments to be confidently assigned a polarity. Those with opposite polarity were rotated by 180° and a final round of refinement was conducted to obtain a structure of uniform polarity. This structure was then used to determine the polarity of 5 tomograms to assess the robustness of the workflow.

6.6.3 *De novo* reference generation – sarcomeric thin filament

84 thin filaments located within the same bundle on one side of the Z-disc were selected for *de novo* reference generation. The respective filaments are shown in Figure 42. These filaments are known to share the same polarity. The initial sampling was conducted in a way that all filaments share the same orientation with respect to the Z-disc. From these filaments, 20,259 subtomograms were extracted at 2x binning (pixel size 6.84 Å). The box size was 128 pixels to accommodate sufficient helical turns for the initial alignment. A starting reference was generated by averaging all particles together, and, due to the in-plane randomization, the structure resembled a featureless cylinder. Initially, multiple rounds of global alignment of the in-plane angle Φ were conducted, followed by local searches of all Euler angles. Shifts were limited to 13.8 Å in each direction along the filament to prevent particles from drifting to non-adjacent positions and therefore skipping individual monomers. The iterative alignment resulted in the emergence of a helical pattern. Aligned particles were re-extracted using unbinned data, but keeping the box size of 128 pixels constant. The sequence of global Φ search followed by local refinement of all Euler angles was iterated several times. The refined structure was resolved at 20.7 Å and was used as input for the polarity determination workflow, as outlined below.

6.6.4 Polarity determination

The polarity determination workflow is based on a multi-reference alignment in STOPGAP [86,97]. It was conducted using 2x binned particles (pixel size 6.84 Å) and a box size of 64. Particle lists are converted to multi-entry lists with two entries per particle, allowing to store the alignment information for both orientations. Input references are obtained *de novo* as outlined above. However, in principle also structures derived from EMDB or from pdb structures may be usable. The input structure is rotated by 180° to obtain a second reference with opposite polarity. Alignment in each round was conducted against the initial references, avoiding local minima from incorporating falsely aligned filaments. The essential alignment parameters are outlined below. The initial polarity assignment was conducted for six iterations, starting with two iterations of global in-plane alignment, two iterations of local out-

of-plane cone search, and two more iterations of global in-plane search. Out-of-plane search can be performed locally, as the initial orientation from the filament segmentation is already close to the true solution. For all search steps, regular hill climbing was conducted, as well as exposure, CTF, cosine, and score weighting. The FFT threshold was set to 800. Importantly, the subtomo mode suffix "_1" forces the alignment algorithm to use the average from the first iteration as reference. As this input corresponds to the *de novo* reference, this structure is exclusively used for alignment. The lowpass of 18 Fourier pixels corresponds to a resolution of 24 Å.

Table 1: Key STOPGAP alignment parameters for the initial polarity determination workflow.

iteration	subtomo mode	search mode	angular increments	iterations	phi angular increments	phi iterations	low pass
1	ali_multiref_1	hc	0	0	4	45	18
2	ali_multiref_1	hc	0	0	4	45	18
3	ali_multiref_1	hc	2	4	0	0	18
4	ali_multiref_1	hc	2	4	0	0	18
5	ali_multiref_1	hc	0	0	4	45	18
6	ali_multiref_1	hc	0	0	4	45	18

These parameters were used for the sarcomere polarity determination, as well as the polarity assignment of 5 tomograms containing podosomes. From these tomograms, a refined and high-resolution subtomogram average was obtained. For the remaining podosome tomograms, this structure was used as input reference. To speed up calculations, instead of two iterations per alignment step, only one was conducted. Furthermore, the number of sampling points per filament was reduced to 100 particles which were randomly selected.

Subvolumes close to the filament edge that do not comprise a full filament within its box anymore, were not considered. Likewise, if a filament was shorter than 100 particles, the entire filament was evaluated. The lowpass filter was set to 29 Fourier pixels which corresponds to a resolution of 15 Å. As the input structure is of high resolution, and the alignment is not considered for downstream processing except for the polarity, the lowpass filter can be set accordingly.

Table 2: Key STOPGAP alignment parameters for the improved polarity determination workflow.

iteration	subtomo mode	search mode	angular increments	iterations	phi angular increments	phi iterations	low pass
1	ali_multiref_1	hc	0	0	4	45	29
2	ali_multiref_1	hc	2	4	0	0	29
3	ali_multiref_1	hc	0	0	4	45	29

The final particle list contained the alignment information and scores for both orientations. For each filament, the respective scores were grouped and compared. To evaluate their difference statistically, paired Student's t-test was performed for each filament. As the scores within each filament approximately follow a normal distribution, the t-test to compare the means was considered appropriate. If the respective p-value was less than 5%, the scores were considered as statistically significant and the higher scoring orientation was assigned as the correct polarity. Of note, other statistical tests were also employed initially that lead to very similar results. Filaments with statistically significant polarities were combined by

rotating all initial particle orientations of the opposite polarity by 180°. As such, a starting particle list with correct polarity was obtained.

For the second run with improved parameters, the unassigned filaments were evaluated for another round. Instead of limiting the search points to 100 per filaments, all particles within the respective filaments were considered. If additional filaments were then considered statistically significant, those were added to the final particle list.
The success rate was determined as the amount of confidently assigned filaments in comparison to all filaments of the respective tomogram.

6.6.5 Subtomogram averaging of actin

All subsequent processing was performed using STOPGAP, v0.7.0 [97]. Subtomogram averaging was performed on a total of 7 tomograms to assess the reliability of the polarity determination workflow. Those seven tomograms contained a total of 1,873,144 particles. Due this size, averaging could not be performed at once, as it would lead to memory issues. Therefore, the initial averaging steps were conducted per tomogram, starting from 2x binned tomograms, and using a box size of 64 pixels. Employing the *de novo* reference as starting model, lowpass filtered to 40 Å, global alignment was first performed for the in-plane Φ angle using 4° steps, followed by local alignment of the out-of-plane angles, another round of in-plane refinement using 2° steps, and a final round of local alignment of all Euler angles within a range of ±8°. The lowpass filter was increased iteratively according to the obtained resolution, until 25 Å for the final alignment. For all iterations, the shifts were limited to ±13.8 Å along the filament axis, to prevent particles from converging to non-neighboring positions. Subsequently, distance cleaning was conducted per filament using a threshold of 20.7 Å, corresponding to 1.5x the oversampling distance. Accordingly, only one sampling point per monomer was retained, leading to a total of 814,503 particles. However, as this number of particles was still too large to be combined, only 4 tomograms were selected for further processing, with a combined 445,636 particles. Additionally, particles were split into half sets. As individual boxes overlap, this could lead to artificial boosting of the FSC, if neighboring particles were put into opposing halfsets. Therefore, particles were separated per filament using a STOPGAP accessory script, written by Ricardo Righetto [253]. The in-plane angle Φ was aligned locally within ±8°, followed by local refinement of the out-of-plane angles within ±8° and another round of local alignment of the Φ angle. For eight more iterations, all Euler angles were refined together within a ±4° range, while successively increasing the lowpass filter according to the obtained resolution.

Particles were re-extracted at bin1 and a box size of 128 pixels. Particles were aligned for 10 more rounds using full cone search of all Euler angles, starting from a range of ±8° until a range of ±1° with 0.25° steps. The lowpass filter was set accordingly for each iteration. The refined structure was used to obtain a binary body mask using *relion_image_handler*. The body mask was multiplied by a sphere with substantial attenuation drop-off, to minimize the mask artefacts along the filament axis. This mask was used to calculate the final resolution of the structure using FSC. Concomitantly, the final structure was sharpened by a B-factor of -1000 Å^2, and the average was resolved to a resolution of 8.8 Å. For this structure and for the unsharpened average, a radially averaged power spectrum was calculated using MATLAB (The MathWorks).

6.6.6 Subtomogram averaging of thin filament

Subtomogram averaging of the thin filament was conducted in a similar way as outlined above. 409,896 subvolumes were extracted using 2x binned data and a box size of 64 pixels. The *de novo* structure of the thin filament was used as starting reference, using a lowpass filter of 40 Å. Initially, the in-plane angle Φ was aligned independently using global alignment, followed by local refinement of all Euler angles in a range of ±8°. Shifts were limited to ±13.8 Å along the main filament axis during refinement. Distance cleaning was conducted as above, leading to 160,617 particles, followed by splitting the dataset into half sets. To assess the position of Tpm azimuthally with respect the actin filament core, the corresponding density was removed from the average using USCF Chimera and the *split_by_color_zone* tool [251]. Each tomogram was then aligned separately against this reference, using global alignment of the in-plane angle, followed by local refinement of all Euler angles within ±8°. Tomograms with structures that returned the same Tpm position were combined, and those examples that contained an M-line in the field of view were kept for generation of the final structure. Accordingly, two tomograms with consistent Tpm position were combined for the final average, corresponding to 56,858 particles. The average was refined using local alignment of all Euler angles, starting from ±8° with 2° increments, to ±3° with 1° increments, and the lowpass filter was adjusted incrementally according to the obtained resolution. The final structures were refined to 15.7 Å, and 17.7 Å for the average in a different Tpm position, respectively, using the FSC=0.143 cutoff. Concomitantly, both structures were sharpened using B-factors of -1300 Å² and -1500 Å², respectively.

6.7 Quantitative analysis of thin filaments

6.7.1 Packing analysis

The packing analysis of the sarcomere dataset was performed by Laura Burbaum, Marion Jasnin, and myself.

Thin and thick filament centerline coordinates were used to analyze the packing of the sarcomere. The analysis is described in Jasnin *et al*. [231] and was adapted to accommodate two types of filaments simultaneously [86]. The quantitative analysis was mainly focused on the A-band, where thin and thick filaments intersect, but did not explicitly remove double-overlap regions around the M-line. However, the overall contribution of these regions is considered small and can therefore be neglected. Nine tomograms were analyzed, containing 4,700 thin and 1,648 thick filaments. For the analysis, the centerline coordinates were resampled every 30 Å, using the script described below.

For the near-neighbor analysis the local direction at each sampling point was calculated to be the local filament tangent. For all points within a given filament, the distance d, and relative orientation θ, were determined with respect to the reference point. Small orientations of $\theta < 10°$ are attributed to equidistant, close-to-parallel filaments. The mean interfilament distance was obtained from the peak maximum, and the range was determined at 2/3 of the peak maximum.

For the local packing analysis, for each point within a given filament the local frame of reference (e1, e2, e3) was defined as follows: e1 is oriented toward the nearest neighbor, e2 points in the filament direction, e3 is defined as the cross-product of e1 and e2. The coordinates of a neighboring position in (e1, e2, e3) conforms to (X, Y, Z). The local frames of reference for

all points were aligned and the occurrences (X, Z) in the e1e3 plane within the distance threshold determined from the near-neighbor analysis were visualized as 2D histogram.

6.8 Quantitative analysis of core filament

Quantitative analysis of core filament parameters was based on the polarity-assessed particle files obtained before subtomogram averaging. All analysis steps were conducted using custom scripts in MATLAB (The MathWorks).

6.8.1 Definition of core filaments

Using a central tomographic slice of the podosome, a polygon was drawn for each podosome as model in IMOD [254]. The polygon should encompass most upright filaments as well as the bulk of the core filaments. The [x,y] polygon coordinates were read into a custom MATLAB (The MathWorks) script, and the positions of all filament coordinates within the boundaries of the polygon were determined using the function *inpolygon*. For each filament, the number of points within these boundaries was determined, and if over 2/3 of the filament was within the boundary, it was considered as core filament. This prevents a harsh cut-off of the core, and ensures that filaments are not split. The podosome center was defined as the arithmetic mean of all core particles.

For the emerging podosome, the core was determined from the filament density alone, as there were no upright filaments present. In a second analysis, the core was defined as a single point in the center of the previous core.

For the neighboring podosome analysis, the second core was projected to be outside of the tomogram boundaries. Accordingly, its position was estimated from the orientation of the radial filaments emerging from it.

6.8.2 Determination of core properties

An ellipse was fit to the polygon points using least squares fitting [255], and the sphericity of the core was determined by calculating the average ratio between the short and long axes. The average of both axes was considered as average core diameter. Core height was determined by taking the Z-coordinates of all core particles and calculating the difference between the minimum and maximum values, while removing the top and bottom 1%, to account for outliers.

6.8.3 Tracing of the ventral membrane

The ventral membrane is inherently difficult to identify in tomograms due to its positioning in the xy plane. As such, it is strongly affected by the missing wedge and difficult to segment. In missing wedge corrected tomograms, it is easier to identify them, but segmentation in xz planes is still very challenging. For these reasons, ventral membrane segmentation was conducted on xy slices. Using IMOD, the traces of the membrane were followed by placing splines along its edges, which were then followed throughout the z axis [254]. Accordingly, several splines with multiple points each were obtained that approximate the location of the

membrane. These points were used to fit a polynomial surface to the data using the *fit* function in MATLAB (The MathWorks) using a second-degree polynomial in x and third-degree polynomial in y, as the tomograms typically contain additional x-tilt. The model is defined as:

$$sf_{x,y} = p_{00} + p_{10} * x + p_{01} * y + p_{20} * x^2 + p_{11} * xy + p_{02} * y^2 + p_{21} * x^2y + p_{12} * xy^2 + p_{03} * y^3$$

The interpolated surface was used to generate a binary, single-pixel thick volume corresponding to the membrane. Using *bwdist*, for each voxel within the tomogram, the closest distance to the membrane was determined.

6.8.4 Fitting plane and determining normal vector

To obtain a reference vector for calculating the filament orientation with respect to the membrane, a plane was fit through the membrane section below the core filament. To determine the boundaries and their corresponding z values, the coordinates from the polygon encompassing the core were projected onto the fitted membrane surface. From this set of 3D points, a plane was fit using the *tom_fit_plane* function from the *tom_toolbox* [82]. The obtained normal vector was used as reference point to calculate the membrane orientation of the filaments.

6.8.5 Determining local orientation and distance

For each core filament, the coordinates of the sampling point closest to the membrane were determined by evaluating the closest distance to the membrane for each point along the filament. The closest distance and the corresponding filament point were stored. The angular information of this point, was used to rotate a unit vector around the z axis. The angle between the obtained rotated vector and the normal vector from fitting a plane through the core membrane was calculated to obtain the filament orientation with respect to the membrane. For each filament, the closest distance and the respective filament orientation were plotted as heat map to reveal sub-categories of core filaments. Filaments with a distance of less than 60 nm and angles with respect to the normal vector of less than 50° were defined as upright filaments, those above 50° but close than 60 nm were defined as shallow core filaments, and filaments above 60 nm were considered as aged core filaments.

6.8.6 Barbed end orientation

For each filament, the orientation of the sampling point closest to the membrane was determined. The angular information of this point was used to rotate a unit vector, and the distance of the new rotated point from the membrane was determined. If the new point was placed closer to the membrane, the filament was considered to have its barbed end toward the membrane, if the rotated point was further away, the pointed end was considered to be placed toward the membrane. Concomitantly, if the difference between both distances was less than 1/6, corresponding to an orientation of ±15°, the filament orientation was considered as flat.

6.9 Quantitative analysis of lateral filaments

Quantitative analysis of lateral filament parameters was based on the polarity-assessed particle files obtained after subtomogram averaging. All analysis steps were conducted using custom scripts in MATLAB (The MathWorks).

6.9.1 Definition of lateral filaments and lateral filament orientation

For each tomogram, the podosome core diameter was determined as described above. For each filament that was not defined as core filament, the closest distance from the podosome center was calculated. If the distance was found to be within 1.25x the core radius, it was considered as lateral filament.

The angular information of the entire filament was employed to rotate a unit vector [0,0,1] along the z axis, by averaging each Euler angle to obtain the general orientation of the filament. The arithmetic mean of the filament was calculated and its distance from the podosome center determined. The rotated unit vector was added to the arithmetic mean and the distance of the new point from the center was calculated. If the distance of the new point was larger than the arithmetic mean of the filament, the filament was considered as radial filament (the definition of radiality is described below), otherwise it was considered as non-radial filament. For each lateral filament, the distance of both filament ends to the podosome core was calculated. Depending on the determined orientation of the filament, these distances were attributed as barbed and pointed ends, respectively.

For the CK666 treated podosomes, where multiple cores were present within the same tomogram, each core was treated individually. As such, several filaments might appear more than once, as they were found to interact with more than one core.

6.9.2 Determination of radial deviation

For each lateral filament, a vector from the podosome center to the arithmetic mean of the filament was evaluated. A unit vector was rotated according to the averaged Euler angles, as described above. The angle between the rotated unit vector and the vector describing the distance between the arithmetic mean of the filament and the podosome center was calculated and described the deviation of the filament orientation from a radial orientation. Therefore, filaments with small angles describe small deviations and are considered as radial, whereas an angle close to 90° is considered as tangential.

6.9.3 Determination of parallel sections

Parallel filament sections were defined for each set of filament modules separately, and subsequently between modules. The local tangent for each point along a filament was calculated as the vector between the points at -5 and +5 position. For the evaluated point, appropriate filaments were determined which were closer than the respective distance threshold. The respective filament IDs were determined. For each neighboring point within the distance criteria, the local tangent was determined. The angle between both tangents was then calculated, and if the deviation was smaller than the angular threshold, the respective points were considered to derive from parallel sections. This procedure was iterated for all sampling points, while ensuring that each parallel section is only evaluated once. The points

located within parallel sections were stored as alternative particle list. For both core and lateral filaments, a deviation of less than 10° was considered as parallel. For core filaments, distance threshold of 15 nm was chosen, for lateral filaments the distance criterion was 20 nm.

To evaluate the parallel sections between different classes, the analysis was performed in a similar way. The search for neighboring filaments was limited to the second filament class that was evaluated. The parallel sections between core filaments were negligible, only antiparallel sections between lateral filaments of opposite polarity contained significant sections and where therefore considered in the analysis.

For quantification of the amount of parallel sections, the number of points derived from parallel sections were compared to the full particle list of the respective filament module.

6.10 Molecular sociology of podosome

Core and lateral filaments were combined, and their refined positions and orientations obtained after subtomogram averaging were used to generate the complete molecular-scale visualization of the podosome shown in Figure 28. The STOPGAP particle files were converted to AV3-style em files [79], which were read by the USCF ChimeraX plugin ArtiaX [256,257]. For each position, the central actin subunit extracted from the obtained subtomogram average of the actin filament was placed into the tomographic volume. The filaments were then colored according to the color code described across this work.

6.10.1 Combined podosome architecture

To analyze the composition of each podosome, the analyzed and classified filament particle lists were combined to obtain a full particle list for each podosome. Cumulative filament length was determined by calculating the distances between adjacent monomers for each filament and summing the total distance. The cumulative filament length for the entire podosome serves as an approximation of the total podosome size. The cumulative filament length for each module was calculated, and the ratio of this length compared to the entire podosome was evaluated for each example. The podosomes were sorted based on total filament length, and each respective module ratio was plotted separately. Linear fits of the evolution of the filament ratios and non-linear fits of the podosome height against filament length analysis were obtained using the *fit* functionalities in MATLAB (The MathWorks).

For the comparison of CK666-treated podosomes, the module ratios were determined as number of filaments, as this allows for an estimation of the total filament nucleation. As the CK666-treated podosomes were smaller than the non-treated examples, the ratios were converted into relative ratios to allow for better comparison.

6.11 Analysis of Arp2/3 complex-mediated branches

6.11.1 Localization of Arp2/3 complex-mediated branches

Template preparation

Template matching (TM) was conducted using STOPGAP, v0.7.0 [97]. A cryo-ET Arp2/3 complex structure obtained from lamellipodia of mouse fibroblast cells (emd-11869) was used as template structure for TM [124]. To reduce template bias, the density corresponding to the ArpC5 subunit was removed from the template using the *Eraser* tool in USCF Chimera. As this density is very pronounced in the structure, only classes where this density remerges will be considered in down-stream processing. A spherical mask was used during TM rather than a tight body mask.

Template matching

Template matching was conducted using STOPGAP v0.7.0 [97], using 8x binned and denoised tomograms (pixel size 15.12 Å). A total of 18 tomograms were matched. As the tomograms were not CTF corrected and the Nyquist frequency was around 30 Å, CTF weighting was omitted during TM, while exposure weighting was performed, as well as noise-correlation and calculation of the Laplacian transform. An angular search step of 15° was chosen, and the template was lowpass filtered to 40 Å.

The resulting score maps were masked to remove the core area to focus on branches in the core periphery, as well as the carbon layer to reduce false-positive hits. Masks were generated in MATLAB (The MathWorks) from model files generated in IMOD, encompassing the core [254]. For each tomogram, the 1000 highest-scoring peaks of the masked score map were extracted, using a distance threshold of 10 pixels and a minimum cluster size of 2. The resulting particle lists were combined into a single particle list, which was employed for averaging. The number of false-positive hits is substantially high, as the branch structure is highly similar to the structure of a bare actin filament, or filaments overlapping in close proximity.

6.11.2 Subtomogram averaging and classification of Arp2/3 complexes

Initial subtomogram averaging and classification were conducted using STOPGAP, v.0.7.0 [97]. 18,000 particles were extracted from 8x binned and non-CTF corrected tomograms using a box size of 64 pixels. Particles were aligned against the template structure used for TM. As the number of false-positive hits was substantial, extensive classification was performed. Based on the pre-aligned particle orientations, classification into 50 classes was conducted with no additional alignment. Starting references were generated over 15 iterations, using Simulated Annealing with a B-factor of 15, which was reduced progressively. Alignment was performed for 20 more iterations until convergence. 8 classes containing appropriate daughter filament density, corresponding to 1600 particles, were selected for further processing. The particles were combined and aligned together for 4 iterations using local alignment within ±8° and 2° increments. Discarded particles were combined and classified again into 50 classes, to ensure no true-positive branches were discarded. 2082 particles showing daughter filament density were selected and combined with the particles from the previous iteration. A second classification was performed using the same parameters as the first classification, but with 8 classes. 4 classes with a total of 700 particles were selected that contained clear density of the

Arp2/3 complex, in particular the ArpC5 subunit, as well as clear discrimination of the actin subunits of the mother and daughter filaments.

Particles were then exported to relion, for additional refinement at higher binning. Starting at 4x binning, one round of 3D refinement was conducted using a body mask around the branch structure. Using 2x binned data, a final round of 3D refinement was conducted, and the post-processed map was considered as final map. It was filtered to 25 Å and sharpened using a B-factor of -1000 Å^2. Additional tilt series refinement in Warp did not improve the resolution and was therefore omitted.

The final structure suffers from preferred orientation, as most branches were found in a flat orientation. The refined Euler angles from STOPGAP were converted to spherical coordinates to generate the orientation heat map displayed in Figure 35.

A pseudo-atomic model of the Arp2/3 complex (pdb 7aqk), containing the complex as well as several monomers of the mother and daughter filaments, was docked into the obtained average using rigid-body fitting in USCF Chimera [124,251].

6.11.3 Quantitative analysis of Arp2/3 complex

Due to low quality of the reconstruction, 3 tomograms were removed, leading to 623 remaining particles from 15 tomograms. The daughter filament vector was calculated as a 70° deviation from the mother filament which was aligned to the x axis, from the branching point to the edge of the box. The branching point was situated at the center of the volume.

For each branch, the vector between the podosome center and the branching point was calculated and converted to a unit vector. The daughter filament vector was rotated according to the refined Euler angles using *tom_pointrotate*. The angle between both vectors was calculated, corresponding to the branch orientation with respect to the podosome core. Furthermore, the length of the vector from the podosome center and the branching point was considered as the distance from the core.

The branching angles for all branches were plotted as histogram (Figure 34). To evaluate the statistical significance of the distribution, p-values were calculated for each bin as follows. From a simulated set of 5000 random distributions of branch orientation (see below), the number of occurrences in which the simulation contained equal or more observations in the respective bin than in the observed distribution, in case of more particles than in the observed distribution, were determined and calculated as p-value, or vice versa if there were fewer particles in the observed distribution.

To visualize the distributions, branches were placed into a 3D volume at their respective location and were colored accordingly, depending on the branching angle from the core.

6.11.4 Simulation of branch distribution

The final particle list containing 623 particles served as basis for the simulation. The Euler angles for each branch were randomized, based on a pre-defined set of Euler angles used for TM. For this particle list, the branch distribution was calculated as described above. This process was repeated for a total of 5000 times. The 5000 distributions were summed, and the mean as well as standard deviation σ were calculated for each bin. For the visualization in Figure 34, the mean and 2*σ were plotted. As the angle between the vector from the podosome

core to the branching point and the daughter filament vector are two vectors in 3D, a random distribution approaches a cosine function. This is in accordance with the observed mean distribution of the simulation.

A second set of simulations was conducted in a similar fashion. Instead of randomizing the Euler angles, the coordinates of the branches were randomized. Two constraints were imposed, the branch had to be within the tomogram boundary, and it had to be outside of the core area that was excluded from the analysis. For each particle list, the distance of the branching point from the podosome center was calculated. The simulation was conducted for 5000 iterations, and the resulting distributions were summed.

6.11.5 Clustering analysis

To analyze potential clustering, the nearest neighbor distances for the first three neighbors were calculated for each branch, and median distances were determined. The analysis was repeated for the 5000 simulated particle lists with random distributions, and the three nearest neighbors were determined. In the split-violin plot in Figure 34, the observed distribution was plotted on the left and compared against the random distribution on the right of the violin, respectively.

6.12 Analysis of actin-associated proteins

6.12.1 Visualization of actin-associated proteins

Actin-associated proteins were identified by eye in denoised and missing wedge-corrected tomograms of unroofed podosomes at higher magnification. Appropriate regions were cropped using MATLAB (The MathWorks). Additional cleaning of the volumes was conducted using USCF Chimera and the *volume eraser* tool. Volumes were visualized as isosurface using USCF ChimeraX [251,256].

6.12.2 Localization of hexagonal complex

A hexagonal complex was identified in the vicinity of the podosome core in several examples. In denoised and missing wedge-corrected tomograms its direct interaction with the plasma membrane could be visualized. A volume around the complex was extracted using MATLAB (The MathWorks). Segmentation of the complex, actin filament, and a putative linker density was conducted in USCF Chimera, and the parts were visualized as isosurface in USCF ChimeraX [251,256].

To obtain a template structure, manual picking was conducted using IMOD [68]. As all complexes were in close vicinity to the membrane, only a few slices per tomogram had to be evaluated. Coordinates were converted to STOPGAP-style star files for subsequent averaging, and particles were extracted using 8x binned data and a box size of 40 pixels [97]. An initial average was obtained from summing over all particles. The average was aligned for four iterations using a range of ±8° and applying C6 symmetry. The structure was used to template match the full data set. For each tomogram, the 100 highest scoring positions were extracted. Particles were extracted at bin 8 and a box size of 40 pixels. All particles were inspected manually, and 331 particles were retained. Particles were exported to Warp, and the

tilt series were reprocessed [248]. Particles were extracted at bin4 and exported to relion v3.1 [62]. Alignment and 3D classification were conducted, resulting in 154 particles. A final round of refinement at bin2 was conducted, and the final structure was symmetrized using C6 symmetry and sharpened using a B-factor of -2000 $Å^2$.

6.13 Visualization

All structures and segmentations were visualized using USCF ChimeraX [256]. Molecular fits were conducted using USCF Chimera [251]. Segmentations were obtained by converting particle lists to *bild* files that were displayed in USCF ChimeraX. For visualization of filament polarity, an arrowhead shaped STL file was created using CAD. This was used as object in the USCF Chimera plugin place_object to visualize filament orientation in 3D [258]. The respective filament modules were visualized and the entire volume was exported as STL file. For each podosome module, STL files were generated and combined to obtain a full representation of the podosome. These were visualized in USCF ChimeraX. The representation containing individual actin monomers instead of arrowheads was generated using USCF ChimeraX plugin ArtiaX [257]. The actin monomer was cropped from the obtained subtomogram average at 8.8 Å resolution, and corresponds to the extracted density in Figure 23C. All plots were generated using MATLAB (The MathWorks).

List of abbreviations

2D	Two dimensional
3D	Three dimensional
A-band	Anisotropic band
ABD	Actin-binding domain
ABP	Actin-binding protein
ADF	Actin-depolymerizing factor
ADP	Adenosyl diphosphate
ARP	Actin-related protein
ATP	Adenosyl triphosphate
CARE	Content-aware image restauration
CC	Cross-correlation
CCC	Constrained cross-correlation
CCD	Charge-Coupled Device
CLEM	Correlative Light Electron Microscopy
CTF	Contrast Transfer Function
DED	Direct Electron Detector
DNA	Desoxyribonucleic acid
DQE	Detective Quantum Efficiency
ECM	Extracellular matrix
EDTA	Ethylenediaminetetraacetic acid
EER	Electron Event Repesentation
EM	Electron microscopy
EMDB	Electron Microscopy Database
ET	Electron tomography
F-actin	Filamentous actin
FCS	Fetal calf serum
FEG	Field emission gun
FH	Formin homology domain
FIB	Focused Ion Beam
FSC	Fourier Shell Correlation
FT	Fourier transform
G-actin	Globular actin
I-band	Isotropic band
M-CSF	Macrophage-colony stimulating factor
MT1-MMP	Membrane type 1 - matrix metalloprotease
MW	Missing wedge
N-WASP	Neural Wiskott-Aldrich syndrome protein
NPF	Nuclear promoting factor
PBS	Phosphate Buffered Saline
PCA	Principle component analysis
PDB	Protein data bank
PFA	Para-formaldehyde
PI	Phosphatidylinositol
PIP	Phosphatidylinositolphosphate
PSF	Point spread function
SD	Subdomain
SEM	Scanning electron microscopy
SNR	Signal-to-noise ratio
SPA	Single-particle analysis
SR	Sarcoplasmic reticulum
TEM	Transmission electron microscopy
TM	Template matching
TPM	Tropomyosin
TPN	Troponin
UV	Ultraviolet
VPP	Volta Phase Plate
WASH	Wiskott-Aldrich syndrome protein and scar homologue
WASP	Wiskott-Aldrich syndrome protein
WAVE	WASP-family verprolin-homologous protein
WBP	Weighted Back-Projection
WRC	WAVE regulatory complex
WT	Wildtype
ZD	Z-disc

Bibliography

1. Watson JD, Crick FH: Molecular structure of nucleic acids; a structure for deoxyribose nucleic acid. *Nature* 1953, 171:737-738.
2. Franklin RE, Gosling RG: Molecular configuration in sodium thymonucleate. *Nature* 1953, 171:740-741.
3. Curry S: Structural Biology: A Century-long Journey into an Unseen World. *Interdiscip Sci Rev* 2015, 40:308-328.
4. Broglie Ld: XXXV. A tentative theory of light quanta. *The London, Edinburgh, and Dublin Philosophical Magazine and Journal of Science* 1924, 47:446-458.
5. Busch H: Berechnung der Bahn von Kathodenstrahlen im axialsymmetrischen elektromagnetischen Felde. *Annalen der Physik* 1926, 386:974-993.
6. Williams DB, Carter CB: *Transmission electron microscopy : a textbook for materials science* edn 2nd. New York: Springer; 2008.
7. Glaeser RM: Specimen Behavior in the Electron Beam. *Methods Enzymol* 2016, 579:19-50.
8. Bragg WH, Bragg WL: The reflection of X-rays by crystals. *Proceedings of the Royal Society of London. Series A, Containing Papers of a Mathematical and Physical Character* 1913, 88:428-438.
9. Franken LE, Grunewald K, Boekema EJ, Stuart MCA: A Technical Introduction to Transmission Electron Microscopy for Soft-Matter: Imaging, Possibilities, Choices, and Technical Developments. *Small* 2020, 16:e1906198.
10. Reimer L, Kohl H: *Transmission electron microscopy : physics of image formation* edn 5th. New York, NY: Springer; 2008.
11. Scherzer O: The Theoretical Resolution Limit of the Electron Microscope. *Journal of Applied Physics* 1949, 20:20-29.
12. Wade RH: A brief look at imaging and contrast transfer. *Ultramicroscopy* 1992, 46:145-156.
13. Abbe E: Beiträge zur Theorie des Mikroskops und der mikroskopischen Wahrnehmung. *Archiv für Mikroskopische Anatomie* 1873, 9:413-468.
14. Knoll M, Ruska E: Das Elektronenmikroskop. *Zeitschrift für Physik* 1932, 78:318-339.
15. McMullan G, Faruqi AR, Henderson R: Direct Electron Detectors. *Methods Enzymol* 2016, 579:1-17.
16. McMullan G, Faruqi AR, Clare D, Henderson R: Comparison of optimal performance at 300keV of three direct electron detectors for use in low dose electron microscopy. *Ultramicroscopy* 2014, 147:156-163.
17. Danev R, Buijsse B, Khoshouei M, Plitzko JM, Baumeister W: Volta potential phase plate for in-focus phase contrast transmission electron microscopy. *Proc Natl Acad Sci U S A* 2014, 111:15635-15640.
18. Schwartz O, Axelrod JJ, Campbell SL, Turnbaugh C, Glaeser RM, Muller H: Laser phase plate for transmission electron microscopy. *Nat Methods* 2019, 16:1016-1020.
19. Kuhlbrandt W: Biochemistry. The resolution revolution. *Science* 2014, 343:1443-1444.
20. Nakane T, Kotecha A, Sente A, McMullan G, Masiulis S, Brown P, Grigoras IT, Malinauskaite L, Malinauskas T, Miehling J, et al.: Single-particle cryo-EM at atomic resolution. *Nature* 2020, 587:152-156.
21. Yip KM, Fischer N, Paknia E, Chari A, Stark H: Atomic-resolution protein structure determination by cryo-EM. *Nature* 2020, 587:157-161.
22. Dubochet J, Adrian M, Chang JJ, Homo JC, Lepault J, McDowall AW, Schultz P: Cryo-electron microscopy of vitrified specimens. *Q Rev Biophys* 1988, 21:129-228.
23. Dubochet J, McDowall AW: VITRIFICATION OF PURE WATER FOR ELECTRON MICROSCOPY. *Journal of Microscopy* 1981, 124:3-4.
24. Cheng Y, Grigorieff N, Penczek PA, Walz T: A primer to single-particle cryo-electron microscopy. *Cell* 2015, 161:438-449.

25. Beck M, Baumeister W: Cryo-Electron Tomography: Can it Reveal the Molecular Sociology of Cells in Atomic Detail? *Trends Cell Biol* 2016, 26:825-837.
26. Turk M, Baumeister W: The promise and the challenges of cryo-electron tomography. *FEBS Lett* 2020, 594:3243-3261.
27. Hart RG: Electron microscopy of unstained biological material: the polytropic montage. *Science* 1968, 159:1464-1467.
28. Medalia O, Weber I, Frangakis AS, Nicastro D, Gerisch G, Baumeister W: Macromolecular architecture in eukaryotic cells visualized by cryoelectron tomography. *Science* 2002, 298:1209-1213.
29. Schneider J, Jasnin M: Capturing actin assemblies in cells using in situ cryo-electron tomography. *Eur J Cell Biol* 2022, 101:151224.
30. Grimm R, Typke D, Barmann M, Baumeister W: Determination of the inelastic mean free path in ice by examination of tilted vesicles and automated most probable loss imaging. *Ultramicroscopy* 1996, 63:169-179.
31. Kuba J, Mitchels J, Hovorka M, Erdmann P, Berka L, Kirmse R, J KO, J DEB, Goetze B, Rigort A: Advanced cryo-tomography workflow developments - correlative microscopy, milling automation and cryo-lift-out. *J Microsc* 2021, 281:112-124.
32. Rigort A, Bauerlein FJ, Villa E, Eibauer M, Laugks T, Baumeister W, Plitzko JM: Focused ion beam micromachining of eukaryotic cells for cryoelectron tomography. *Proc Natl Acad Sci U S A* 2012, 109:4449-4454.
33. Schaffer M, Mahamid J, Engel BD, Laugks T, Baumeister W, Plitzko JM: Optimized cryo-focused ion beam sample preparation aimed at in situ structural studies of membrane proteins. *J Struct Biol* 2017, 197:73-82.
34. Marko M, Hsieh C, Schalek R, Frank J, Mannella C: Focused-ion-beam thinning of frozen-hydrated biological specimens for cryo-electron microscopy. *Nat Methods* 2007, 4:215-217.
35. Wagner FR, Watanabe R, Schampers R, Singh D, Persoon H, Schaffer M, Fruhstorfer P, Plitzko J, Villa E: Preparing samples from whole cells using focused-ion-beam milling for cryo-electron tomography. *Nat Protoc* 2020, 15:2041-2070.
36. Villa E, Schaffer M, Plitzko JM, Baumeister W: Opening windows into the cell: focused-ion-beam milling for cryo-electron tomography. *Curr Opin Struct Biol* 2013, 23:771-777.
37. Berger C, Dumoux M, Glen T, Yee NB, Mitchels JM, Patakova Z, Darrow MC, Naismith JH, Grange M: Plasma FIB milling for the determination of structures in situ. *Nat Commun* 2023, 14:629.
38. Sartori A, Gatz R, Beck F, Rigort A, Baumeister W, Plitzko JM: Correlative microscopy: bridging the gap between fluorescence light microscopy and cryo-electron tomography. *J Struct Biol* 2007, 160:135-145.
39. Schwartz CL, Sarbash VI, Ataullakhanov FI, McIntosh JR, Nicastro D: Cryo-fluorescence microscopy facilitates correlations between light and cryo-electron microscopy and reduces the rate of photobleaching. *J Microsc* 2007, 227:98-109.
40. Arnold J, Mahamid J, Lucic V, de Marco A, Fernandez JJ, Laugks T, Mayer T, Hyman AA, Baumeister W, Plitzko JM: Site-Specific Cryo-focused Ion Beam Sample Preparation Guided by 3D Correlative Microscopy. *Biophys J* 2016, 110:860-869.
41. Klumpe S, Fung HKH, Goetz SK, Zagoriy I, Hampoelz B, Zhang X, Erdmann PS, Baumbach J, Muller CW, Beck M, et al.: A modular platform for automated cryo-FIB workflows. *Elife* 2021, 10.
42. Mastronarde DN: Automated electron microscope tomography using robust prediction of specimen movements. *J Struct Biol* 2005, 152:36-51.
43. Turonova B, Marsalek L, Slusallek P: On geometric artifacts in cryo electron tomography. *Ultramicroscopy* 2016, 163:48-61.
44. Schmid MF, Booth CR: Methods for aligning and for averaging 3D volumes with missing data. *J Struct Biol* 2008, 161:243-248.

45. Knauer V, Hegerl R, Hoppe W: Three-dimensional reconstruction and averaging of 30 S ribosomal subunits of Escherichia coli from electron micrographs. *J Mol Biol* 1983, 163:409-430.
46. Forster F, Hegerl R: Structure determination in situ by averaging of tomograms. *Methods Cell Biol* 2007, 79:741-767.
47. Wan W, Briggs JA: Cryo-Electron Tomography and Subtomogram Averaging. *Methods Enzymol* 2016, 579:329-367.
48. Liu YT, Zhang H, Wang H, Tao CL, Bi GQ, Zhou ZH: Isotropic reconstruction for electron tomography with deep learning. *Nat Commun* 2022, 13:6482.
49. Crowther RA, Derosier DJ, Klug A: The Reconstruction of a Three-Dimensional Structure from Projections and its Application to Electron Microscopy. *Proceedings of the Royal Society of London Series A* 1970, 317:319-340.
50. Hagen WJH, Wan W, Briggs JAG: Implementation of a cryo-electron tomography tilt-scheme optimized for high resolution subtomogram averaging. *J Struct Biol* 2017, 197:191-198.
51. Turonova B, Hagen WJH, Obr M, Mosalaganti S, Beugelink JW, Zimmerli CE, Krausslich HG, Beck M: Benchmarking tomographic acquisition schemes for high-resolution structural biology. *Nat Commun* 2020, 11:876.
52. Brilot AF, Chen JZ, Cheng A, Pan J, Harrison SC, Potter CS, Carragher B, Henderson R, Grigorieff N: Beam-induced motion of vitrified specimen on holey carbon film. *J Struct Biol* 2012, 177:630-637.
53. Campbell MG, Cheng A, Brilot AF, Moeller A, Lyumkis D, Veesler D, Pan J, Harrison SC, Potter CS, Carragher B, et al.: Movies of ice-embedded particles enhance resolution in electron cryo-microscopy. *Structure* 2012, 20:1823-1828.
54. Zheng SQ, Palovcak E, Armache JP, Verba KA, Cheng Y, Agard DA: MotionCor2: anisotropic correction of beam-induced motion for improved cryo-electron microscopy. *Nat Methods* 2017, 14:331-332.
55. Guo H, Franken E, Deng Y, Benlekbir S, Singla Lezcano G, Janssen B, Yu L, Ripstein ZA, Tan YZ, Rubinstein JL: Electron-event representation data enable efficient cryoEM file storage with full preservation of spatial and temporal resolution. *IUCrJ* 2020, 7:860-869.
56. Schur FK, Obr M, Hagen WJ, Wan W, Jakobi AJ, Kirkpatrick JM, Sachse C, Krausslich HG, Briggs JA: An atomic model of HIV-1 capsid-SP1 reveals structures regulating assembly and maturation. *Science* 2016, 353:506-508.
57. Wan W, Kolesnikova L, Clarke M, Koehler A, Noda T, Becker S, Briggs JAG: Structure and assembly of the Ebola virus nucleocapsid. *Nature* 2017, 551:394-397.
58. Grant T, Grigorieff N: Measuring the optimal exposure for single particle cryo-EM using a 2.6 A reconstruction of rotavirus VP6. *Elife* 2015, 4:e06980.
59. Grigorieff N: Three-dimensional structure of bovine NADH:ubiquinone oxidoreductase (complex I) at 22 A in ice. *J Mol Biol* 1998, 277:1033-1046.
60. Rohou A, Grigorieff N: CTFFIND4: Fast and accurate defocus estimation from electron micrographs. *J Struct Biol* 2015, 192:216-221.
61. Mindell JA, Grigorieff N: Accurate determination of local defocus and specimen tilt in electron microscopy. *J Struct Biol* 2003, 142:334-347.
62. Zivanov J, Nakane T, Scheres SHW: Estimation of high-order aberrations and anisotropic magnification from cryo-EM data sets in RELION-3.1. *IUCrJ* 2020, 7:253-267.
63. Turonova B, Schur FKM, Wan W, Briggs JAG: Efficient 3D-CTF correction for cryo-electron tomography using NovaCTF improves subtomogram averaging resolution to 3.4A. *J Struct Biol* 2017, 199:187-195.
64. Turonova B, Schur FKM, Wan W, Briggs JAG: Efficient 3D-CTF correction for cryo-electron tomography using NovaCTF improves subtomogram averaging resolution to 3.4 angstrom. *Journal of Structural Biology* 2017, 199:187-195.

65. Khavnekar S, Erdmann P, Wan W: TOMOMAN: Streamlining Cryo-electron Tomography and Subtomogram Averaging Workflows Using TOMOgram MANager. *Microsc Microanal* 2023, 29:1020.
66. Fernandez JJ, Li S: TomoAlign: A novel approach to correcting sample motion and 3D CTF in CryoET. *J Struct Biol* 2021, 213:107778.
67. Mastronarde DN: Accurate, automatic determination of astigmatism and phase with Ctfplotter in IMOD. *J Struct Biol* 2024, 216:108057.
68. Kremer JR, Mastronarde DN, McIntosh JR: Computer visualization of three-dimensional image data using IMOD. *J Struct Biol* 1996, 116:71-76.
69. Mastronarde DN, Held SR: Automated tilt series alignment and tomographic reconstruction in IMOD. *J Struct Biol* 2017, 197:102-113.
70. Castano-Diez D: The Dynamo package for tomography and subtomogram averaging: components for MATLAB, GPU computing and EC2 Amazon Web Services. *Acta Crystallogr D Struct Biol* 2017, 73:478-487.
71. De Rosier DJ, Klug A: Reconstruction of three dimensional structures from electron micrographs. *Nature* 1968, 217:130-134.
72. Crowther RA, Amos LA, Finch JT, De Rosier DJ, Klug A: Three dimensional reconstructions of spherical viruses by fourier synthesis from electron micrographs. *Nature* 1970, 226:421-425.
73. Gilbert PF: The reconstruction of a three-dimensional structure from projections and its application to electron microscopy. II. Direct methods. *Proc R Soc Lond B Biol Sci* 1972, 182:89-102.
74. Frangi AF, Niessen WJ, Vincken KL, Viergever MA: Multiscale vessel enhancement filtering. *Medical Image Computing and Computer-Assisted Intervention - Miccai'98* 1998, 1496:130-137.
75. Buades A, Coll B, Morel JM: A review of image denoising algorithms, with a new one. *Multiscale Modeling & Simulation* 2005, 4:490-530.
76. Buchholz T-O, Jordan M, Pigino G, Jug F: Cryo-care: content-aware image restoration for cryo-transmission electron microscopy data. In *2019 IEEE 16th International Symposium on Biomedical Imaging (ISBI 2019)*: IEEE: 2019:502-506.
77. Weigert M, Schmidt U, Boothe T, Muller A, Dibrov A, Jain A, Wilhelm B, Schmidt D, Broaddus C, Culley S, et al.: Content-aware image restoration: pushing the limits of fluorescence microscopy. *Nat Methods* 2018, 15:1090-1097.
78. Lehtinen J, Munkberg J, Hasselgren J, Laine S, Karras T, Aittala M, Aila T: Noise2Noise: Learning Image Restoration without Clean Data. *International Conference on Machine Learning, Vol 80* 2018, 80.
79. Forster F, Medalia O, Zauberman N, Baumeister W, Fass D: Retrovirus envelope protein complex structure in situ studied by cryo-electron tomography. *Proc Natl Acad Sci U S A* 2005, 102:4729-4734.
80. Schur FK: Toward high-resolution in situ structural biology with cryo-electron tomography and subtomogram averaging. *Curr Opin Struct Biol* 2019, 58:1-9.
81. Hrabe T, Chen Y, Pfeffer S, Cuellar LK, Mangold AV, Forster F: PyTom: a python-based toolbox for localization of macromolecules in cryo-electron tomograms and subtomogram analysis. *J Struct Biol* 2012, 178:177-188.
82. Nickell S, Forster F, Linaroudis A, Net WD, Beck F, Hegerl R, Baumeister W, Plitzko JM: TOM software toolbox: acquisition and analysis for electron tomography. *J Struct Biol* 2005, 149:227-234.
83. Castano-Diez D, Kudryashev M, Arheit M, Stahlberg H: Dynamo: a flexible, user-friendly development tool for subtomogram averaging of cryo-EM data in high-performance computing environments. *J Struct Biol* 2012, 178:139-151.
84. Walz J, Typke D, Nitsch M, Koster AJ, Hegerl R, Baumeister W: Electron Tomography of Single Ice-Embedded Macromolecules: Three-Dimensional Alignment and Classification. *J Struct Biol* 1997, 120:387-395.

85. Frangakis AS, Bohm J, Forster F, Nickell S, Nicastro D, Typke D, Hegerl R, Baumeister W: Identification of macromolecular complexes in cryoelectron tomograms of phantom cells. *Proc Natl Acad Sci U S A* 2002, 99:14153-14158.
86. Burbaum L, Schneider J, Scholze S, Bottcher RT, Baumeister W, Schwille P, Plitzko JM, Jasnin M: Molecular-scale visualization of sarcomere contraction within native cardiomyocytes. *Nat Commun* 2021, 12:4086.
87. Lamm L, Righetto RD, Wietrzynski W, Poge M, Martinez-Sanchez A, Peng T, Engel BD: MemBrain: A deep learning-aided pipeline for detection of membrane proteins in Cryo-electron tomograms. *Comput Methods Programs Biomed* 2022, 224:106990.
88. Henderson R: Avoiding the pitfalls of single particle cryo-electron microscopy: Einstein from noise. *Proc Natl Acad Sci U S A* 2013, 110:18037-18041.
89. Martinez-Sanchez A, Kochovski Z, Laugks U, Meyer Zum Alten Borgloh J, Chakraborty S, Pfeffer S, Baumeister W, Lucic V: Template-free detection and classification of membrane-bound complexes in cryo-electron tomograms. *Nat Methods* 2020, 17:209-216.
90. Sandberg K, Brega M: Segmentation of thin structures in electron micrographs using orientation fields. *J Struct Biol* 2007, 157:403-415.
91. Rigort A, Gunther D, Hegerl R, Baum D, Weber B, Prohaska S, Medalia O, Baumeister W, Hege HC: Automated segmentation of electron tomograms for a quantitative description of actin filament networks. *J Struct Biol* 2012, 177:135-144.
92. Rice G, Wagner T, Stabrin M, Sitsel O, Prumbaum D, Raunser S: TomoTwin: generalized 3D localization of macromolecules in cryo-electron tomograms with structural data mining. *Nat Methods* 2023, 20:871-880.
93. de Teresa-Trueba I, Goetz SK, Mattausch A, Stojanovska F, Zimmerli CE, Toro-Nahuelpan M, Cheng DWC, Tollervey F, Pape C, Beck M, et al.: Convolutional networks for supervised mining of molecular patterns within cellular context. *Nat Methods* 2023, 20:284-294.
94. Moebel E, Martinez-Sanchez A, Lamm L, Righetto RD, Wietrzynski W, Albert S, Lariviere D, Fourmentin E, Pfeffer S, Ortiz J, et al.: Deep learning improves macromolecule identification in 3D cellular cryo-electron tomograms. *Nat Methods* 2021, 18:1386-1394.
95. Lamm L, Zufferey S, Righetto RD, Wietrzynski W, Yamauchi KA, Burt A, Liu Y, Zhang H, Martinez-Sanchez A, Ziegler S, et al.: MemBrain v2: an end-to-end tool for the analysis of membranes in cryo-electron tomography. *bioRxiv* 2024:2024.2001.2005.574336.
96. Tegunov D, Xue L, Dienemann C, Cramer P, Mahamid J: Multi-particle cryo-EM refinement with M visualizes ribosome-antibiotic complex at 3.5 A in cells. *Nat Methods* 2021, 18:186-193.
97. Wan W, Khavnekar S, Wagner J: STOPGAP, an open-source package for template matching, subtomogram alignment, and classification. *bioRxiv* 2023:2023.2012.2020.572665.
98. Scheres SH, Chen S: Prevention of overfitting in cryo-EM structure determination. *Nat Methods* 2012, 9:853-854.
99. van Heel M, Schatz M: Fourier shell correlation threshold criteria. *J Struct Biol* 2005, 151:250-262.
100. Saxton WO, Baumeister W: The correlation averaging of a regularly arranged bacterial cell envelope protein. *J Microsc* 1982, 127:127-138.
101. Rosenthal PB, Henderson R: Optimal determination of particle orientation, absolute hand, and contrast loss in single-particle electron cryomicroscopy. *J Mol Biol* 2003, 333:721-745.
102. Himes BA, Zhang P: emClarity: software for high-resolution cryo-electron tomography and subtomogram averaging. *Nat Methods* 2018, 15:955-961.
103. Zivanov J, Oton J, Ke Z, von Kugelgen A, Pyle E, Qu K, Morado D, Castano-Diez D, Zanetti G, Bharat TAM, et al.: A Bayesian approach to single-particle electron cryo-tomography in RELION-4.0. *Elife* 2022, 11.
104. Blanchoin L, Boujemaa-Paterski R, Sykes C, Plastino J: Actin dynamics, architecture, and mechanics in cell motility. *Physiol Rev* 2014, 94:235-263.
105. Svitkina T: The Actin Cytoskeleton and Actin-Based Motility. *Cold Spring Harb Perspect Biol* 2018, 10.

106. Dominguez R, Holmes KC: Actin structure and function. *Annu Rev Biophys* 2011, 40:169-186.
107. Pollard TD: Actin and Actin-Binding Proteins. *Cold Spring Harb Perspect Biol* 2016, 8.
108. Kabsch W, Mannherz HG, Suck D, Pai EF, Holmes KC: Atomic structure of the actin:DNase I complex. *Nature* 1990, 347:37-44.
109. Graceffa P, Dominguez R: Crystal structure of monomeric actin in the ATP state. Structural basis of nucleotide-dependent actin dynamics. *J Biol Chem* 2003, 278:34172-34180.
110. Gunning PW, Ghoshdastider U, Whitaker S, Popp D, Robinson RC: The evolution of compositionally and functionally distinct actin filaments. *J Cell Sci* 2015, 128:2009-2019.
111. Oda T, Iwasa M, Aihara T, Maeda Y, Narita A: The nature of the globular- to fibrous-actin transition. *Nature* 2009, 457:441-445.
112. Blanchoin L, Pollard TD: Hydrolysis of ATP by polymerized actin depends on the bound divalent cation but not profilin. *Biochemistry* 2002, 41:597-602.
113. Merino F, Pospich S, Funk J, Wagner T, Kullmer F, Arndt HD, Bieling P, Raunser S: Structural transitions of F-actin upon ATP hydrolysis at near-atomic resolution revealed by cryo-EM. *Nat Struct Mol Biol* 2018, 25:528-537.
114. Huxley HE: Electron Microscope Studies on the Structure of Natural and Synthetic Protein Filaments from Striated Muscle. *J Mol Biol* 1963, 7:281-308.
115. Pollard TD: Rate constants for the reactions of ATP- and ADP-actin with the ends of actin filaments. *J Cell Biol* 1986, 103:2747-2754.
116. Carlier MF: Measurement of Pi dissociation from actin filaments following ATP hydrolysis using a linked enzyme assay. *Biochem Biophys Res Commun* 1987, 143:1069-1075.
117. Oosterheert W, Blanc FEC, Roy A, Belyy A, Sanders MB, Hofnagel O, Hummer G, Bieling P, Raunser S: Molecular mechanisms of inorganic-phosphate release from the core and barbed end of actin filaments. *Nat Struct Mol Biol* 2023, 30:1774-1785.
118. Oosterheert W, Klink BU, Belyy A, Pospich S, Raunser S: Structural basis of actin filament assembly and aging. *Nature* 2022, 611:374-379.
119. Sept D, McCammon JA: Thermodynamics and kinetics of actin filament nucleation. *Biophys J* 2001, 81:667-674.
120. Lappalainen P, Kotila T, Jegou A, Romet-Lemonne G: Biochemical and mechanical regulation of actin dynamics. *Nat Rev Mol Cell Biol* 2022, 23:836-852.
121. Machesky LM, Atkinson SJ, Ampe C, Vandekerckhove J, Pollard TD: Purification of a cortical complex containing two unconventional actins from Acanthamoeba by affinity chromatography on profilin-agarose. *J Cell Biol* 1994, 127:107-115.
122. Robinson RC, Turbedsky K, Kaiser DA, Marchand JB, Higgs HN, Choe S, Pollard TD: Crystal structure of Arp2/3 complex. *Science* 2001, 294:1679-1684.
123. Amann KJ, Pollard TD: The Arp2/3 complex nucleates actin filament branches from the sides of pre-existing filaments. *Nat Cell Biol* 2001, 3:306-310.
124. Fassler F, Dimchev G, Hodirnau VV, Wan W, Schur FKM: Cryo-electron tomography structure of Arp2/3 complex in cells reveals new insights into the branch junction. *Nat Commun* 2020, 11:6437.
125. Svitkina TM, Borisy GG: Arp2/3 complex and actin depolymerizing factor/cofilin in dendritic organization and treadmilling of actin filament array in lamellipodia. *J Cell Biol* 1999, 145:1009-1026.
126. Small JV: Organization of actin in the leading edge of cultured cells: influence of osmium tetroxide and dehydration on the ultrastructure of actin meshworks. *J Cell Biol* 1981, 91:695-705.
127. Pollard TD: Regulation of actin filament assembly by Arp2/3 complex and formins. *Annu Rev Biophys Biomol Struct* 2007, 36:451-477.
128. Rottner K, Stradal TEB, Chen B: WAVE regulatory complex. *Curr Biol* 2021, 31:R512-R517.

129. Fassler F, Javoor MG, Datler J, Doring H, Hofer FW, Dimchev G, Hodirnau VV, Faix J, Rottner K, Schur FKM: ArpC5 isoforms regulate Arp2/3 complex-dependent protrusion through differential Ena/VASP positioning. *Sci Adv* 2023, 9:eadd6495.
130. Hetrick B, Han MS, Helgeson LA, Nolen BJ: Small molecules CK-666 and CK-869 inhibit actin-related protein 2/3 complex by blocking an activating conformational change. *Chem Biol* 2013, 20:701-712.
131. Pruyne D, Evangelista M, Yang C, Bi E, Zigmond S, Bretscher A, Boone C: Role of formins in actin assembly: nucleation and barbed-end association. *Science* 2002, 297:612-615.
132. Xu Y, Moseley JB, Sagot I, Poy F, Pellman D, Goode BL, Eck MJ: Crystal structures of a Formin Homology-2 domain reveal a tethered dimer architecture. *Cell* 2004, 116:711-723.
133. Merino F, Pospich S, Raunser S: Towards a structural understanding of the remodeling of the actin cytoskeleton. *Semin Cell Dev Biol* 2020, 102:51-64.
134. Mockrin SC, Korn ED: Acanthamoeba profilin interacts with G-actin to increase the rate of exchange of actin-bound adenosine 5'-triphosphate. *Biochemistry* 1980, 19:5359-5362.
135. Vinson VK, De La Cruz EM, Higgs HN, Pollard TD: Interactions of Acanthamoeba profilin with actin and nucleotides bound to actin. *Biochemistry* 1998, 37:10871-10880.
136. Carlier MF, Laurent V, Santolini J, Melki R, Didry D, Xia GX, Hong Y, Chua NH, Pantaloni D: Actin depolymerizing factor (ADF/cofilin) enhances the rate of filament turnover: implication in actin-based motility. *J Cell Biol* 1997, 136:1307-1322.
137. McCullough BR, Grintsevich EE, Chen CK, Kang H, Hutchison AL, Henn A, Cao W, Suarez C, Martiel JL, Blanchoin L, et al.: Cofilin-linked changes in actin filament flexibility promote severing. *Biophys J* 2011, 101:151-159.
138. Chan C, Beltzner CC, Pollard TD: Cofilin dissociates Arp2/3 complex and branches from actin filaments. *Curr Biol* 2009, 19:537-545.
139. Edwards M, Zwolak A, Schafer DA, Sept D, Dominguez R, Cooper JA: Capping protein regulators fine-tune actin assembly dynamics. *Nat Rev Mol Cell Biol* 2014, 15:677-689.
140. Isenberg G, Aebi U, Pollard TD: An actin-binding protein from Acanthamoeba regulates actin filament polymerization and interactions. *Nature* 1980, 288:455-459.
141. Rao JN, Madasu Y, Dominguez R: Mechanism of actin filament pointed-end capping by tropomodulin. *Science* 2014, 345:463-467.
142. Liem RK: Cytoskeletal Integrators: The Spectrin Superfamily.*Cold Spring Harb Perspect Biol* 2016, 8.
143. Morley SC: The actin-bundling protein L-plastin: a critical regulator of immune cell function. *Int J Cell Biol* 2012, 2012:935173.
144. Klein MG, Shi W, Ramagopal U, Tseng Y, Wirtz D, Kovar DR, Staiger CJ, Almo SC: Structure of the actin crosslinking core of fimbrin. *Structure* 2004, 12:999-1013.
145. Jansen S, Collins A, Yang C, Rebowski G, Svitkina T, Dominguez R: Mechanism of actin filament bundling by fascin. *J Biol Chem* 2011, 286:30087-30096.
146. Sjoblom B, Salmazo A, Djinovic-Carugo K: Alpha-actinin structure and regulation. *Cell Mol Life Sci* 2008, 65:2688-2701.
147. Ribeiro Ede A, Jr., Pinotsis N, Ghisleni A, Salmazo A, Konarev PV, Kostan J, Sjoblom B, Schreiner C, Polyansky AA, Gkougkoulia EA, et al.: The structure and regulation of human muscle alpha-actinin. *Cell* 2014, 159:1447-1460.
148. Sutherland-Smith AJ: Filamin structure, function and mechanics: are altered filamin-mediated force responses associated with human disease? *Biophys Rev* 2011, 3:15-23.
149. Ithychanda SS, Hsu D, Li H, Yan L, Liu DD, Das M, Plow EF, Qin J: Identification and characterization of multiple similar ligand-binding repeats in filamin: implication on filamin-mediated receptor clustering and cross-talk. *J Biol Chem* 2009, 284:35113-35121.
150. Peskin CS, Odell GM, Oster GF: Cellular motions and thermal fluctuations: the Brownian ratchet. *Biophys. J.* 1993, 65:316-324.
151. Hill TL, Kirschner MW: Bioenergetics and kinetics of microtubule and actin filament assembly-disassembly. *International review of cytology* 1982, 78:1-125.

152. Hill TL: Microfilament or microtubule assembly or disassembly against a force. *Proc Natl Acad Sci U S A* 1981, 78:5613-5617.
153. Dmitrieff S, Nedelec F: Amplification of actin polymerization forces. *J Cell Biol* 2016, 212:763-766.
154. Footer MJ, Kerssemakers JW, Theriot JA, Dogterom M: Direct measurement of force generation by actin filament polymerization using an optical trap. *Proc. Natl. Acad. Sci. U.S.A.* 2007, 104:2181-2186.
155. Mogilner A, Oster G: Cell motility driven by actin polymerization. *Biophys. J.* 1996, 71:3030-3045.
156. Wu JQ, Pollard TD: Counting cytokinesis proteins globally and locally in fission yeast. *Science* 2005, 310:310-314.
157. Mueller J, Szep G, Nemethova M, de Vries I, Lieber AD, Winkler C, Kruse K, Small JV, Schmeiser C, Keren K, et al.: Load Adaptation of Lamellipodial Actin Networks. *Cell* 2017, 171:188-200 e116.
158. Prass M, Jacobson K, Mogilner A, Radmacher M: Direct measurement of the lamellipodial protrusive force in a migrating cell. *J Cell Biol* 2006, 174:767-772.
159. Jasnin M, Hervy J, Balor S, Bouissou A, Proag A, Voituriez R, Schneider J, Mangeat T, Maridonneau-Parini I, Baumeister W, et al.: Elasticity of podosome actin networks produces nanonewton protrusive forces. *Nat Commun* 2022, 13:3842.
160. Vale RD, Milligan RA: The way things move: looking under the hood of molecular motor proteins. *Science* 2000, 288:88-95.
161. Vicente-Manzanares M, Ma X, Adelstein RS, Horwitz AR: Non-muscle myosin II takes centre stage in cell adhesion and migration. *Nat Rev Mol Cell Biol* 2009, 10:778-790.
162. von der Ecken J, Heissler SM, Pathan-Chhatbar S, Manstein DJ, Raunser S: Cryo-EM structure of a human cytoplasmic actomyosin complex at near-atomic resolution. *Nature* 2016, 534:724-728.
163. Davies LC, Jenkins SJ, Allen JE, Taylor PR: Tissue-resident macrophages. *Nat Immunol* 2013, 14:986-995.
164. Maridonneau-Parini I: Control of macrophage 3D migration: a therapeutic challenge to limit tissue infiltration. *Immunol Rev* 2014, 262:216-231.
165. Varol C, Mildner A, Jung S: Macrophages: development and tissue specialization. *Annu Rev Immunol* 2015, 33:643-675.
166. Benoit M, Desnues B, Mege JL: Macrophage polarization in bacterial infections. *J Immunol* 2008, 181:3733-3739.
167. Mantovani A, Biswas SK, Galdiero MR, Sica A, Locati M: Macrophage plasticity and polarization in tissue repair and remodelling. *J Pathol* 2013, 229:176-185.
168. Qian BZ, Pollard JW: Macrophage diversity enhances tumor progression and metastasis. *Cell* 2010, 141:39-51.
169. Frantz C, Stewart KM, Weaver VM: The extracellular matrix at a glance. *J Cell Sci* 2010, 123:4195-4200.
170. Jarvelainen H, Sainio A, Koulu M, Wight TN, Penttinen R: Extracellular matrix molecules: potential targets in pharmacotherapy. *Pharmacol Rev* 2009, 61:198-223.
171. Butcher DT, Alliston T, Weaver VM: A tense situation: forcing tumour progression. *Nat Rev Cancer* 2009, 9:108-122.
172. Van Goethem E, Poincloux R, Gauffre F, Maridonneau-Parini I, Le Cabec V: Matrix architecture dictates three-dimensional migration modes of human macrophages: differential involvement of proteases and podosome-like structures. *J Immunol* 2010, 184:1049-1061.
173. Van Goethem E, Guiet R, Balor S, Charriere GM, Poincloux R, Labrousse A, Maridonneau-Parini I, Le Cabec V: Macrophage podosomes go 3D. *Eur J Cell Biol* 2011, 90:224-236.
174. Wolf K, Te Lindert M, Krause M, Alexander S, Te Riet J, Willis AL, Hoffman RM, Figdor CG, Weiss SJ, Friedl P: Physical limits of cell migration: control by ECM space and nuclear deformation and tuning by proteolysis and traction force. *J Cell Biol* 2013, 201:1069-1084.

175. Linder S: The matrix corroded: podosomes and invadopodia in extracellular matrix degradation. *Trends Cell Biol* 2007, 17:107-117.
176. Linder S, Wiesner C: Feel the force: Podosomes in mechanosensing. *Exp Cell Res* 2016, 343:67-72.
177. van den Dries K, Nahidiazar L, Slotman JA, Meddens MBM, Pandzic E, Joosten B, Ansems M, Schouwstra J, Meijer A, Steen R, et al.: Modular actin nano-architecture enables podosome protrusion and mechanosensing. *Nat Commun* 2019, 10:5171.
178. Linder S, Cervero P, Eddy R, Condeelis J: Mechanisms and roles of podosomes and invadopodia. *Nat Rev Mol Cell Biol* 2023, 24:86-106.
179. Linder S, Higgs H, Hufner K, Schwarz K, Pannicke U, Aepfelbacher M: The polarization defect of Wiskott-Aldrich syndrome macrophages is linked to dislocalization of the Arp2/3 complex. *J Immunol* 2000, 165:221-225.
180. Linder S, Nelson D, Weiss M, Aepfelbacher M: Wiskott-Aldrich syndrome protein regulates podosomes in primary human macrophages. *Proc Natl Acad Sci U S A* 1999, 96:9648-9653.
181. Burns S, Thrasher AJ, Blundell MP, Machesky L, Jones GE: Configuration of human dendritic cell cytoskeleton by Rho GTPases, the WAS protein, and differentiation. *Blood* 2001, 98:1142-1149.
182. Destaing O, Saltel F, Geminard JC, Jurdic P, Bard F: Podosomes display actin turnover and dynamic self-organization in osteoclasts expressing actin-green fluorescent protein. *Mol Biol Cell* 2003, 14:407-416.
183. Osiak AE, Zenner G, Linder S: Subconfluent endothelial cells form podosomes downstream of cytokine and RhoGTPase signaling. *Exp Cell Res* 2005, 307:342-353.
184. Murphy DA, Diaz B, Bromann PA, Tsai JH, Kawakami Y, Maurer J, Stewart RA, Izpisua-Belmonte JC, Courtneidge SA: A Src-Tks5 pathway is required for neural crest cell migration during embryonic development. *PLoS One* 2011, 6:e22499.
185. Murphy DA, Courtneidge SA: The 'ins' and 'outs' of podosomes and invadopodia: characteristics, formation and function. *Nat Rev Mol Cell Biol* 2011, 12:413-426.
186. David-Pfeuty T, Singer SJ: Altered distributions of the cytoskeletal proteins vinculin and alpha-actinin in cultured fibroblasts transformed by Rous sarcoma virus. *Proc Natl Acad Sci U S A* 1980, 77:6687-6691.
187. Tarone G, Cirillo D, Giancotti FG, Comoglio PM, Marchisio PC: Rous sarcoma virus-transformed fibroblasts adhere primarily at discrete protrusions of the ventral membrane called podosomes. *Exp Cell Res* 1985, 159:141-157.
188. Labernadie A, Bouissou A, Delobelle P, Balor S, Voituriez R, Proag A, Fourquaux I, Thibault C, Vieu C, Poincloux R, et al.: Protrusion force microscopy reveals oscillatory force generation and mechanosensing activity of human macrophage podosomes. *Nat Commun* 2014, 5:5343.
189. Linder S, Cervero P: The podosome cap: past, present, perspective. *Eur J Cell Biol* 2020, 99:151087.
190. Cervero P, Himmel M, Kruger M, Linder S: Proteomic analysis of podosome fractions from macrophages reveals similarities to spreading initiation centres. *Eur J Cell Biol* 2012, 91:908-922.
191. van den Dries K, Schwartz SL, Byars J, Meddens MB, Bolomini-Vittori M, Lidke DS, Figdor CG, Lidke KA, Cambi A: Dual-color superresolution microscopy reveals nanoscale organization of mechanosensory podosomes. *Mol Biol Cell* 2013, 24:2112-2123.
192. Panzer L, Trube L, Klose M, Joosten B, Slotman J, Cambi A, Linder S: The formins FHOD1 and INF2 regulate inter- and intra-structural contractility of podosomes. *J Cell Sci* 2016, 129:298-313.
193. Joosten B, Willemse M, Fransen J, Cambi A, van den Dries K: Super-Resolution Correlative Light and Electron Microscopy (SR-CLEM) Reveals Novel Ultrastructural Insights Into Dendritic Cell Podosomes. *Front Immunol* 2018, 9:1908.
194. Cambi A, Chavrier P: Tissue remodeling by invadosomes. *Fac Rev* 2021, 10:39.
195. van den Dries K, Bolomini-Vittori M, Cambi A: Spatiotemporal organization and mechanosensory function of podosomes. *Cell Adh Migr* 2014, 8:268-272.

196. van den Dries K, Meddens MB, de Keijzer S, Shekhar S, Subramaniam V, Figdor CG, Cambi A: Interplay between myosin IIA-mediated contractility and actin network integrity orchestrates podosome composition and oscillations. *Nat Commun* 2013, 4:1412.
197. Kuo SL, Chen CL, Pan YR, Chiu WT, Chen HC: Biogenesis of podosome rosettes through fission. *Sci Rep* 2018, 8:524.
198. Georgess D, Machuca-Gayet I, Blangy A, Jurdic P: Podosome organization drives osteoclast-mediated bone resorption. *Cell Adh Migr* 2014, 8:191-204.
199. Luxenburg C, Geblinger D, Klein E, Anderson K, Hanein D, Geiger B, Addadi L: The architecture of the adhesive apparatus of cultured osteoclasts: from podosome formation to sealing zone assembly. *PLoS One* 2007, 2:e179.
200. Akisaka T, Yoshida A: Scattered podosomes and podosomes associated with the sealing zone architecture in cultured osteoclasts revealed by cell shearing, quick freezing, and platinum-replica electron microscopy. *Cytoskeleton (Hoboken)* 2019, 76:303-321.
201. Bouissou A, Proag A, Bourg N, Pingris K, Cabriel C, Balor S, Mangeat T, Thibault C, Vieu C, Dupuis G, et al.: Podosome Force Generation Machinery: A Local Balance between Protrusion at the Core and Traction at the Ring. *ACS Nano* 2017, 11:4028-4040.
202. Linder S, Hufner K, Wintergerst U, Aepfelbacher M: Microtubule-dependent formation of podosomal adhesion structures in primary human macrophages. *J Cell Sci* 2000, 113 Pt 23:4165-4176.
203. Weber K, Hey S, Cervero P, Linder S: The circle of life: Phases of podosome formation, turnover and reemergence. *Eur J Cell Biol* 2022, 101:151218.
204. Tsujita K, Itoh T: Phosphoinositides in the regulation of actin cortex and cell migration. *Biochim Biophys Acta* 2015, 1851:824-831.
205. Zhou Y, Feng Z, Cao F, Liu X, Xia X, Yu CH: Abl-mediated PI3K activation regulates macrophage podosome formation. *J Cell Sci* 2020, 133.
206. Oikawa T, Itoh T, Takenawa T: Sequential signals toward podosome formation in NIH-src cells. *J Cell Biol* 2008, 182:157-169.
207. Huveneers S, Arslan S, van de Water B, Sonnenberg A, Danen EH: Integrins uncouple Src-induced morphological and oncogenic transformation. *J Biol Chem* 2008, 283:13243-13251.
208. Rohatgi R, Ho HY, Kirschner MW: Mechanism of N-WASP activation by CDC42 and phosphatidylinositol 4, 5-bisphosphate. *J Cell Biol* 2000, 150:1299-1310.
209. Foxall E, Pipili A, Jones GE, Wells CM: Significance of kinase activity in the dynamic invadosome. *Eur J Cell Biol* 2016, 95:483-492.
210. Cory GO, Garg R, Cramer R, Ridley AJ: Phosphorylation of tyrosine 291 enhances the ability of WASp to stimulate actin polymerization and filopodium formation. Wiskott-Aldrich Syndrome protein. *J Biol Chem* 2002, 277:45115-45121.
211. Gu Z, Kordowska J, Williams GL, Wang CL, Hai CM: Erk1/2 MAPK and caldesmon differentially regulate podosome dynamics in A7r5 vascular smooth muscle cells. *Exp Cell Res* 2007, 313:849-866.
212. Van Audenhove I, Debeuf N, Boucherie C, Gettemans J: Fascin actin bundling controls podosome turnover and disassembly while cortactin is involved in podosome assembly by its SH3 domain in THP-1 macrophages and dendritic cells. *Biochim Biophys Acta* 2015, 1853:940-952.
213. Labernadie A, Bouissou A, Delobelle P, Balor S, Voituriez R, Proag A, Fourquaux I, Thibault C, Vieu C, Poincloux R, et al.: Protrusion force microscopy reveals oscillatory force generation and mechanosensing activity of human macrophage podosomes. *Nat. Commun.* 2014, 5:5343.
214. Proag A, Bouissou A, Mangeat T, Voituriez R, Delobelle P, Thibault C, Vieu C, Maridonneau-Parini I, Poincloux R: Working together: spatial synchrony in the force and actin dynamics of podosome first neighbors. *ACS Nano* 2015, 9:3800-3813.
215. Marchisio PC, Bergui L, Corbascio GC, Cremona O, D'Urso N, Schena M, Tesio L, Caligaris-Cappio F: Vinculin, talin, and integrins are localized at specific adhesion sites of malignant B lymphocytes. *Blood* 1988, 72:830-833.

216. Zambonin-Zallone A, Teti A, Grano M, Rubinacci A, Abbadini M, Gaboli M, Marchisio PC: Immunocytochemical distribution of extracellular matrix receptors in human osteoclasts: a beta 3 integrin is colocalized with vinculin and talin in the podosomes of osteoclastoma giant cells. *Exp Cell Res* 1989, 182:645-652.
217. Squire JM: Architecture and function in the muscle sarcomere. *Curr Opin Struct Biol* 1997, 7:247-257.
218. Huxley H, Hanson J: Changes in the cross-striations of muscle during contraction and stretch and their structural interpretation. *Nature* 1954, 173:973-976.
219. Huxley HE: Electron microscope studies of the organisation of the filaments in striated muscle. *Biochim Biophys Acta* 1953, 12:387-394.
220. Takahashi K, Hattori A: Alpha-actinin is a component of the Z-filament, a structural backbone of skeletal muscle Z-disks. *J Biochem* 1989, 105:529-536.
221. Wang K, Wright J: Architecture of the sarcomere matrix of skeletal muscle: immunoelectron microscopic evidence that suggests a set of parallel inextensible nebulin filaments anchored at the Z line. *J Cell Biol* 1988, 107:2199-2212.
222. Huxley HE: The Mechanism of Muscular Contraction. *Science* 1969, 164:1356-1365.
223. Huxley AF, Niedergerke R: Structural changes in muscle during contraction; interference microscopy of living muscle fibres. *Nature* 1954, 173:971-973.
224. Sweeney HL, Houdusse A: Structural and functional insights into the Myosin motor mechanism. *Annu Rev Biophys* 2010, 39:539-557.
225. Lymn RW, Taylor EW: Mechanism of adenosine triphosphate hydrolysis by actomyosin. . *Biochemistry* 1971, 10:4617-4624.
226. Geeves MA: Review: The ATPase mechanism of myosin and actomyosin. *Biopolymers* 2016, 105:483-491.
227. Yamada Y, Namba K, Fujii T: Cardiac muscle thin filament structures reveal calcium regulatory mechanism. *Nat Commun* 2020, 11:153.
228. Lehman W, Craig R, Vibert P: Ca(2+)-induced tropomyosin movement in Limulus thin filaments revealed by three-dimensional reconstruction. *Nature* 1994, 368:65-67.
229. Clarke M, Schatten G, Mazia D, Spudich JA: Visualization of actin fibers associated with the cell membrane in amoebae of Dictyostelium discoideum. *Proc Natl Acad Sci U S A* 1975, 72:1758-1762.
230. Morone N, Usukura E, Narita A, Usukura J: Improved unroofing protocols for cryo-electron microscopy, atomic force microscopy and freeze-etching electron microscopy and the associated mechanisms. *Microscopy (Oxf)* 2020, 69:350-359.
231. Jasnin M, Asano S, Gouin E, Hegerl R, Plitzko JM, Villa E, Cossart P, Baumeister W: Three-dimensional architecture of actin filaments in Listeria monocytogenes comet tails. *Proc Natl Acad Sci U S A* 2013, 110:20521-20526.
232. Martins B, Sorrentino S, Chung WL, Tatli M, Medalia O, Eibauer M: Unveiling the polarity of actin filaments by cryo-electron tomography. *Structure* 2021, 29:488-498 e484.
233. Akisaka T, Yoshida A: Visualization of structural organization of ventral membranes of sheared-open resorbing osteoclasts attached to apatite pellets. *Cell Tissue Res* 2015, 360:347-362.
234. Schoumacher M, Goldman RD, Louvard D, Vignjevic DM: Actin, microtubules, and vimentin intermediate filaments cooperate for elongation of invadopodia. *Journal of Cell Biology* 2010, 189:541-556.
235. Breitsprecher D, Kiesewetter AK, Linkner J, Urbanke C, Resch GP, Small JV, Faix J: Clustering of VASP actively drives processive, WH2 domain-mediated actin filament elongation. *EMBO J* 2008, 27:2943-2954.
236. Gordon AM, Huxley AF, Julian FJ: The variation in isometric tension with sarcomere length in vertebrate muscle fibres. *J Physiol* 1966, 184:170-192.

237. Schiotz OH, Kaiser CJO, Klumpe S, Morado DR, Poege M, Schneider J, Beck F, Klebl DP, Thompson C, Plitzko JM: Serial Lift-Out: sampling the molecular anatomy of whole organisms. *Nat Methods* 2023.
238. Tamborrini D, Wang Z, Wagner T, Tacke S, Stabrin M, Grange M, Kho AL, Rees M, Bennett P, Gautel M, et al.: Structure of the native myosin filament in the relaxed cardiac sarcomere. *Nature* 2023, 623:863-871.
239. Wang Z, Grange M, Pospich S, Wagner T, Kho AL, Gautel M, Raunser S: Structures from intact myofibrils reveal mechanism of thin filament regulation through nebulin. *Science* 2022, 375:eabn1934.
240. Wang Z, Grange M, Wagner T, Kho AL, Gautel M, Raunser S: The molecular basis for sarcomere organization in vertebrate skeletal muscle. *Cell* 2021, 184:2135-2150 e2113.
241. Woldeyes RA, Nishiga M, Vander Roest AS, Engel L, Giri P, Montenegro GC, Wu AC, Dunn AR, Spudich JA, Bernstein D, et al.: Cryo-electron tomography reveals the structural diversity of cardiac proteins in their cellular context. *bioRxiv* 2023.
242. Foster HE, Ventura Santos C, Carter AP: A cryo-ET survey of microtubules and intracellular compartments in mammalian axons. *J Cell Biol* 2022, 221.
243. He S, Scheres SHW: Helical reconstruction in RELION. *J Struct Biol* 2017, 198:163-176.
244. Lucas BA, Himes BA, Xue L, Grant T, Mahamid J, Grigorieff N: Locating macromolecular assemblies in cells by 2D template matching with cisTEM. *Elife* 2021, 10.
245. Schorb M, Haberbosch I, Hagen WJH, Schwab Y, Mastronarde DN: Software tools for automated transmission electron microscopy. *Nat Methods* 2019, 16:471-477.
246. Zhang K: Gctf: Real-time CTF determination and correction. *J Struct Biol* 2016, 193:1-12.
247. Zheng S, Wolff G, Greenan G, Chen Z, Faas FGA, Barcena M, Koster AJ, Cheng Y, Agard DA: AreTomo: An integrated software package for automated marker-free, motion-corrected cryo-electron tomographic alignment and reconstruction. *J Struct Biol X* 2022, 6:100068.
248. Tegunov D, Cramer P: Real-time cryo-electron microscopy data preprocessing with Warp. *Nat Methods* 2019, 16:1146-1152.
249. Martinez-Sanchez A, Garcia I, Asano S, Lucic V, Fernandez JJ: Robust membrane detection based on tensor voting for electron tomography. *J Struct Biol* 2014, 186:49-61.
250. Stalling D, Westerhoff M, Hege H-C: 38 - amira: A Highly Interactive System for Visual Data Analysis. In *Visualization Handbook*. Edited by Hansen CD, Johnson CR: Butterworth-Heinemann; 2005:749-767.
251. Pettersen EF, Goddard TD, Huang CC, Couch GS, Greenblatt DM, Meng EC, Ferrin TE: UCSF Chimera--a visualization system for exploratory research and analysis. *J Comput Chem* 2004, 25:1605-1612.
252. Kroon D-J: https://www.mathworks.com/matlabcentral/fileexchange/24409-hessian-based-frangi-vesselness-filter, MATLAB Central File Exchange. Retrieved February 9, 2024.
253. Righetto RD: https://github.com/rdrighetto/STOPGAP Retrieved February 9, 2024.
254. Kremer JR, Mastronarde DN, McIntosh JR: Computer Visualization of Three-Dimensional Image Data Using IMOD. *Journal of Structural Biology* 1996, 116:71-76.
255. Gal O: https://www.mathworks.com/matlabcentral/fileexchange/3215-fit_ellipse, MATLAB Central File Exchange. Retrieved February 9, 2024.
256. Goddard TD, Huang CC, Meng EC, Pettersen EF, Couch GS, Morris JH, Ferrin TE: UCSF ChimeraX: Meeting modern challenges in visualization and analysis. *Protein Science* 2018, 27:14-25.
257. Ermel UH, Arghittu SM, Frangakis AS: ArtiaX: An electron tomography toolbox for the interactive handling of sub-tomograms in UCSF ChimeraX. *Protein Sci* 2022, 31:e4472.
258. Qu K, Glass B, Dolezal M, Schur FKM, Murciano B, Rein A, Rumlova M, Ruml T, Krausslich HG, Briggs JAG: Structure and architecture of immature and mature murine leukemia virus capsids. *Proc Natl Acad Sci U S A* 2018, 115:E11751-E11760.

Acknowledgements

There are many people I would like to thank, without whom this thesis would not exist.

I am grateful to Professor Wolfgang Baumeister, for giving me this unique opportunity to work in the field of cryo-electron tomography and the possibility to learn and explore so many exciting things during my time in his department.

I especially want to thank Marion Jasnin for her guidance, mentorship, and friendship. I am forever grateful for your support, our endless discussions about new data, exciting results and also everything else not science-related. It was a pleasure to work closely with you and be part of your scientific journey. I am happy for your success and excited to see your new lab taking off. I wish you all the best for the future.

I would like to thank Jürgen Plitzko for his continuous support, and together with John Briggs for establishing and maintaining a research infrastructure in the department that is second to none, and generously sharing it with the remaining members of the Baumeister group.

The projects of this thesis were collaborative efforts. Collaborations are one of the most important aspects of science and something I always enjoyed very much. In this regard, I wish to thank Renaud Poincloux and his team, especially Stéphanie Balor and Javier Ray-Barroso, for the long-term collaboration on the podosome project. Through establishing and providing cells, this allowed me to focus exclusively on tomography and data analysis, my favorite part. Moreover, the scientific discussions were always very insightful. I also really enjoyed meeting all of you at the Invadosome conference.

The sarcomere project was a very efficient collaboration with Laura Burbaum who I also wish to thank. When I saw these tomograms for the first time, I was super excited to start working on it. Most of the work was also done during the COVID-related lockdowns, but we managed to make good progress despite the circumstances.

There are many people in the department I would like to acknowledge. Birgit Book for her assistance in all organizational topics and PhD-related questions, and Inga Wolf for maintaining all computer hardware. I especially want to thank Florian Beck for maintaining the computing infrastructure, for his countless insights into processing-related questions and helpful feedback whenever I was stuck, William Wan for many discussions that taught me the basics of subtomogram averaging, Matthias Pöge, Ricardo Righetto, Philipp Erdmann and Sagar Khavnekar for help in various processing-related matters, and Victoria Trinkaus for her help at the FIBs. Moreover, I want to thank the entire Baumeister/Plitzko department. It was a privilege to work with so many great scientists and people. I will always remember our parties, concerts, volleyball sessions, and all the casual beers behind the department.

Most importantly, I want to thank my parents and my family for their love, their endless support, and their understanding during my academic journey.

Finally, I would like to thank my partner and best friend, Laura Hehl. Thank you for always believing in me and supporting me. You are the best thing in my life.